Development of a Very Flexible Testbed Aircraft for the Validation of Nonlinear Aeroelastic Codes

by

Jessica Renee Jones

A dissertation submitted in partial fulfillment

of the requirements for the degree of
Doctor of Philosophy
(Aerospace Engineering)
in the University of Michigan
2017

Doctoral Committee:

Professor Carlos E.S. Cesnik, Chair
Professor Peretz P. Friedmann
Professor Daniel J. Inman
Professor Yin Lu Young

Jessica R. Jones
jrenejo@umich.edu
ORCID iD: 0000-0002-1964-029X

Dedication

To God

To my mother

Acknowledgements

I would like to thank my advisor, Prof. Carlos Cesnik for his invaluable guidance over the years. I would also like to thank my committee for their advice and suggestions during the review of this dissertation.

I would also like to acknowledge the support of the many sponsors for this work. The flight test and development of X-HALE has been supported in part by the Air Force Research Laboratory under the Michigan/AFRL Collaborative Center in Aeronautical Sciences (MACCAS). The technical monitor was Edward Alyanak (AFRL/RZ). Additional funds were also provided by the University of Michigan's Active Aeroelasticity and Structures Research Laboratory. The X-56A modeling effort was supported by the NASA Fixed Wing Program with Peter Suh as the technical monitor. Additional acknowledgements are offered to Lockheed Martin for providing details of the X-56A aircraft. Additional technical assistance from Ben Smith of Aurora Flight Sciences is highly appreciated. I am also grateful for the three years of support from the National Science Foundation Graduate Student Research Fellowship under Grant No. DGE 0718128. Opinions, interpretations, conclusions, and recommendations are those of the author and are not necessarily endorsed by the United States Government.

A thousand million thank yous to all of the high school students, undergrads (U-M and non-UM), and grad students who have contributed to the X-HALE project, many of whom are referenced in this dissertation. A special thanks goes to Keith Shaw for being a phenomenal pilot and endless fount of knowledge and stories. A shout-out as well to my X-HALE collaborator and labmate Zi Yang Pang—one day we'll fly away.

The support and friendship of my fellow A^2SRL-ians, both past and present has been greatly appreciated, including my dissertation buddy Ryan Klock, Christopher Lupp, Eric Huang, Ryan Kitson, Renato Medeiros, Patricia Teixeira, Maj. Steve Chetcuti, Maj. Matt Obenchain, Kalyan Nadella, Devesh Kumar, Prof. Yangfeng Shen, and Prof. Weihua Su.

I also want to thank my IMPACT family, especially my wonderful friends Joy Jeyaratnam, Anita Luong, Yining Lu for being my life outside the lab. You were constant sources of humor, dramas, and nourishment, both physical and spiritual. Words fail to express how much you all mean to me, so the next time we meet, I will use chocolate.

Finally, I owe my deepest gratitude to my staunchest cheerleader, my sister, Jasmine Jones, for her lifelong support. Completing this journey together isn't the end of an era, it's the beginning of one.

Table of Contents

List of Tables

List of Figures

List of Appendices

List of Abbreviations

1-D	one-dimensional
2-D	two-dimensional
3-D	three-dimensional
7FEW	seven lb of fuel, empty water ballast
n-dof	n-degree-of-freedom
ac	aerodynamic center
ABT	antisymmetric coupled bending-torsion structural mode
ATSB	antisymmetric torsion coupled with symmetric bending coupled mode
ATV	aeroelastic test vehicle
BFF	body freedom flutter
CAD	computer aided design
CFD	computational fluid dynamics
DAQ	data acquisition system
EFEW	empty fuel, empty water ballast
FFEW	full fuel, empty water ballast
GVT	ground vibration testing
HALE	high altitude long endurance
FEM	finite element method
FEA	finite element analysis
FFT	fast Fourier transform
FRF	frequency response function
LE	leading edge
TE	trailing edge
RA	reference axis
RPM	rotations per minute
RRV	risk reduction vehicle

SBT	coupled bending-torsion structural mode
UAV	unmanned aerial vehicle
VFA	very flexible aircraft
V-f	velocity frequency
V-g	velocity-damping
VLM	vortex lattice method
X-HALE	experimental high altitude long endurance aircraft

List of Symbols

A	amplitude
A_{eng}	area of propeller disk
b	semi-chord
C^{Ba}	rotation matrix from body frame to aerodynamic frame
C_D	aircraft drag coefficient
c_d	airfoil drag coefficient
C_L	aircraft lift coefficient
c_l	airfoil lift coefficient
$c_{l\alpha}$	airfoil lift coefficient slope with respect to angle of attack
C_M	aircraft moment coeffient
c_m	airfoil moment coeffient
c_n	chord of element n
D	aircraft drag
D^{bw}	directional cosine from frame b to w
d_{ac}	aerodynamic drag per unit length acting at the aerodynamic center
d_{ra}	aerodynamic drag per unit length acting at the reference axis
d_i	drag in aircraft region i
d	distance between the reference axis and midchord
E	Young's modulus
EA	axial bending stiffness
EI_{yy}	in-plane (fore-aft) bending stiffness
EI_{zz}	vertical bending stiffness
$EI_{xy}, EI_{yz}, EI_{xz}$	coupled bending stiffness terms
F_i	applied force in global frame ($i = X$, Y, or Z)
f	frequency
g	acceleration of gravity

g_n	ratio of chord length between element 1 and element n
GJ	torsional modulus of rigidity
h	nodal displacement vector
I_{xx}, I_{yy}, I_{zz}	mass moment of inertia in local beam coordinate frame about the x, y, z axis of rotation
I_{xy}, I_{xz}, I_{yz}	coupled mass moment of inertia in local beam coordinate frame
$J_{h\varepsilon}$	Jacobian matrix for strain and displacement
K_{FF}	generalized stiffness matrix
K_{ca}	generalized stiffness matrix for absolute constraint
K_{cr}	generalized stiffness matrix for relative constraint
K_ε	propeller wake spreading constant
k_{ij}	components of cross-sectional stiffness matrix ($i,j = 1,2,3,4$)
L	aircraft lift
l_{ac}	lift per unit length acting at the airfoil aerodynamic center
l_n	length of element n
l_{ra}	lift per unit length acting at the reference axis
M_i	beam internal bending moment in global frame ($i = X$, Y, or Z)
m_j	beam internal bending moment in local beam coordinate frame ($j = 1$, 2, or 3)
m_{ac}	pitching moment per unit length acting at the airfoil aerodynamic center
m_{ra}	pitching moment per unit length acting at the reference axis
m	mass
p_x, p_y, p_z	nodal position in x, y, z coordinates
q_{ref}	dynamic pressure at reference velocity
R	generalized load
R_{ca}	generalized load due to absolute constraint
R_{eng}	radius of the propeller disk
R_n	reference node at the nth spanwise station ($n= 1,2,3\ldots$)
$R_{\hat{n}}(\varphi)$	rotation matrix of angle φ about axis $\hat{n}$
S_{ij}	cross-sectional stiffness constant in local beam coordinate frame
s	location along the span

T	applied torsional moment in global frame
T_{eng}	engine thrust
u,v,w	displacement in local beam coordinate frame
U_{ref}	reference velocity
U_{∞}	freestream velocity
U	velocity
V	voltage
ΔV_{eng}	velocity increment behind propeller disk
X,Y,Z	coordinate directions in a global frame
x,y,z	coordinate directions in a local beam coordinate frame
α	airfoil angle of attack
ε	beam element strain
ε_b	outer shear layer boundary
ε_c	inner shear layer boundary
κ_i	curvature in the local beam coordinate frame
λ_0	aerodynamic inflow term
$\lambda_{ca}, \lambda_{cr}$	Lagrangian multiplier
η_i	row sum of the Jacobian matrix
Π	virtual work
ρ	material density
ϑ	twist angle of the reference axis in a local beam coordinate frame
φ	aircraft roll angle
θ	aircraft pitch angle
ψ	aircraft yaw angle
ν	Poisson's ratio
$\bar{\omega}_x, \bar{\omega}_y, \bar{\omega}_z$	nodal orientation vectors in a local beam coordinate frame

Abstract

Development of a Very Flexible Testbed Aircraft for the Validation of Nonlinear Aeroelastic Codes

by

Jessica R. Jones

Chair: Carlos E.S. Cesnik

This dissertation presents the development, analysis, and flight testing of an unmanned aeroelastic testbed aircraft. The experimental, remotely-piloted aircraft was designed to be aeroelastically representative of very flexible aircraft. Known as X-HALE, this Experimental High-Altitude Long-Endurance aircraft exhibited geometrically nonlinear behavior and displayed specific aeroelastic characteristics that are present in full-scale HALE vehicle designs.

Three X-HALE configurations were constructed and characterization of their elastic, inertia, and aerodynamic properties were used to create a nonlinear model for aeroelastic analysis. Each configuration was instrumented with a suite of sensors to allow the collection of high quality elastic and flight dynamic data. Flight tests of each configuration were performed and the presence of the desired nonlinear aeroelastic behavior was confirmed, including coupling between elastic deformation and rigid body flight dynamics and unstable, but controllable lateral oscillations. Data gathered during flight was processed for use in validation of nonlinear aeroelastic solvers.

Aeroelastic simulations of select maneuvers from the flight tests of each X-HALE configuration were performed using the reduced–order nonlinear strain-based finite element framework implemented in the University of Michigan Nonlinear Aeroelastic Simulation Toolbox (UM/NAST). The correlations support validation of UM/NAST's capability to model the coupled aeroelastic and flight dynamic behavior of highly flexible aircraft.

A number of parallel studies were conducted to support the flight test simulations and UM/NAST validation effort. The NASA-Lockheed Martin X-56A was used to illustrate the process of creating a nonlinear aeroelastic model from high fidelity structural and aerodynamic data. The nonlinear model's structural and aerodynamic response was compared to results from high fidelity solvers, and flutter predictions were performed. To expand the modeling capability of UM/NAST, updates to the aerodynamic and kinematic constraint formulation were implemented. A propeller module was developed which incorporates downwash effects into the existing 2-D unsteady aerodynamic framework. Expanded definitions for nodal displacement constraints using the Lagrange multiplier method were implemented, allowing the modeling of mixed displacement and rotation boundary conditions as well as complex inter-member connections.

CHAPTER 1. Introduction

This chapter provides an overview of the challenges faced when performing aeroelastic analysis of very flexible aircraft. A brief introduction to very flexible aircraft and their applications is given, as well as the aircraft characteristics that differentiate this class of aircraft from conventional designs. A history of the development of nonlinear aeroelastic solvers and their capabilities is presented, and the formulation and capabilities of the University of Michigan Nonlinear Aeroelastic Simulation Toolbox is introduced. A discussion of ground vibration testing as a method of experimental model validation is presented, and lessons learned from flight tests of landmark flexible aircraft provide a basis for the experiment presented in this dissertation. Finally, the primary goals of this dissertation are summarized and its key contributions are listed.

1.1 Overview of Very Flexible Aircraft

In recent years, there has been a growing interest in the class of unmanned aerial vehicles known as High Altitude Long Endurance (HALE) aircraft. These aircraft are characterized by their ability to loiter at altitudes far higher than conventional cruise altitudes and flight durations that are measured in days and weeks rather than hours. These capabilities uniquely qualify these aircraft for applications previously reserved for satellites, including intelligence, surveillance, and reconnaissance (ISR) missions, atmospheric monitoring, and communications networking.

The altitude and endurance requirements of HALE flight lead to vehicles characterized by low structural weight and high lift-to-drag ratio. This translates to very lightweight designs with high-aspect-ratio wings, which results in aircraft structures that are so flexible that traditional, linear approaches to modeling their dynamic behavior are insufficient.

Zerweckh et al.[1] and van Schoor and von Flotow[2] presented studies based on the flight tests of the ultra-light, human-powered MIT Light Eagle. The Light Eagle was built from lightweight materials, including graphite-epoxy composite, foam, and mylar. It had an aspect ratio of 39.4 and a takeoff gross weight of 110 kg. It exhibited equilibrium wing deformation of

approximately 8% of the semispan, and the natural frequencies of the structure were below several of the rigid body frequencies. With this aircraft, they demonstrated that the traditional approach of modeling rigid-body and flexible dynamics separately did not adequately capture the behavior of very flexible aircraft. They concluded that the flexibility of the aircraft structure as well as the full unsteady aerodyamic loads must be included in the flight dynamics model for the design and control of very flexible aircraft.

The deformation experienced by HALE-type aircraft during trimmed flight is often large enough to be considered geometrically nonlinear, and the elastic frequencies of these light, flexible structures leads to coupling with the rigid body modes, usually short period, phugoid and/or dutch-roll modes. Thus, traditional methods of analyzing fluid-structure interaction, commonly involving linear finite element models coupled with nonlinear, unsteady CFD,[3] are insufficient for the aeroelastic analysis of these aircraft. Improved analysis methods, typically in time domain, that take into account the nonlinear subsystem interactions present during different phases of the aircraft flight are required for full understanding of their flight dynamics and stability.[4]

In 2003, a spotlight focused on the aeroelastic modeling community when the Helios, a NASA-Aerovironment prototype HALE aircraft, was destroyed during an endurance test flight. The mishap report released by NASA attributed the loss of the aircraft to a fundamental lack of understanding of the nonlinear, coupled aeroelastic behavior of very flexible aircraft. In order to advance the field of knowledge and prevent future mishaps, the authors made the following recommendation:[4]

> "Develop more advanced, multidisciplinary …'time-domain' analysis methods appropriate to highly flexible, 'morphing' vehicles. Develop ground-test procedures and techniques appropriate to this class of vehicle to validate new analysis methods and predictions."

1.2 Nonlinear Modeling and Analysis of HALE Aircraft

Researchers have taken many different approaches to improving the capability of existing aeroelastic tools for the study of very flexible aircraft. In the typical aircraft design process, a built-up FEM model is used to analyze the structural behavior and some detailed description of the aircraft aerodynamic properties, derived from CFD or wind tunnel data, is combined with it

to generate an aeroelastic model. The most direct approach to improving upon these existing tools is to couple a geometrically nonlinear structural analysis solver with a nonlinear computational fluid dynamics solver to provide a high fidelity aeroelastic analysis environment. Garcia, Seber, and Bendiksen coupled nonlinear beam and plate finite element models to CFD to study high aspect ratio wings in transonic flight regimes.[5,6] Cesnik and co-workers coupled a quasi-3D nonlinear structural model with unstructured, deformable CFD to perform high fidelity analysis of HALE aircraft in compressible flow.[7,8] These high-fidelity methods are very accurate, but are usually computationally expensive and do not account for the rigid body effects from flight dynamics. For HALE aircraft in low speed flows, this expense is not necessarily warranted. A simplified beam-based elastic aircraft representation with unsteady potential flow equations is sufficient to capture the nonlinear aeroelastic behavior.

A number of approaches to creating these simplified models have been developed in parallel over the years. Drela developed an integrated simulation method, implemented in the aeroelastic design software ASWING.[9] The structural dynamics of aircraft were modeled using a nonlinear displacement-based beam formulation to capture arbitrarily large deformations. Aerodynamic loads were calculated with an unsteady vortex/source-lattice method and coupled to the structural dynamics and 6-DOF flight dynamic equations to generate solutions to the aeroelastic equations of motion.

Ritter and Cesnik[10] used a modal approach to capture the nonlinear structural behavior of a very flexible high-aspect-ratio UAV with a displacement-based finite element model. Aerodynamic loads were generated with an unsteady vortex lattice code and coupled to the structural model to generate the aeroelastic and free-flight behavior of this UAV. Simulations of of the UAV during trimmed flight and its response to control surface and gust excitation were performed for comparison with other nonlinear aeroelastic codes and flight test data.[11,12]

Patil, Hodges, and Cesnik used a geometrically-exact mixed-form beam formulation[13] to perform nonlinear aeroelastic analysis on a Daedalus-based HALE aircraft.[14,15,16] The beam formulation is coupled with 2-D finite state unsteady aerodynamic loads[17] and 6-DOF flight dynamic equations to yield the nonlinear aeroelastic equations of motion. Their studies found that natural frequency, trim solution, and flight dynamic modes changed significantly as a function of tip displacement. Furthermore, stability analysis methods that accounted for wing flexibility and deformation produced distinctly different results than the traditional linear

analysis which assumed negligible deformation. Following these studies, Patil and Hodges[18,19] developed the Nonlinear Aeroelastic Trim and Stability of HALE Aircraft (NATASHA) analysis tool. It utilizes in part the formulation developed in Reference 13, replacing the mixed-form beam formulation with a fully intrinsic form. This tool has been used to perform studies of gust response and ground vibration testing on aircraft with high aspect ratio wings.[20,21]

Cesnik and co-workers[22–27] developed the University of Michigan Nonlinear Aeroelastic Simulation Toolbox (UM/NAST), a time-domain nonlinear aeroelastic formulation that uses a strain-based, geometrically nonlinear beam model coupled with 2-D finite state unsteady aerodynamic loads[17] to simulate the aeroelastic behavior of various aircraft configurations. UM/NAST's capabilities include fully nonlinear trim, steady state, and dynamic solutions, as well as linearized stability analysis for controller design and flutter prediction. This code has been used to perform studies on a wide range of aircraft configurations, including conventional transport aircraft, blended-wing-body, flying wing, and joined-wing aircraft.[22,28–30]

1.3 U-M Nonlinear Aeroelastic Simulation Toolbox

The University of Michigan's Active Aeroelasticity and Structures Research Lab (A^2SRL) developed the Nonlinear Aeroelastic Simulation Toolbox (UM/NAST), which implements a strain-based beam formulation capable of performing trim, static, and time-domain dynamic analysis of nonlinear aeroelastic behavior for a variety of aircraft configurations.[26] This toolbox is especially useful for the study of very flexible HALE aircraft because their defining characteristics often result in coupled structural and flight dynamic behavior not adequately captured using linear analysis approaches.

The UM/NAST aeroelastic equations are built on three primary reference frames. The global frame *G* is fixed in space, and provides the reference for static and dynamic simulations. The body-fixed frame *B* follows the position and orientation of the model origin within the global frame. In the body frame, B_x is positive toward the right wingtip of the model, B_y is positive towards the leading edge of the model, and B_z is positive upwards, normal to the other axes. When modeling a structure with no elastic deformation, the global and body-fixed coordinate frames are all that is needed to fully describe the instantaneous state of the aircraft. The heading angle ψ is a rotation about the B_z axis, the body angle of attack is given as a rotation about the B_x axis, and the roll angle is a rotation about the B_y axis. In order to introduce elasticity

into the equations of motion, an additional set of local, nodal coordinate frames *w* are introduced, where w_i describes the instantaneous position and orientation of the *i*th node in the structure relative to the body frame *B*. The relationship between these frames is illustrated in Figure 1.1.

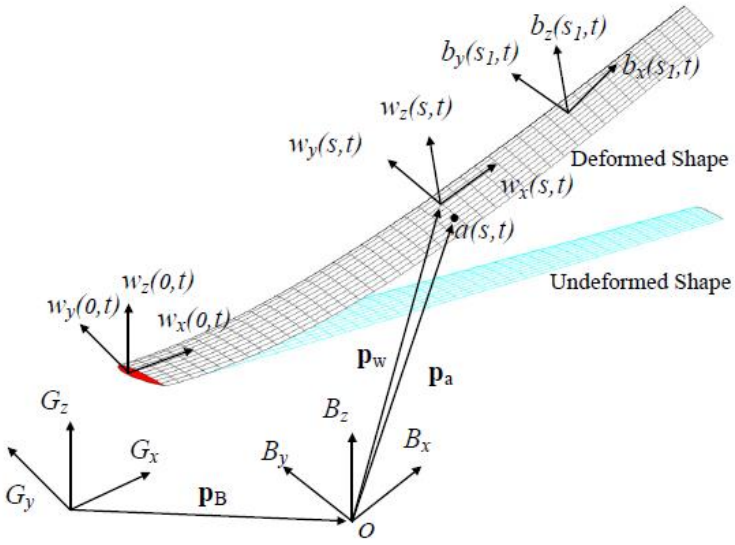

Figure 1.1. Diagram of beam reference frames in UM/NAST

A strain-based beam formulation is used to model the position and orientation of each node in the beam model. The formulation uses nonlinear, 3-node constant strain elements with four degrees of freedom at each node: extension, torsion, out-of-plane (OP) bending, and in-plane (IP) bending. The beam twist and displacement can be recovered from strain directly using the strain-curvature kinematic relationship.[22]

An additional reference frame is derived to describe the orientation of the unsteady aerodynamic forces acting at each node. The lift, drag, and moment about the aerodynamic center is defined at each structural node using a 2-D potential flow representation. Increments to the local aerodynamic forces and moments due to unsteady, tip loss, or compressibility effects are introduced into the equations using discrete parameters that are described in detail by Su.[26]

UM/NAST is capable of performing several types of aeroelastic simulations. Linear and nonlinear static aeroelastic analysis is used to solve the steady state, coupled elastic and aerodynamic solutions. When combined with the rigid body states, the static solution can be used to find the model inputs required to achieve aeroelastic trim, force and moment equilibrium at a given flight condition. Linearized and fully nonlinear solutions of the time-domain equations of motion are implemented to perform dynamic simulations. Linearization of the elastic equations

of motion about undeformed and deformed conditions can be used to calculate the natural frequencies and mode shapes of various structures. Linearization of the full equations of motion, including elastic motion, rigid body motion, and aerodynamic inflow states facilitates analysis of stability boundaries and characterization of envelope-critical behavior like flutter. The formulation may be used to study a wide range of models, including simple beams, joined-wing configurations, blended-wing-body, flying wing, and conventional aircraft.

1.4 Model Creation for Very Flexible Aircraft

Palacios and co-workers[31] compared generalized versions of several published formulations for structural and aerodynamic solvers. They found that the intrinsic- and strain-based formulations outperformed traditional displacement-based solvers in terms of computational efficiency as well as overall effectiveness in capturing the geometrically nonlinear structural behavior of flexible flying-wing type aircraft. A key aspect of the behavior that these formulations are able to capture is the blending of the structural and flight dynamic modes of very flexible aircraft (VFA). The low natural frequencies of the structure couple with and alter the rigid body modes such that they are no longer distinct from each other nor easily correlatable with the rigid-body modes of traditional fixed wing aircraft.

In addition to their ability to capture nonlinear behavior, a significant advantage of these lower-order codes over higher-fidelity CSD/CFD solutions is the speed and ease of which key aeroelastic parameters can be adjusted. This ease makes them ideal to support the development of HALE vehicles from conceptual design through flight testing. However, while the aircraft models used for these codes are simple in comparison to their higher fidelity counterparts, the creation of an accurate model for use in these codes is not a trivial process.

Singh and Nicols used a NASTRAN model consisting of quadrilateral shells to calculate equivalent beam stiffnesses and inertias of a horizontal stabilizer for use in wind tunnel and flutter analysis.[32] Malcolm and Laird performed a similar procedure on an ANSYS model of wind turbine blades to calculate cross-sectional beam stiffness matrices for use in ADAMS.[33] Smith used the FEM wingbox model of the NASA Common Research Model to develop a beam model of the wing for use in aeroelastic tailoring.[34] Love and co-workers derived a beam model for body freedom flutter analysis in ASWING from the NASTRAN model of the Lockheed Martin Sensorcraft Swept Flying Wing.[35] Jones and Cesnik[36] developed a nonlinear aeroelastic

model of the X-56A blended wing body demonstrator for use in parametric studies involving weight distribution effects on the flutter envelope. The common thread through each of these studies was that the creation of simplified models involves careful consideration of modeling choices and design assumptions.

1.5 Model Validation for HALE Aircraft

An important factor that improves the quality of aircraft models and the predictions that they provide is the use of experimental ground-based test data in their creation and validation.

Ground vibration testing (GVT) is a valuable experimental tool to obtain mode shapes and frequencies of an aircraft structure, and the test permits the validation and tuning of the numerical models used during the design process. The process of conducting a GVT for a conventionally flexible aircraft is known. A detailed finite element model (FEM) of the aircraft, usually created during the aircraft design stages, is used to perform linear static and modal analysis of the aircraft structure. The methodology for the GVT involves evaluating the type of supports needed to isolate elastic frequencies, the method of excitation, and the type of instrumentation required to recover the predicted mode shapes. During the GVT, the modal response of the aircraft is measured under conditions that approximate its configuration during flight. The experimental data is then compared to the numerical predictions from the FEM, and stiffness and inertia parameters are tuned so that the predicted mode shapes and frequencies match the experiment within some pre-determined threshold of error. The GVT-validated FEM model can then be used for a number of additional static and dynamic simulations with confidence that the results will reflect the behavior of the as-built aircraft. However, these known methods work best in structures that exhibit linear behavior and small deformations. Predicting and measuring dynamic response in the presence of structural nonlinearities is an ongoing challenge in vibration testing.

Charmbalis and coworkers[37] investigated the effect of nonlinear stiffness on the mode frequencies of two cantilevered structures, a simple beam and a joined wing. They increased the tip deflection of the structures using tip masses and measured significant changes in frequency due to the induced geometric nonlinearities. Britt and coworkers[38] conducted an investigation into nonlinear effects on the modal response of the cantilevered Vulture wing wind tunnel model. They performed a modal analysis of the cantilevered model in two different configurations: the

model oriented horizontally, as in flight, and the model in a nose-down, "vertical" orientation. As expected, when modeled without gravity load, the numerical predictions of the modal response for the two configurations was identical. When effect of gravity was added, the deformation experienced by the horizontal configuration was significantly larger due to the lower stiffness of the structure in the out-of-plane direction compared to the in-plane direction. The horizontal model also exhibited considerable differences in the predicted mode frequencies as a result of the nonlinear stiffness effects caused by the large deformation. Two GVT tests were performed on the horizontal and vertical configurations to validate these results.

The implications of these findings is quite important for the characterization and model validation of very flexible aircraft. VFA's experience significant deformation during normal flight. In order to assess the aircraft's modal response under conditions approximating free flight, these large deformations should be replicated during testing. However, the presence of structural nonlinearities caused by large wing deformations will complicate the numerical analysis and its correlation with experimental data. Although it has been shown that the modal response of the aircraft is dependent on its deformation state, it is not yet clear how this dependence can be properly captured and translated back to the numerical model during experimental validation.[37,38]

There are also practical challenges involved with ground vibration testing of light, highly flexible structures. Chang and Hodges[39] presented a procedure for modeling the ground vibration test of a flexible flying wing. They demonstrated a numerical framework that coupled the stiffness of the suspension system with a flexible wing and showed the importance of the right support stiffness when attempting to separate the rigid body and elastic modes. Böswald and co-workers described the challenges of performing ground vibration testing and subsequent tuning of a FEM model for the Solar Impulse electric aircraft.[40,41] The Solar Impulse has a wing span rivaling the size of a commercial jetliner, but its airframe is many times lighter. The structure was so lightweight that apparent mass effects of the air needed to be considered while tuning the FEM model to the experimental data gathered during the test.

Despite their difficulty, ground-based tests for experimental validation of the structural models of VFA are necessary to ensure their accuracy and required for regulatory certification. Thus, efforts are ongoing to develop methodology and tools that will assist in the experimental validation of very flexible aircraft.

1.6 Flight Testing

Attempts to validate flight-dynamics-coupled, nonlinear aeroelastic solvers and evaluate their usefulness in the design and analysis of VFA have been made. These validation efforts use the limited set of experimental data available for the different components of the analysis, including ground-based tests, wind tunnel tests, and data from validated linear aeroelastic solvers (e.g., NASTRAN).[29,42,43] However, there is no publicly available experimental data of a VFA in free flight for use in validation of these solvers. Several VFA have been successfully flight tested in the past, and the conclusions and lessons learned were made available to further the study of this class of aircraft.

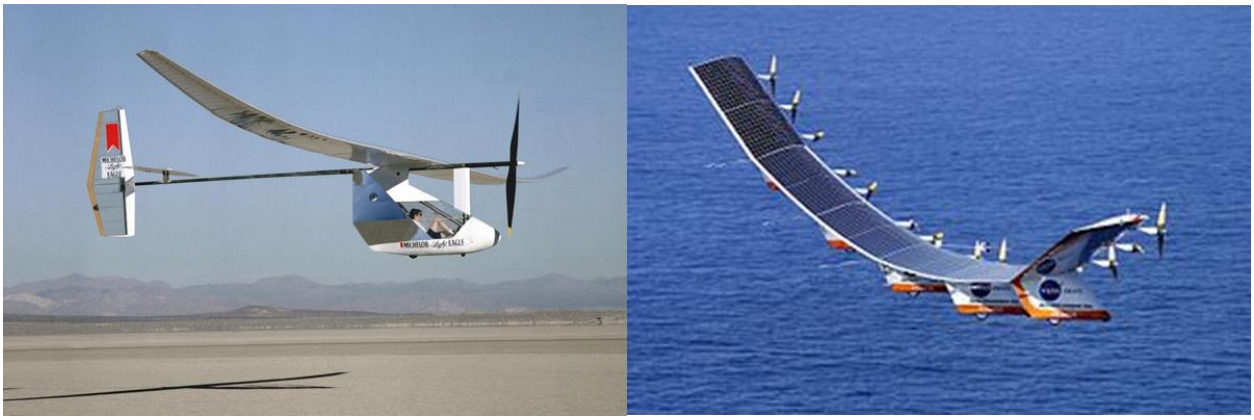

Figure 1.2. HALE Aircraft Daedalus (l) and Helios (r), courtesy of NASA

The 1990 flight tests of the MIT Light Eagle[1] highlighted several of the aircraft behaviors they observed while performing parameter identification on the highly flexible vehicle. Ailerons were judged to be a poor method of actuating turns due to significant adverse yaw they generated, so a rudder was used to perform lateral maneuvers by taking advantage of the roll-yaw coupling in the aircraft. The highly flexible structure was also slow to respond to roll and yaw inputs--high frequency inputs had little effect on the rigid body motion but excited the structural modes instead. These experiences led them to conclude that a rigid body assumption could be valid for modeling the response to low frequency excitation, but a fully flexible aircraft model was necessary for capturing the coupled elastic and rigid body response to higher frequency excitations.

The mishap of the NASA Helios[4] also served as a valuable learning experience for those working with VFA. The Helios designers were able to accurately predict the aircraft's wing deformation in calm conditions, however their analyses failed to adequately capture the aircraft's

sensitivity to disturbances. When the Helios encountered significant turbulence during a takeoff climb, it induced a increasing amplitude pitch-plunge oscillation that coupled with the wing's natural bending mode. The aircraft could not recover to its equilibrium deformation condition, and the divergent phugoid oscillations, coupled with increasingly large wing dihedral, exceeded the structural limits of the wing and led to the loss of the aircraft.

Figure 1.3. Facebook Aquila (l), Titan Solara 50 (mid), Qinetiq Zephyr 7(r)[*]

In a more recent, but very similar case, the Titan Solara 50[44] encountered a large, unexpected area of thermals during takeoff maneuvers early in their flight. The atmospheric conditions resulted in an overspeed condition characterized by increasing amplitude pitch oscillations and large structural deformations that could not be stabilized. Like the Helios, the overspeed conditions resulted in structural failure and the loss of the aircraft.

Flight tests are an essential part of the aircraft design cycle, and VFA are subject to unique challenges not faced by conventional aircraft designers. Their lightweight structures, extreme flexibility, and sensititity to disturbance result in aircraft that are both difficult to anticipate and unforgiving of error. Conventional aircraft flight testing is supported by aeroelastic analysis and prediction tools that are used widely and extensively validated, however such tools for VFA are still under active development. One of the primary hurdles to completing development on these various tools is the lack of experimental data available for VFA. To date, no fully coupled nonlinear aeroelasticity/flight dynamics experimental data exists in the public domain that could be used for the validation of integrated formulations for analysis and design of VFA.

1.7 Goals of this Dissertation

The University of Michigan's experimental high-altitude long-endurance (X-HALE) aircraft is intended to address the need for publicly available relevant aeroelastic data to support

[*] courtesy of Facebook, Inc, Titan Aerospace, QinetiQ Group, respectively

validation of nonlinear aeroelastic solvers.[30] This dissertation details the development and flight testing of the X-HALE, as well as the numerical investigations that were conducted in support of these tests.

Chapter 2 details the process of creating and validating an aeroelastic model for UM/NAST using data from the Lockheed Martin X-56A flutter demonstrator. Chapter 3 details a number of improvements to the UM/NAST implementation and formulation that enhance the code's modeling capability. Chapters 4 and 5 present the development, characterization, and flight test data of three X-HALE configurations. Chapter 6 presents correlations for a subset of the flight test data with UM/NAST and provides some suggestions for further model development and formulation improvement. Chapter 7 summarizes the primary conclusions and key contributions of this dissertation and outlines areas of future study for the X-HALE project. The goals of this dissertation fall into three categories:

1. Improve flexible aircraft modeling capability of UM/NAST
    a. Implement pinned and mixed absolute constraints for modeling of complex boundary conditions
    b. Implement pinned relative constraints to allow modeling of ground vibration test supports and structures with complex intermember interfaces
    c. Incorporate propeller downwash effects into the finite state aerodynamic formulation
2. Gather experimental data to validate coupled free-flight aeroelastic solutions
    a. Design and build unmanned testbed aircraft capable of gathering high-quality aeroelastic data in flight
    b. Characterize elastic, inertia, and aerodynamic properties of testbed aircraft for creation of numerical models
    c. Gather experimental aeroelastic data from free-flight tests of unmanned testbed aircraft
3. Correlate numerical predictions of aircraft behavior with experimental data
    a. Generate predictions of aeroelastic trim, stability, and free-flight maneuver behavior for unmanned testbed aircraft
    b. Generate correlations between UM/NAST free-flight predictions and the measured flight dynamic behavior of unmanned testbed aircraft

CHAPTER 2. A Simplified Aeroelastic Model for the X-56A Aircraft

This chapter details the process used to reduce the high fidelity structural and aerodynamic properties of the X-56A blended-wing-body aircraft into a simplified aeroelastic model. The aircraft geometry was reduced to a simplified beam representation. The cross-sectional elastic properties were calculated from the static response of a GVT-validated finite element model. The distributed and concentrated inertia properties were extracted from the same finite element model. Two-dimensional spanwise aerodynamic coefficients were derived from the wind tunnel measurements of lift, drag, and pitching moment of a rigid aircraft model. The aeroelastic model created with these properties was implemented in the the University of Michigan Nonlinear Aeroelastic Toolbox and used to investigate the impact of aerodynamic loads and weight distribution on the X-56A flutter response.

2.1 Overview of the X-56A Aircraft

The X-56A Multi-Utility Aeroelastic Demonstrator, also known as the Multi-Utility Technology Testbed, is a joint venture among Lockheed Martin Skunk Works, the Air Force Research Laboratory, and NASA's Armstrong Flight Research Center. The subscale blended-wing-body aircraft has an aspect ratio of 14 with a wingspan of 27.8 feet. The goal of the venture is to provide a platform to study active flutter suppression technologies and provide data to advance the state of the art of "performance aggressive" aircraft.[45,46] Its modular wing design allows for flight tests at various payload and wing stiffness configurations, as well as allowing the aircraft to be modified to a joined wing design.[47,48]

Aeroelastic analysis of the X-56A using wind-tunnel tests and a GVT-validated finite element model indicated that the flutter boundary would be outside the aircraft's flight envelope, which was undesirable given the nature of the testbed.[49] Several subsequent studies were performed using a wide range of aeroelastic tools in order to verify these results and determine the effectiveness of using the payload configuration to reduce the flutter speed.[49–53] In this

chapter, the development of a simplified model for use with a nonlinear aeroelastic formulation is presented. This model was used to perform an independent investigation of the X-56A flutter response, particularly of the impact of the aerodynamic formulation used and varying weight distribution on the flutter envelope. This work is an extension of Reference 36.

Figure 2.1. X-56A Multi-Utility Technology Testbed, courtesy of Lockheed Martin

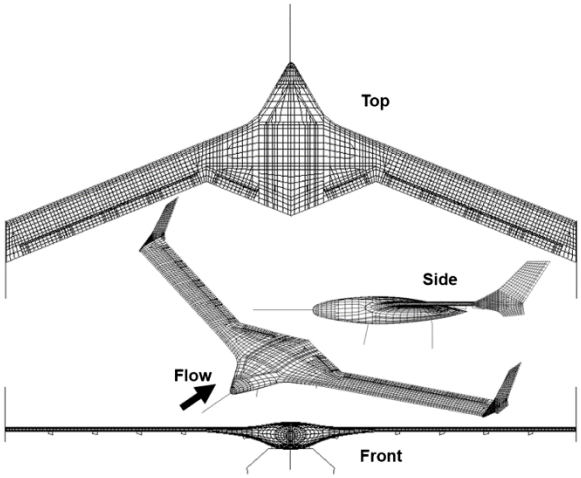

Figure 2.2. X-56A baseline FEM model[52]

2.2 Development of the Model

The elastic and inertia properties of the X-56A were provided through a detailed finite element model, illustrated in Figure 2.2. The model was generated and analyzed with MSC NASTRAN and validated with results from ground vibration tests.[49] Aerodynamic force and moment coefficients for the full aircraft were generated using nonlinear CFD and verified with wind tunnel tests on a rigid model, and the aircraft outer mold line was provided for the calculation of spanwise aerodynamic properties. These constitute the data provided by Lockheed Martin from which the X-56A aeroelastic model for UM/NAST was created.

2.2.1 Conversion of Built-up Model to Beam Model

In order to convert the detailed aerodynamic and finite element models into a beam-level representation, the cross-sectional elastic, inertia, and aerodynamic properties of the vehicle must be obtained along the span in the regions of interest.[35] For UM/NAST, the spanwise regions of interest are chordwise strips designated by a reference node. The conversion process distills all of the information of the built-up model into concentrated values relative to these reference node

locations. Figure 2.3 details the information required and the various software tools used in this process.

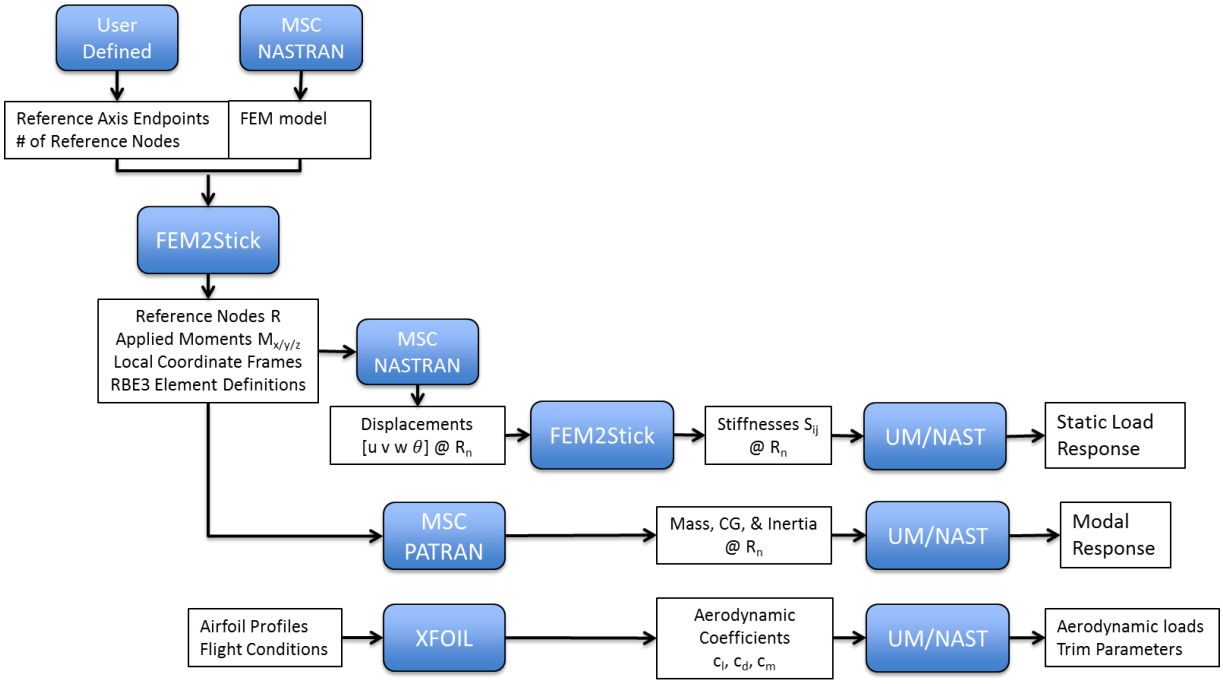

Figure 2.3. Conversion process from built-up FEM model to UM/NAST model

A built-up FEM model and a CAD model of the X-56A were provided as input data for the conversion process. FEM2STICK, a MATLAB-based software tool developed in collaboration with Ben Smith of Aurora Flight Sciences, was used to generate the cross-sectional stiffnesses along the selected beam reference line.[34] MSC NASTRAN/PATRAN, a commercial finite element analysis tool, was used to calculate spanwise concentrated inertias and perform static and modal analyses on the FEM model for conversion and comparison to the UM/NAST beam model. XFOIL, a subsonic airfoil analysis software, was used to calculate the local aerodynamic coefficients from airfoils derived from the wing cross-section.[54] UM/NAST was used to create the aeroelastic model from the beam reference axis, cross-sectional stiffnesses and inertias, and airfoil aerodynamic coefficients. UM/NAST's static analysis module was used to verify the stiffnesses by calculating the static load response of the beam model to compare against the FEM model. The aerodynamic coefficients were verified similarly by comparing the steady-state aerodynamic loads generated by UM/NAST against the reference aircraft aerodynamic loads provided. UM/NAST's modal analysis module was used to validate the

inertias by comparing the mode shapes and frequencies of the beam model against the FEM model.

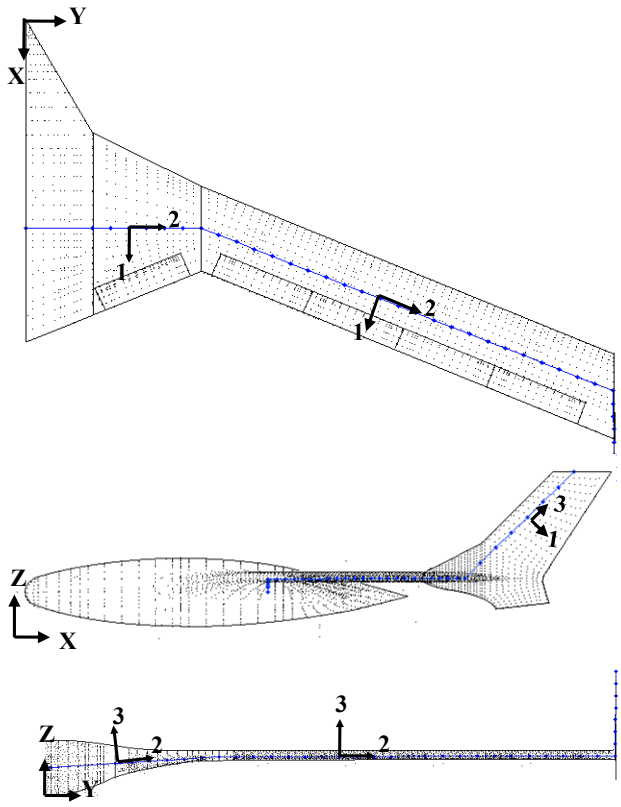

Figure 2.4. X-56A reference frames

2.2.2 Definition of the Reference Axis

To begin the conversion from the built-up model to beam model, a set of 10, 20, 30, and 40 reference nodes were defined along the X-56A wingspan. These reference nodes were evenly distributed along the span at the midchord, and the locus of these points formed the beam reference axis. The reference axis, which is not necessarily the elastic axis, is shown in Figure 2.5. All lengths are normalized by the aircraft's mean aerodynamic chord unless otherwise specified.

2.3 Elastic Properties

For each set of reference nodes, the cross-sectional stiffnesses along the span of the wing were generated and used create a massless wing in UM/NAST. The UM/NAST wing and NASTRAN model were subjected to a series of static loads, and the deformations were compared. The reference node set that yielded the best static comparison to the NASTRAN model was used for further model development.

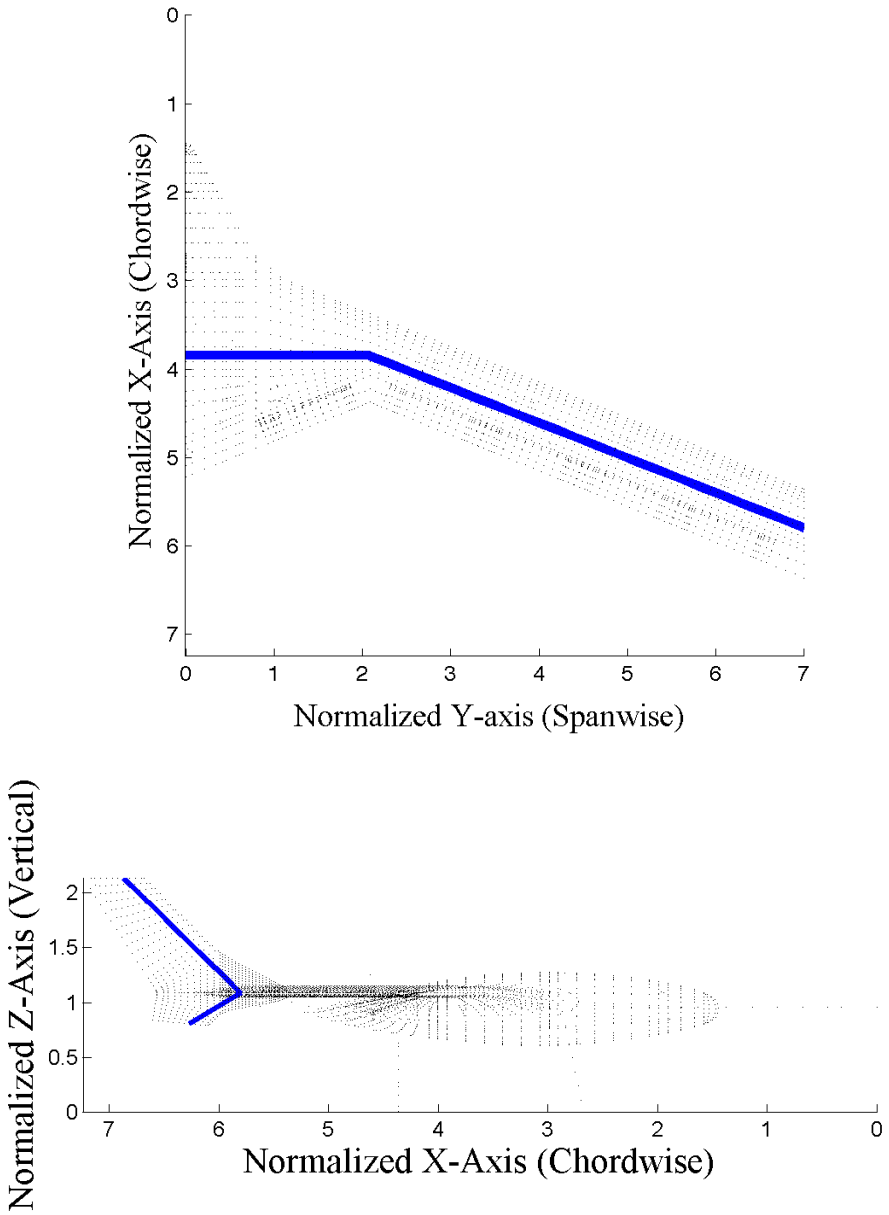

Figure 2.5. X-56A beam reference axis along the wing (top) and in the winglet (bottom)

2.3.1 Calculation of Cross-sectional Stiffnesses

The beam bending moment-curvature relationship is used to calculate the cross-sectional stiffnesses along the wingspan. A moment applied to the wingtip produces curvatures in three perpendicular directions, corresponding to torsion, vertical bending, and in-plane bending. The internal, local moments *m* are a coordinate transformation of the applied moments *M*, defined as:

$$\begin{Bmatrix} m_1 \\ m_2 \\ m_3 \end{Bmatrix}_{3x1} = \left[R_{\hat{n}}(\varphi)\right]_{3x3} \begin{Bmatrix} M_X \\ M_Y \\ M_Z \end{Bmatrix}_{3x1} \tag{2.1}$$

where $R_{\hat{n}}(\varphi)$ represents the rotation matrix from the global reference frame to the local beam reference frame, with a rotation of angle φ about the nodal orientation unit vector $\hat{n}$.

The relationship between the internal moments and the resulting beam curvatures at a given cross section within the wing can be expressed using a symmetric 3x3 matrix of stiffness constants:

$$\begin{Bmatrix} m_1 \\ m_2 \\ m_3 \end{Bmatrix}_{3x1} = \begin{bmatrix} S_{vertical} & S_{vert/tors} & S_{vert/inpl} \\ S_{vert/tors} & S_{torsion} & S_{tors/inpl} \\ S_{vert/inpl} & S_{tors/inpl} & S_{inplane} \end{bmatrix}_{3x3} \begin{Bmatrix} \kappa_1 \\ \kappa_2 \\ \kappa_3 \end{Bmatrix}_{3x1} \tag{2.2}$$

The beam curvatures are the spanwise derivatives of the beam twist and bending rates. For geometrically linear, straight beams, the curvature κ is defined as:

$$\begin{Bmatrix} \kappa_1 \\ \kappa_2 \\ \kappa_3 \end{Bmatrix} = \begin{Bmatrix} w'' \\ \vartheta' \\ -v'' \end{Bmatrix} \qquad \text{with} \quad (\cdot)' = \frac{\partial}{\partial Y} \tag{2.3}$$

This equation must be solved at each reference node in order to calculate the representative stiffness of each cross-sectional slice of the built-up model. Since this beam constitutive relationship is linear with respect to the curvatures, it only needs to be evaluated once. To automate the stiffness calculation process detailed by Singh and Nicols,[32] FEM2Stick uses a set of user-defined start and end points and chordwise location to define a reference line composed of a desired number of reference nodes. These reference nodes are defined as RBE3 interpolation elements in NASTRAN, thus the displacements and rotations at the reference nodes

are not independent, but are representative of the motion of all of the neighboring elements in their region and are given in the local beam coordinate frame.

Three perpendicular moments are defined in the global XYZ frame and applied to the wingtip of the FEM wing model in NASTRAN. These moments and their deformation response are small enough that the linear curvature definition described above is valid. The deformation of the wing is interpolated by the RBE3 elements into local displacements and rotations at each reference node location from which FEM2STICK calculates twist rate and in-plane and vertical bending curvatures using a central finite-difference method. The moment-curvature equation is employed as the next step to generate the cross-sectional torsion and bending stiffnesses and coupling terms at each reference node. As mentioned earlier, four reference node sets—10, 20, 30, and 40 nodes—are considered for the generation of stiffnesses. The spanwise distribution of cross-sectional stiffness constants and coupling terms for each reference node set is shown in Figure 2.6 through Figure 2.11.

2.3.2 Tuning the Stiffnesses

For all four reference node sets, the procedure outlined above is able to capture the overall stiffness distribution of the wing, and the stiffness values all fall within the same order of magnitude. If the structure being analyzed were straight and composed of a homogenous material, all four reference node sets would yield virtually identical stiffness results. However, in addition to the tapered wing-body region and swept main wing, the X-56A wing FEM model contains a variety of internal structures whose effect can be seen as local stiffness spikes in the 20, 30, and 40 node sets, but are absent in the 10-node set. Furthermore, the discretization of the FEM model yields elements with an average width that is 3% of the semispan, which is too coarse for the 40-node discretization. This crowding in the 40-node set forces the reference nodes to interpolate information from elements that do not belong to their respective regions, overlapping with neighboring regions and yielding spurious stiffness values as a result. The 30-node discretization is the maximum number of evenly-spaced reference nodes that this FEM model can accommodate, where each reference node region in the wing-body contains a single chordwise column of elements.

The FEM model also includes five control surfaces that compose over 90% of the wing's trailing edge. Each control surface is composed of flexible shell elements, and modelled hinges allow them to move independently of the main wing when actuated. During loading, these

control surfaces deflect relative to the bending and rotation of the wing reference axis. Although these deflections are extremely small relative to the wing's overall motion, they are major contributors to many of the local stiffness spikes in the in-plane and vertical bending stiffnesses, shown in Figure 2.12 through Figure 2.14. The torsional stiffness is not as strongly affected as the bending stiffness terms.

2.3.3 Static Response Predictions

In order to verify that the static behavior of the FEM model was adequately described by the beam model, the calculated stiffnesses were used to create a massless wing in UM/NAST. Three perpendicular tip loads acting in the X, Y, and Z directions were applied to both the FEM and UM/NAST wing models, and their responses were compared. The error in wingtip displacement of the UM/NAST model compared to the FEM model is shown in . Both the 20-node and 30-node versions of the UM/NAST model show good agreement with the FEM model with errors in the tip deflection of less than 1%, so either of these reference node configurations are sufficient to capture the static structural behavior of the wing. The 30-reference-node configuration was chosen for the rest of the model development since a higher discretization was desired when deriving the inertias. A comparison of the UM/NAST 30-node beam and FEM response to static loads is shown in Figure 2.15 through Figure 2.17.

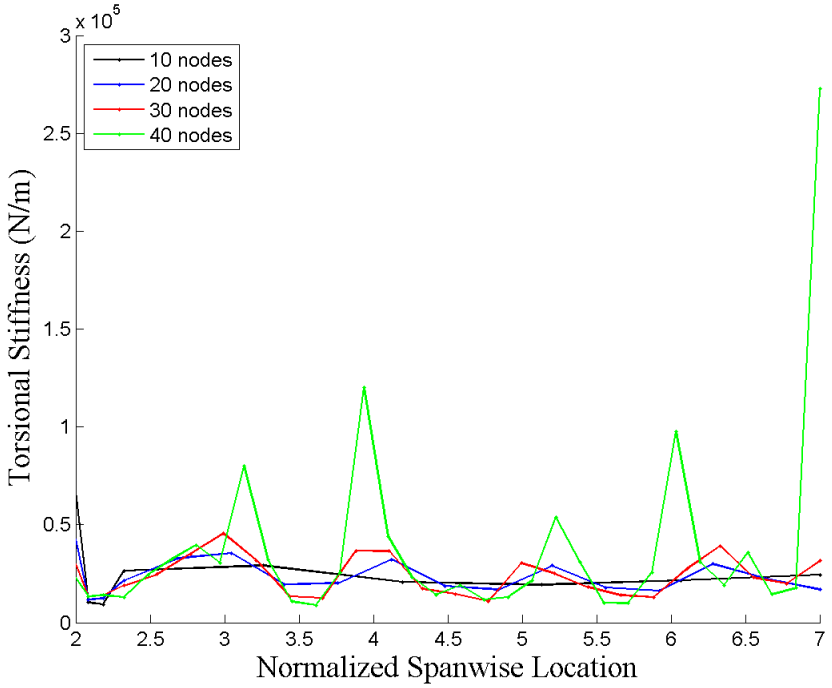

Figure 2.6. X-56A torsional stiffness constants along the semi-span

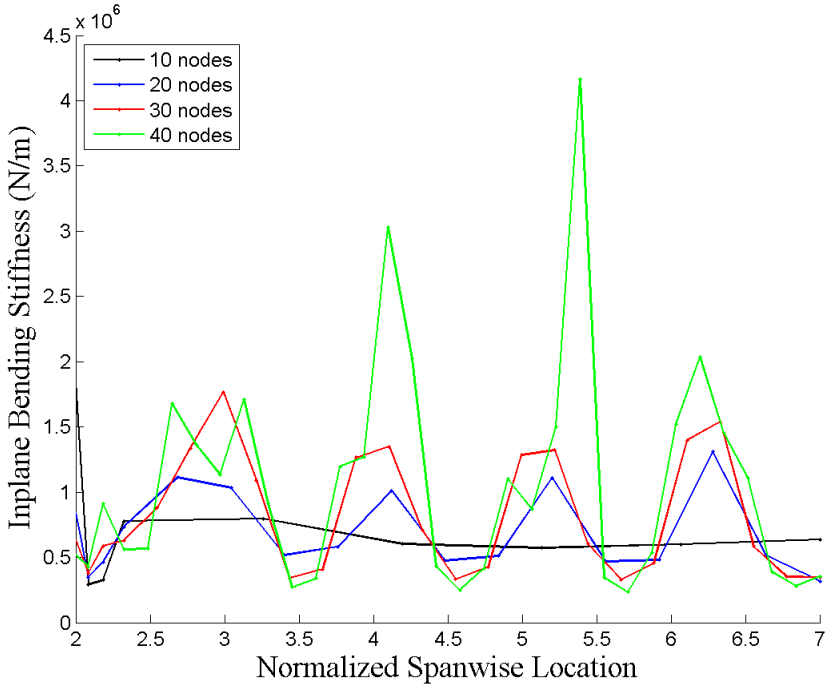

Figure 2.7. X-56A in-plane bending stiffness constants along the semi-span

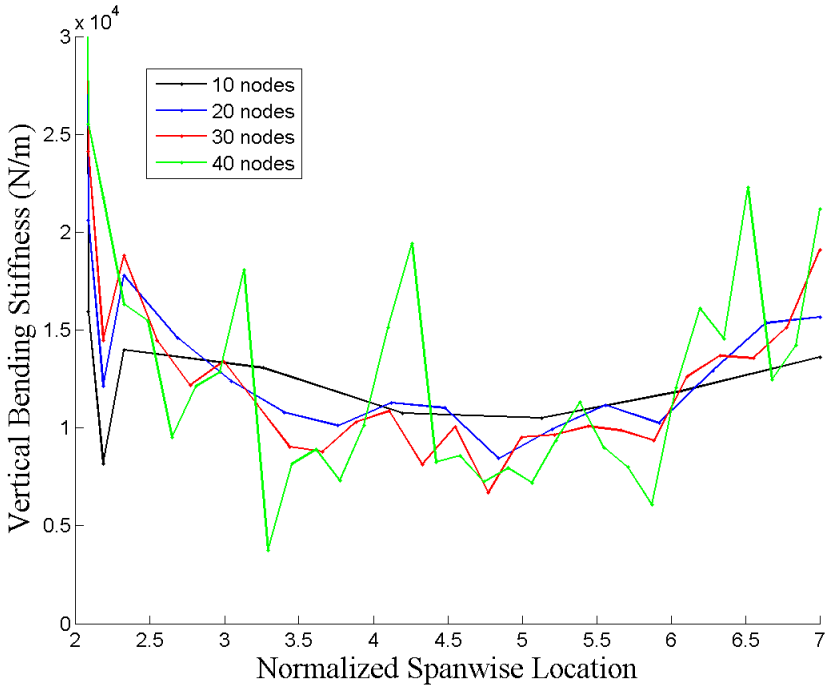

Figure 2.8. X-56A vertical bending stiffness constants along the semi-span

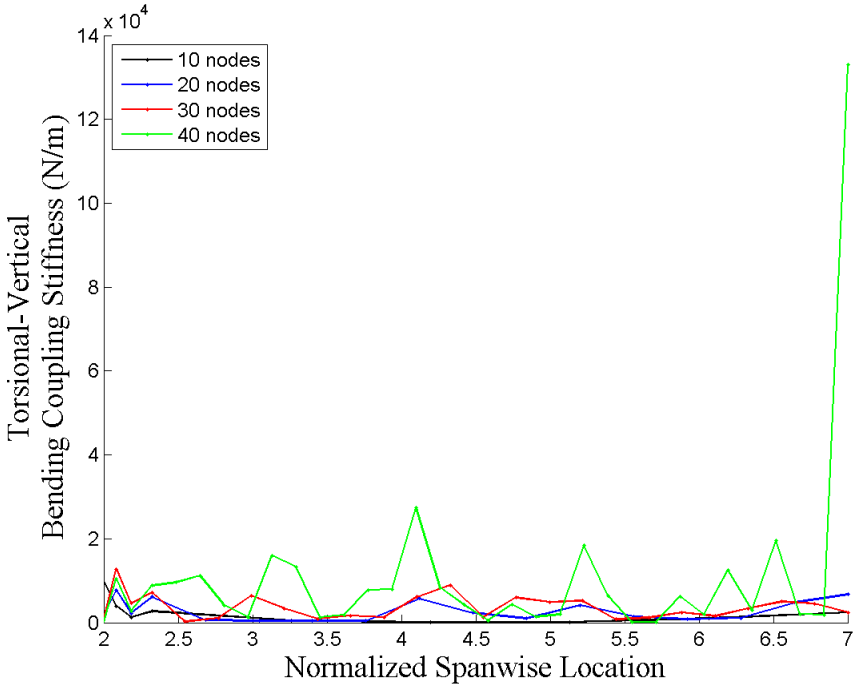

Figure 2.9. X-56A torsion-vertical bending stiffness coupling terms

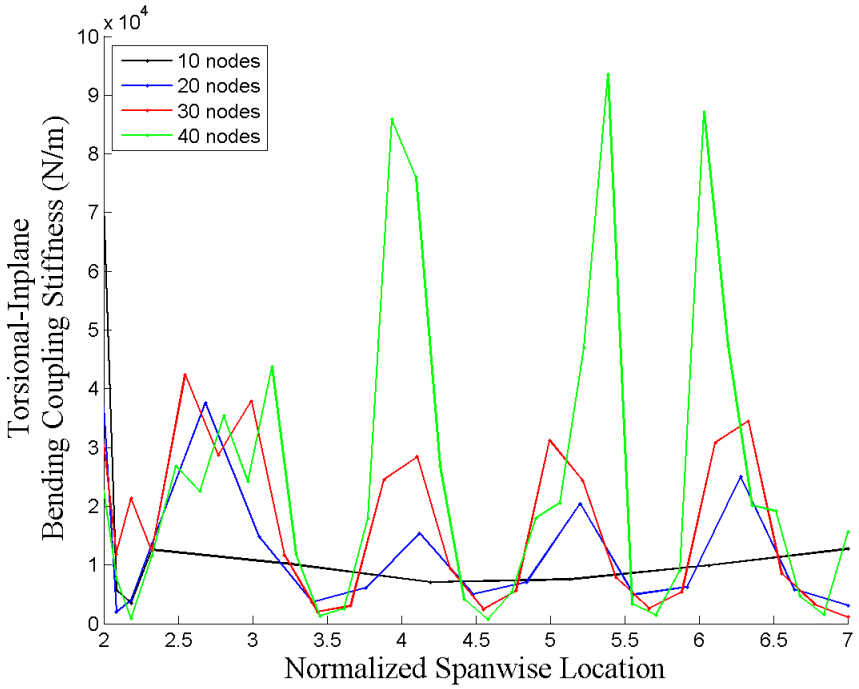

Figure 2.10. X-56A torsion-in-plane bending stiffness coupling terms

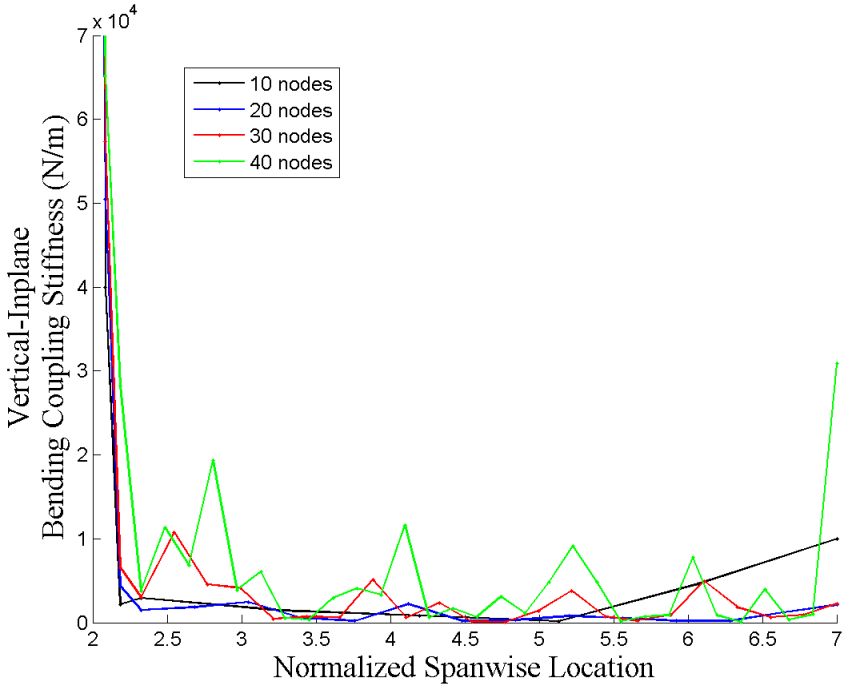

Figure 2.11. X-56A vertical-in-plane bending stiffness coupling terms

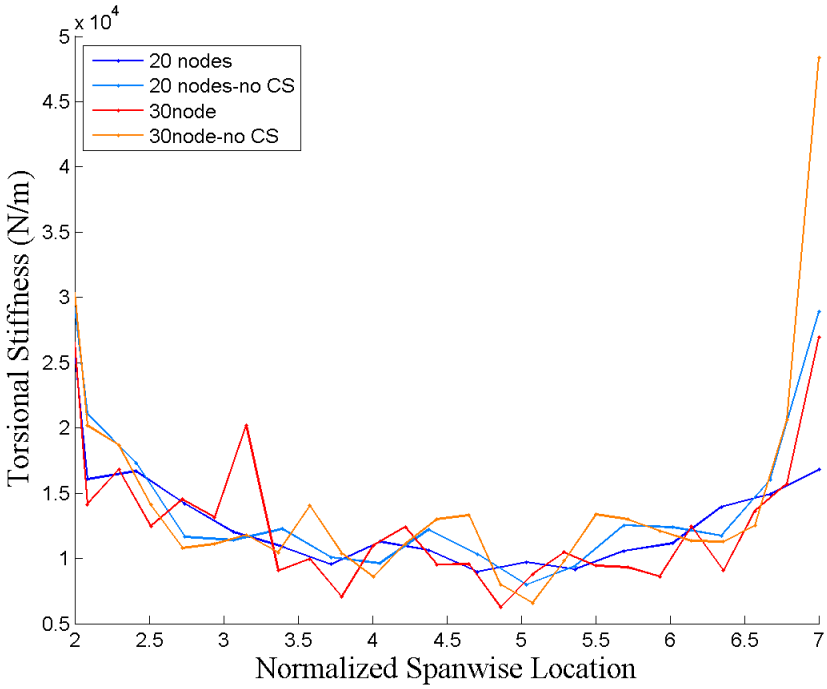

Figure 2.12. Comparison of torsional stiffness with and without control surfaces

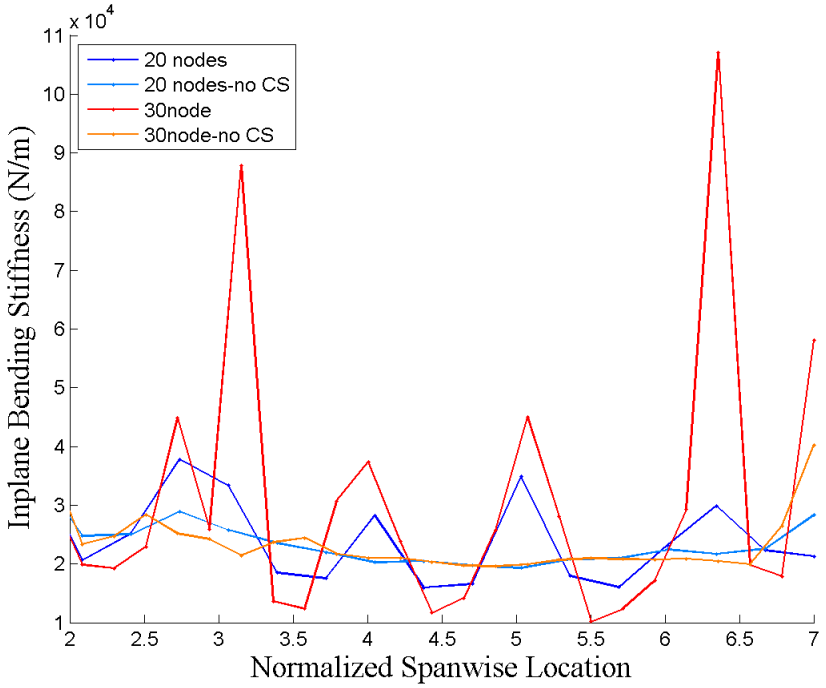

Figure 2.13. Comparison of in-plane bending stiffness with and without control surfaces

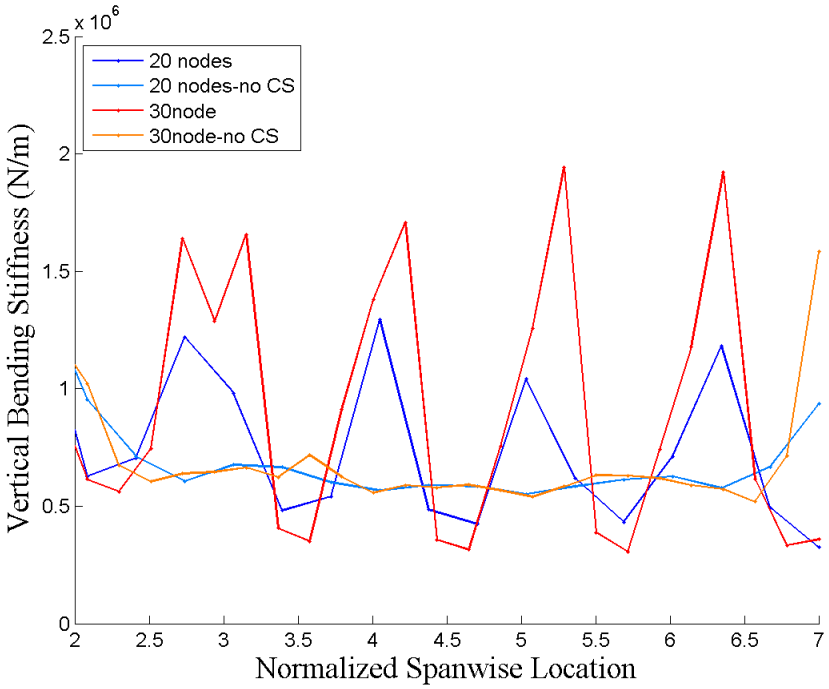

Figure 2.14. Comparison of vertical bending stiffness with and without control surfaces

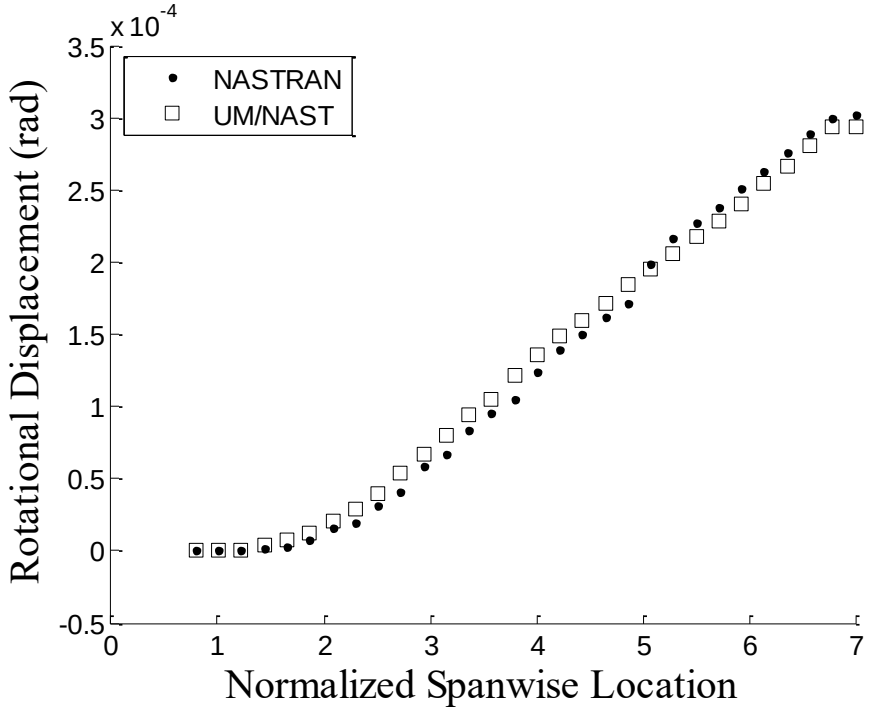

Figure 2.15. NASTRAN FEM and UM/NAST beam model displacement due to wingtip moment

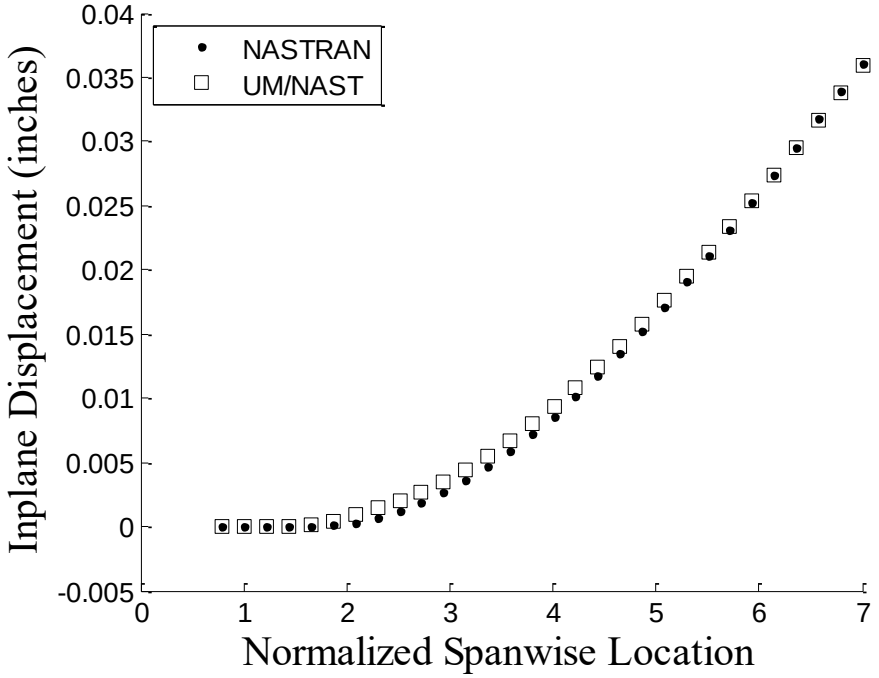

Figure 2.16. NASTRAN FEM and UM/NAST beam model displacement due to wingtip in-plane force

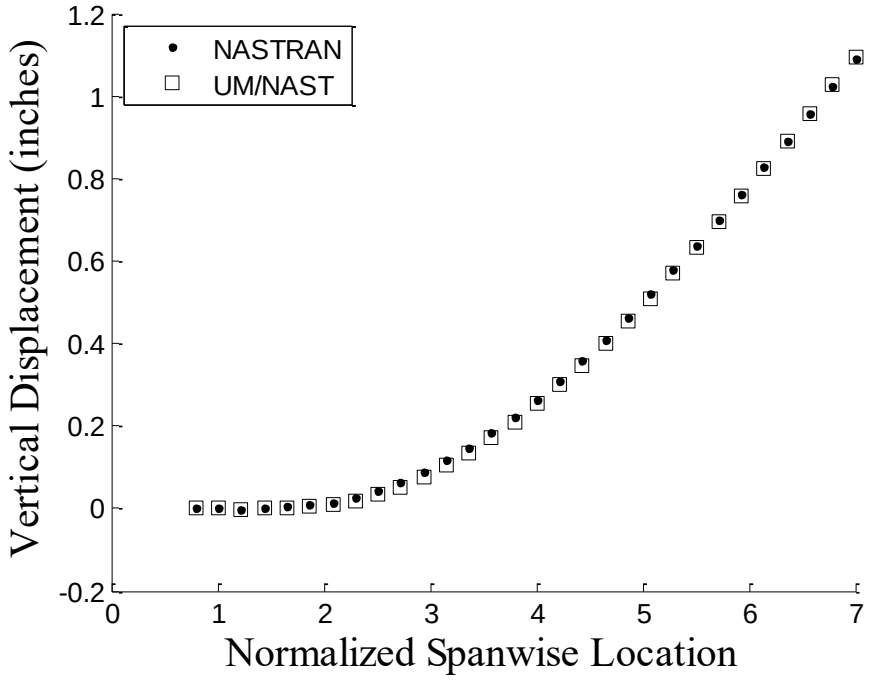

Figure 2.17. NASTRAN FEM and UM/NAST beam model displacement due to wingtip vertical force

Table 2.1. Wingtip displacement error for UM/NAST compared to FEM

Load Applied	Displacement Component	20 nodes	30 nodes
Torsion T	θ	0.9%	0.67%
In-plane Force F_X	v	0.54%	0.66%
Vertical Force F_Z	w	0.4%	0.33%

2.4 **Inertia Properties**

2.4.1 Calculation of Cross-sectional Inertias

The FEM model contained distributed structural mass in the form of element densities as well as nonstructural point masses and inertias. UM/NAST allows for the specification of both distributed and concentrated inertias, but only concentrated inertias were used in this model for simplicity. In order to calculate the concentrated inertia properties for the reference beam, the distributed and point inertia values were extracted from the FEM model. This could have been done by hand, or using any suitable FEM modelling tool. For this study, the Mass Properties

Tool of MSC Patran was used. The wing was sliced into regions corresponding to the stations of the 20 and 30 reference node sets, and the mass, center of gravity, and concentrated inertias were calculated for each region. Four additional regions were used to define the inertia of the winglet. The center of gravity of each region was designated as the location of a point mass in the UM/NAST model. Figure 2.18 shows the location of these point masses, which represent the mass of each wing region, relative to the wing reference node positions. Figure 2.19 and Figure 2.20 show the spanwise distribution of mass and cross-sectional inertias, respectively. The mass values are normalized by the total mass of the wing. Inertia was measured about the center of gravity in the local 1, 2, and 3 axes and normalized by the mass-weighted wing reference area. The center of gravity positions are normalized by the aircraft mean aerodynamic chord. A comparison between the wing's total mass and center of gravity is given in Table 2.2**.**

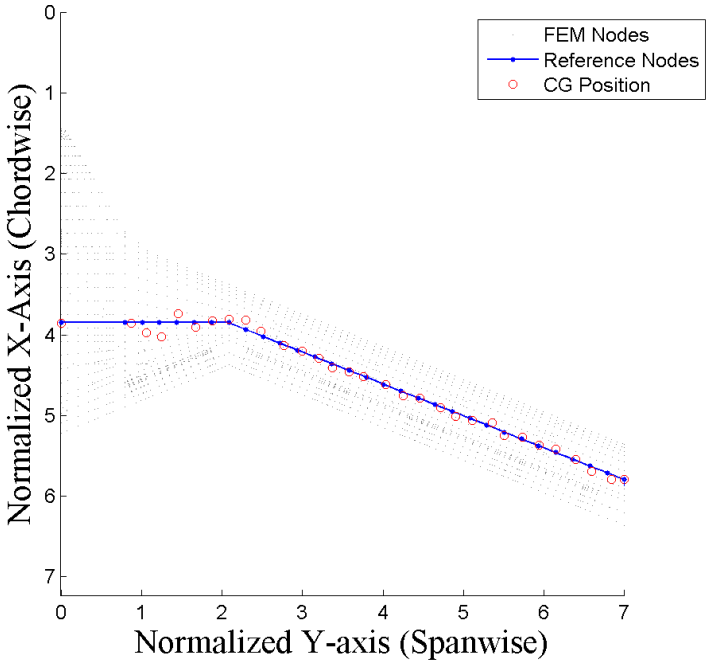

Figure 2.18. Lumped mass center of gravity locations relative to reference nodes

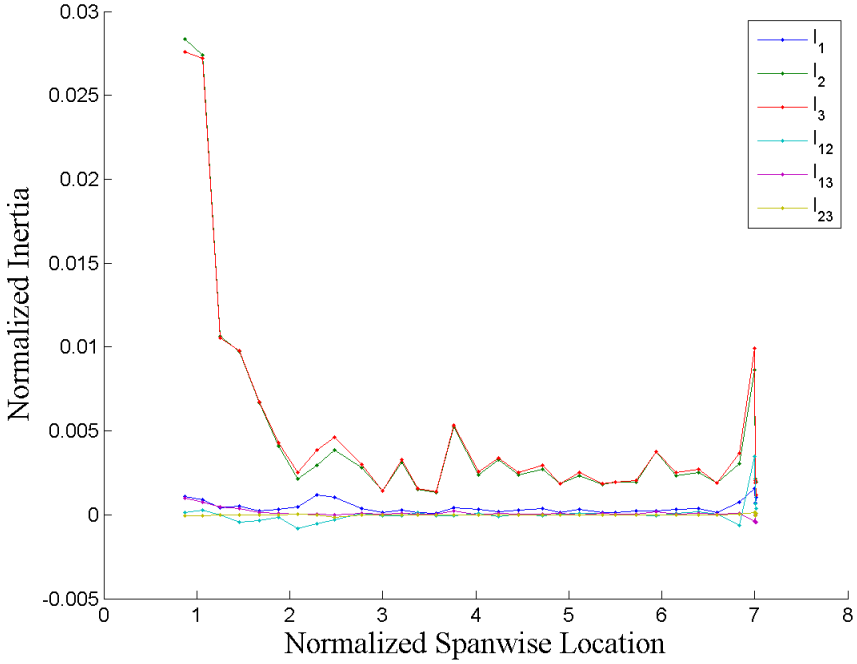

Figure 2.19. X-56A spanwise inertia distribution

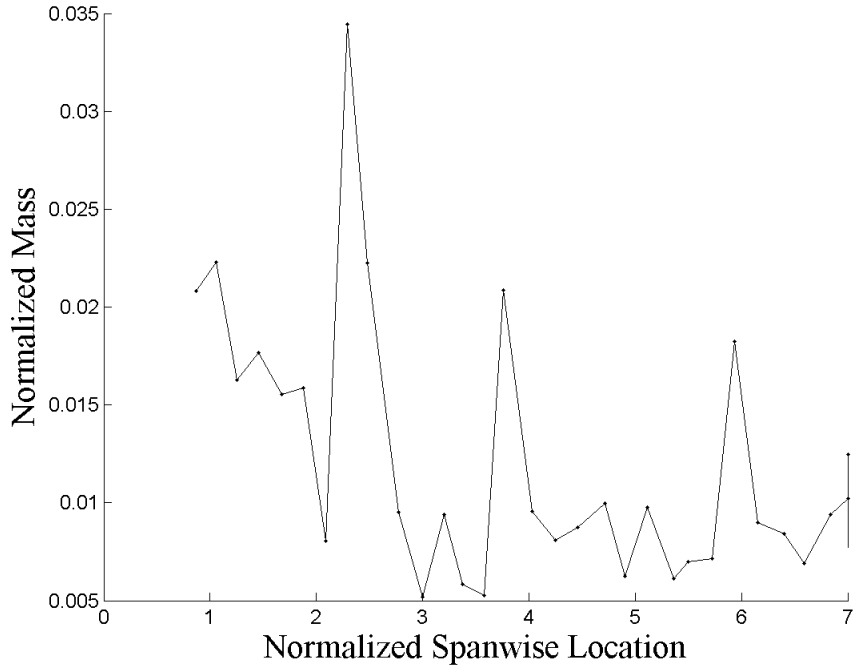

Figure 2.20. X-56A spanwise mass distribution

Table 2.2. Total mass and center of gravity of the wing model

Property	NASTRAN	UM/NAST	%Error
Normalized Mass	100	99.97	0.03%
Normalized CG_X	7.41	7.40	0.11%
Normalized CG_Y	3.69	3.66	0.94%
Normalized CG_Z	4.33	4.44	-2.55%

2.4.2 Dynamic Response Prediction

As the stiffness constants were verified against static deflections, the inertia values extracted from the FEM also need to be verified. The inertia properties presented in the previous section were used to generate the initial modal frequencies in UM/NAST. By tuning the inertias, the UM/NAST frequencies were adjusted to match the NASTRAN model, which had been validated with ground vibration tests. Two X-56A models were developed through this process: Model A incorporated control surface motion in the stiffnesses and modelled their weight offset with rigid rods. The inertias of Model A were split between the main reference beam and control surface rods. Model B neglected control surface motion altogether, and all inertias are concentrated around the main reference beam. The frequency correlation of the first four modes from NASTRAN and the UM/NAST models are presented in Table 2.3. The frequencies are normalized against the first vertical bending frequency from the NASTRAN model. The corresponding mode shapes are shown in Figure 2.21.

The control surfaces and winglet participate significantly in many of the lower frequency modes, yet the UM/NAST beam models were still able to capture the mode coupling that occurs, even without a detailed model of the dynamics of the control surfaces. The simpler Model B performed better in capturing the modal frequencies and mode coupling, while Model A replicated the shape of the entire mode more closely. For the purposes of this study, the frequencies and mode coupling are more important than the mode shapes themselves, so Model B was used for the further model development, including the creation of the aerodynamic loads and flutter analysis.

Table 2.3. Normalized natural frequencies of NASTRAN and UM/NAST models

Mode Shape	Normalized Frequency			% Error from Reference	
	NASTRAN Ref. Model	UM/NAST Model A	UM/NAST Model B	UM/NAST Model A	UM/NAST Model B
1st vertical bending	1.00	0.97	0.99	2.89%	0.74%
1st torsion, coupled with vertical bending	4.87	4.63	4.91	4.97%	-0.67%
1st in-plane, coupled with vertical bending & torsion	5.28	5.02	5.29	4.87%	-0.20%
2nd torsion, coupled with vertical bending	6.61	6.16	6.51	6.87%	1.52%

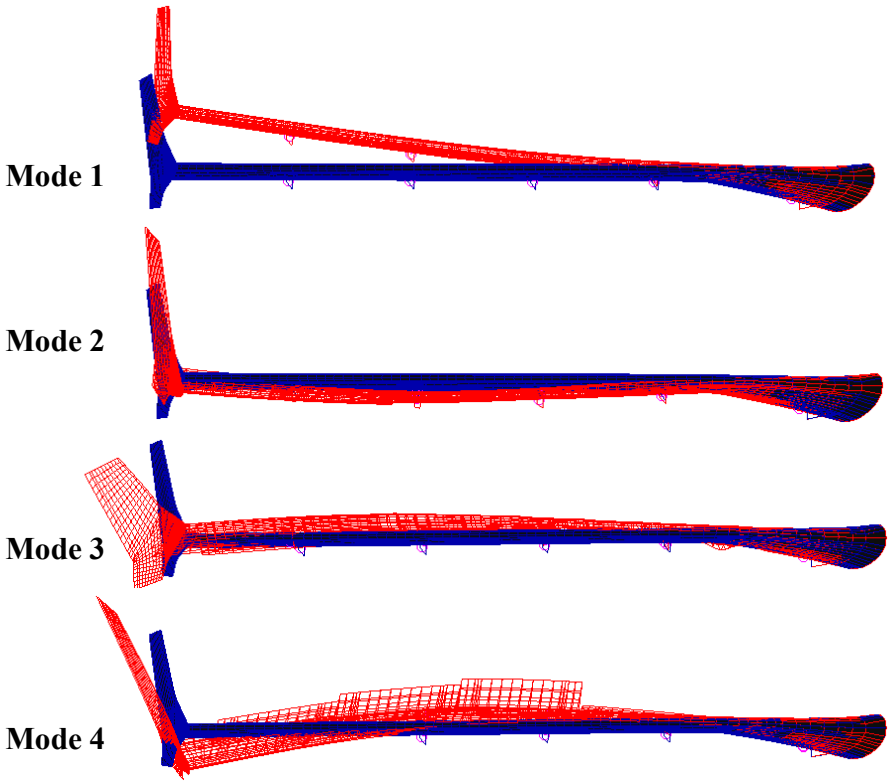

Figure 2.21. X-56A natural mode shapes

2.5 Aerodynamic Properties

The UM/NAST aerodynamic solver uses the same discretization as the structural solver and generates the aerodynamic loads at each structural node using Peters' finite-state inflow

theory.[17] The cross-sectional lift, drag, and pitching moment about the aerodynamic center of each airfoil is defined by Equation 2.4 in terms of user-supplied aerodynamic coefficients and coefficient derivatives, and orientation and motion of the local nodal frame. The cross-sectional loads are integrated across the span to generate the full lift, drag, and pitching moment of the aircraft. This aerodynamic formulation assumes infinite, straight wings. An elliptical correction factor may be applied to the aerodynamic load distribution to approximate finite wing effects, but there is no reduction of lift due to sweep built into this aerodynamic formulation. For a full derivation of the the aerodynamic loads, refer to the work of Su.[26]

$$
\begin{aligned}
l_{ac} &= \pi\rho b^2\left(-\ddot{z}+\dot{y}\dot{\alpha}-d\ddot{\alpha}\right)+c_{l\alpha}\rho b\dot{y}^2\left[-\frac{\dot{z}}{\dot{y}}+\left(\frac{1}{2}b-d\right)\frac{\dot{\alpha}}{\dot{y}}-\frac{\lambda_0}{\dot{y}}\right]+\rho b\dot{y}^2 c_{l\delta}\delta \\
m_{ac} &= \pi\rho b^3\left[\frac{1}{2}\ddot{z}-\dot{y}\dot{\alpha}-\left(\frac{1}{8}b-\frac{1}{2}d\right)\ddot{\alpha}\right]+2\rho b^2\dot{y}^2\left(c_{m0}+c_{m\delta}\delta\right) \\
d_{ac} &= -\rho b\dot{y}^2 c_{d0}
\end{aligned}
\tag{2.4}
$$

Wind-tunnel validated lift, drag, and moment coefficients for the X-56A full aircraft were provided by NASA for various angles of attack, sideslip angles, and control surface deflections. Figure 2.22 shows the aerodynamic coefficients provided for the full aircraft at zero angle of attack and zero sideslip angle, with no control surface deflection, at the reference airspeed V_{ref}. These total aircraft loads must be discretized into cross-sectional coefficients for use in the UM/NAST aerodynamic framework.

The airfoil profile, chord, and incidence angle of the X-56A vary along the span, most significantly in the center wing-body region in the first 30% of the span. The main wing maintains a constant airfoil profile and chord. Several stations were chosen along the span and shown in Figure 2.23, and the airfoils extracted at these stations were used as the basis for calculating the spanwise loads of the X-56A. The following sections present two approaches to producing the cross-sectional coefficients. The first method uses XFOIL,[55] a panel method code used for viscous and inviscid analysis of airfoil sections, to generate 2-D coefficients along the span. The second method uses an unsteady Vortex Lattice Method to generate 3-D coefficients along the span.

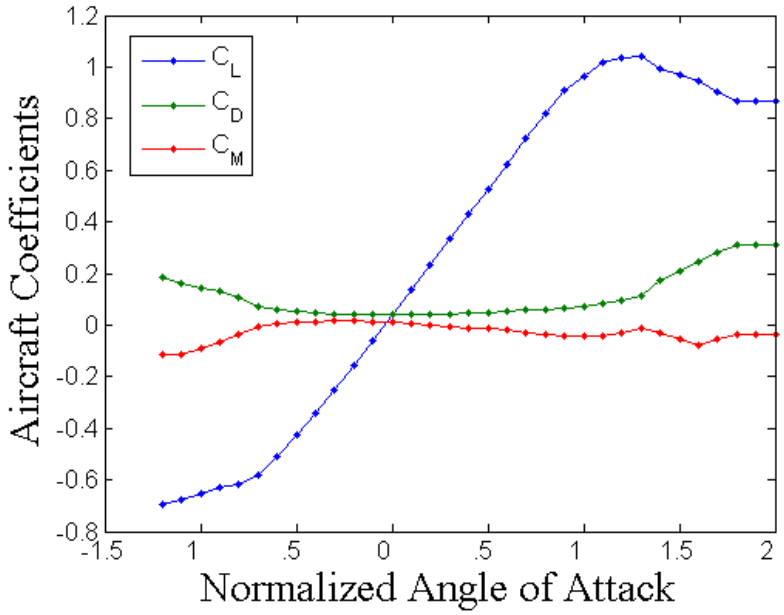

Figure 2.22. X-56A aircraft aerodynamic coefficients

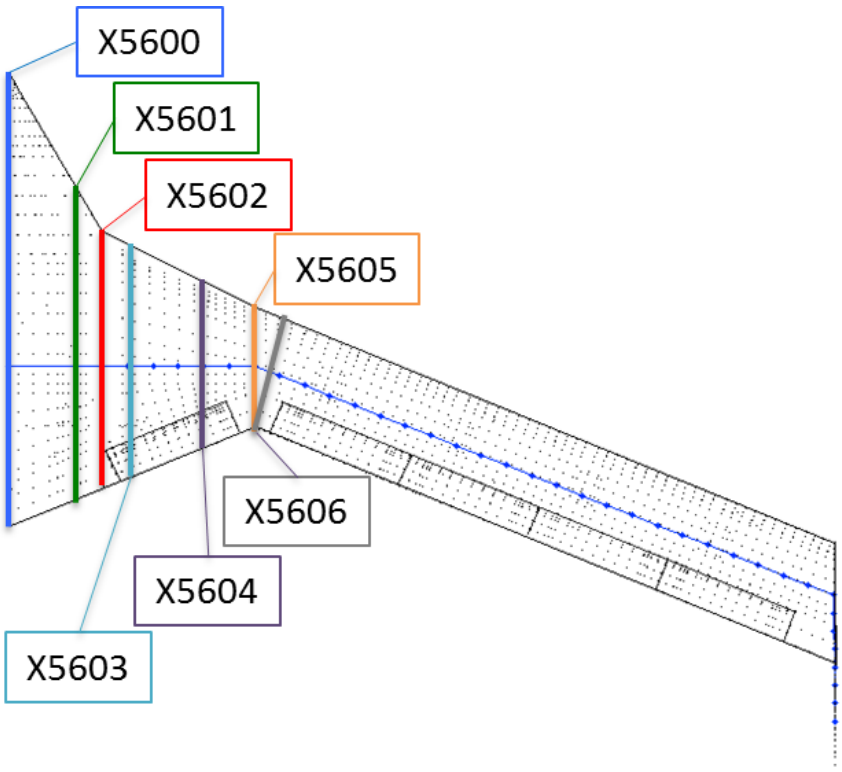

Figure 2.23. X-56A spanwise airfoil stations

2.5.1 XFOIL Derived Coefficients

The lift, drag, and moment coefficients versus the stall-normalized local angle of attack for each profile were generated using XFOIL and shown in Figure 2.24, Figure 2.25, and Figure 2.26 respectively.

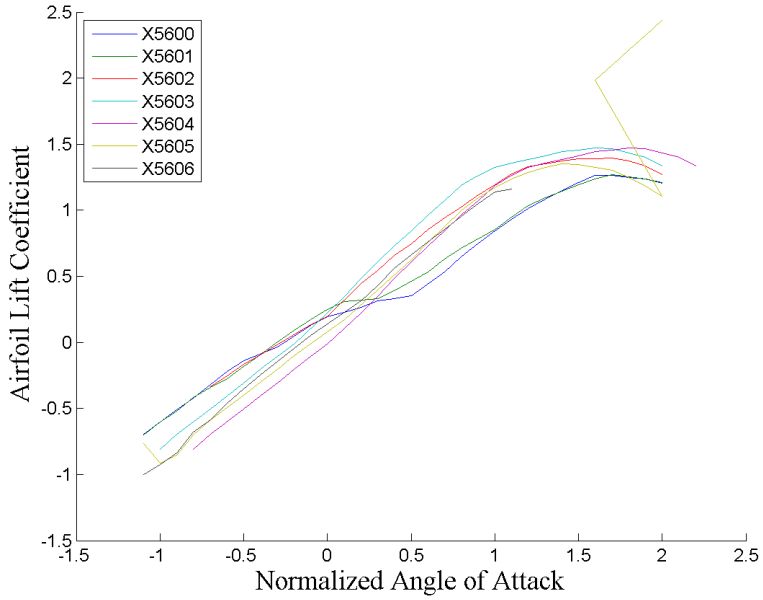

Figure 2.24. X-56A cross-sectional lift coefficient at chosen spanwsie stations

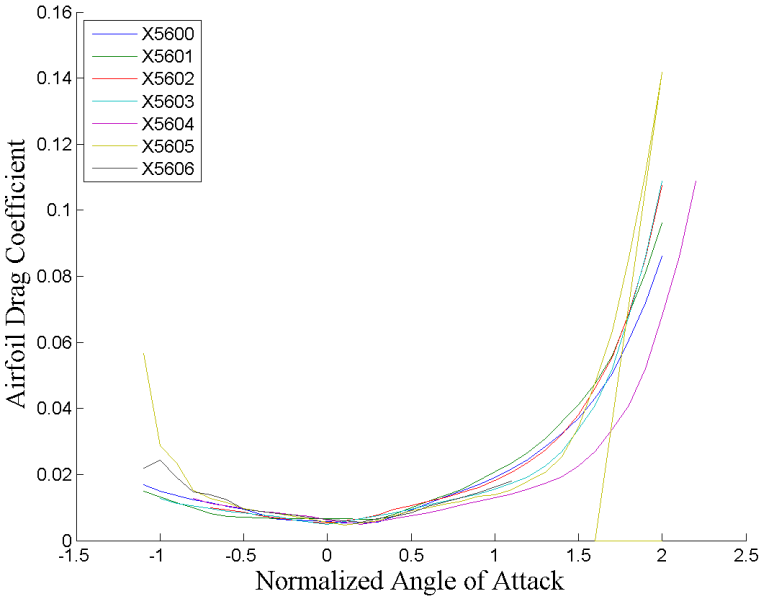

Figure 2.25. X-56A cross-sectional drag coefficients at chosen spanwise stations

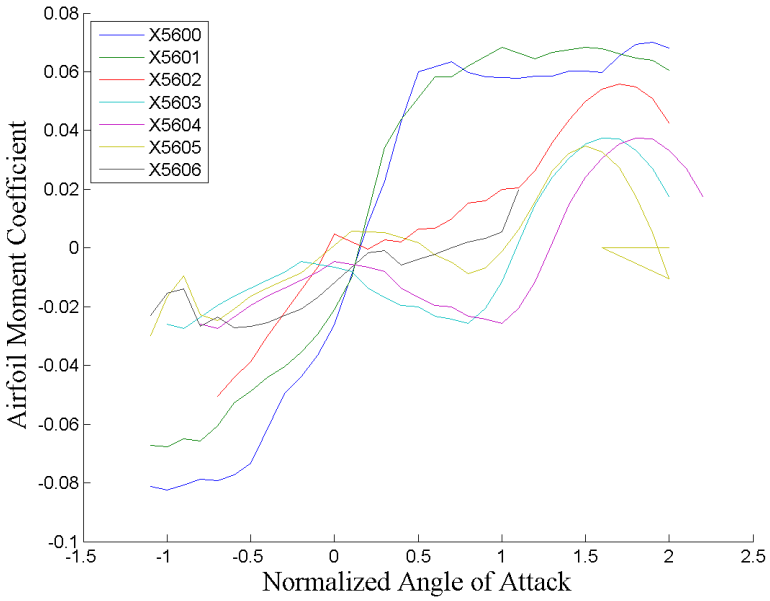

Figure 2.26. X-56A cross-sectional moment coefficient at chosen spanwise stations

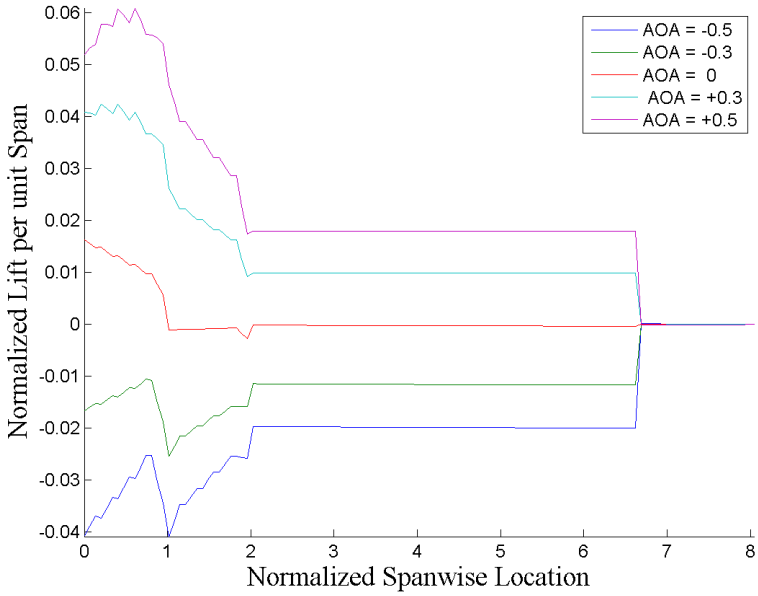

Figure 2.27. X-56A UM/NAST lift distribution over the semispan

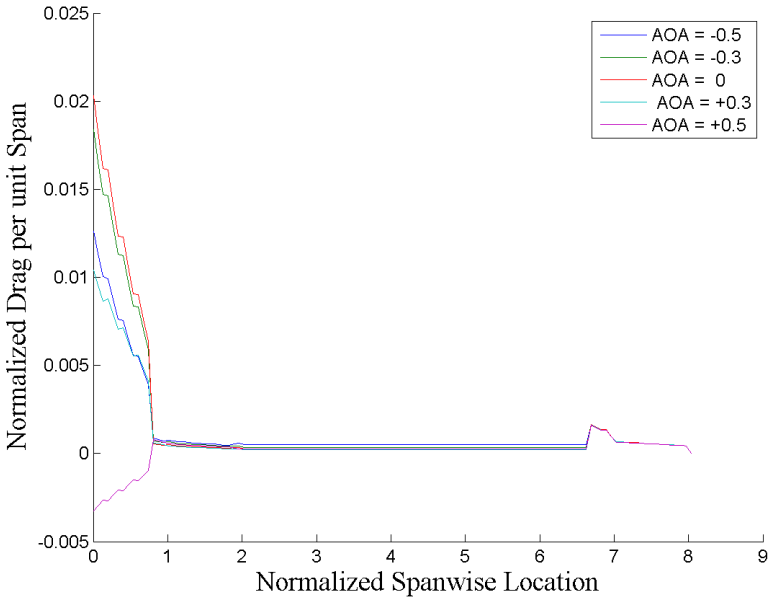

Figure 2.28. X-56A UM/NAST lift distribution over the semispan

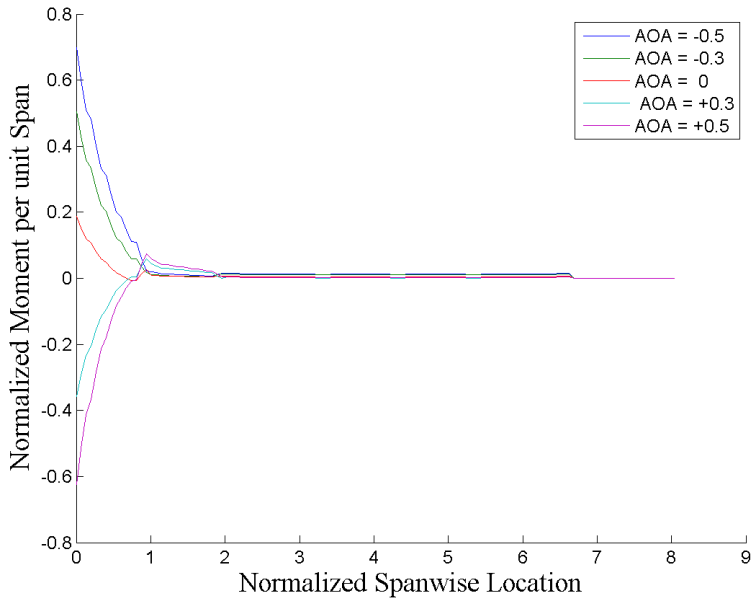

Figure 2.29. X-56A UM/NAST moment distribution over the semispan

Since the X-56 structural model is symmetric about the center of the aircraft, the aerodynamic loads are assumed to be symmetric as well. These loads were generated using the wing model with 30 reference nodes, as defined in Section 2.3.3. However, the wind tunnel data provided as a reference case was measured using a rigid model, so the UM/NAST model was

also made rigid in this comparison to remove any deformation effects from the aerodynamic loads.

The lift, drag, and moment distributions along the semispan of the UM/NAST model, derived from the XFOIL airfoil coefficients, are shown in Figure 2.27 through Figure 2.29. The total lift, drag, and moment of the aircraft for the wind tunnel test-corrected data is compared to the UM/NAST model in Figure 2.30 through Figure 2.32. The aircraft span is normalized by the reference chord. Angle of attack is normalized by the stall angle of the aircraft, and the aerodynamic loads are normalized against the dynamic pressure and surface area of the aircraft.

The UM/NAST total lift of the aircraft matches well with the wind tunnel data between ±0.5 normalized angle, and stall begins to set in outside of that range, evidenced by the flattening of the lift curve slope. Using XFOIL viscous drag coefficients, UM/NAST underpredicted the total drag on the aircraft and failed to capture the stall behavior. This is likely due to the drag contributions of the landing gear, engines, and other body-mounted equipment that disrupt the flow over the aircraft but are not modeled in UM/NAST. The aircraft moment was also significantly underpredicted.

A position-based correction was applied to the XFOIL drag and moment coefficients in order to improve the match of the total aircraft loads. The aircraft was divided into four regions – the center body, the body-flap region, the wing, and the winglet—and symmetry about the centerline of the aircraft is assumed. At each angle of attack, the difference in the total aircraft load between the wind-tunnel test data and the XFOIL-based UM/NAST loads was defined as the load delta ΔD.

$$\Delta D = D_{test} - D_{NAST} \tag{2.5}$$

The necessary load correction Δd_i for each region *i* of the aircraft is expressed with respect to the load delta:

$$\Delta d_i = \Delta D(\frac{d_i}{D_{NAST}}) \tag{2.6}$$

Each region contains *n* nodes, and these aerodynamic nodes are collocated with the structural nodes defined in Section 2.3.3. The chord was allowed to vary at each node to account for the tapering of the wing. At each node *n*, the load coefficient $c_{d,n}$ is weighted by the element chord c_n. The ratio g_n of the *n*th weighted coefficient relative to the load coefficient of the first node in the region is given as:

$$g_n = c_n \cdot c_{d,n} / c_1 \cdot c_{d,1} \tag{2.7}$$

The nodal drag coefficients are integrated along the span to yield the regional drag coefficient. Rearranging the integral equation yields an expression for the drag coefficient at the first node and its relation to the regional drag coefficient:

$$\Delta D = \int (\Delta d_i)ds = 0.5 q_{ref} \sum_{n=1}^{N} (l_{n+1} - l_n)(d_n + d_{n+1}) \Rightarrow \quad c_{d,1} = \frac{\Delta d_i}{0.5 q_{ref} (l_2 - l_1)(g_n + g_{n+1})} c_1 \tag{2.8}$$

Replacing the generic load coefficients in Equations 2.5 through 2.8 with the cross-sectional drag and moment coefficient yields the correction equations for those aircraft loads. Even without additional information about the spanwise coefficients or accounting for sweep effects, these corrections are able to approximate the spanwise loads. The comparison of aircraft load between the wind tunnel reference and UM/NAST using XFOIL lift and corrected XFOIL drag and moment coefficients are given in Figure 2.33 through Figure 2.35.

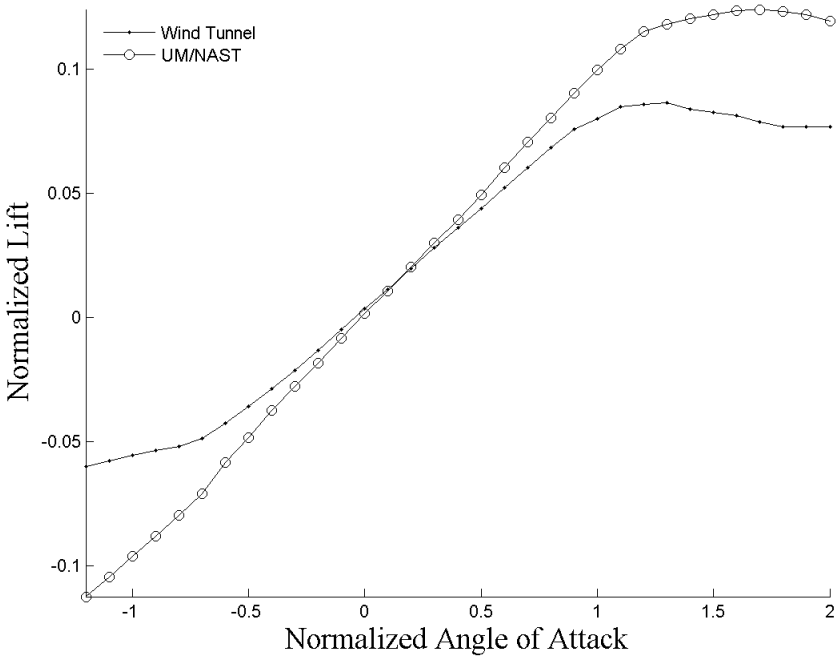

Figure 2.30. X-56A wind tunnel vs XFOIL-based UM/NAST lift

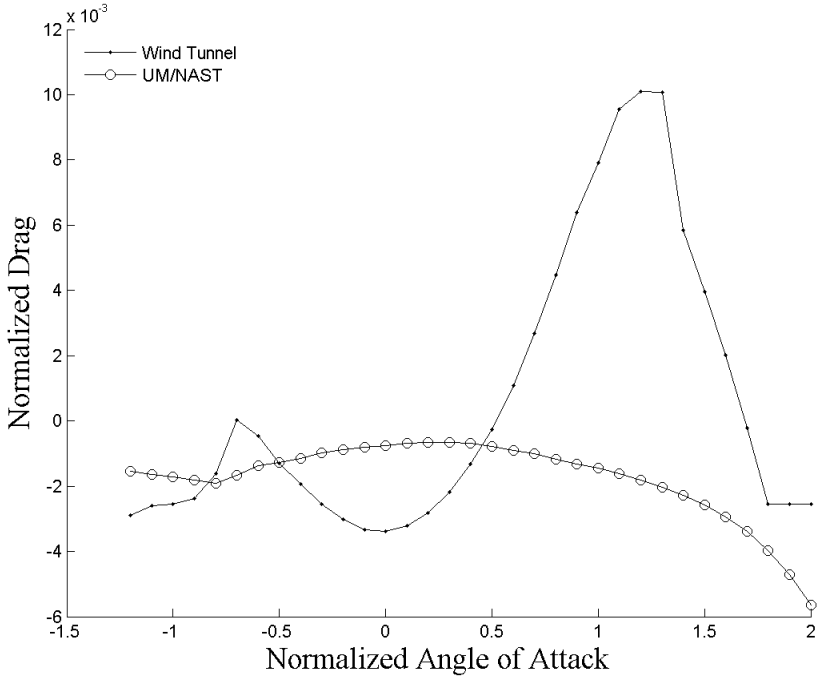

Figure 2.31. X-56A wind tunnel vs XFOIL-based UM/NAST drag

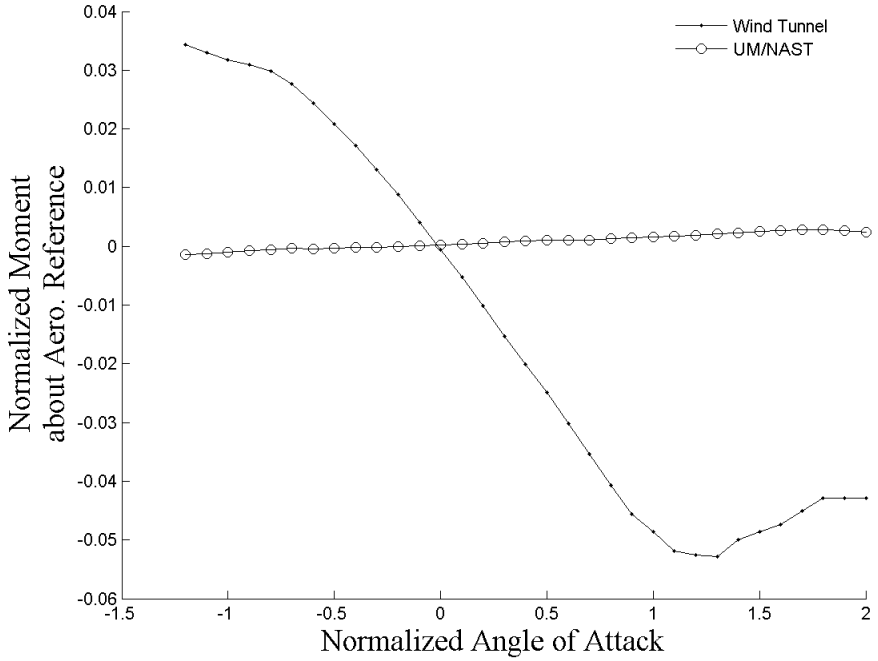

Figure 2.32. X-56A wind tunnel vs XFOIL-based UM/NAST moment about reference axis

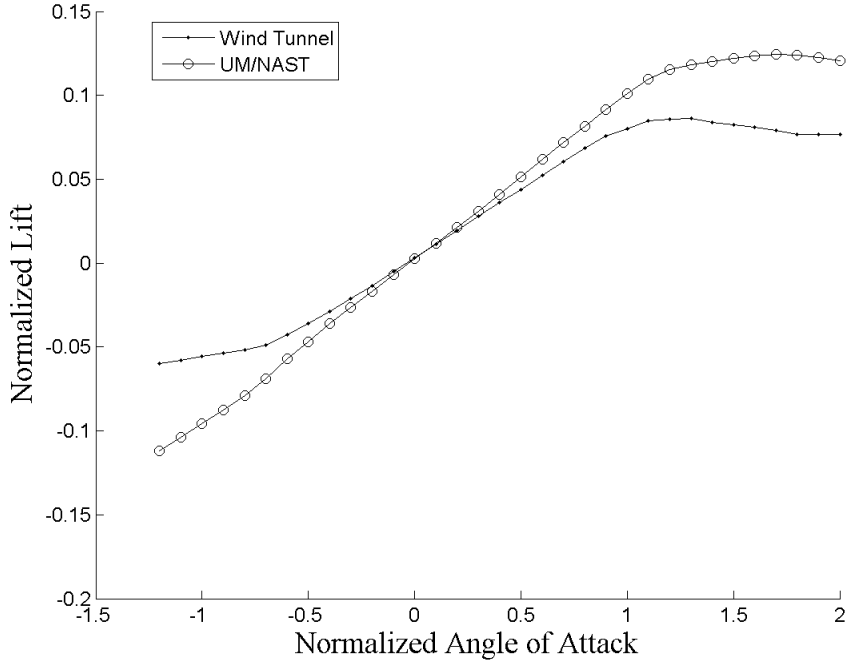

Figure 2.33. X-56A wind tunnel vs XFOIL-based UM/NAST lift

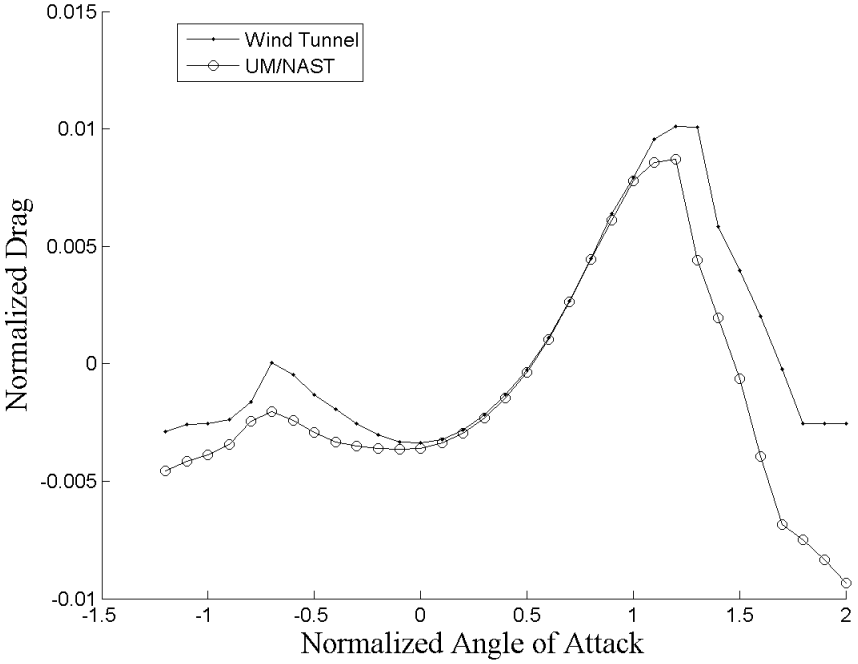

Figure 2.34. X-56A wind tunnel vs corrected XFOIL-based UM/NAST drag

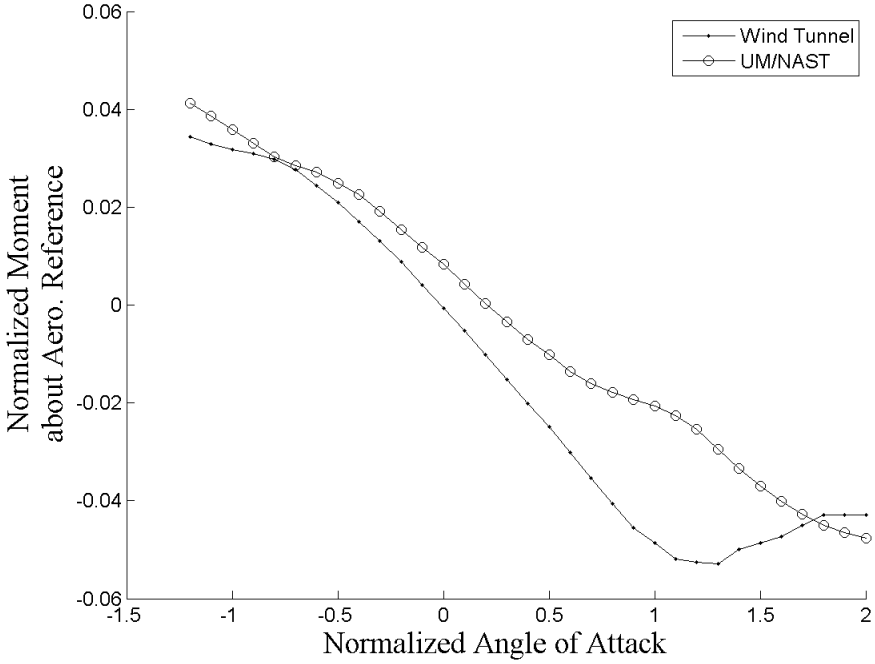

Figure 2.35. X-56A wind tunnel vs corrected XFOIL-based UM/NAST moment about reference axis

2.5.2 VLM Derived Coefficients

In order to introduce sweep effects into the aerodynamic model, a steady vortex lattice panel method (VLM) was used to calculate the lift distribution along the wing. The aircraft was divided into four regions– center-body, wing-body, wing, and winglet—and the number of panels defined in each region is listed in Table 2.4. The chordwise discretization remains constant over the entire span, while the spanwise discretization for each member was chosen to give a panel width of approximately 1-inch. The chordwise panels are arranged along the camber line at each spanwise station, where the camber is defined using the seven airfoils extracted for the previous XFOIL analysis. The resulting lift distribution is shown in Figure 2.36.

To compare to the wind-tunnel reference data, the panel-generated distributed lift is integrated across the span to determine the total aircraft lift. When compared to the reference data, the panel distribution underestimates the lift-curve slope, and doesn't capture the lift plateau due to stall. An incidence-dependent scale factor η can be defined at each angle of attack as:

$$\eta = \frac{L_{REF}}{L_{VLM}} \tag{2.9}$$

This scale factor is used to adjust the value of VLM integral in Equation 2.10 to match the reference data, as shown in Equation 2.11.

$$L_{VLM} = \int_{-b}^{b} l_{ac}(x)dx = \sum_{n} l_{ac,n}\Delta x_n \tag{2.10}$$

$$L_{REF} = \eta L_{VLM} = \sum_{n} \eta l_{ac,n}\Delta x_n \tag{2.11}$$

When the scale factor applied to the VLM lift distribution, this yields the lift curve shown in Figure 2.37. The VLM is an inviscid method, so the corrected XFOIL viscous drag and pitching moment coefficients are used with this VLM-derived lift to generate the resulting rigid-wing aerodynamic load distributions from UM/NAST are shown in Figure 2.38 through Figure 2.40.

Table 2.4. VLM discretization of X-56A model

Aircraft Region	Chordwise # Panels	Spanwise # Panels
Center Body	20	10
Wing Body	20	15
Wing	20	60
Winglet	20	15

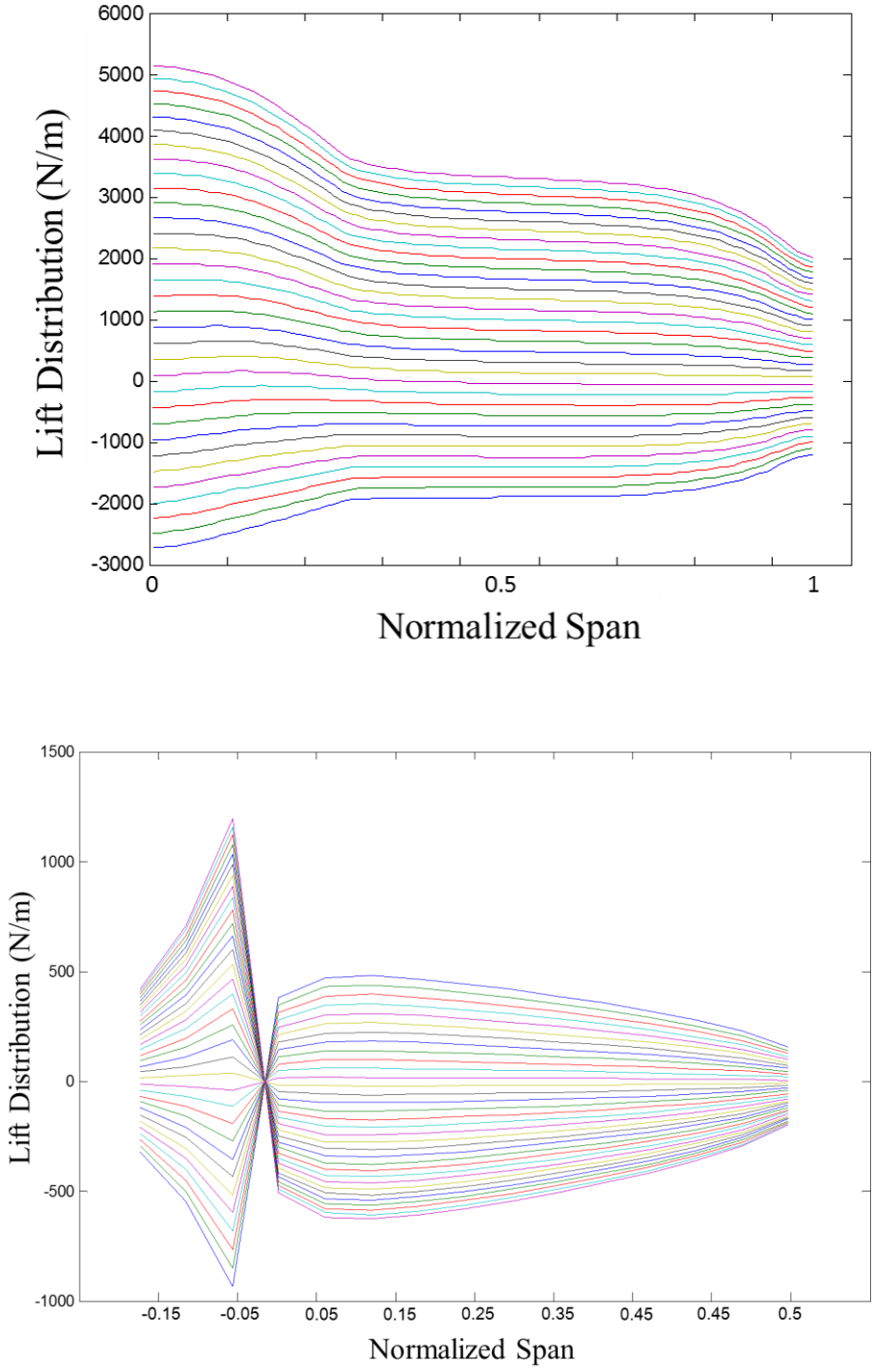

Figure 2.36. X-56A VLM lift distribution along the semispan (top) and winglet (bottom)

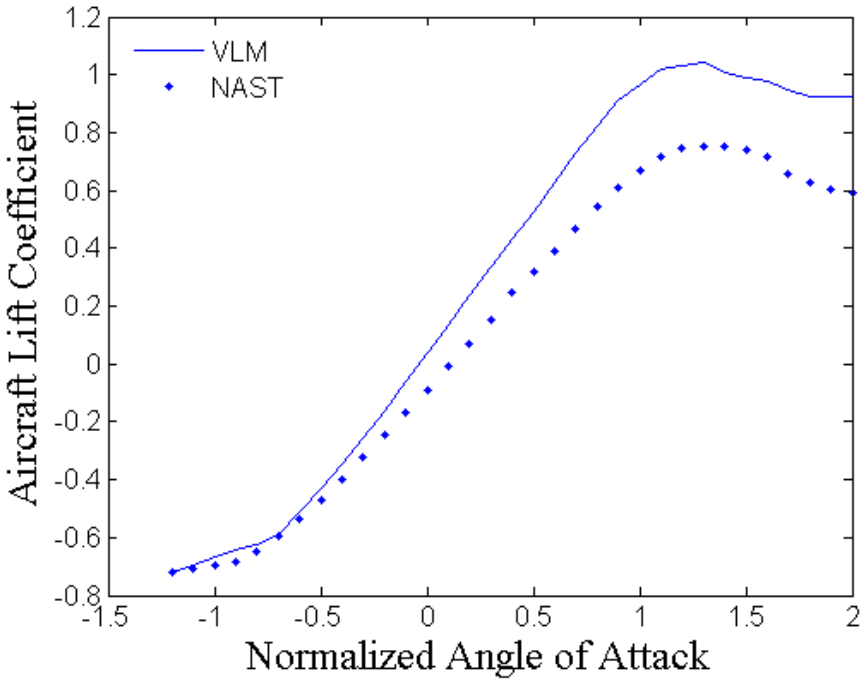

Figure 2.37. X-56A total lift from VLM compared to wind tunnel reference

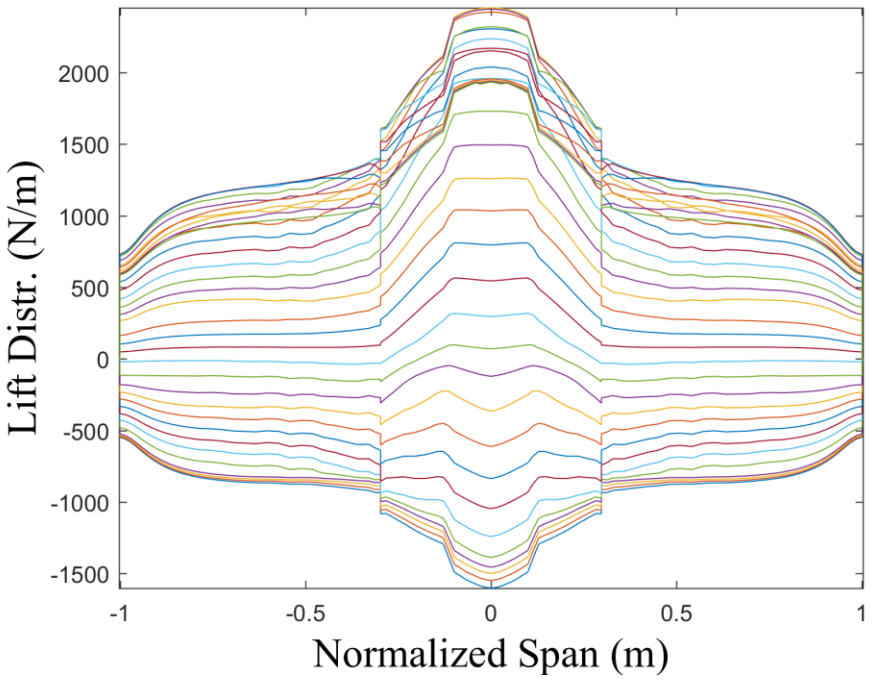

Figure 2.38. Final lift distribution for X-56A UM/NAST model

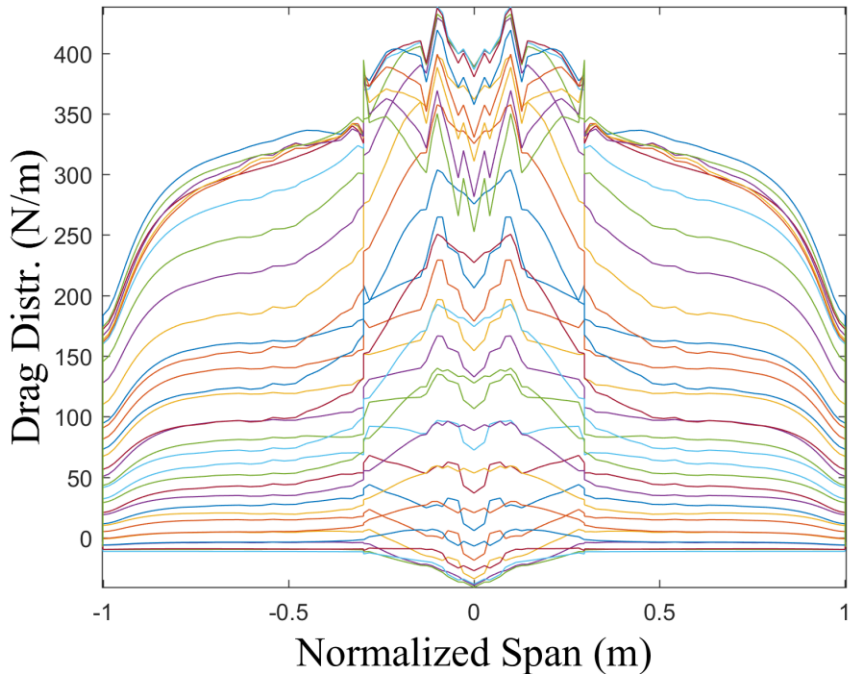

Figure 2.39. Final drag distribution for X-56A UM/NAST model

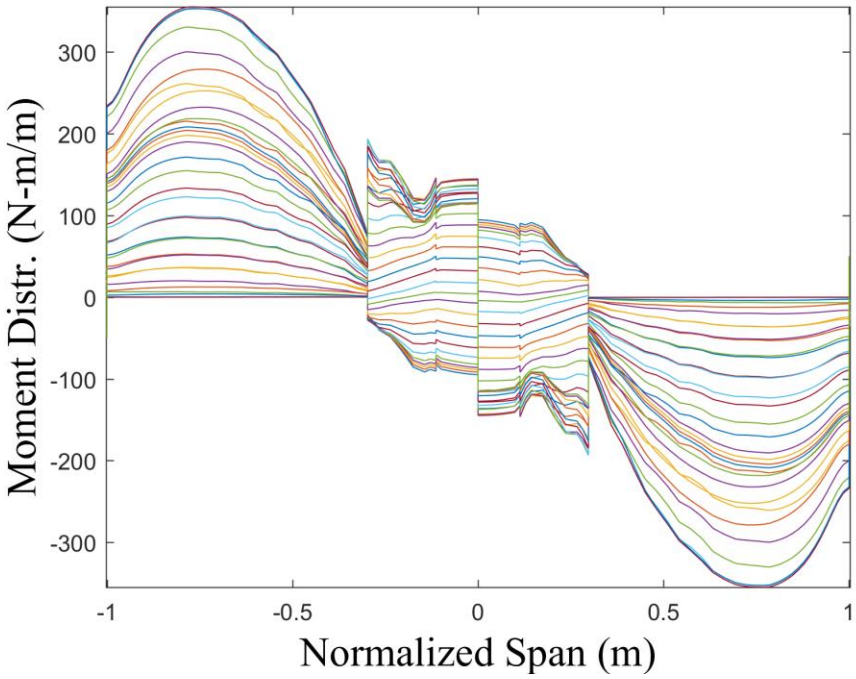

Figure 2.40. Final moment distribution for X-56A UM/NAST model

2.6 Aeroelastic Studies

The UM/NAST model created in Sections 2.1 through 2.5 is a simplified representation of the X-56A aircraft, and it is able to replicate the elastic, modal, and aerodynamic behavior of the fully built-up model. With this model, we can conduct a wide range of aeroelastic analyses, including static aeroelastic trim and flutter on a number of different payload configurations.

2.6.1 Aeroelastic Trim Analysis

The UM/NAST trim algorithm minimizes the residual forces and moments on the aircraft by performing a nonlinear static analysis at the desired trimmed flight condition and adjusting the trim parameters to minimize the residual loads. The parameters used to trim the X-56A model are the body angle of attack, the body sideslip angle, engine thrust, and the control surface deflections. The X-56 model has two engines located in the center body region, and during trim, the thrust from both engines are constrained to be identical. There are five trailing edge control surfaces distributed along the semispan of the aircraft: the body flap is located in the wing-body region, and four ailerons are located in the wing. During trim, the body flaps are allowed to deflect independently, while the ailerons are linked in asymmetric, doublet pairs. The ailerons are numbered according to their position along the span, with CS1 designating the aileron pair closest to the center body and CS4 designated the aileron pair near the wingtips. A series of aeroelastic trim analyses were performed on this model to illustrate of the impact of using the 3D VLM-derived lift distribution over the 2D XFOIL-based lift. The viscous drag and moment coefficients for both cases are the XFOIL-corrected coefficients. The trim solutions at the speed V_{ref} are compared for the VLM-derived loads and the XFOIL-based loads in Table 2.5.

When the VLM lift distribution was used, there was not enough lift at small angles of attack to balance the weight of the vehicle, so a higher angle of attack was sought and the body flaps were fully deployed in order to adjust the lift in the center body region. When the XFOIL lift coefficients were used, ignoring the decrease in lift due to wing sweep, there was more lift available at smaller angles of attack, and the body flaps were not as heavily utilized. However, the increased drag due to lift was reflected by a larger required engine thrust. The wing deformation and VLM-derived aerodynamic load distribution at several trim conditions are shown in Figure 2.41 through Figure 2.43.

Table 2.5. Effect of VLM lift on trim parameters at V_{ref}

Normalized Trim Parameter	Trim Solution (VLM)	Trim Solution (XFOIL Wing)
Body Angle of Attack (deg)	2.13	1.19
Body Angle of Sideslip (deg)	0.00	0.00
Engine Thrust (N)	64.51	69.04
Control Surface CS1 (deg)	0.09	0.09
Control Surface CS2 (deg)	0.09	0.09
Control Surface CS3 (deg)	0.08	0.08
Control Surface CS4 (deg)	0.06	0.06
Left Body Flap (deg)	-4.00	-0.87
Right Body Flap (deg)	-4.00	-0.88

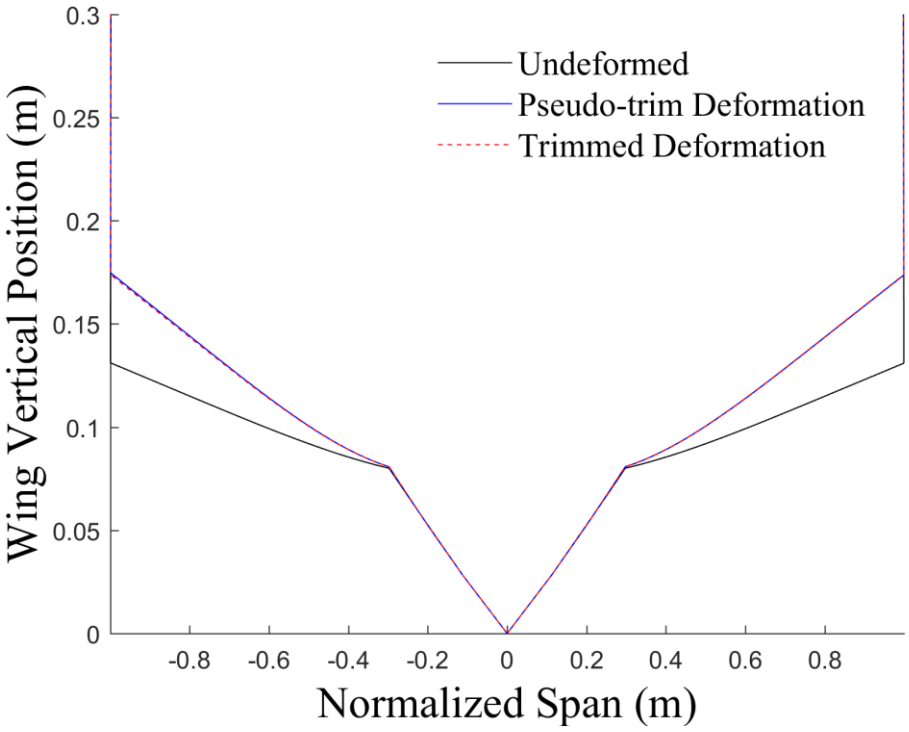

Figure 2.41. VLM-derived wing deformation at trim

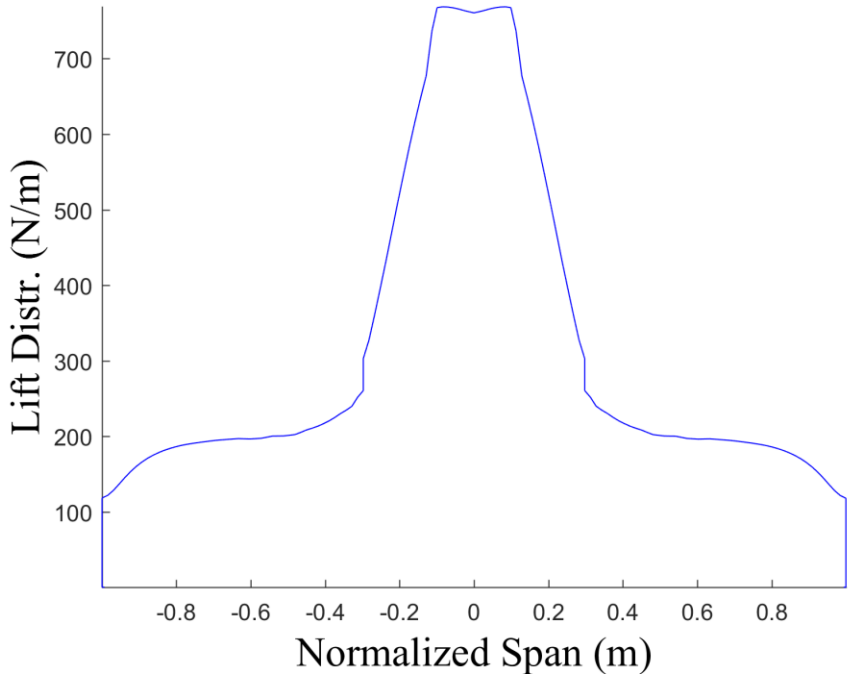

Figure 2.42. VLM-derived lift distribution at pseudo-trim

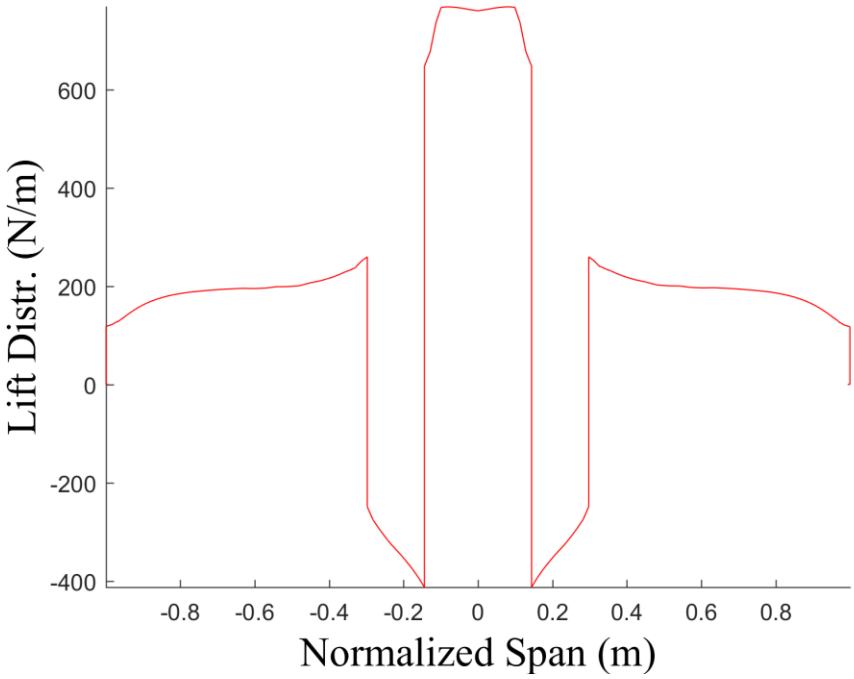

Figure 2.43. VLM-derived lift distribution at trim

2.6.2 Dynamic Aeroelastic Analysis

This section details the investigation of the aerodynamic load definition and payload configuration on the flutter boundary. In the nonlinear flutter analysis, a series of search speeds around the expected flutter boundary was defined. At each search speed, the free-flight model was linearized about the trimmed condition for that speed. The aeroelastic modes and frequencies were extracted from the linearized model for calculation of the flutter boundary. Finally, a nonlinear time-marching simulation of the aircraft configuration was performed to verify the flutter boundary and behavior. Flutter analysis was performed on three aircraft weight configurations: Empty Fuel Empty Water (EFEW), 7lb Fuel Empty Water (7FEW), and Full Fuel Empty Water (FFEW).

The EFEW configuration, the baseline model derived in previous sections, was used to explore the choice of trim condition and aerodynamic formulation on the flutter boundary. The flutter speed, frequency, and mode results are compiled in Table 2.6 for a cantilevered configuration (no rigid body motion allowed) and a free-flight configuration. The computed flutter boundaries were found using aerodynamic distributions generated using the XFOIL-based lift coefficients and the VLM-based lift distribution.

The next study investigates the effect of different payload configurations on the flutter boundary. These analyses use the VLM lift distribution with corrected viscous drag and moment as the aerodynamic model. As with the previous study, at each search speed, the models are linearized about their trim condition before the aeroelastic modes and frequencies are extracted for flutter calculation. The results are listed in Table 2.7 and shown in Figure 2.45 through Figure 2.50. For the cantilevered condition, the flutter speeds and frequencies are similar for each payload configuration. Since the varying payload is concentrated in the rigid center-body region, the inertia effects of the changing payload are negligible when rigid-body motion is removed from the problem. Interestingly, the first symmetric bending-torsion mode is not the flutter mode, instead the antisymmetric wing-bending torsion mode loses damping first. In the free-flight condition, the flutter speed increases as the payload weight increases. The flutter mode of the EFEW configuration is symmetric body freedom flutter, as expected. However, the flutter mode of the heavier configurations is an antisymmetric wing-bending torsion structural mode coupled with rigid body pitch. Although this is consistent with the flutter mode seen in the cantilevered condition, it is unexpected that an asymmetric mode would go unstable before the

much lower frequency symmetric modes. This was found to be due to the trim conditions used to linearize each model. Although the model itself is symmetric, there is some asymmetry in the trimmed aerodynamic loads introduced by the slight difference in the left and right body flap deflections.

In order to eliminate the effect of this asymmetry in the aerodynamic load distribution, a set of pseudo-trim parameters were defined. For each configuration, the body angle of attack is set to 2 degrees, the engine thrust is set to the trimmed value for $1.2V_{ref}$, and no control surface deflections were used. The flutter boundary found using this pseudo-trim condition is given in Table 2.8 and the V-g diagrams comparing the flutter boundary for all three configurations are shown in Figure 2.51 and Figure 2.52. Using pseudo-trim, the flutter mode for both the EFEW and 7FEW configurations is the symmetric body freedom flutter, followed closely by the higher frequency antisymmetric body freedom flutter mode. In the FFEW configuration, this trend is reversed as the antisymmetric mode loses damping just before the symmetric mode. This result suggests that the flutter speed may be very sensitive to the aerodynamic distribution, and flight conditions that result in non-symmetric aerodynamic loads, such as high-speed maneuvers or gust excitation, may be used to excite flutter. However, using these excitation methods may result in behavior that is different from the the flutter behavior computed assuming symmetric aerodynamic loads.

Table 2.6. Flutter boundary for EFEW model using different aerodynamic models

Aerodynamic Model	Configuration	Speed U_f	Frequency f_f (Hz)	Mode
XFOIL Lift, Drag, Moment	Cantilevered:	1.26	3.09	3BT
	Free-free:	1.19	3.98	ATSB
VLM Lift + XFOIL Drag, Moment	Cantilevered:	1.47	2.90	3BT
	Free-free:	1.23	3.02	ABFF

Table 2.7. Flutter boundary for trimmed X-56A configurations

Model Name	Configuration	Speed U_f	Frequency f_f (Hz)	Mode
EFEW	EFEW Cantilevered:	1.16	2.77	3BT
	Free-free:	0.89	0.79	SBFF
7FEW	7FEW Cantilevered:	1.09	2.59	1BT
	Free-free	0.95	2.70	ABFF
FFEW	FFEW Cantilevered:	1.16	2.62	1BT
	Free-free	1.04	2.87	ABFF

Table 2.8. Flutter boundary for X-56A configurations using pseudo-trim

Model Name	Configuration	Speed U_f	Frequency f_f (Hz)	Mode
EFEW	EFEW Cantilevered:	1.54	3.03	3BT
	Free-free:	1.13	0.92	SBFF
7FEW	7FEW Cantilevered:	1.54	3.01	3BT
	Free-free:	1.18	0.84	SBFF
FFEW	FFEW Cantilevered:	1.54	3.01	3BT
	Free-free:	1.18	2.89	ABFF

Mode 1: Symmetric Body Freedom Flutter (SBFF)

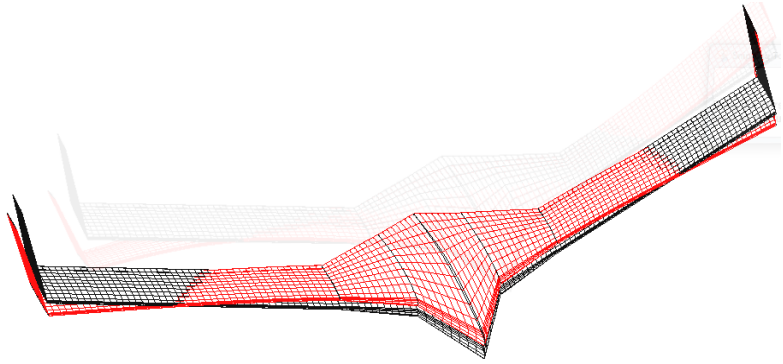

Mode 2: Symmetric Bending Torsion (SBT)

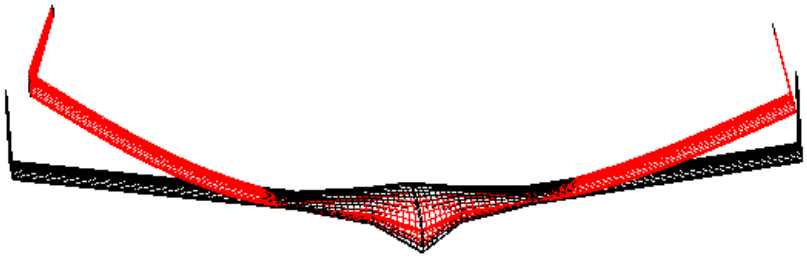

Mode 3: Antisymmetric Body Freedom Flutter (ABFF)

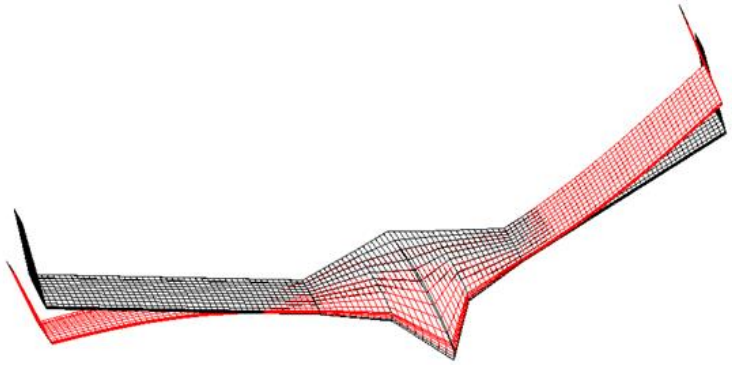

Mode 4: Antisymmetric Torsion, Symmetric Bending+pitch (ATSB)

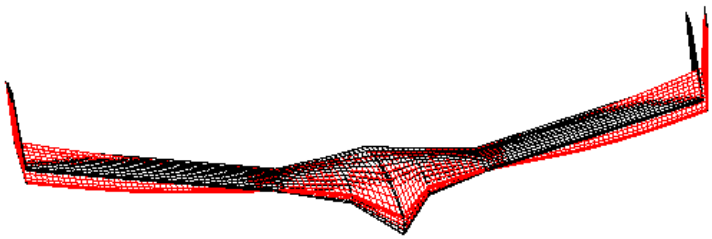

Figure 2.44. Flutter modes for free-flight configurations

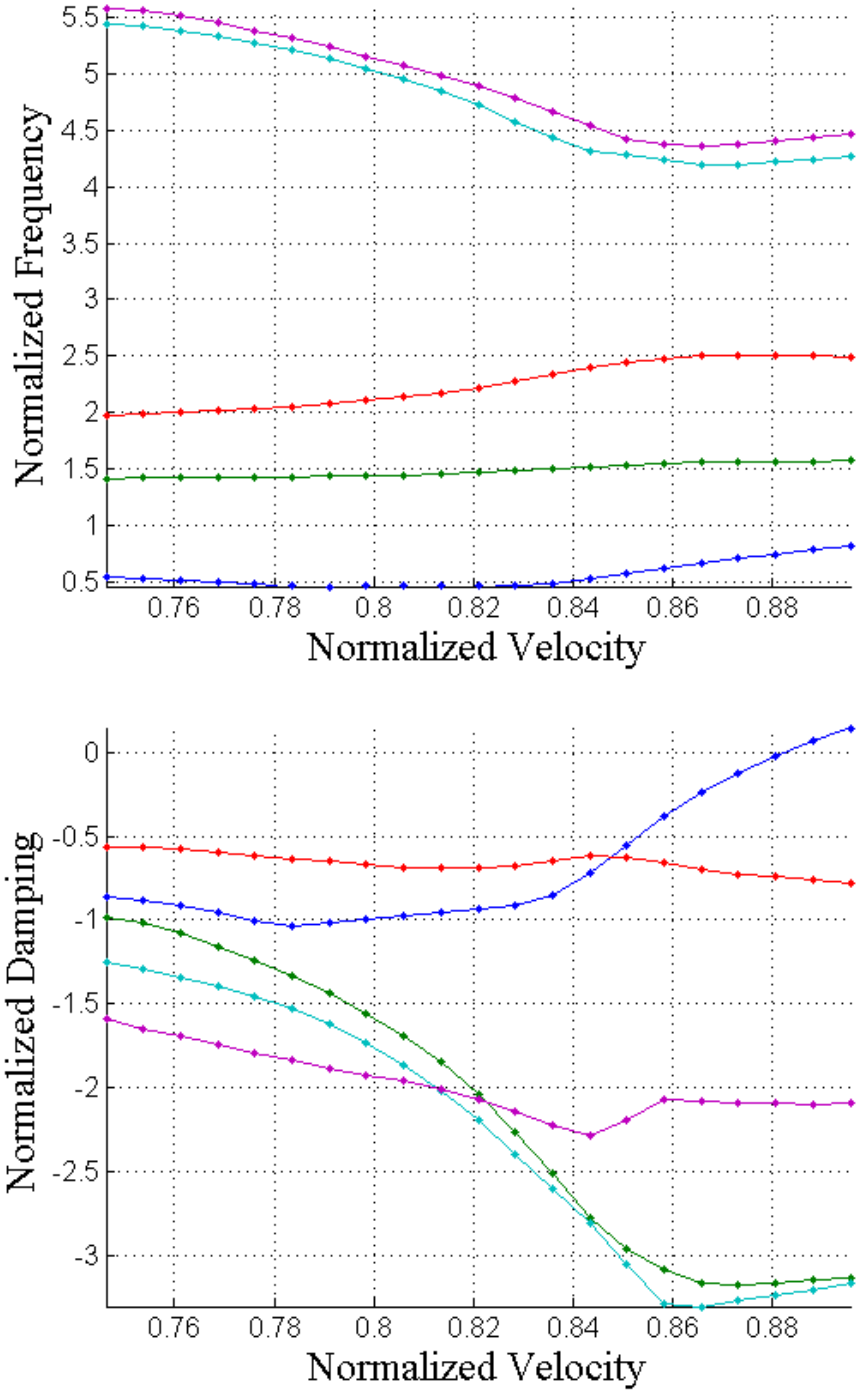

Figure 2.45. V-g diagram for trimmed, free-flight EFEW configuration

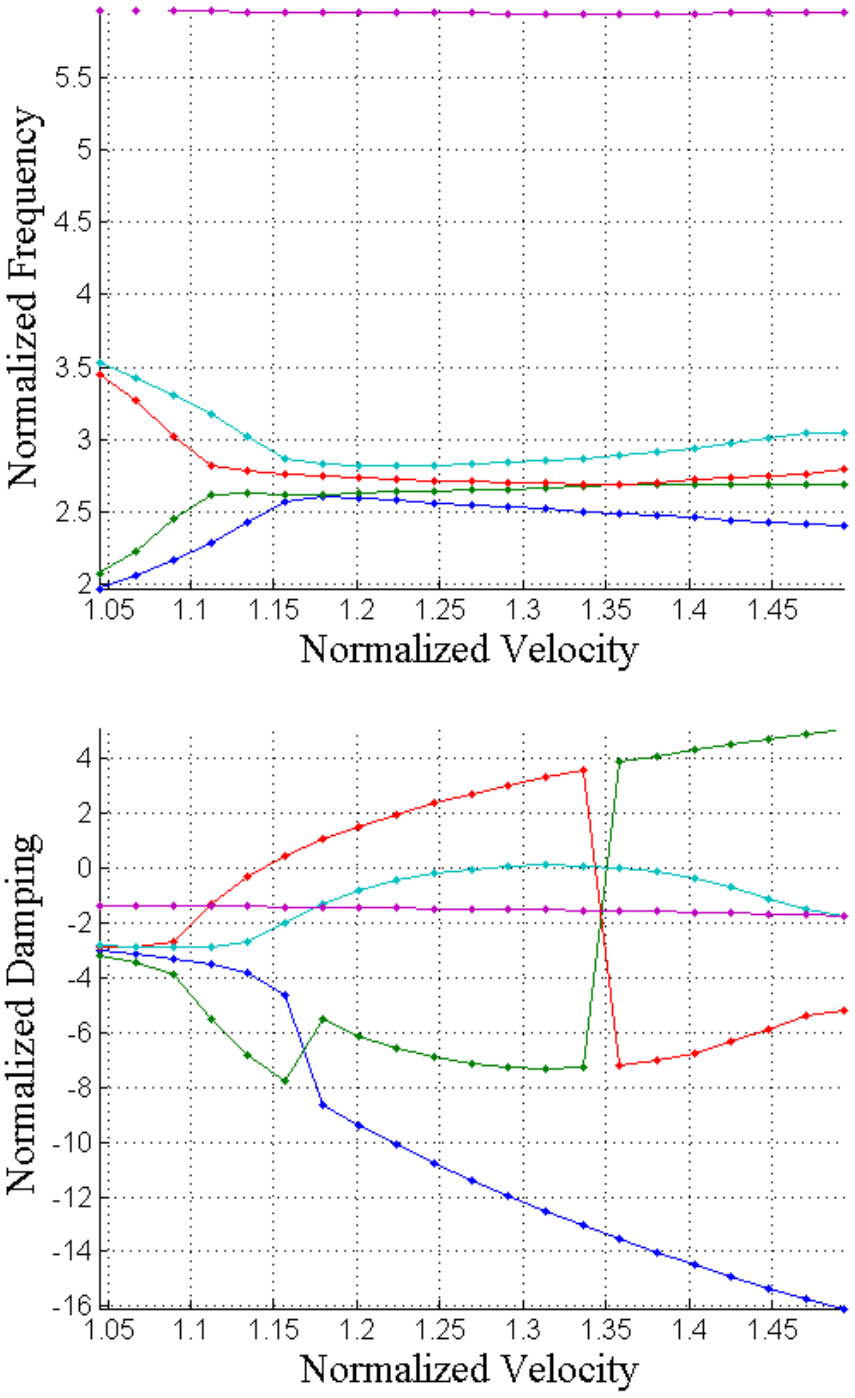

Figure 2.46. V-g diagram for trimmed, cantilevered EFEW configuration

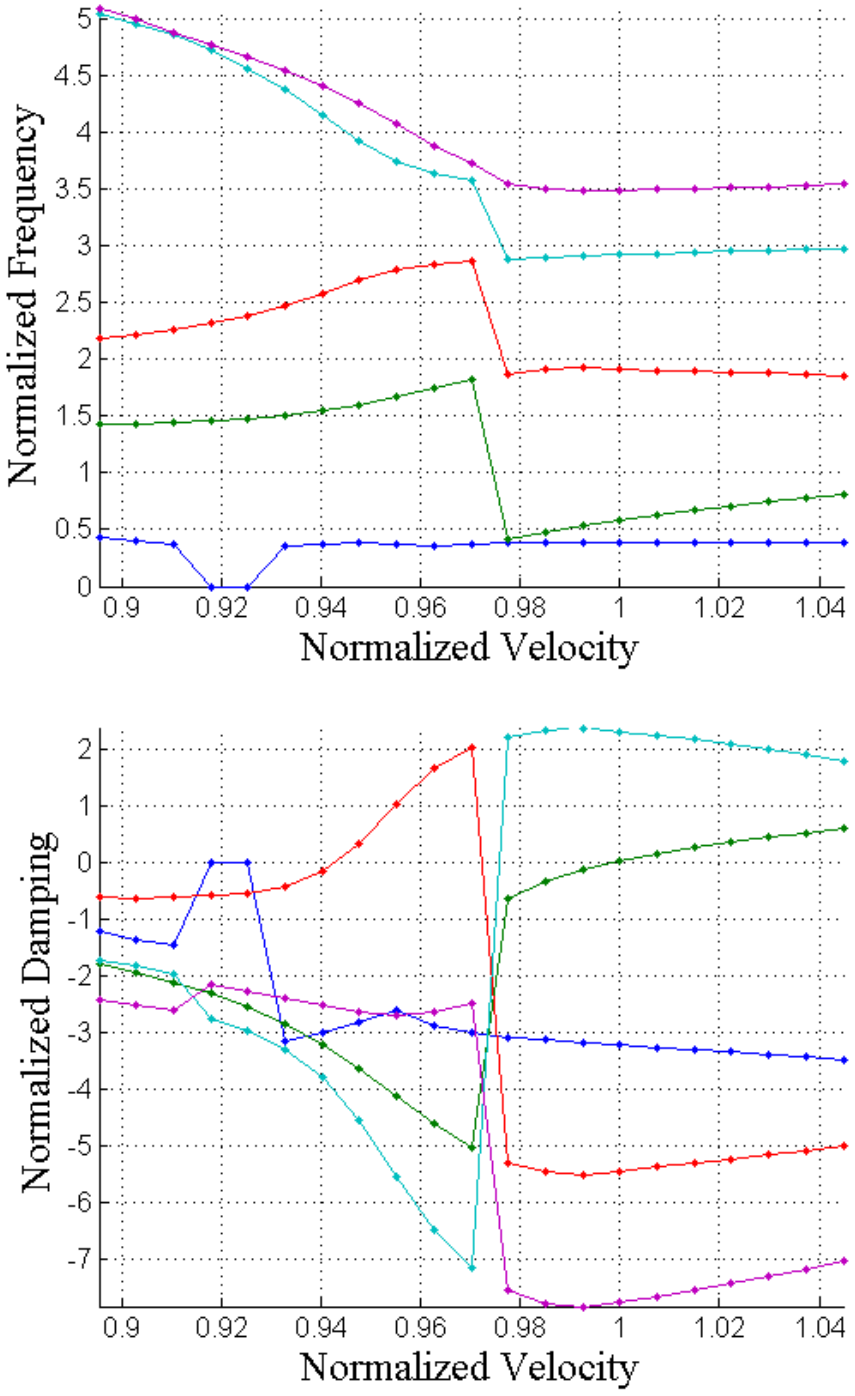

Figure 2.47. V-g diagram for trimmed, free-flight 7FEW configuration

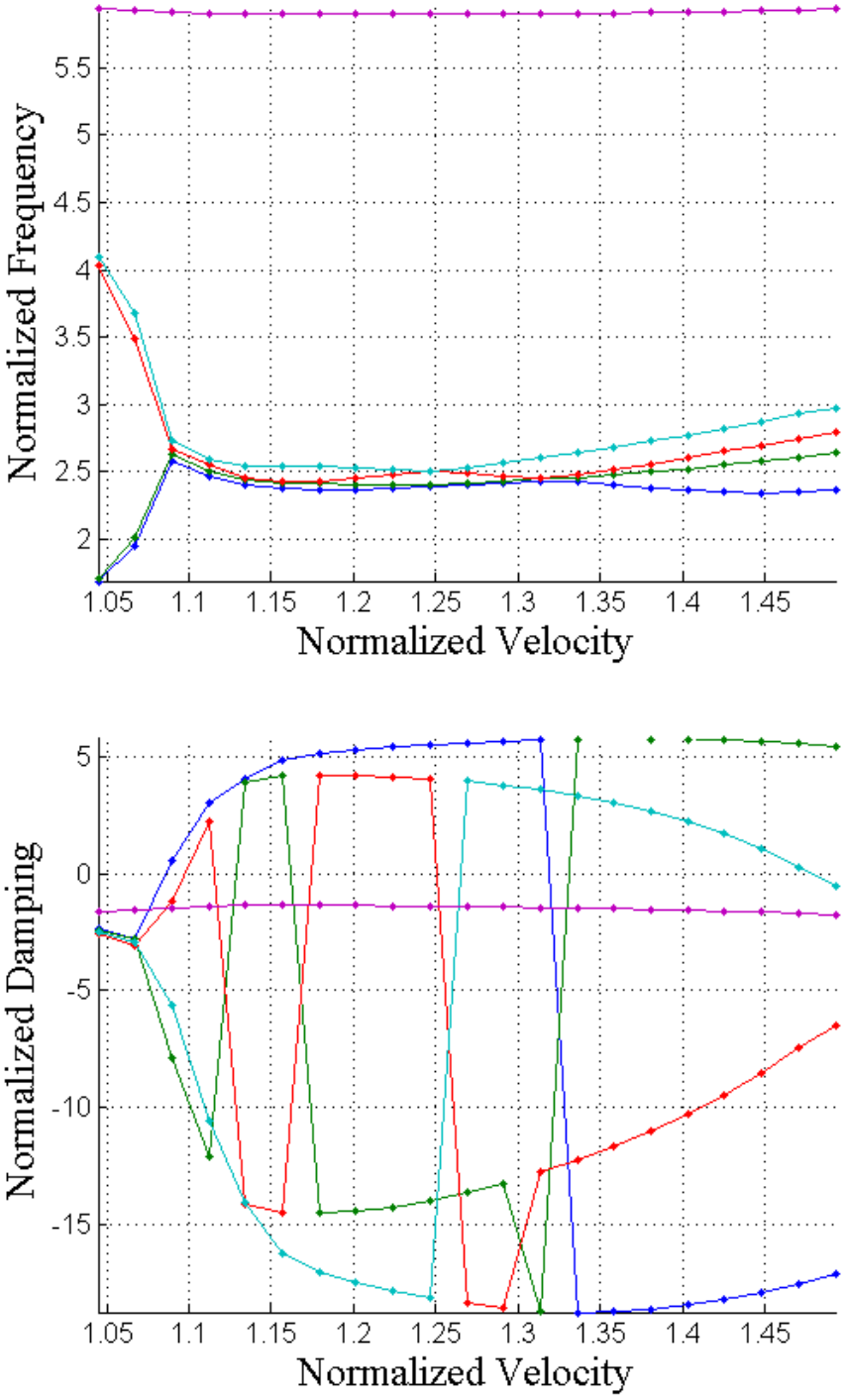

Figure 2.48. V-g diagram for trimmed, cantilevered 7FEW configuration

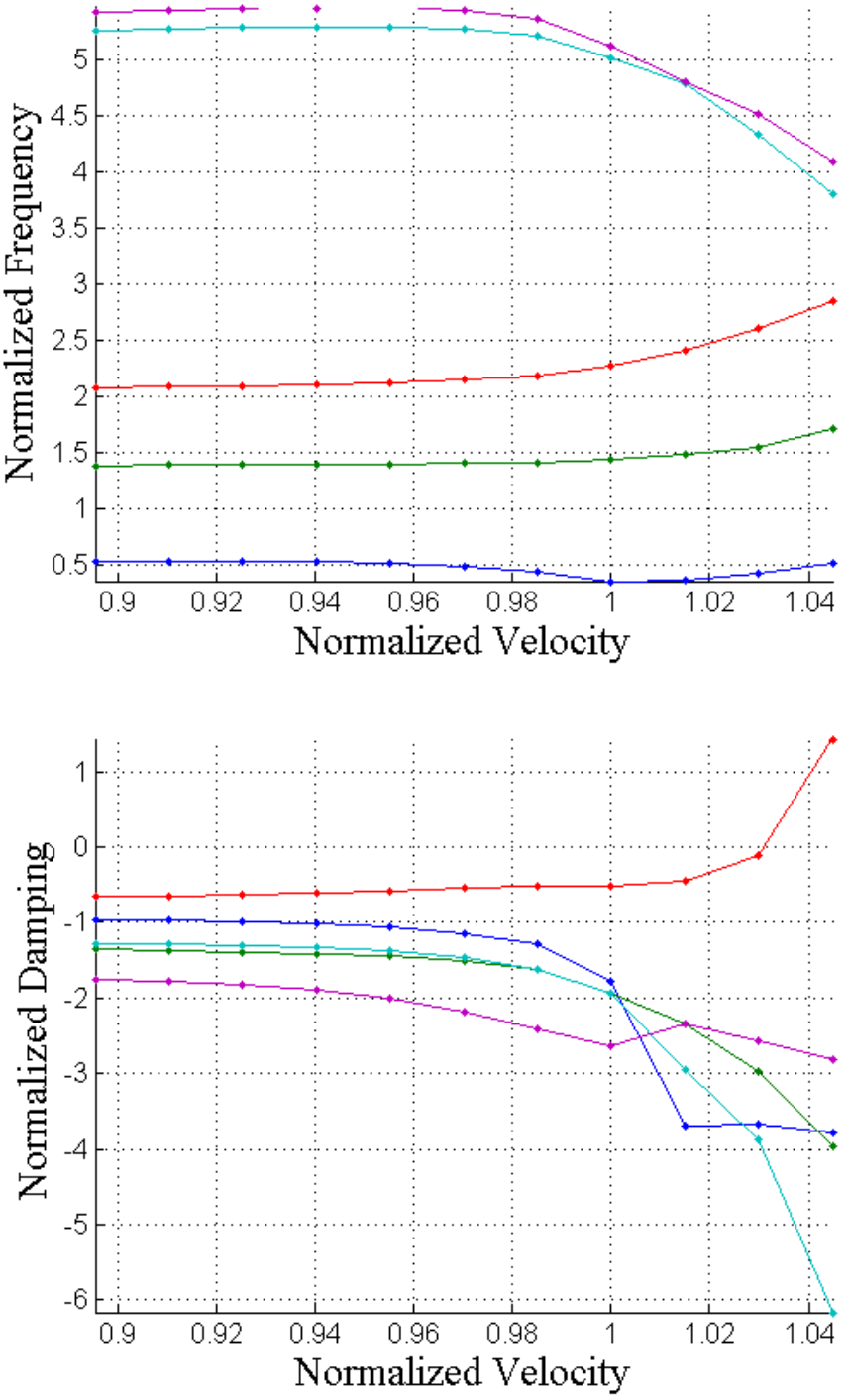

Figure 2.49. V-g diagram for trimmed, free-flight FFEW configuration

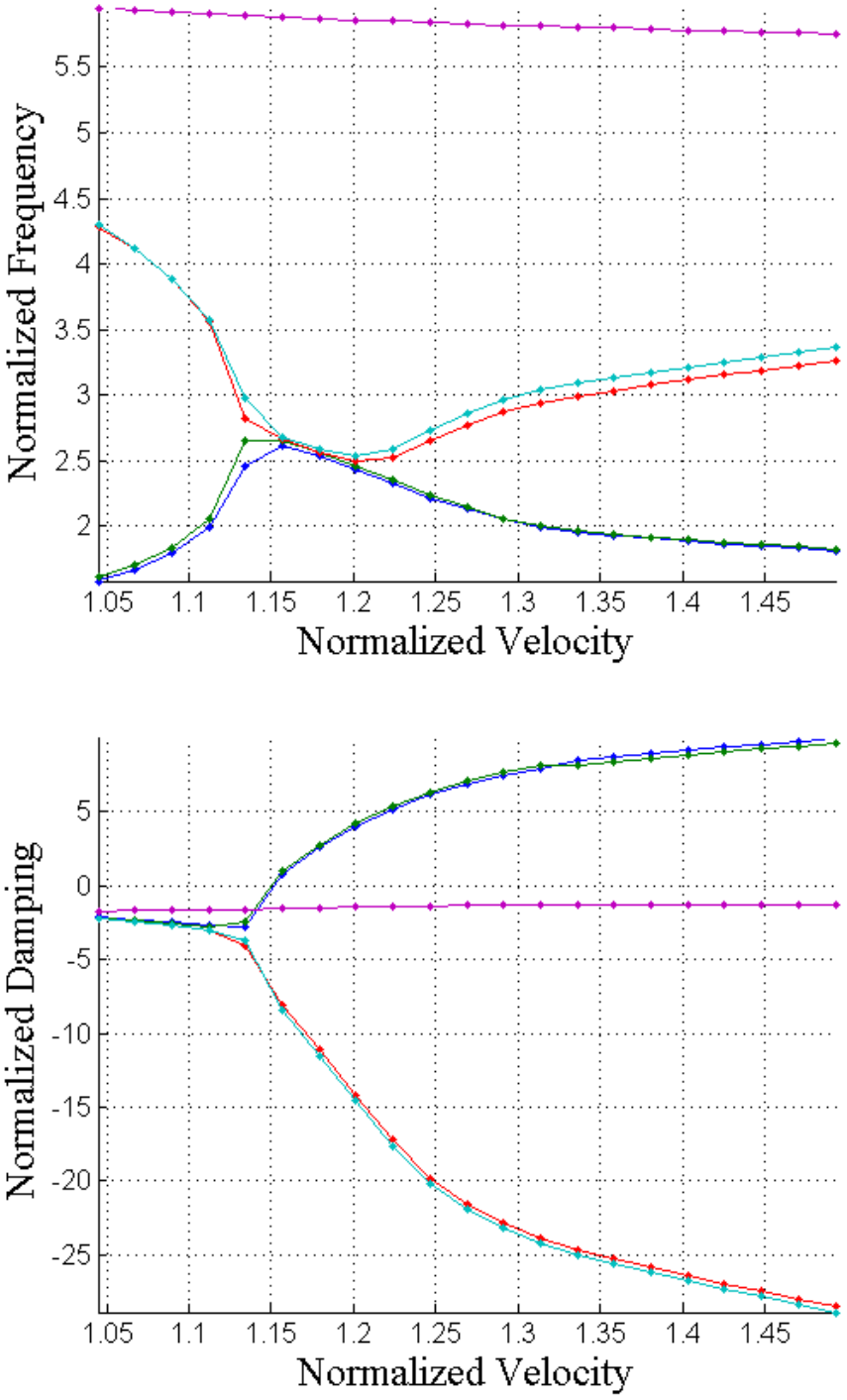

Figure 2.50. V-g diagram for trimmed, cantilevered FFEW configuration

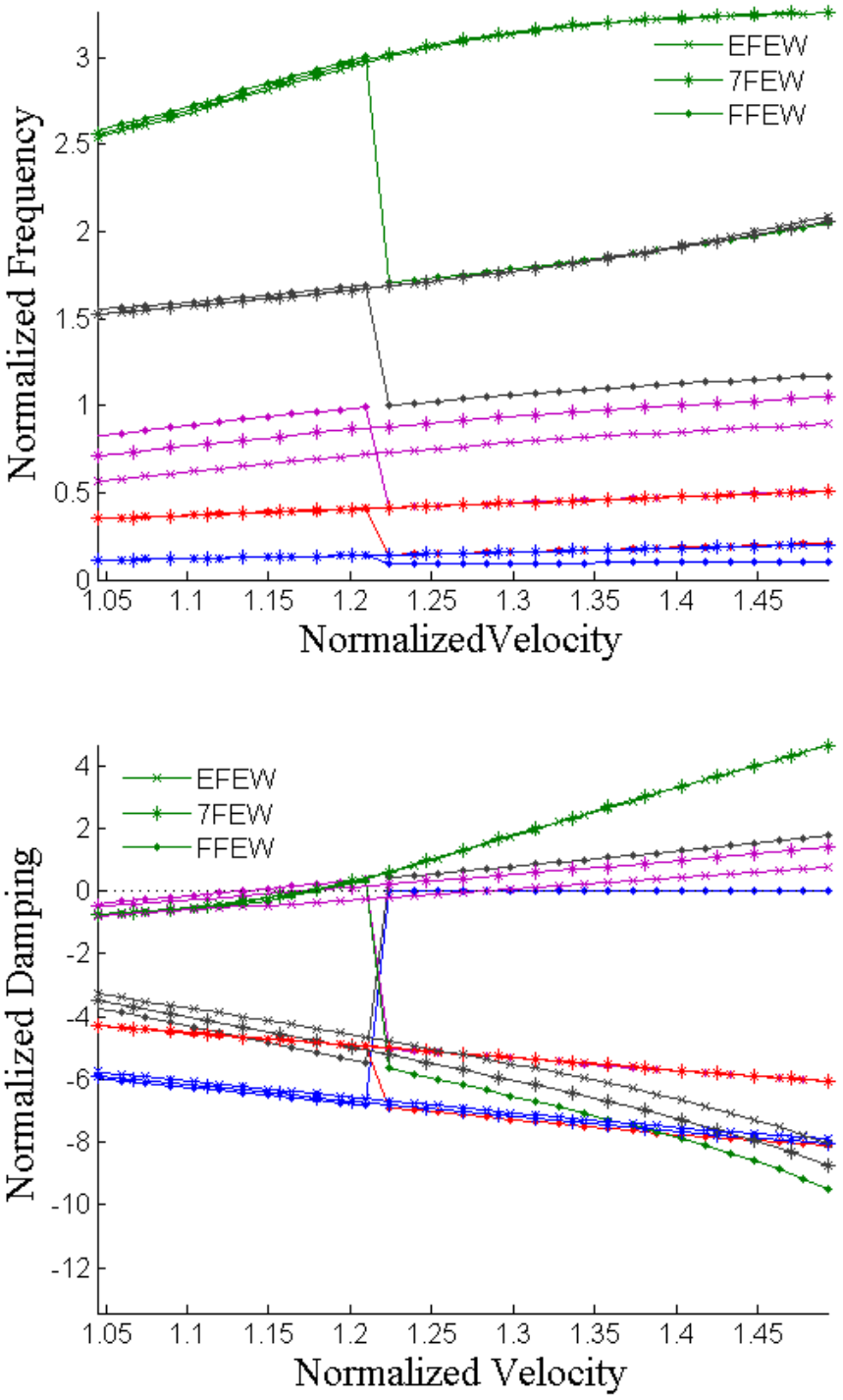

Figure 2.51. Comparison of flutter boundary for EFEW, 7FEW, FFEW using pseudo-trim

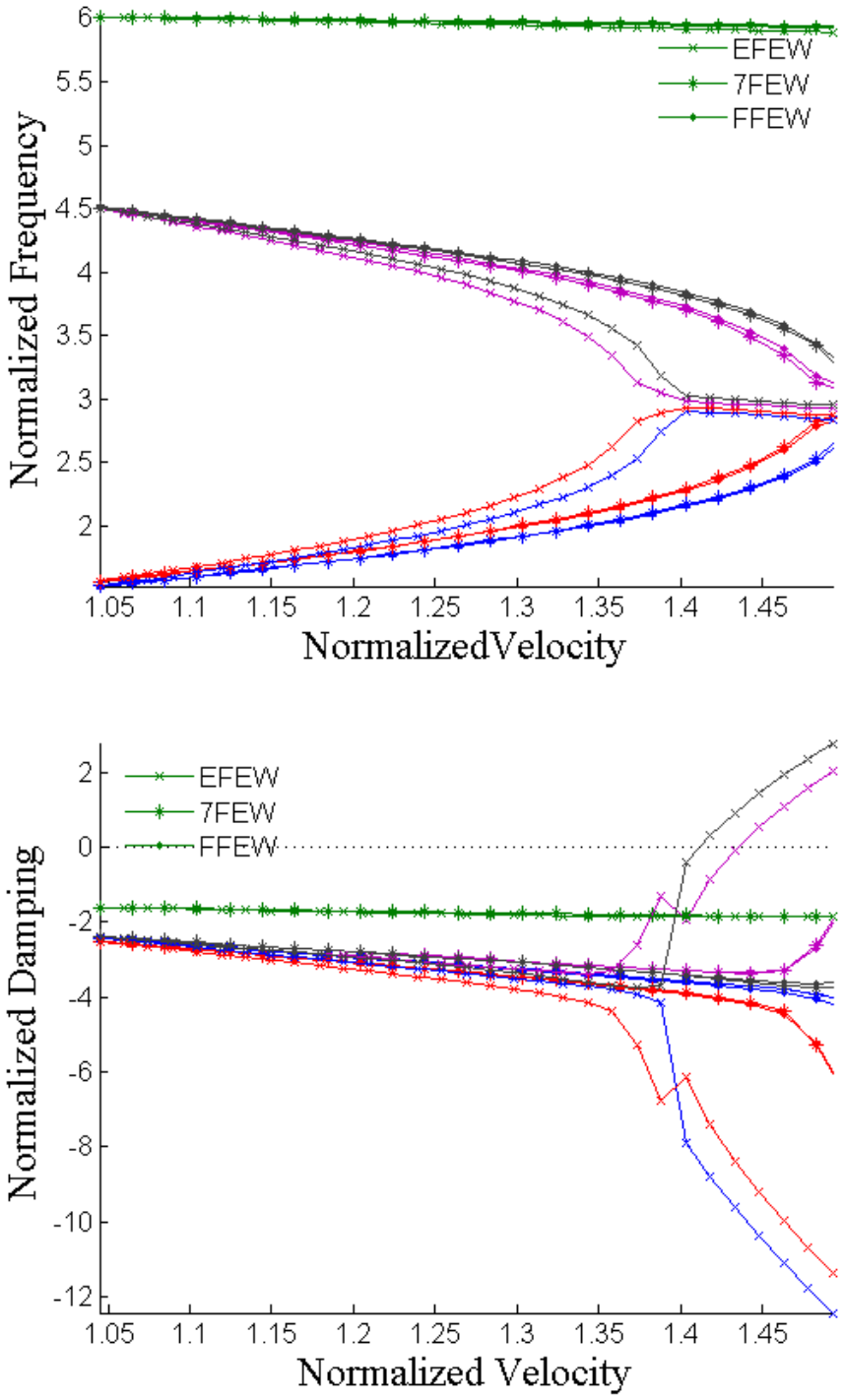

Figure 2.52. Comparison of flutter boundary for cantilevered EFEW, 7FEW, FFEW using pseudo-trim

2.7 Concluding Remarks

This chapter presented the results of a detailed procedure for converting a built-up aircraft model into a simplified aeroelastic model suitable for input into a reduced-order nonlinear aeroelastic solver. The X-56A Multi-Utility Aerolastic Demonstrator served as the test model for the procedure, while UM/NAST was used to perform the nonlinear simulations. Structural and inertia data for the X-56A was obtained through a GVT-validated FEM model. Aerodynamic data was provided in the form of CAD models of the aircraft's outer mold line and lift, drag, and moment coefficients from CFD that were validated by wind tunnel tests. The final beam model consisted of 30 reference nodes distributed evenly along the span. The cross-sectional stiffnesses and inertias calculated about each reference node were verified by comparing the UM/NAST static and modal solutions to the FEM results. The simplified model was able to replicate the deformations resulting from static loads, and the modal frequencies were also within 2% error of the FEM model for the first four structural modes. The aerodynamic loads were subject to more error due to the lack of information about the spanwise distribution, so a steady vortex lattice panel method was used to generate the lift distribution, and XFOIL was used to calculate the airfoil viscous drag and moment. The aerodynamic loads calculated with these two tools were adjusted with scalar correction factors to match the reference aerodynamic data for the full aircraft. The resulting nonlinear aeroelastic model was used to perform trim and flutter analysis on three payload configurations of the X-56A. The results indicate that the flutter speed increases as the vehicle weight increases which aligns with results presented by other investigators. Furthermore, as the weight increases, the flutter mode becomes very sensitive to small asymmetries in the aerodynamic load.

CHAPTER 3. Improvements to UM/NAST Numerical Framework

Nodal constraints were implemented in UM/NAST using the formulation presented by Su.[26] This initial constraint implementation of UM/NAST allowed only a single absolute constraint and a single relative constraint to be defined in the modelled structure. Furthermore, the only allowable types of boundary conditions were clamped or pinned absolute constraints, and clamped relative constraints. An expansion to the existing implementation was required to allow the number and type of nodal constraints to be arbitrarily defined for a structure. This expanded implementation improves UM/NAST's capability to model a wider range of structural boundary conditions, including those needed to replicate a spring-suspended ground vibration test. The first half of this chapter reiterates the constraint formulation and describes the expansions to the implementation that were undertaken for this work.

The second half of this chapter introduces the UM/NAST capability to model the aerodynamic wake of propeller-driven engines. This work is intended to improve the fidelity of UM/NAST's engine-structure interaction to support flight test correlations as well as comparisons to other nonlinear aeroelastic codes. This new propeller wake module is used to demonstrate the effects of propeller downwash on the disturbance response of a flexible aircraft model. The concluding section presents some key findings from these studies and suggestions for additional future work to expand this capability.

3.1 Expanding the UM/NAST Constraint Formulation

In order to implement constraints in the UM/NAST kinematic framework, Lagrangian multipliers were introduced into the energy functional that defines the motion of the beam elements. The virtual work of the beam is defined in terms of the element strain strain ε, as:

$$\Pi^* = \frac{1}{2}\int_L k(s)\varepsilon^2 ds - R\varepsilon \tag{3.1}$$

where the other terms are the cross-sectional stiffness *k*, cross-sectional position along the span *s*, and generalized load *R*.

The position and orientation of each node in the structure is described by a 12x1 vector *h* with the components:

$$\bar{h} = \begin{bmatrix} p_x & p_y & p_z & \bar{\omega}_x & \bar{\omega}_x & \bar{\omega}_z \end{bmatrix}^T \tag{3.2}$$

The elements p_x, p_y, and p_z describe the x, y, and z position of the node within the body frame. The elements ω_i are not scalars, but 3x1 orthogonal unit vectors that describe the orientation of the local nodal frame to the aircraft body frame. This nodal position vector is derived from the element-wise strain, and the details of the derivation are given in the work of Brown.[22]

3.1.1 Absolute Displacement Constraint Formulation

Using the Lagrangian multiplier λ_{ca}, the displacement vector *h* is constrained to a particular value. For an absolute constraint the position and orientation vector *h* at a given point *l* along the span is defined to be equal to the initial position h^0, implying zero displacemement or rotation, i.e.,

$$\Pi^* = \frac{1}{2}\int_L k(s)\varepsilon^2 ds - R\varepsilon + \lambda_{ca}\left[h(l) - h^0(l)\right] \tag{3.3}$$

The static equilibrium equation for an elastic structure with absolute constraints is given by:

$$\begin{bmatrix} K_{FF} & \left(K_{ca}\right)_i^T \\ \left(K_{ca}\right)_i & 0 \end{bmatrix}\begin{bmatrix} \varepsilon_{i+1} \\ \left(\lambda_{ca}\right)_{i+1} \end{bmatrix} = \begin{bmatrix} R_i \\ \left(R_{ca}\right)_i \end{bmatrix} \tag{3.4}$$

where K_{FF} is the generalized stiffness matrix derived from the energy functional in Equation 3.1, and the constraint generalized stiffness and load are defined as:

$$\begin{aligned} \left(K_{ca}\right)_i &= \left[J_{h\varepsilon}\left(l\right)\right]_i \\ \left(R_{ca}\right)_i &= \left(K_{ca}\right)_i \varepsilon_i - \left[h_i\left(l\right) - h^0\left(l\right)\right] \end{aligned} \tag{3.5}$$

The matrix K_{ca} is singular when first constructed due to the linear dependence of the rotation elements in the *h*-vector. Recall that the *h*-vector contains three orthogonal unit vectors to describe the local frame orientation. Each unit vector is defined as:

$$\begin{aligned}\left\|\bar{\omega}_x\right\| &= \omega_{xx}^2 + \omega_{xy}^2 + \omega_{xz}^2 = 1 \\ \left\|\bar{\omega}_y\right\| &= \omega_{yx}^2 + \omega_{yy}^2 + \omega_{yz}^2 = 1 \\ \left\|\bar{\omega}_z\right\| &= \omega_{zx}^2 + \omega_{zy}^2 + \omega_{zz}^2 = 1\end{aligned} \tag{3.6}$$

Furthermore, the orthogonality relationship between the vectors is defined as

$$\begin{aligned}\omega_x \times \omega_y &= 0 \\ \omega_y \times \omega_z &= 0 \\ \omega_z \times \omega_x &= 0\end{aligned} \tag{3.7}$$

Since the nine rotation components are related by these six equations, only three of the components are needed to be able to fully define the orientation frame. The rows of K_{ca} associated with the superfluous components are linearly dependent.

The first constraint case is the full absolute constraint – also known as the cantilevered/clamped condition. To implement this constraint, the rows of K_{ca} corresponding to the position and independent rotations of the constrained node are identified.

A predefinition approach[26] is used to determined using the set of linearly independent rotation elements. The rows of K_{ca} corresponding to elements of $\bar{\omega}_x$ are extracted, as shown in Equations (3.8) and (3.9).

$$K_{ca} = J_{h\varepsilon}(l) = \left[\frac{\partial \bar{h}}{\partial \varepsilon}(l)\right] = \begin{bmatrix} \frac{\partial \bar{p}}{\partial \varepsilon_1} & \frac{\partial \bar{p}}{\partial \varepsilon_n} \\ \frac{\partial \bar{\omega}_x}{\partial \varepsilon_1} & \frac{\partial \bar{\omega}_x}{\partial \varepsilon_n} \\ \frac{\partial \bar{\omega}_y}{\partial \varepsilon_1} & \frac{\partial \bar{\omega}_y}{\partial \varepsilon_n} \\ \frac{\partial \bar{\omega}_z}{\partial \varepsilon_1} & \frac{\partial \bar{\omega}_z}{\partial \varepsilon_n} \end{bmatrix}_{12x12} \tag{3.8}$$

$$\sum_{i=1}^{n} \frac{\partial \omega_x}{\partial \varepsilon_i}_{3x1} = \sum_{i=1}^{n} \begin{bmatrix} \frac{\partial \omega_{xx}}{\partial \varepsilon_i} \\ \frac{\partial \omega_{xy}}{\partial \varepsilon_i} \\ \frac{\partial \omega_{xz}}{\partial \varepsilon_i} \end{bmatrix} = \begin{bmatrix} \eta_x \\ \eta_y \\ \eta_z \end{bmatrix} \tag{3.9}$$

The nonzero row sum η_j indicates which of the three rotation elements are needed to form a linearly independent set. If $\eta_j = 0$, the independent set is given by $\omega_{xj}, \omega_{yj+1}, \omega_{yj+2}$, where the subscript *j* corresponds to the direction indices *x*, *y*, and *z*. The reduced constraint stiffness matrix is shown in Equation (3.10).

$$K_{ca} = \begin{bmatrix} \frac{\partial \overline{p}}{\partial \varepsilon_1} & \frac{\partial \overline{p}}{\partial \varepsilon_n} \\ \frac{\partial \omega_{x(j)}}{\partial \varepsilon_1} & \frac{\partial \omega_{x(j)}}{\partial \varepsilon_n} \\ \frac{\partial \omega_{y(j+1)}}{\partial \varepsilon_1} & \frac{\partial \omega_{y(j+1)}}{\partial \varepsilon_n} \\ \frac{\partial \omega_{z(j+2)}}{\partial \varepsilon_1} & \frac{\partial \omega_{z(j+2)}}{\partial \varepsilon_n} \end{bmatrix}_{6x6} \quad (3.10)$$

Figure 3.1 and Figure 3.2 demonstrate the use of multiple clamped absolute constraints in a simple 1-m beam. The body frame origin is clamped at the root of the beam, and the position and rotation of the constrained nodes, indicated in red, are clamped relative to the origin. A vertical 150-N point force, designated as "F" in the figures, is applied to the beam in the locations at the nodes indicated in green.

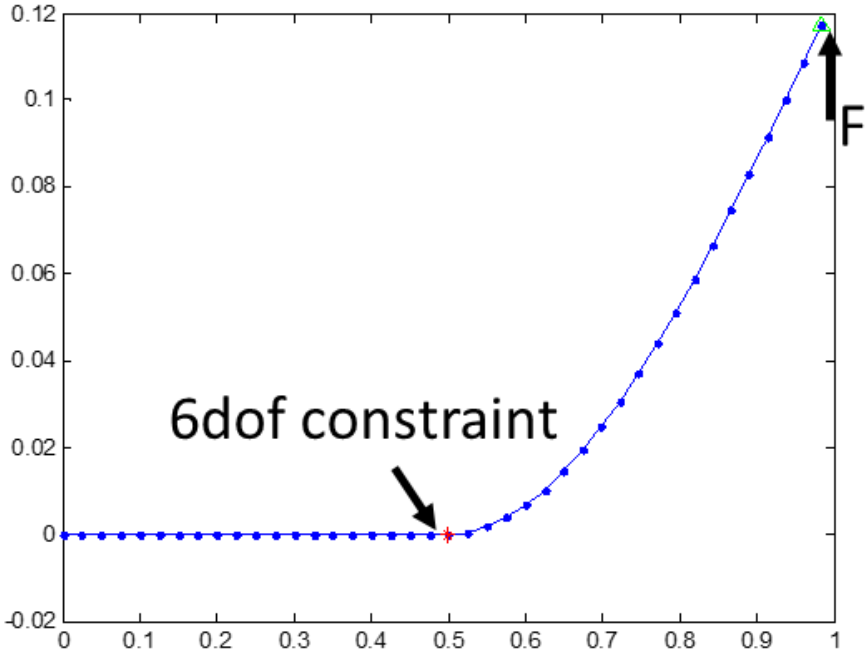

Figure 3.1. Beam with two clamped constraints: root and midpoint

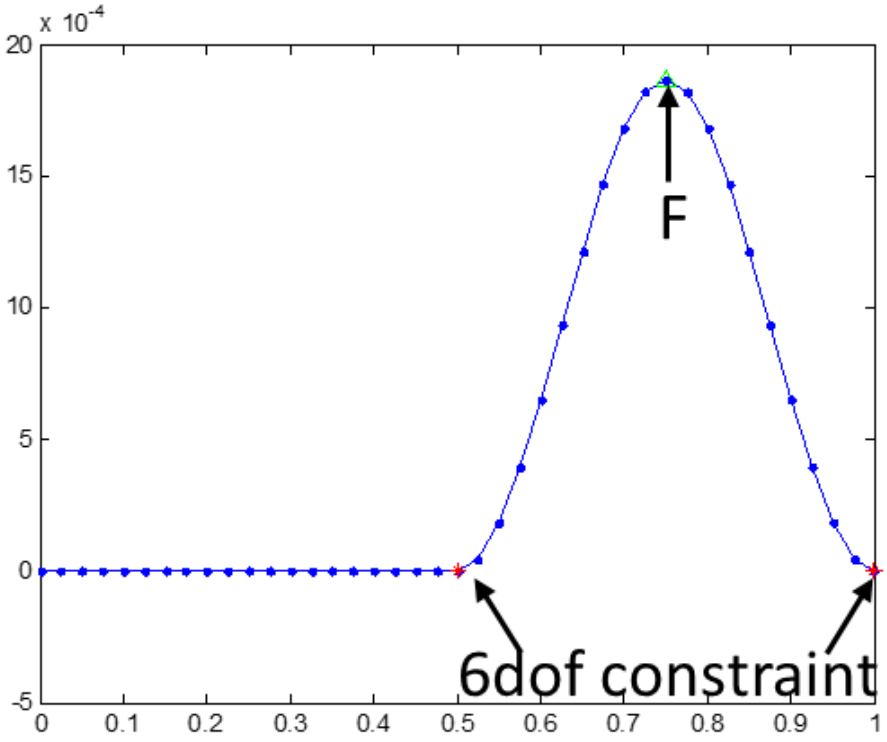

Figure 3.2. Beam with three clamped constraints: root, midpoint, tip

The second constraint case is a pin-type constraint, where only the three position elements p_B are constrained, but the nodal rotation is unconstrained. The reduced constraint stiffness matrix for this case is given by:

$$K_{ca} = \left[\frac{\partial \overline{p}}{\partial \varepsilon_1} \quad \cdots \quad \frac{\partial \overline{p}}{\partial \varepsilon_n} \right]_{3x3} \tag{3.11}$$

Figure 3.3 and Figure 3.4 demonstrate mixed constraint cases with the same 1-m beam. In Figure 3.3, the beam is clamped at the root and pinned at the midpoint. In Figure 3.4, the beam is clamped at the root and the tip, and pinned at the midpoint. In both cases, the constrained nodes are indicated in red, and a vertical 150-N force is applied at the nodes indicated in green. In addition to the simple beam cases shown here, the mixed clamped-pin constraint condition may be used to model the boundary conditions imposed on a flexible wing passing through a rigid fuselage.

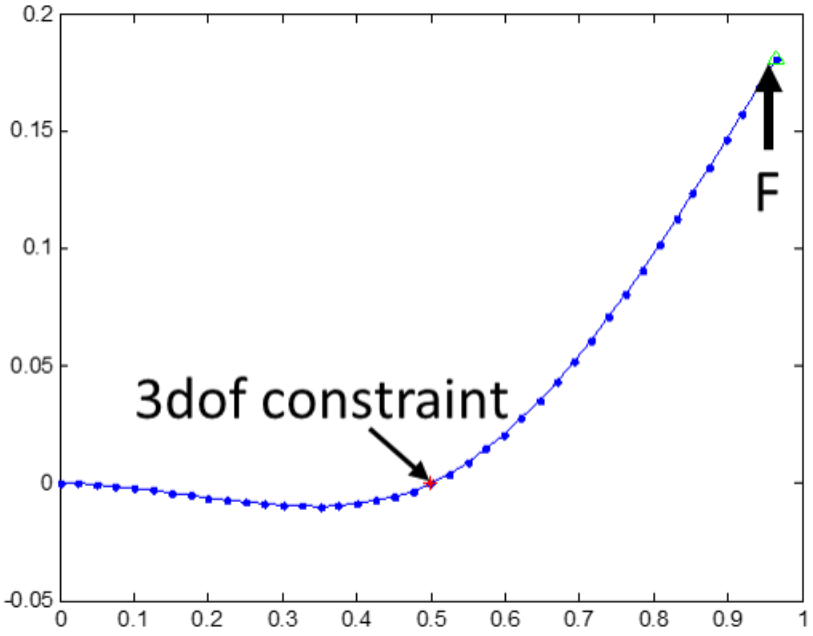

Figure 3.3. Beam with two constraints: clamped root and pinned midpoint

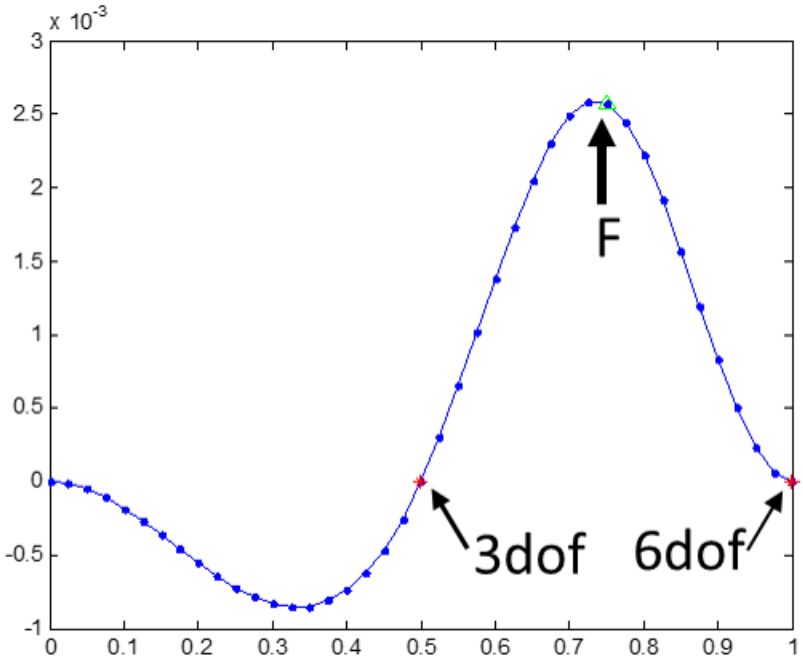

Figure 3.4. Beam with mixed absolute constraints: clamped root/tip and pinned midpoint

3.1.2 Relative Displacement Constraint Formulation

The absolute constraints defined the nodal position and orientation relative to the body frame origin. In a relative displacement constraint, the position and orientation of two collocated, but nonsequential nodes h_{mu} and h_{nv} are defined to be identical. This allows the two nonsequential nodes to act as a single point. The displacement at each node is given in its local orientation frame *w*, so both *h*-vectors must be rotated into the same local frame using directional cosines D^{bw} before assessing the constraint. This process is described by Equations3.12 and 3.13. The definition of the energy functional with the relative constraint is given by Equation 3.14.

$$\left(h_r^b\right)_{mu} = \left(h_r^b\right)_{nv} \tag{3.12}$$

$$D_{mu}^{bw}\left(h_r\right)_{mu} - D_{nv}^{bw}\left(h_r\right)_{nv} = 0 \tag{3.13}$$

$$\Pi^* = \frac{1}{2}\int_L k(s)\varepsilon^2 ds - R\varepsilon + \lambda_{cr}\left[D_{mu}^{bw}h_{mu} - D_{nv}^{bw}h_{nv}\right] \tag{3.14}$$

The static equilibrium equation for an elastic structure with relative constraints is given as:

$$\begin{bmatrix} K_{FF} & \left(K_{cr}\right)_i^T \\ \left(K_{cr}\right)_i & 0 \end{bmatrix}\begin{bmatrix} \varepsilon_{i+1} \\ \left(\lambda_{cr}\right)_{i+1} \end{bmatrix} = \begin{bmatrix} R_i \\ \left(R_{cr}\right)_i \end{bmatrix} \tag{3.15}$$

where K_{FF}, *R* are the same terms used in the equilibrium equations with absolute constraints, and the constraint stiffness and generalized load matrices are defined as:

$$\begin{aligned} \left(K_{cr}\right)_i &= D_{mu}^{bw}\left(J_{h\varepsilon}\left(mu\right)\right)_i - D_{nv}^{bw}\left(J_{h\varepsilon}\left(nv\right)\right)_i \\ \left(R_{cr}\right)_i &= \left(K_{cr}\right)_i \varepsilon_i - \left[D_{mu}^{bw}\left(h_{mu}\right) - D_{nv}^{bw}\left(h_{nv}\right)_i\right] \end{aligned} \tag{3.16}$$

For the full derivation of these equations, refer to the work by Shearer.[24] As with the absolute constraint, the position and orientation vector *h* at a particular node has a maximum of six independent elements— three positions and three of the nine rotation elements.

A demonstration of the clamped relative constraint is shown in Figure 3.5. Two separate beams are clamped at their respective roots, and their endpoints are co-located when the beam has zero deformation, shown in black. A clamped relative constraint is imposed at these co-located tip nodes so that the six independent degrees of freedom—three position and three orientation elements—are identical. A 150-N force is applied at the tip and the resulting displacement of the joined structure is shown in blue. This constraint type replicates the conditions seen in a joined wing, as demonstrated in the work of Su.[26]

The second constraint case is a pin-type relative constraint, where the position p_B is constrained, but the co-located nodes are free to rotate. This constraint is meant to describe a linkage between two separate structures, such as a braced or suspended structure. Figure 3.6 shows how a relative constraint may be used to create a braced beam model. Shown is a 2-m span beam with a a separate bracing beam attached at its midpoint. Both the main beam and the brace are clamped at their roots, and the relative constraint is used to pin the tip of the brace to the midpoint of the main beam. A 150-N force is applied at the tip of the main beam, and the resulting displacement of the braced structure is shown in Figure 3.6. With the relative constraint, the brace adds additional stiffness to the main beam, but does not constrain the curvature.

In the case of the joined wing and braced wing, the beams being pinned together have identical properties. To model a suspended beam, the main beam of the braced model is used, and the brace is made vertical and its properties are redefined. In the case shown in Figure 3.7, the new support is defined as a rod-like member, with high rigidity in the bending and torsional degrees of freedom and a low extensional stiffness. When a 150-N force is applied at the tip of the main beam, the beam is allowed to deform freely, and the support extends to match the vertical displacement. With this pinned relative constraint, UM/NAST's modal analysis can be performed on a spring-supported structure, replicating the conditions of a suspended ground vibration test.

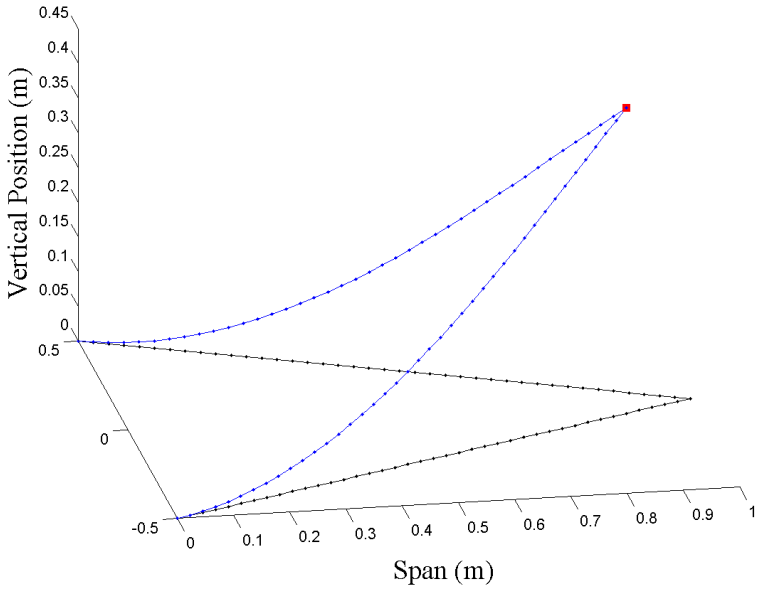

Figure 3.5. Beams with clamped relative constraint

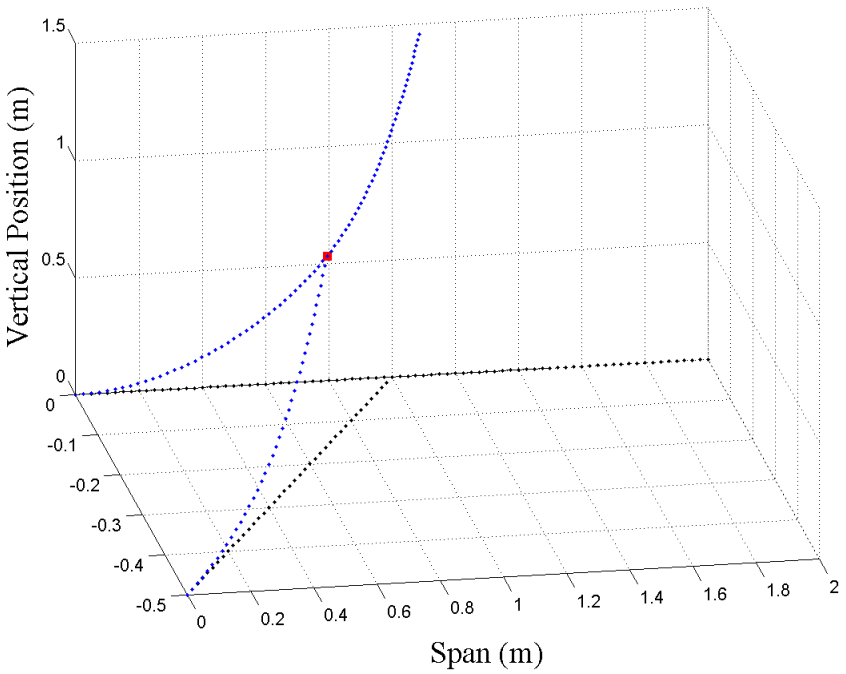

Figure 3.6. Braced beam with pinned relative constraint

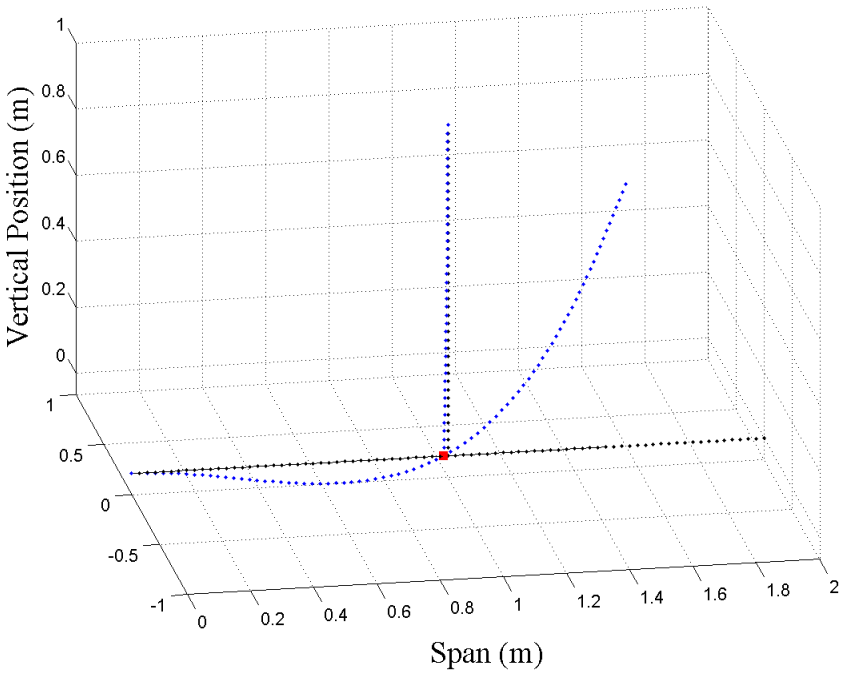

Figure 3.7. Suspended beam with pinned relative constraint

3.2 Improvements to UM/NAST Aerodynamic Formulation

State of the art HALE aircraft and many novel high-efficiency, flexible aircraft designs use propeller-driven engines for propulsion. The current design trend for these aircraft, characterized by their high aspect ratio wings and low structural weight, is the usage of multiple engines distributed throughout the span to maximize control authority as well as provide thrust and lifting capability. The experimental aircraft LEAPTech uses distributed propellers to maximize L/D and maximize efficiency over the wing in a technique known as "blowing."[56] Multi-engine designs also allow designers to tailor the mass and structural placement of the propulsion units for optimum modal performance.

In the current version of UM/NAST, the thrust of the engines are modeled as body-following point forces at specified locations along the wing. The modelled engine has no impact or dependency on the aircraft aerodynamics. This section details the process of incorporating propeller downwash and wake effects into the UM/NAST aerodynamic model. It is expected that the additional aerodynamic loads from the propellers will cause a significant change to the aircraft behavior.

3.2.1 Theoretical Background

UM/NAST[26] utilizes 2-D finite state inflow theory to model the unsteady aerodynamics of an aircraft's lifting surfaces. This theory assumes incompressible flow, and, as a 2D method, there is no aerodynamic interaction between cross-sections.

The aerodynamic coefficients are defined at each structural node, allowing variation of the aerodynamic load along the span of lifting surfaces. The equations for the aerodynamic loads on each nodal cross-section, defined about the aerodynamic center, is given by

$$\begin{aligned} l_{ac} &= \pi\rho b^2\left(\ddot{z}+\dot{y}\dot{\alpha}-d\ddot{\alpha}\right)+c_{l\alpha}\rho b\dot{y}^2\left[-\frac{\dot{z}}{\dot{y}}+\left(\frac{1}{2}b-d\right)\frac{\dot{\alpha}}{\dot{y}}-\frac{\lambda_0}{\dot{y}}\right]+\rho b\dot{y}^2 c_{l\delta}\delta \\ m_{ac} &= \pi\rho b^3\left[\frac{1}{2}\ddot{z}^2-\dot{y}\dot{\alpha}-\left(\frac{1}{8}b-\frac{1}{2}d\right)\ddot{\alpha}\right]+2\rho b^2\dot{y}^2\left(c_{m0}+c_{m\delta}\delta\right) \\ d_{ac} &= -\rho b\dot{y}^2 c_{d0} \end{aligned} \tag{3.17}$$

where $c_{l\alpha}$ is the lift curve slope with respect to angle of attack, $c_{l\delta}$ and $c_{m\delta}$ are the lift- and moment-curve slopes due to control surface deflection. In this formulation, the aerodynamic center is assumed to be the quarter-chord of the local airfoil. The effective angle of attack for an airfoil at a given location on the wing is a function of the twist angle as well as structural motion,

given in terms of the rates and acceleration $\dot{y}$, $\dot{z}$, and $\ddot{z}$ of the node. Unsteady effects are introduced into the lift equation by the λ operator, which incorporates induced flow due to free vorticity in the form of inflow states. All of these loads are defined in the local aerodynamic frame.

To combine these loads with the gravitational and external loads acting on the vehicle, the aerodynamic loads at each node are shifted to the reference axis rotated into the body frame. The equations for the local aerodynamic forces and moments are given by Equations 3.18.

$$\begin{aligned} l_{ra} &= l_{ac} \\ m_{ra} &= l_{ac} + \left(\frac{1}{2}b + d\right) l_{ac} \\ d_{ra} &= d_{ac} \end{aligned} \tag{3.18}$$

The rotation of the local lift, drag, and moment into body frame forces and moments are given in Equation 3.19.

$$f^{aero} = C^{Ba_1} \begin{bmatrix} 0 \\ d_{ra} \\ l_{ra} \end{bmatrix}, \quad m^{aero} = C^{Ba_1} \begin{bmatrix} m_{ra} \\ 0 \\ 0 \end{bmatrix} \tag{3.19}$$

When modelling the effect of a propeller-driven engine on an aeroelastic system, there are several factors to account for. The rotation of the propeller and inertia of the engine itself will contribute to the vibration of the structure. This structural influence can be modeled simply by assigning concentrated masses to represent the engines. Additional fidelity may be added by incorporating the flexibility of the engine attachment into the model, allowing the thrust vector orientation to vary independently of the local wing angle of attack. In the formulation presented in this chapter, the elastic motion of the engine relative to the wing will be neglected. The engine's mass will be modeled as concentrated inertia, and the thrust will be modeled as a constant body-follower force, so that the thrust vector orientation will vary as the structure deforms.

Of greater interest in this study is the aerodynamic effects on the bodies downstream of the propeller. The downwash of the propeller will change the effective magnitude and direction of the velocity on the lifting surfaces in its wake. The 2-D finite state formulation does not allow for interference effects between lifting surfaces, so, although it is important, this effect will be

neglected in the current study. In this formulation, we also make the assumption that the propellers are not near the end of the wing, so additional treatment of tip effects is not considered here. This formulation is based heavily on the propeller wake formulation developed for ASWING.[9]

A diagram illustrating the sequence of calculations for the UM/NAST propeller module is shown in Figure 3.8. The module requires only basic information about the engine to incorporate downwash and wake effects into this implementation, making it ideal for use during all phases of the aircraft design and flight testing. The module takes the user-defined propeller radius, rpm, engine maximum thrust and torque and calculates the initial velocity increment due to the flow of air through the propeller. From this initial value, the geometry of the propeller wake is determined. For each structural node within the wake, the module outputs the final axial and transverse velocity increment due to the propwash, which is added to the local free stream velocity and incorporated into the calculation of nodal lift, drag, and aerodynamic moment.

3.2.2 Propeller Downwash Formulation

Disk Actuator (Momentum) Theory is used to calculate the initial velocity increment to the flow behind the propeller disk. This theory is an application of Bernoulli's principle to the flow through the motor, and as such, adheres to the incompressible flow assumption used by the overarching aerodynamic formulation of UM/NAST.

The flow far upstream of the propeller is assumed to be at rest, while the flow through the disk is assumed to be equal to the freestream velocity U_∞. Due to conservation of momentum, flow passing through propeller disk is accelerated, producing thrust. The initial velocity increment just behind the propeller disk is given as:

$$\Delta V_{eng} = \sqrt{V_\infty^2 + \frac{2T_{eng}}{\rho A_{eng}}} - V_\infty \tag{3.20}$$

This initial velocity increment ΔV_{eng} is used to calculate the inner and outer shear layer boundaries of the wake, given in Equation 3.21 and Equation 3.22 respectively. The wake boundaries are used to identify portions of the the lifting surface that lie within the propeller

wake. Mixing Layer theory gives the shear boundaries as a function of a propeller constant K_ε, the free stream velocity V_∞, and the propeller induced velocity increment.

$$\varepsilon_c = K_\varepsilon \frac{\left|\Delta V_{eng}\right|}{V_\infty + 1.0\Delta V_{eng}} \quad (3.21)$$

$$\varepsilon_b = K_\varepsilon \frac{\left|\Delta V_{eng}\right|}{V_\infty + 0.5\Delta V_{eng}} \quad (3.22)$$

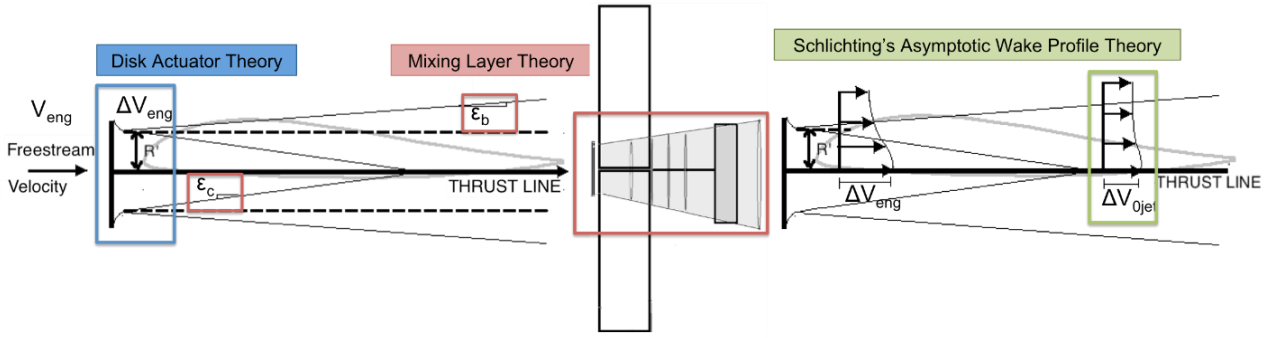

Figure 3.8. Diagram of the UM/NAST propeller formulation for a single component

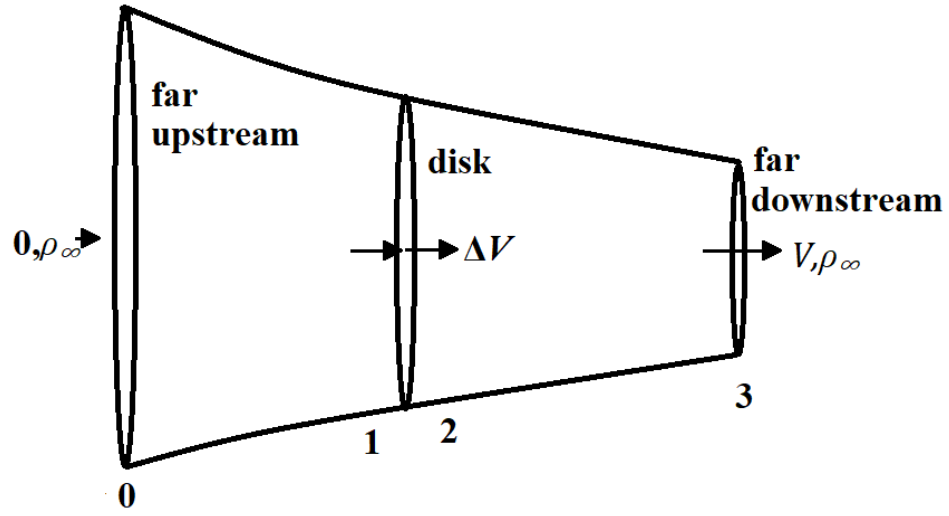

Figure 3.9. Propeller streamtube in momentum theory

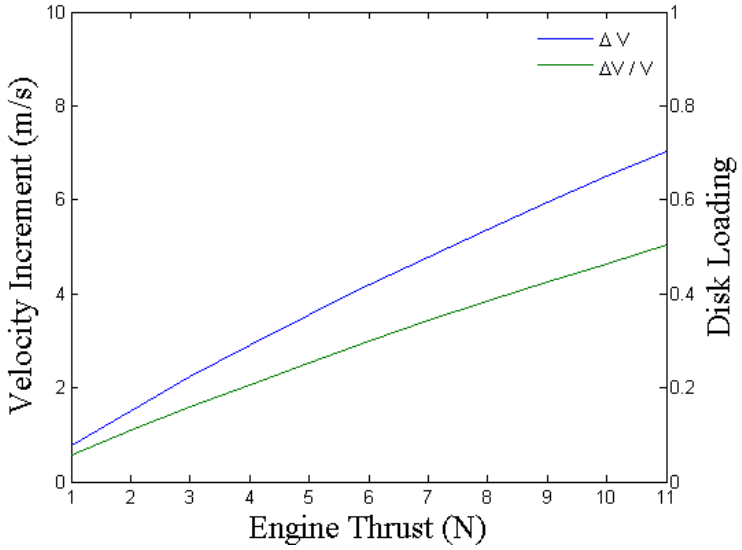

Figure 3.10. Thrust vs velocity increment for a 12-in diameter propeller

Schlicting's Mixing Layer Theory[57] gives the geometry of the wake as a function of the radius of the flow just behind the propeller disk R'_{eng} and the shear layer boundaries. A conical wake is assumed, such that the radius of the wake at any point y behind the propeller disk may defined linearly. The radius b_{jet} of the outer shear layer expands as the distance behind the propeller increases, while the inner shear layer radius c_{jet} shrinks, merging into the thrust line at a distance y_{mix} behind the propeller disk.

$$b_{jet} = R'_{eng} + y\sin(\varepsilon_b)$$
$$c_{jet} = \begin{cases} R'_{eng} - y\sin(\varepsilon_c), & y < y_{mix} \\ 0, & y \geq y_{mix} \end{cases} \tag{3.23}$$

$$y_{mix} = \frac{R'_{eng}}{\varepsilon_c} \tag{3.24}$$

The velocity inside the wake is not assumed constant at each axial cross-section. Rather, Schlicting's Asymptotic Wake Profile Theory considers the velocity increment to vary depending on radial distance from the thrust line. The axial velocity increment is given as:

$$\Delta V_{0\,jet} = \sqrt{\frac{1}{4}\frac{k_1^2}{k_2^2}V_{eng}^2 + \frac{F_{eng}}{\rho\pi k_2}} - \frac{1}{2}\frac{k_1}{k_2}V_{eng} \tag{3.25}$$

The velocity increment ΔV_{jet} for nodes within the inner mixing layer (near the thrust line), and within the outer mixing layer are given by:

$$\Delta V_{jet} = \begin{cases} 0 & , \quad r_{jet} > b_{jet} \\ \Delta V_{eng}\left\{1-[(r_{jet}-c_{jet})/(b_{jet}-c_{jet})]^{3/2}\right\}^2 & , \quad b_{jet} > r_{jet} > c_{jet} \\ \Delta V_{eng} & , \quad c_{jet} > r_{jet} \end{cases} \tag{3.26}$$

Nodes that are located beyond the outer shear layer boundary $r_{jet} > b_{jet}$ are outside of the wake, so there is no increase to velocity. There is also a tangential, swirl velocity component ΔW_{jet} due to the propeller torque.

This swirl velocity increment is defined as:

$$\Delta W_{eng} = \frac{-M_{eng}}{\pi\rho\left[k_3 V_\infty + k_4 \Delta V_{eng}\right]} \tag{3.27}$$

$$\Delta W_{jet} = \begin{cases} 0 & , \quad r_{jet} > b_{jet} \\ \Delta W_{eng}\left\{1-[(r_{jet}-c_{jet})/(b_{jet}-c_{jet})]^{3/2}\right\}^2 & , \quad b_{jet} > r_{jet} > c_{jet} \\ \Delta W_{eng} & , \quad c_{jet} > r_{jet} \end{cases} \tag{3.28}$$

The *k* constants used in the axial and swirl velocity increments $\Delta V_{0\,jet}$, ΔW_{eng} are defined in terms of the mixing layer boundaries:

$$\begin{aligned} k_1 &= c_{jet}^2 + \frac{9}{10}c_{jet}(b_{jet}-c_{jet}) + \frac{9}{35}(b_{jet}-c_{jet})^2 \\ k_2 &= c_{jet}^2 + \frac{243}{385}c_{jet}(b_{jet}-c_{jet}) + \frac{243}{1820}(b_{jet}-c_{jet})^2 \\ k_3 &= \frac{2}{3}c_{jet}^3 + \frac{9}{10}c_{jet}^2(b_{jet}-c_{jet}) + \frac{9}{35}c_{jet}(b_{jet}-c_{jet})^2 + \frac{1}{9}(b_{jet}-c_{jet})^3 \\ k_4 &= \frac{2}{3}c_{jet}^3 + \frac{243}{385}c_{jet}^2(b_{jet}-c_{jet}) + \frac{243}{1820}c_{jet}(b_{jet}-c_{jet})^2 + \frac{2}{45}(b_{jet}-c_{jet})^3 \end{aligned} \tag{3.29}$$

3.2.3 Static Aeroelastic Simulations

Simulations of the aerodynamic load and static aeroelastic deformation were performed with a 4-meter span, high aspect ratio flying wing aircraft model. This model has three propeller-driven engines distributed at 1-meter increments along the span of the wing. Behind each motor is a horizontal tail. The horizontal tail is attached to the wing structure with a tailboom modelled as a rigid non-lifting beam. The wing is modeled as a reflexed EMX-07 airfoil, while the tails are symmetric NACA0012 airfoils. The three engines are identical, and the engine parameters are

given in Table 3.1. Two static aeroelastic cases were considered. In Case 0, shown in Figure 3.12, the aircraft angle of attack and control surface deflections are set to zero. In Case 1, shown in Figure 3.13, the aircraft is trimmed for steady level flight using angle of attack, deflection of horizontal tails, and three motors distributed across the span.

The results for Case 0, shown in Figure 3.12, show that the velocity increment from the propellers results in a considerable increase in lift for the portions of the main wing and tail that are directly behind the propeller. The increase in drag and moment resulting from the axial and swirl velocity increment, respectively, are much lower than the lift increase and the effect is concentrated primarily at the nodes closest to the motor. Incorporating the axial and swirl velocity increment due to propeller downwash results in significant changes to the spanwise lift distribution, which in turn affects the spanwise deformation and twist distribution. The next section will demonstrate the impact on aircraft response and stability.

Table 3.1. Propeller module simulation inputs

Free stream velocity:	14 m/s
Propeller Radius:	6 inches (0.1524m)
Engine RPM	7000 rpm (733 rad/s)
Engine Thrust (maximum)	11.77 N
Engine Torque:	0.3274 N-m
Engine Offset from Leading Edge	0.2315 m

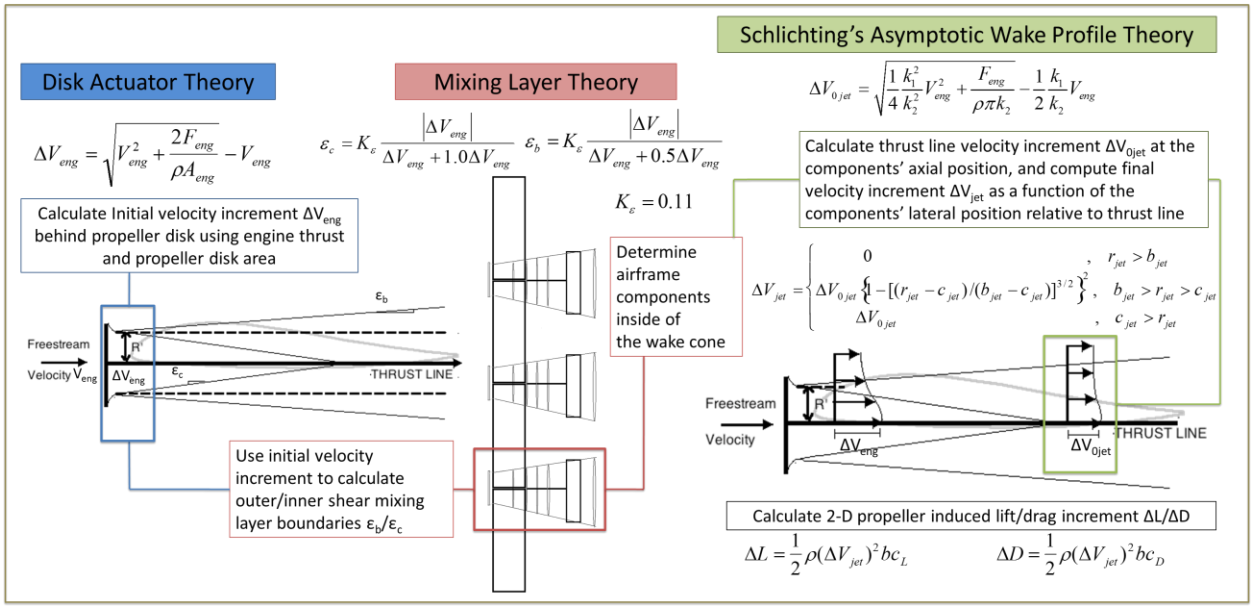

Figure 3.11. Diagram of the UM/NAST propeller formulation for full vehicle

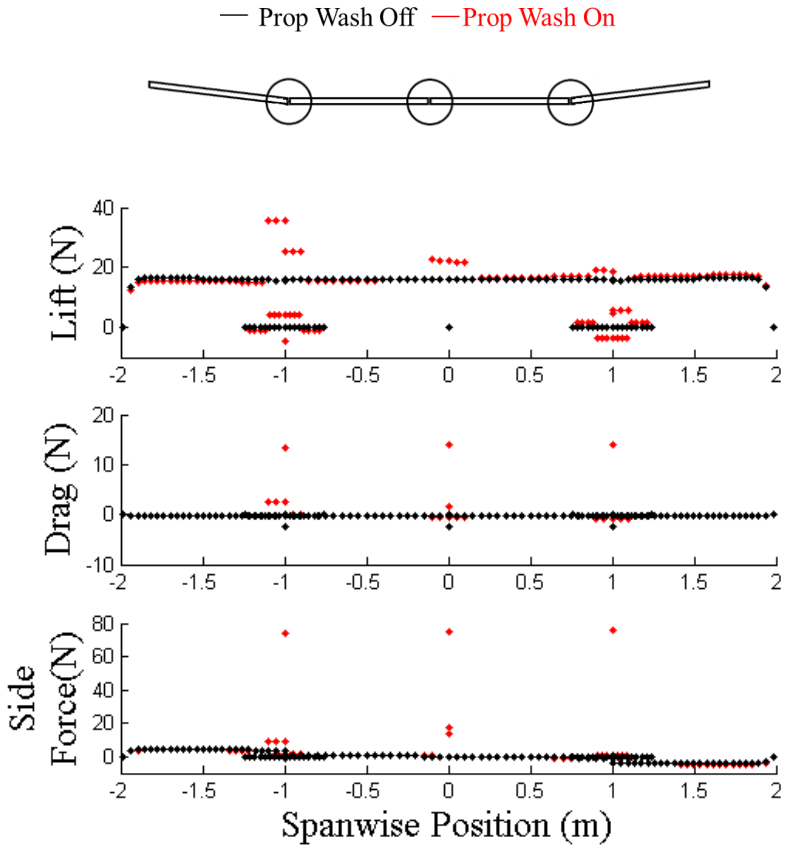

Case 0: Static aerodynamic load

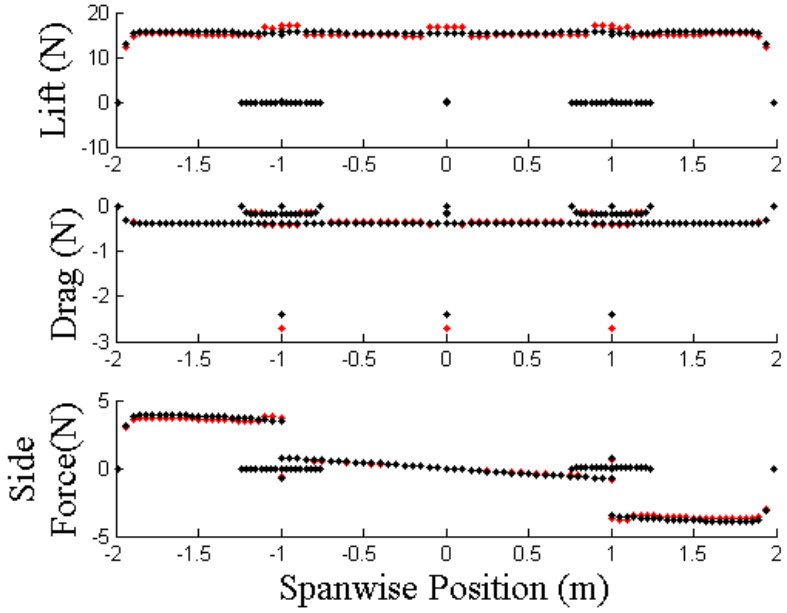

Case 1: Trimmed aerodynamic load

Figure 3.12. Aerodynamic load on a 4-meter aircraft model with and without propeller downwash

Table 3.2. Comparison of aeroelastic trim parameters

Trim Parameter	Without Prop Wash	With Prop Wash
Angle of Attack	-0.34 deg	-0.58 deg
Elevator Deflection	0.15 deg	0.38 deg
Wingtip Deflection	0.261 m	0.241 m

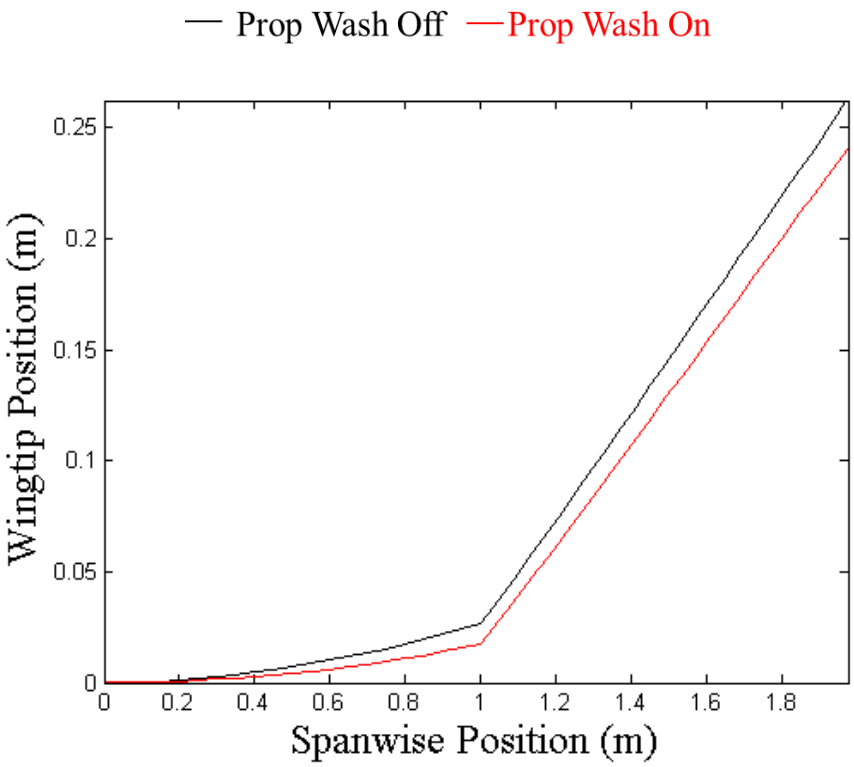

Static Deformation during trim

Figure 3.13. Trimmed wingtip position of the 4-meter aircraft model with and without propeller downwash

3.2.4 Dynamic Aeroelastic Simulation

A time-marching simulation with the 4-meter aircraft model is performed. A ten-degree aileron doublet of 0.25 Hz is applied to the trimmed aircraft in trim. After a single period, the ailerons are returned to their trimmed positions and the response is allowed to develop for fifteen seconds. The elastic response of the aircraft is shown in Figure 3.14 and Figure 3.15, and the rigid body response is shown in Figure 3.16 and Figure 3.17 .The model with propeller downwash implemented is shown in red.

It is clear that the propeller downwash causes significant changes to the aircraft response. Without downwash, the aircraft is stable, returning to equilibrium within five seconds of the end of the aileron excitation. The wingtips experience an oscillation that grows in amplitude, however, the period lengthens, indicating that this is not limit cycle oscillation, but a structural motion that will dampen out over time. When propeller downwash is implemented, the roll response increases dramatically, and rather than settling back to equilibrium, the amplitude and frequency of the roll oscillations remains constant. Since the aircraft was not initially unstable, this suggests that the aileron input, combined with the propeller downwash, has excited a marginally stable lateral mode. The wing deformation grows as well, indicating that the excited roll mode is coupled with wing bending as well.

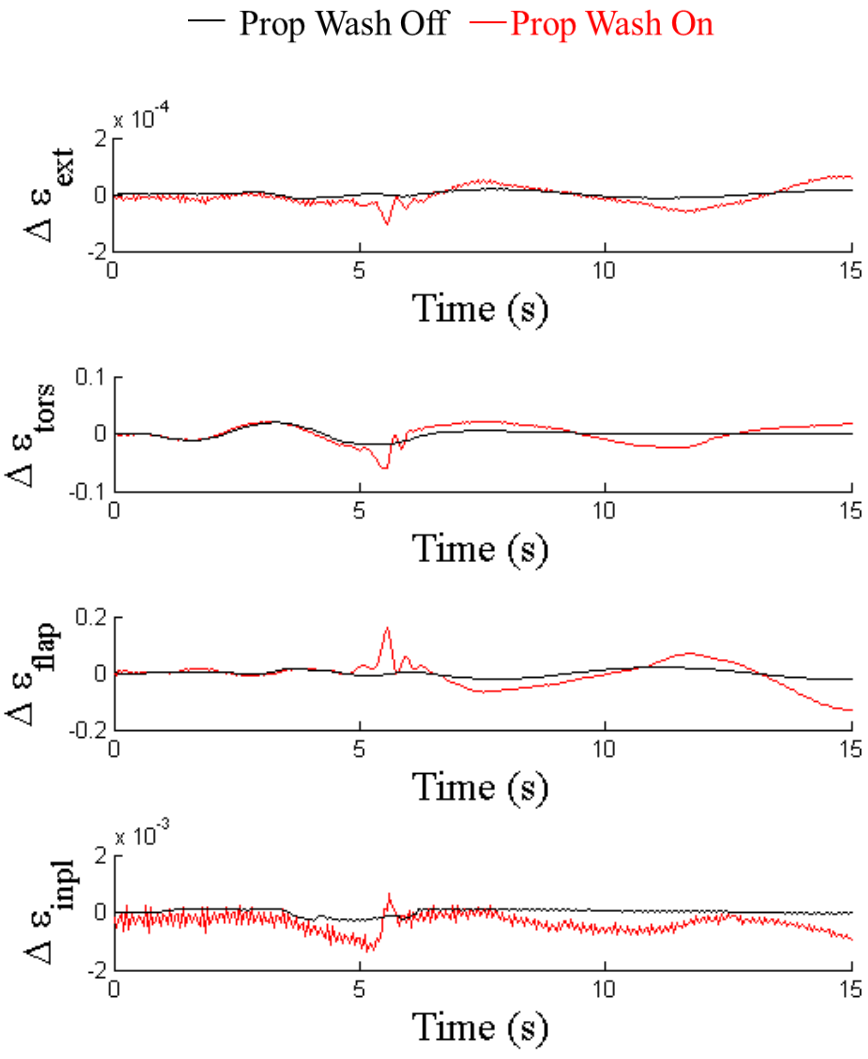

Figure 3.14. Wing root strain of 4-meter aircraft model after aileron doublet

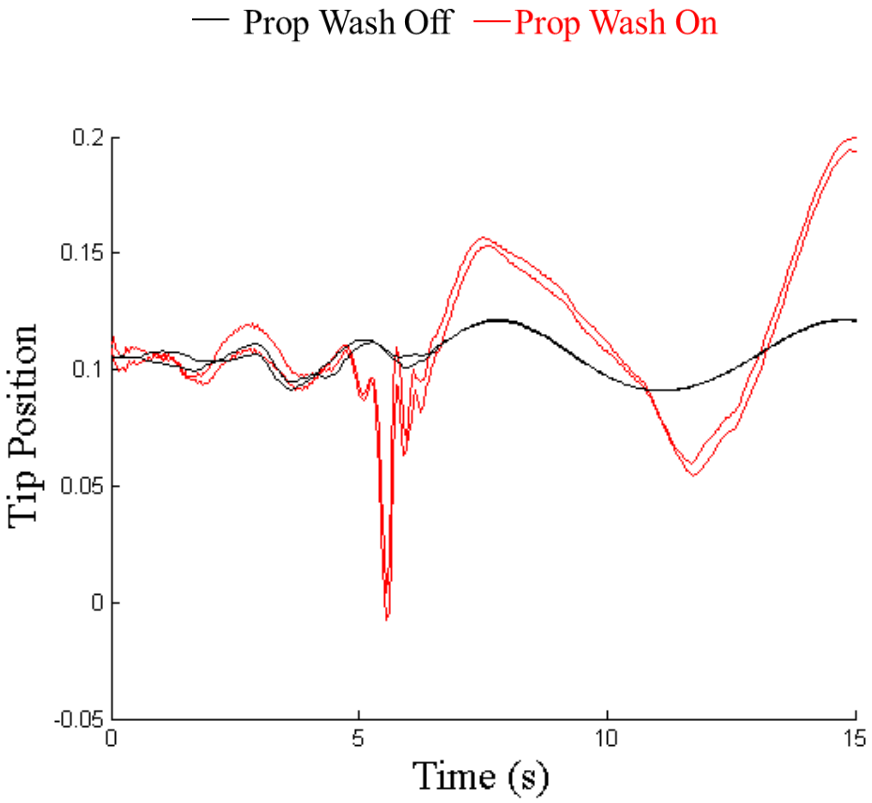

Figure 3.15. Wingtip Position of 4-meter aircraft model after aileron doublet

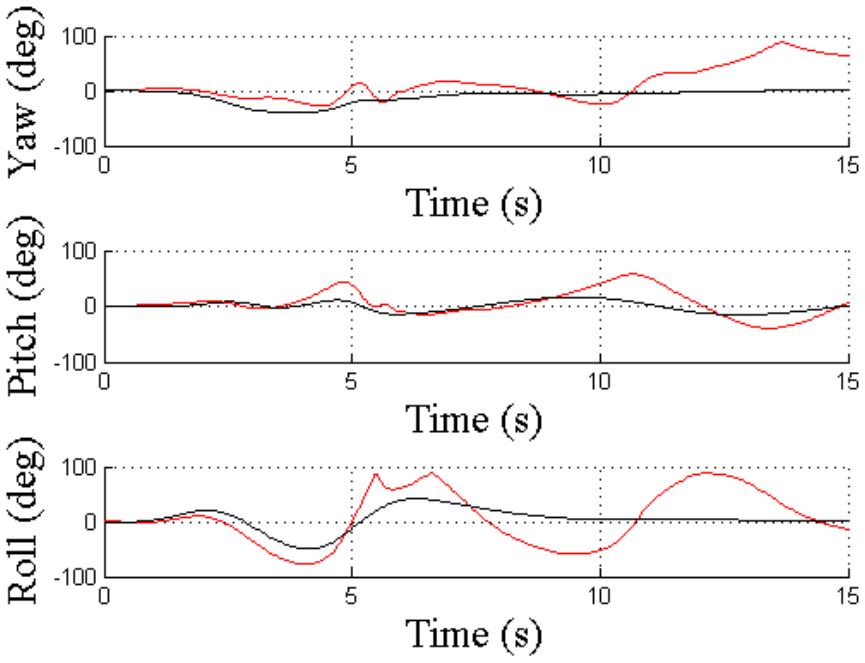

Figure 3.16. Body orientation of 4-meter aircraft model after aileron doublet

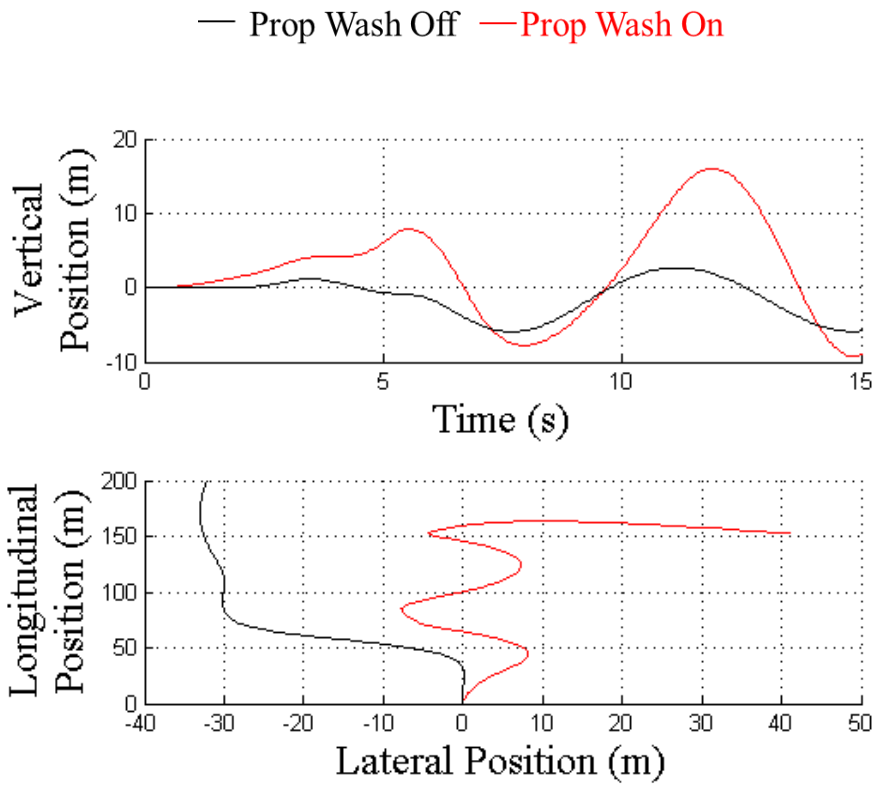

Figure 3.17. Body position of 4-meter aircraft model after aileron doublet

3.3 Conclusion and Future Work

Incorporating propeller downwash into the aeroelastic equations demonstrates that these wake effets are an important contributor to the aircraft trim and stability, particularly for very flexible aircraft. The axial velocity increment on the lifting surfaces within the propeller's helical wake produces significant changes in the spanwise lift. This velocity increment appears small, however it results in an effective loss of lateral stability.

The model considered in this chapter is nearly linear, and previous aeroelastic analysis of this model concluded that it is stable even under a large and prolonged aileron excitation. However, this study suggests that serious roll instability may be encountered during flight due to the propeller wake interactions with the wing, motor pod, and tail, and it is expected that the aeroelastic data gathered during flight tests will confirm the presence of this marginal behavior.

The formulation presented in this chapter does not incorporate the thrust dependence on free-stream velocity or the intermember interference between surfaces within the propeller wake. Future studies will address and improve upon these aspects of the propeller module.

CHAPTER 4. Development and Characterization of the X-HALE Aeroelastic Testbed

This chapter details the development and characterization of the Experimental High-Altitude Long-Endurance aircraft, known as X-HALE. X-HALE is an unmanned testbed intended to provide high-quality in-flight aeroelastic data to support the validation of nonlinear aeroelastic formulations. The design criteria used for X-HALE is presented first, followed by a brief description of the aircraft components and the manufacturing process for each. Three X-HALE configurations were developed for this work, and the purpose and aeroelastic instrumentation of each configuration is presented. The measurement of the elastic, inertia, and aerodynamic properties of each aircraft configuration is detailed along with a discussion of measurement errors and assumptions made. These aircraft properties were used to create simplified aeroelastic models of each configuration for analysis with the University of Michigan Nonlinear Aeroelastic Simulation Toolbox (UM/NAST). The properties of each model are summarized and predictions of the trimmed static deformation, modal response, and flight dynamic behavior are presented. This work is a continuation of the work of Cesnik and co-workers,[30,58] and the results in this chapter reference the works of Jones[59] and Pang et al[60] as well as the unpublished work of several collaborators.

4.1 Overview of the X-HALE Unmanned Aeroelastic Testbed

An experimental high-altitude long endurance testbed aircraft (X-HALE)[30] was designed so to be:

1. aeroelastically respresentative of VFA aircraft, represented by coupling between the rigid body and flexible states;
2. linearly stable under trimmed flight with enough control authority to excite various nonlinear vehicle responses; and

3. capable of static wing deformations with tip deflection greater than 30% of the semispan.

The design also presents an unstable (but controllable) Dutch-roll coupled first wing bending mode when subjected to large disturbances. This lateral behavior would have been very difficult to test in a wind tunnel environment. The choice of construction, materials, and geometry were such that they allow accurate characterization of the stiffness and inertia properties of the aircraft.[30]

Figure 4.1. The X-HALE unmanned aeroelastic testbed on the ground (l) and at takeoff (r).

4.2 X-HALE Airframe Design

The X-HALE unmanned aircraft is a flexible, high-aspect-ratio wing-boom-tail type aircraft. The main wing is constructed from identical 1-m wing segments with 0.2-m chord. The wing tip segments are mounted with a 10-degree dihedral to augment the lateral stability of the aircraft. Five engine pods are distributed at one meter intervals along the wingspan, containing electric motors, batteries, and the instrumentation payload, which is described further in later sections. Attached to each motor pod is a tapered carbon fiber boom with a 0.11-m-chord horizontal tail. A dimensioned drawing of the 6-meter X-HALE configuration is shown in Figure 4.2. A diagram of basic layout of the X-HALE vehicles and position terminology is given in Figure 4.3.

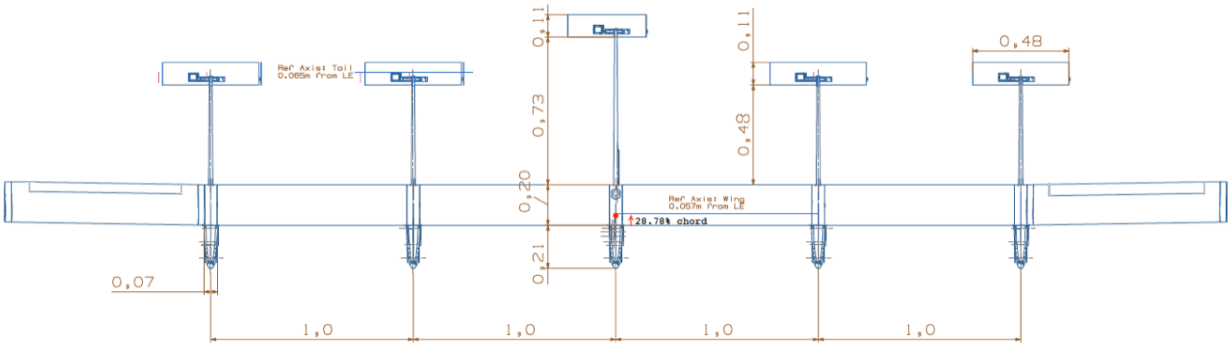

Figure 4.2. Dimensioned layout of the 6-meter X-HALE configurations

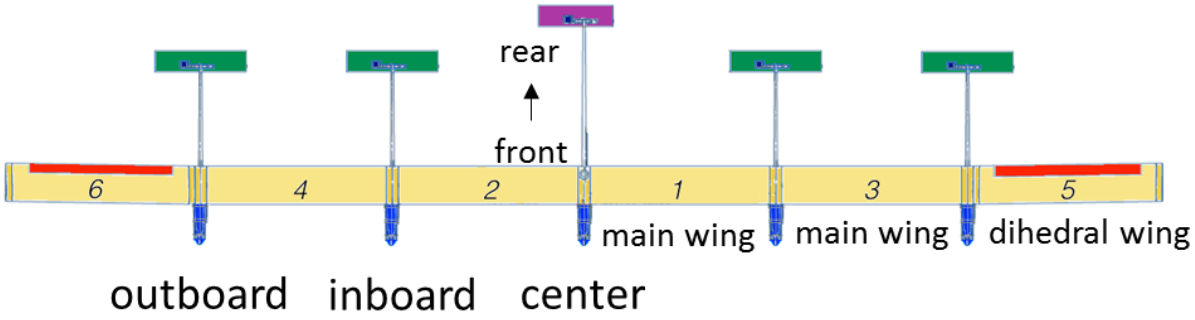

Figure 4.3. Diagram of X-HALE positions and terminology

4.2.1 Wings

The primary lifting surface of the X-HALE aircraft is the high-aspect-ratio wing. The wing is modular, composed of 1-meter long segments that can be removed or added in order to adjust the wingspan and aspect ratio. Each wing segment contains a semi-rectangular wing spar, fabricated by wrapping several plies of glass fiber reinforced-epoxy around a core of low-density, high-strength structural foam. This wing spar is the main structural component of aircraft. Aerodynamically shaped leading- and trailing-edge foam supports are added to spar to create the reflexed profile of an EMX-07 airfoil. The spar and aerodynamically shaped foam are wrapped with an additional layer of fiberglass-epoxy fabric, which provides additional torsional rigidity to the wing.

There are two types of wings used on the X-HALE: main wings and dihedral wings. The wing types, shown in Figure 4.5, have identical geometry and construction, but the dihedral wings undergo an additional manufacturing step. The dihedral wings are equipped with control surfaces and are meant to be installed only in the furthest outboard positions. In earlier X-HALE

configurations, an aileron was cut into the trailing edge of the dihedral wings, and a servo was embedded in the underside near the inboard edge for actuation. In the later configuration, the ailerons were fixed in place and roll spoilers were installed on the top of the wing. The servo position remained the same. A pair of dihedral wings with ailerons are shown in Figure 4.5, and a dihedral wing with a deployed roll spoiler is shown in Figure 4.6.

4.2.2 Tails

Similarly to the wings, the tails are constructed of aerodynamically shaped structural foam wrapped in glass-fiber composite. The tails do not have a spar; instead, each tail has a recessed cutout on its upper surface for the servo actuator assembly, and this assembly acts as the load-bearing element of the tails. There are two types of tails used on the X-HALE: the horizontal tail and the center tail, shown in Figure 4.7. The two tail types share identical construction, but the installation of the servo varies between the tail types. The horizontal tails are fully movable control surfaces, meaning that the entire airfoil rotates when a control surface deflection is commanded. They are attached to the four outboard motor pods to act as elevators. The servo assembly can be adjusted to expand or restrict the tail's range of motion, depending on the amount of pitch authority desired for a particular flight. The center tail is attached to the central motor pod, and it rotates between the horizontal and vertical orientation to provide additional aerodynamic damping during unstable lateral maneuvers.[61]

Each tail is connected to its respective motor pod using a hollow, tapered carbon fiber boom, seen in Figure 4.7. The wide end of the tail boom is pressure-fit onto a cruciform carbon fiber tail connector, and the tail connector is attached directly to the rear of the motor pod spine.

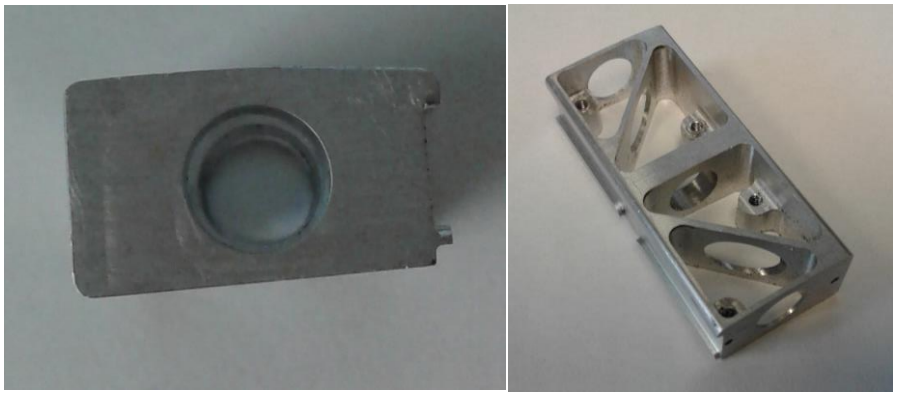

Figure 4.4. Machined aluminum wing joiner

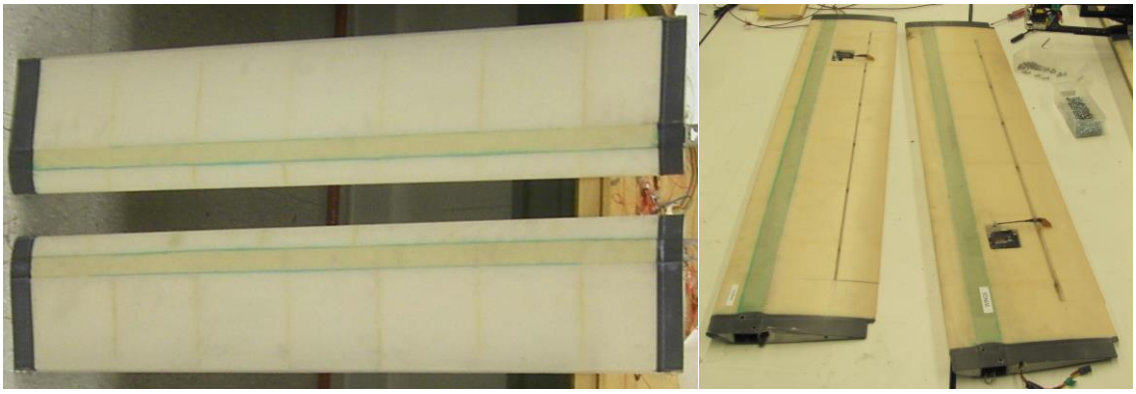

Figure 4.5. X-HALE main wings (l) and dihedral wings (r)

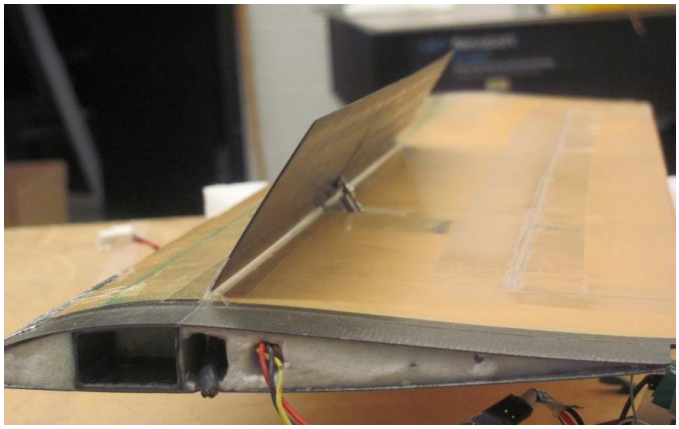

Figure 4.6. Dihedral wing segment with roll spoiler installed

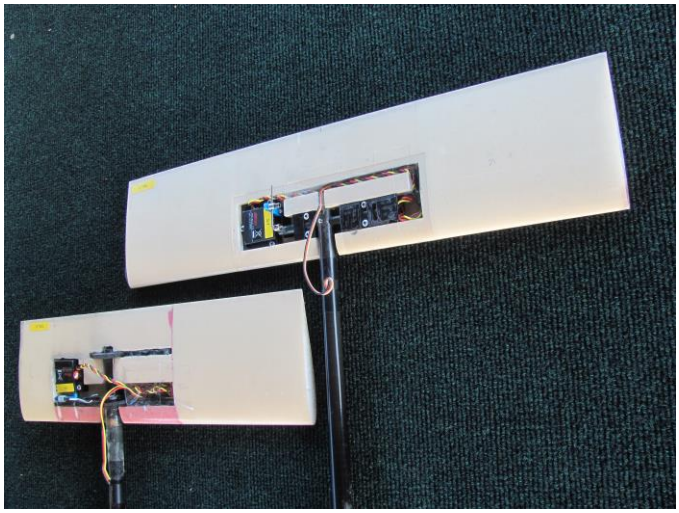

Figure 4.7. Assembled center tail (l) and horizontal tail (r)

4.2.3 Motor Pods

The motor pods consist of two elements. The main element is a graphite/epoxy spine cut from a 3-mm thick carbon fiber plate. The plate is constructed from 17-21 plies of unidirectional graphite-epoxy composite, arranged in a quasi-isotropic layup. The motor, landing gear, tail, and payload components are mounted to the spine using machined aluminum or plastic mounts. An example of an assembled spine with steel ballast plates is shown in Figure 4.8. The second element of the motor pod is the fairing, a molded fiberglass skin used to provide an aerodynamic surface for the motor pods as well as protect the payload that is mounted to the spine. The fairing, shown in Figure 4.9, has a profile similar to a NACA 0018 airfoil, however several modifications to the shape were made to accommodate the electronics contained within the pod. These modifications include a increased curvature on the right side to accommodate the bulk of the wiring, and an open vent on the left side for forced-air cooling of the onboard computers.

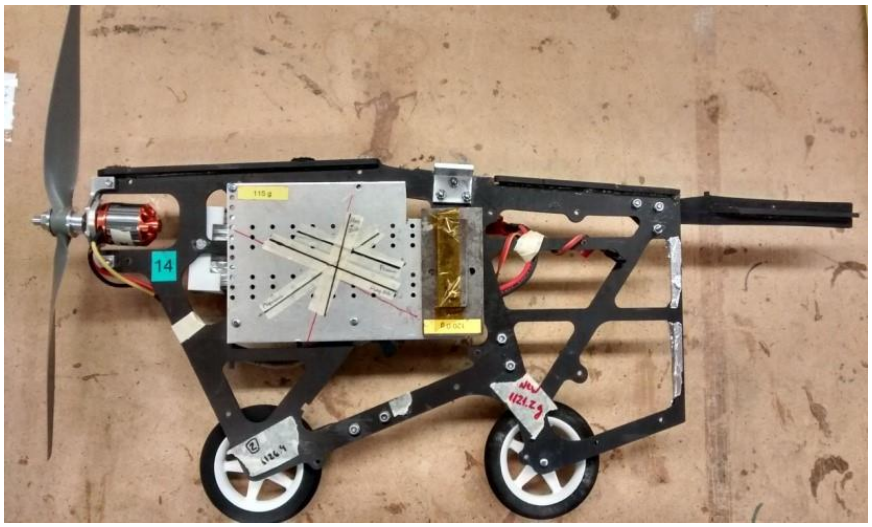

Figure 4.8. Carbon fiber spine with tail connector and aluminum L-brackets

4.2.4 Component Connections

The X-HALE's modular design allows for the swapping of components, enabling rapid changes in the configuration as well as the replacement of worn or faulty parts. The three aircraft components (wing, tail, and motor pod) attach to each other by way of the wing joiner, the tail connector, and the L-bracket.

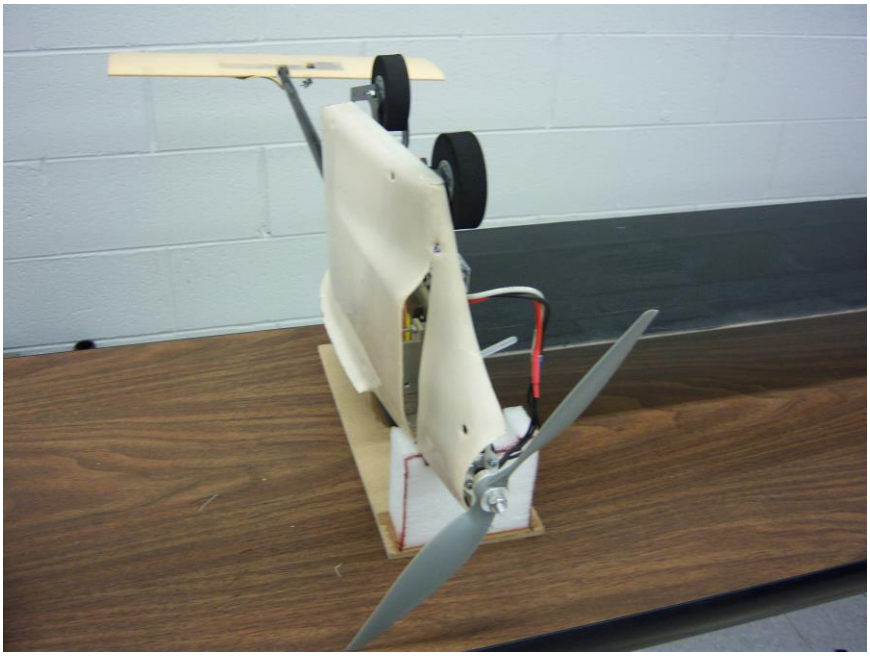

Figure 4.9. Motor pod with aerodynamic fairing

The wing joiner is a precisely machined, lightweight aluminum block that fits into the wingbox to connect individual wing segments. These joiners, shown in Figure 4.4, transmit bending and torsion loads uniformly from spar to spar, enabling the fully assembled wing to behave as a continuous beam. The joiner is a critical component to transfer loads, particularly during the large deformations that the X-HALE was designed to experience.

In addition to connecting the wing segments, the joiner provides a strong attachment point for the motor pods to connect to the wing. An aluminum L-bracket, shown at the top of the spine in Figure 4.8, facilitates this connection.

A cruciform carbon fiber tail connector extends to the rear of the spine. As its name implies, the tail connector provides an attachment point for each of the tails. The hollow, tapered carbon fiber tail boom is pressure fit onto the tail connector and the connector is attached directly to the spine.

The center tail experiences large aerodynamic side forces when oriented vertically. These side forces, coupled with the long moment arm of the tail relative to the attachment point at the joiner, generate a large twisting moment on the center spine which results in significant “tail-wagging” during rolling and yawing maneuvers. In order to eliminate this unwanted motion, piano wire is used to brace the center tail against the inboard pods.

4.3 Flight Control System

The X-HALE is radio-controlled by the pilot on the ground. A 2.4 GHz transmitter communicates the pilot's commands to a 9-channel DSM receiver on the X-HALE's central motor pod. Figure 4.10 shows a diagram of the X-HALE and the relative placement of the control surfaces within the aircraft. The key channels and their corresponding control inputs are throttle (forward thrust), rudder (differential thrust), aileron or spoileron, elevator, and a switch for the center tail.

Thrust is generated by five 1200-g electric outrunner motors mounted to the motor pods, shaded blue in Figure 4.10. Each motor is equipped with a 12-inch diameter propeller and a 6000 mAh 3-cell lithium-polymer battery. An electronic speed controller regulates the motor rpm and ensures consistent power draw at different throttle settings as the battery is discharged. The spanwise distribution of the motors allows directional control via differential thrust, i.e., a turn is commanded by increasing power to the outboard motors of one side while decreasing power to the outboard motors of the opposite side.

The four horizontal tails, shaded green in Figure 4.10, are controlled by a single elevator channel. The elevators deflect in unison to provide pitch authority for climbing and descent maneuvers. The center tail, shaded purple in Figure 4.10, is controlled by a dual-state switch. The tail flips between discrete horizontal and vertical orientations as needed to increase the airframe's lateral damping and arrest the unstable Dutch-roll/wing bending mode when it is excited. Figure 4.11 shows the center tail in its vertical and horizontal orientations during flight.

Two types of roll-control surfaces are used in the X-HALE: ailerons and roll spoilers. Ailerons, shaded red in Figure 4.10, are trailing edge control surfaces that changes the camber of the wing's airfoil profile, changing effective angle of attack of the wing. The X-HALE ailerons are controlled by a single channel and differentially actuated. When one side deflects downward, the other side deflects upward, and the upward deflection is greater than the downward deflection. The ailerons were used to introduce disturbances to the trimmed vehicle, however there are two major factors that make them inappropriate for use with the X-HALE. The downward deflection of the aileron results in more drag than the upward deflection, generating an detrimental yaw moment during rolling maneuvers. This yaw moment is known as adverse yaw, and it can significantly degrade the handling qualities of the aircraft. In addition to generating an adverse yaw moment, the increase in trailing edge lift from the aileron deflection

creates a twisting moment at the wingtip, changing the spanwise angle of attack. If the wing twist is sufficiently large, it can cancel out or even reverse the effect of the aileron in a phenomenon known as control surface reversal. If reversal occurs, the ailerons are rendered ineffective.

Roll spoilers were used as an alternative to ailerons in later X-HALE configurations. The roll spoiler is a thin flap that lies on the upper surface of the wing. The spoilers, shaded pink in Figure 4.10, have the same chordwise dimension as the ailerons and are located in the same spanwise position. The spoiler leading edge is aligned with the aft edge of the wingbox spar. The roll spoilers are controlled by the aileron channel, and when actuated, one spoiler deploys outward, disrupting the flow around the wing. The flow disruption reduces the lift on one wing, generating a roll moment, and the flat plate drag of the deployed spoiler generates a yaw moment as well. The non-deployed spoiler remains flush with the wing.

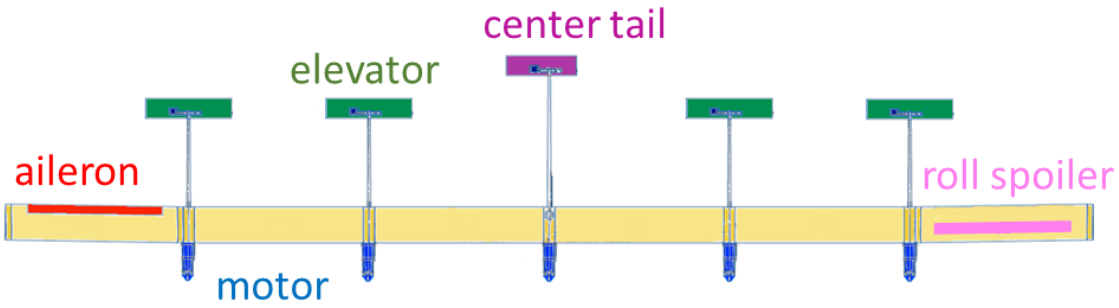

Figure 4.10. Diagram of X-HALE control surfaces.

Figure 4.11: X-HALE RRV with center tail in horizontal (l) and vertical (r) configurations during flight.

4.4 X-HALE Structural Characterization

The X-HALE has a relatively simple airframe design to allow for complete characterization of the various components. Accurate, complete knowledge of the airframe's aerodynamic, inertia, and elastic characteristics are necessary both for modeling the aircraft and comparing experimental and computational results. Several ground tests were performed on the

manufactured aircraft components to measure their properties in preparation for flight tests and simulations.

4.4.1 Measurement of Component Elastic Properties

The X-HALE wing segments are individually relatively rigid, and each of them may be modeled and characterized using linear beam analysis methods. However, when joined together into the full X-HALE wingspan, the full wing is capable of very large deformations in the geometrically nonlinear range. To verify that the constructed wing matches the designed stiffness properties, the out-of-plane (vertical) bending and torsional stiffness constants of an individual and a pair of wing segments were measured using a custom-made rig.[62]

There are two types of wings defined: a main wing and a dihedral wing. The wing types, shown in Figure 4.5, have identical geometry and construction, but the dihedral wings are equipped with control surfaces. The dihedral wings used in the RRV-4 and RRV-6A have an aileron cut into the trailing edge, and the RRV-6B wings have roll spoilers installed.

The wing segment was mounted vertically into the rig shown in Figure 4.12. The segment was clamped at the bottom to enforce a zero-displacement, zero-slope cantilevered boundary. A collar, shown in a close-up in Figure 4.13, was attached to the free end of the wing. To create an external load, calibrated masses were hung from the collar using two steel cables. When the cables were oriented in the same direction, as shown on the left side of Figure 4.13, the load induced an out-of-plane bending moment and a measurable displacement. When the cables were oriented in opposite directions, the hanging masses produced torque, inducing twist along the wing segment.

A laser measurement system was used to record the displacements and twist at several points along the span of the wing as it was loaded and unloaded. Using the linear strain-displacement relation, the cross-sectional bending stiffness *EI* and torsional stiffness *GJ* of each wing segment was calculated from the displacement values under the various load conditions. The measured displacement values are the bending displacement δ_i and twist angle θ_i at each spanwise measurement point *i.* Equation 4.1 define the cross-sectional torsional stiffnesses as:

$$GJ_i = \frac{mgdh_i}{2\theta_i} \tag{4.1}$$

Equation 4.2 defines the cross-sectional bending stiffness as:

$$EI_i = \frac{mgh_i^2(3L - h_i)}{6\delta_i} \tag{4.2}$$

where the measured quantities are the displacements, the height of the measurement point h_i, the applied load mg, the distance between the laser measurement heads d, and total length of the wing L. The stiffness values are averaged across all measurement points and load conditions to yield an average stiffness for each wing segment.These individual wing measurements are listed in APPENDIX C.

The set of individual wings used in each X-HALE configuration are referred to as batches, and the batches were created and characterized at different points in time. Stiffness measurements were performed on a subset of wings belonging to each batch. The individual wing stiffnesses of each batch were consistent within experimental error, which permits the assumption of constant wing stiffness for each batch. Due to changes in the personnel constructing and measuring the wings, the stiffness values vary between batches of wings, thus each X-HALE configuration has a different average wing stiffness. The design stiffness of the wing given by Cesnik and co-workers[30] is listed with the measured batch stiffnesses in Table 4.1.

Table 4.1. Measured cross-sectional wing stiffness values

Configuration		Out-of-Plane Bending EI		Torsion GJ	
		Average N-m^2	Std. Deviation N-m^2	Average N-m^2	Std. Deviation N-m^2
Design Stiffness[30]	Single Wing	119.57	--	72.25	--
RRV-4[63]	Single Wing	112.3	5.3	55.8	4.8
	Double Wing	115.2	6.9	59.0	2.9
RRV-6A[64,65]	Single Wing (main)	105.7	7.2	56.9	7.6
	Single Wing (dih.)	76.3	7.3	54.3	11.0
RRV-6B[66,67]	Double Wing	118.0	3.2	58.8	5.3

The “single wing” designation refers to measurements made on individual meter-long wing segments. The “double wing” designation refers to measurements made on two wing segments joined by an aluminum joiner. The majority of the stiffness tests were conducted on individual wings in order to get an average stiffness for use in creating the X-HALE numerical model. The double wing measurement performed on the RRV-4 batch was used to demonstrate

that joining the wing segments did not significantly alter the stiffness properties. The single wing measurements of the RRV-6B were significantly different from previous batches, and considerably higher than the design value, so a double wing section was measured to verify the results. The double wing measurement was consistent with both the design stiffness and the double-wing tests peformed on the RRV-4 batch of the wings. Since previous batch measurements showed that the single-wing and double-wing values should not be signicantly different, the single wing measurements were discarded and the double wing measurements used as the batch stiffness.

The design stiffnesses[30] were based on the material properties listed in APPENDIX A, and the analysis was performed using UM/VABS, a composite structures analysis tool. The measured out-of-plane bending stiffness averaged 6-12% lower than the design stiffness, while the torsional stiffness averaged nearly 23% lower than the design value.

When creating the aeroelastic model, the measured single-wing stiffness values were used for out-of-plane bending and torsional stiffness. The extension, in-plane, and stiffness coupling values were not measured, so the design values for these parameters are used for the aeroelastic model without correction. The lower stiffness values decrease the natural frequency of the elastic modes. Further analysis, detailed in later sections, show that the measured stiffness does not signicantly alter the desired coupling behavior of the elastic and flight-dynamic modes. From this data, we expect that the fully assembled X-HALE wing structure will exhibit large deformations in flight and geometrically nonlinear behavior as designed.

4.4.2 Measurement of Mass and Inertia Properties

The key inertia properties of the airframe components are the mass, center of gravity, and mass moments of inertia. The mass of each component is measured using simple scales. The center of gravity of each component is found by suspending the component from two single points and projecting the vertical line through the component. The location where these lines intersect gives the center of gravity.

Two measurement devices were used to measure the mass moment of inertia of the various components: an air bearing and a bifilar pendulum. This section summarizes the methodology for each test. The component mass, center of gravity, and inertia measurements for each configuration are summarized in Table 4.5, Table 4.9, and Table 4.13.

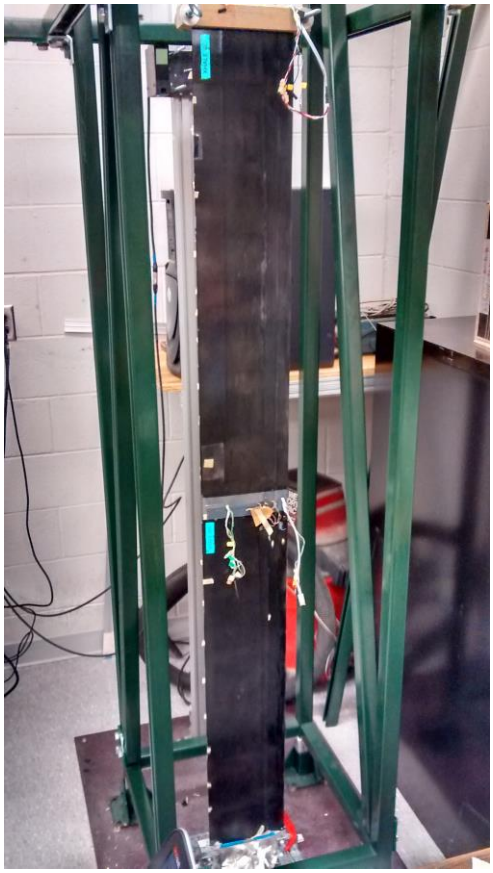

Figure 4.12. Double-wing section in stiffness testing rig

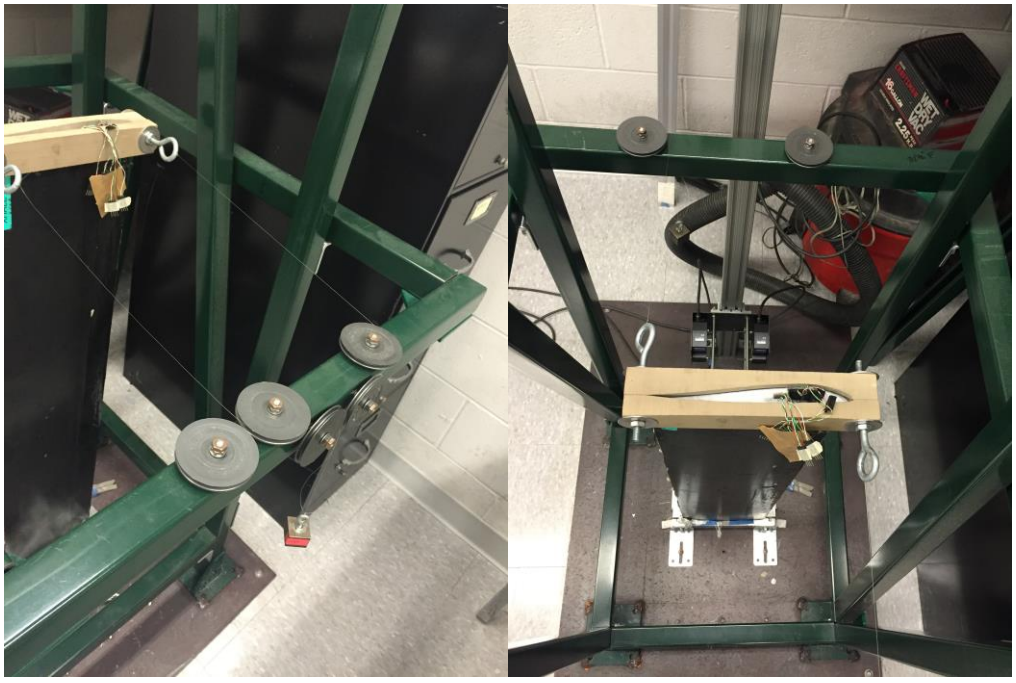

Figure 4.13. Test rig setup for a wing in bending (l) and torsion (r)

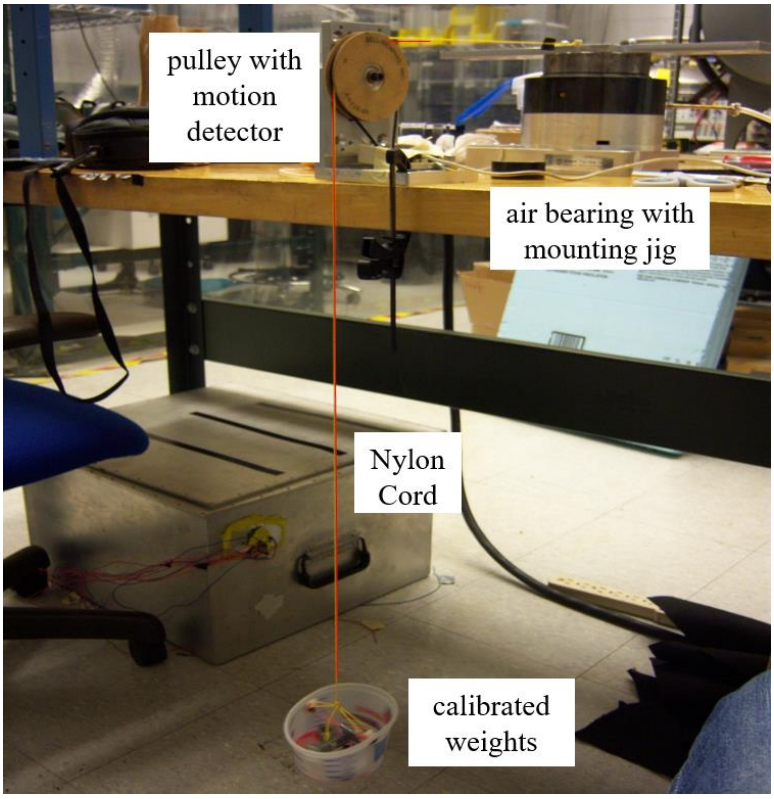

Figure 4.14. Diagram of air-bearing test setup

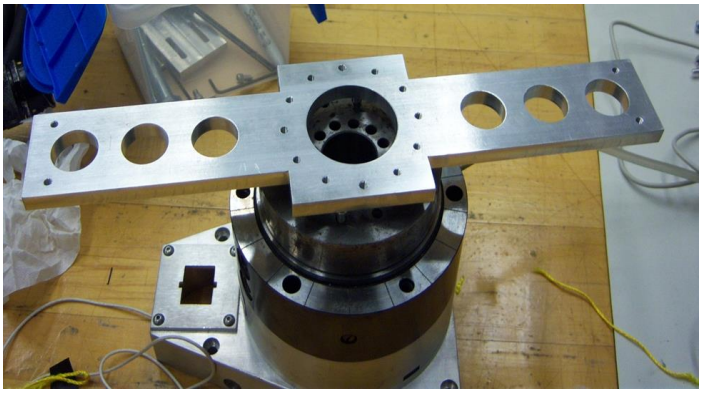

Figure 4.15. Air bearing with mounting jig

A diagram of the air-bearing setup is given in Figure 4.14.[68] The component to be measured is mounted to the platform of a low-friction air bearing using an aluminum jig, shown in Figure 4.15. A small calibrated weight is attached to the air bearing spindle using a inextensible Kevlar wire via a pulley. The calibrated weight is dropped from a measured height, and the falling weight applies a torque to the spindle, spinning the air bearing with a rotational acceleration proportional to the mass' linear acceleration due to gravity.

The rotational inertia about the component's center of gravity is found from the following equation:

$$I_{cg} = \frac{(mgr - m\alpha r^2)}{\alpha} = \frac{(mg - ma)r^2}{a} \tag{4.3}$$

where r is the radius of the air-bearing spindle and m is the mass of the calibrated weight. The rotational acceleration α is re-written in terms of r and the linear acceleration a, which is measured by a potentiometer located within the pulley.

The air bearing was used to measure the planar moment of inertia (I_{xx}) of an assembled motor pod. The experimental values obtained using this method were consistent with inertia values generated using CAD models.[68] However, obtaining an accurate measurement of the vertical (I_{yy}) and axial moments of inertia (I_{zz}) proved to be very difficult due to the shape of the motor pod. The air-bearing test requires the component to be mounted at its center of gravity, but for these orientations, component "wobble" led to inconsistent results. These results are detailed in the reports by Moyes and co-workers.[69] The axial (I_{yy}) moment of inertia is of considerable importance to accurate modeling of the X-HALE, as it is the inertia component associated with out-of-plane bending in elastic deformation and roll in rigid body motion. So, the bifilar pendulum was used for a more reliable method of obtaining these inertia values for the various aircraft components.

A bifilar pendulum was used to measure the mass moment of inertia of the motor pods, wing segments, tail booms, and horizontal tails. The pendulum was composed of two parallel Kevlar wires hanging from a steel strut, attached to two endpoints of the component. The component is given an initial twist perturbation about the axis of rotation, then released. The restoring moment due the force of gravity results in a damped oscillation about the rotation axis and the average period of rotation is measured and used to estimate the moment of inertia. Figure 4.17 shows the setup of the pendulum for the measurement of the axial inertia I_{zz} of a wing segment.

The linear equation of motion for the bifilar pendulum is given as:

$$\ddot{\theta} + (\frac{mgL^2}{4hI_{cg}})\theta = 0 \tag{4.4}$$

where the pendulum rotation angle θ is expressed in terms of the object mass m, object length L, and pendulum cable height h, and rotational inertia I_{cg}.

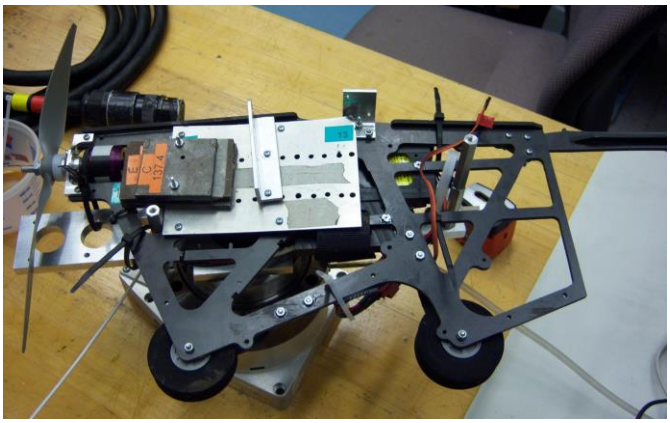

Setup for I_{xx} measurement

Setup for I_{yy} measurement

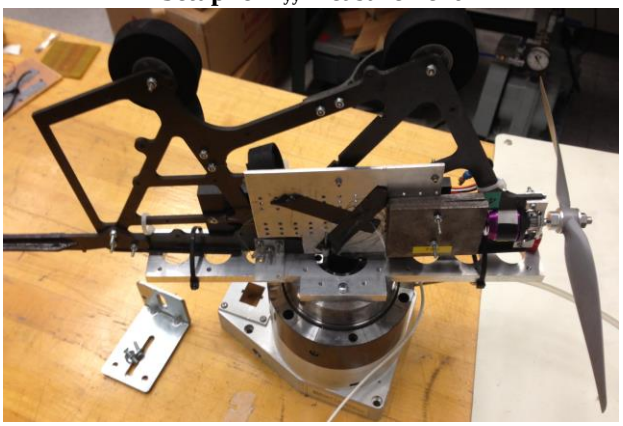

Setup for I_{zz} measurement

Figure 4.16. Motor pod mounted on air bearing

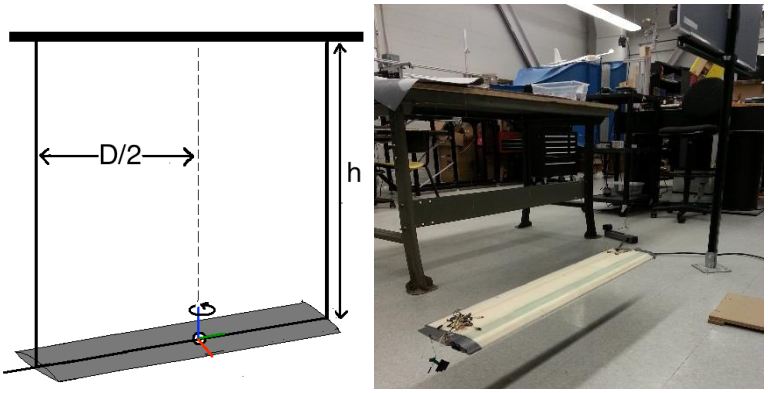

Figure 4.17. Bifilar pendulum test setup for a wing segment

Assuming the angles are small and the oscillations are undamped, the pendulum twist angle has the assumed solution,

$$\theta(t) = A\sin(\omega t) \tag{4.5}$$

where ω is the circular frequency and A is the amplitude of the oscillations. By substituting the solution into the equation of motion, the moment of inertia about the center of gravity may be derived as,

$$I_{cg} = \frac{mgL^2}{4h\omega^2} \tag{4.6}$$

This method yields moment of inertia measurements consistent with values generated using CAD for the wings and tails.[70] However, the assumptions required by this method, namely, that of undamped oscillations, do not hold for the measurements of the motor pods. The pods exhibit considerable aerodynamic drag about all three axes of rotation, so an empirical-based expression for moment of inertia from the fully nonlinear, damped equations of motion is used.[71]

$$\ddot{\theta} + \left(\frac{K_D}{I}\dot{\theta}\left|\dot{\theta}\right| + \frac{C}{I}\dot{\theta}\right) + \left(\frac{mdD^2}{4IL}\right)\frac{\sin\theta}{\sqrt{1-0.5\left(\frac{D}{L}\right)^2(1-\cos\theta)}} = 0 \tag{4.7}$$

The results of the moment of inertia tests are summarized in the configuration tables in Section 4.6, and the measurements are described in detail in the reports by Lu.[72]

4.5 X-HALE Aerodynamic Properties

The aerodynamic properties of the X-HALE lifting surfaces are given as cross-sectional coefficients that are integrated along the span. The X-HALE wing segments are defined by a

0.2m chord EMX-07 reflexed airfoil, the tails are defined by a 0.11-m chord NACA 0012 airfoil, and the motor pods are defined by a 0.38-m chord NACA 0018 airfoil.[30] The ventral fins are defined as NACA 0010 airfoils, and their chords are listed in the configuration descriptions in Section 4.6. The roll spoilers are treated as flat plates that deploy into the flow. The cross-sectional lift, drag, and moment coefficients of each component for a range of angles of attack were generated using XFOIL.The chord-normalized airfoil profile for each component and calculated coefficients are tabulated in APPENDIX D. The following section details calculations and experimental measurements of aerodynamic properties of the assembled aircraft.

4.5.1 Numerical Estimation of the Aerodynamic Center

A numerical estimation of the location of the X-HALE's aerodynamic center was performed using two widely used open-source tools. The center of pressure for the X-HALE lifting surfaces is calculated using the Athena Vortex Lattice Code (AVL),[73] whose capabilities include configuration development and aerodynamic analysis of rigid aircraft. The lift coefficient slope of the wing and tail were calculated using XFOIL.

Assuming the X-HALE is a rigid aircraft, the aircraft pitching moment about its aerodynamic center can be expressed in terms of the lift L generated by the wing and tail, that is,

$$M_{ac} = (x_{ac} - x_{cp,wing})L_{wing} + (x_{ac} - x_{cp,tail})L_{tail} \tag{4.8}$$

where the x_{ac} is the chord-wise position of the aerodynamic center from the aircraft nose, and $x_{cp,\,wing}$ and $x_{cp,\,\text{tail}}$ are the chord-wise positions of the center of pressure of the wing and tail, respectively.

Nondimensionalizing the equation with dynamic pressure gives its coefficient form in terms of the offset between the aerodynamic center and center of pressure and the lift coefficient slopes for the wing and tail, yielding[74]

$$C_{M_{ac}} = \frac{1}{\bar{c}}\left((x_{ac} - x_{cp,wing})C_{L,wing} + \frac{S_{tail}}{S_{wing}}(x_{ac} - x_{cp,tail})C_{L,tail} \right) \tag{4.9}$$

$$x_{ac} = \frac{\frac{\partial C_{L,wing}}{\partial \alpha} x_{cp,wing} + n\frac{S_{tail}}{S_{wing}}\frac{\partial C_{L,tail}}{\partial \alpha} x_{cp,tail}}{\frac{\partial C_{L,wing}}{\partial \alpha} + n\frac{S_{tail}}{S_{wing}}\frac{\partial C_{L,tail}}{\partial \alpha}} \tag{4.10}$$

AVL accounts for camberline effects, but neglects the thickness of a particular lifting surface. XFOIL does not incorporate sweep effects.

4.5.2 Low Aspect Ratio Aerodynamic Correction

A low-aspect ratio wing approximation for the side force coefficient derivative with respect to angle of attack is used to approximate the aerodynamic load on the ventral fins:[75]

$$c_{SF,\alpha} = \frac{2\pi qS}{\left(\frac{2}{AR}\right) + \sqrt{1 + \left(\frac{2}{AR}\right)^2}} \tag{4.11}$$

4.5.3 Wind Tunnel Measurement of Aerodynamic Effects

As with many HALE-type vehicles, the fully assembled vehicle is too large to test in the wind tunnel facilities available. A numerical model for the aircraft was created using aerodynamic coefficients, however many simplifying assumptions were used when generating these coefficients. By using XFOIL, it was assumed that the lifting surfaces have a perfect airfoil shape, and that there are no modifications or attachments that significantly alter the flow. The strip-theory framework used in UM/NAST neglects component interaction altogether, so effect of wake shadowing, blockage, and other interference effects on the aerodynamic loads is not modelled. The wind tunnel tests detailed in this section represent an effort to gain more knowledge about 1) propeller-wake interference effects on the motor pod's aerodynamic fairing, ventral fin, and horizontal tail, 2) local wing-fairing interference effects, and 3) propeller downwash effects on the fairing.

Table 4.2. Properties of the University of Michigan wind tunnels and their balances

Tunnel Parameter	Subsonic Low Turbulence 5x7	Edward A Stalker 2x2 Subsonic	Units
Type	Closed-circuit	Open-circuit Eiffel	
Test Section Height	7	2	ft
Test Section Width	5	2	ft
Test Section Length	25	4	ft
Max. Tunnel Speed	170 (76)	110 (49)	mph (m/s)
Max Lift	600	50	lb
Max Drag	120	50	lb
Max Side Force	80	50	lb
Max Pitch Moment	3000	75	in-lb
Max Roll Moment	3000	75	in-lb
Max Yaw Moment	1800	25	in-lb

Figure 4.18. External view of test section of the University of Michigan 5x7 wind tunnel

Figure 4.19. Internal view of test section of University of Michigan 5x7 wind tunnel

4.5.4 Propeller Wake Interference Effects on the Pod-Fin-Tail Assembly

Wind tunnel tests were performed on representative section of the X-HALE to measure the aerodynamic loads. Figure 4.20 shows the wind tunnel model, which consists of a single motor pod, a ventral fin, and a horizontal tail. Tests were conducted with and without the aerodynamic fairing (exposing the carbon fiber spine and payload components to the flow), with and without the ventral fin, and with the motor powered on and off. When the motor is powered down during a test, the propeller is still in place and spins freely in the oncoming flow. However, at the speeds being tested, the spinning propeller has a negligible effect on the lift, drag, and aerodynamic moments. Additional detail on the wind tunnel setup and calibration is given in the report by Brown and workers[76].

4.5.4.1 Drag and Yaw Moment Effect of Fairing

A demonstration of the change in drag and yaw moments due to the fairing was conducted. For this test, the motor was run at 100% power and there was no ventral fin, which corresponds to the configuration shown in Image A of Figure 4.20. For the data shown in Figure 4.21, the line style indicates the pod's pitch angle of attack relative to the wind tunnel free stream. The solid line represents data from tests at angle of attack $\alpha = 0^{\circ}$, the dashed line represents $\alpha = -10^{\circ}$, and the dotted line represents $\alpha = +10^{\circ}$.

For all angles of attack and sideslip angles, the aerodynamic fairing adds considerable drag to the model. For the nonzero angles of attack, the drag increase is large, but stays relatively constant with respect to sideslip angle. Also, the relationship between drag and sideslip is mostly quadratic for the nonzero angles of attack.

At zero angle of attack however, the slope of the drag-sideslip angle curve is nearly linear, indicating that the negative sideslip angles have much less drag than the positive sideslip angles. This is due to the presence of the cooling vents on the fairing. At negative sideslip angles, the vents are on the suction side of the fairing. The pressure side of the fairing presents a smooth surface to the oncoming flow, so the drag behavior of the model is airfoil-like. As the sideslip angle increases, the smooth side becomes the suction side. The vent, positioned near the leading edge of the pressure side, causes premature flow separation and a significant increase in drag over the fairing-off configuration.

As expected, the yaw moment is increasingly negative (counterclockwise) for negative sideslip angles, following the drag trend. However, the yaw moment is still negative at zero sideslip angle ($\beta=0^{o}$). This negative yaw moment is not overcome until the wind tunnel model reaches $\beta\sim+8^{o}$ in the fairing-off configuration, and $\beta\sim+10^{o}$ in the fairing-on configuration. The yaw moment is larger for the fairing-on configuration, due to the increased drag on the left side of the model. Yet, the behavior trends of both fairing-on and fairing-off configurations is very similar across all angles of attack, which indicates that the fairing is exacerbating the negative moment present in the wind tunnel model, but it is not the source.

In a conventional aircraft, an undesirable yaw moment could be eliminated by adjusting the rudder trim position to cancel out the additional yaw moment. However, the X-HALE aircraft has no rudder; instead it uses differential thrust to execute lateral maneuvers. In order to effectively eliminate the yaw moment from the aircraft using differential thrust, an asymmetric

thrust profile across the span must be used. However, any change in the thrust profile will result in a change in the spanwise lift as well, generating a roll moment. Thus, trimming the negative yaw moment is a nontrivial task that involves all of the lateral degrees of freedom and control surfaces.

a. Model with no ventral fin at positive angle of attack

b. Model with ventral fin at zero angle of attack

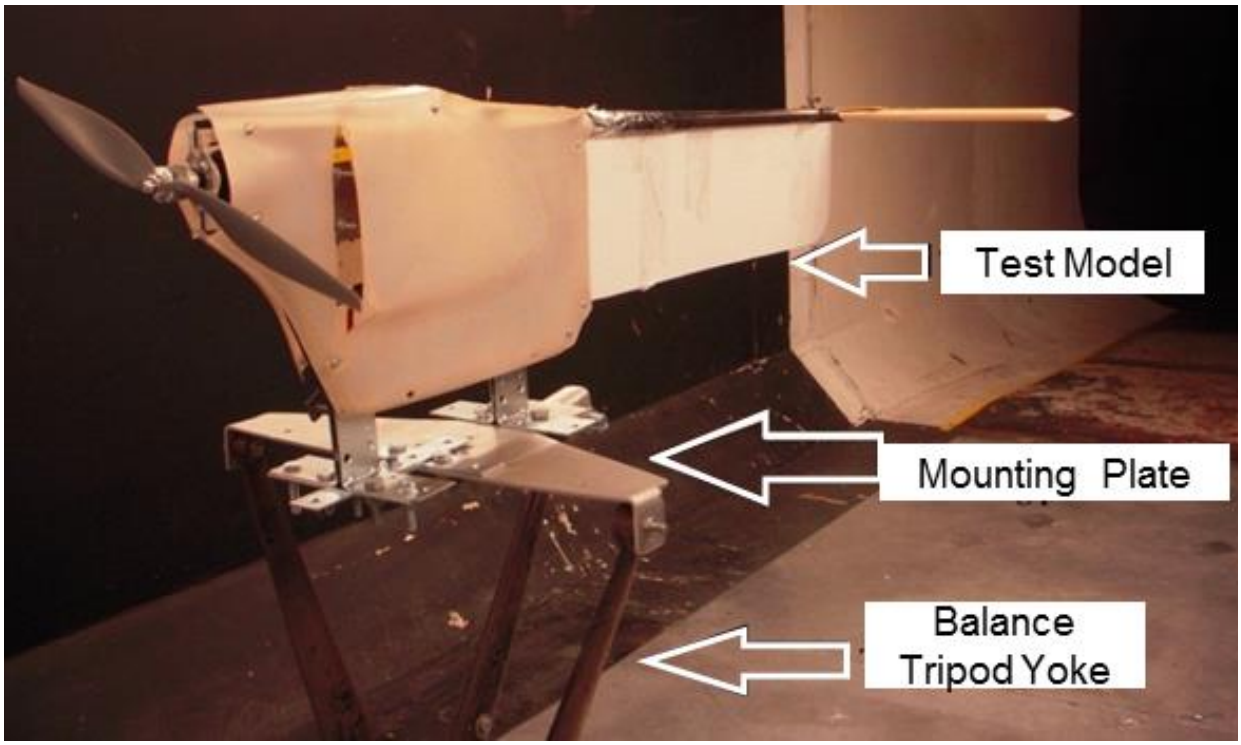

c. Model with ventral fin with setup test setup

Figure 4.20. X-HALE pod-fin-tail wind tunnel model in the fairing-on configuration

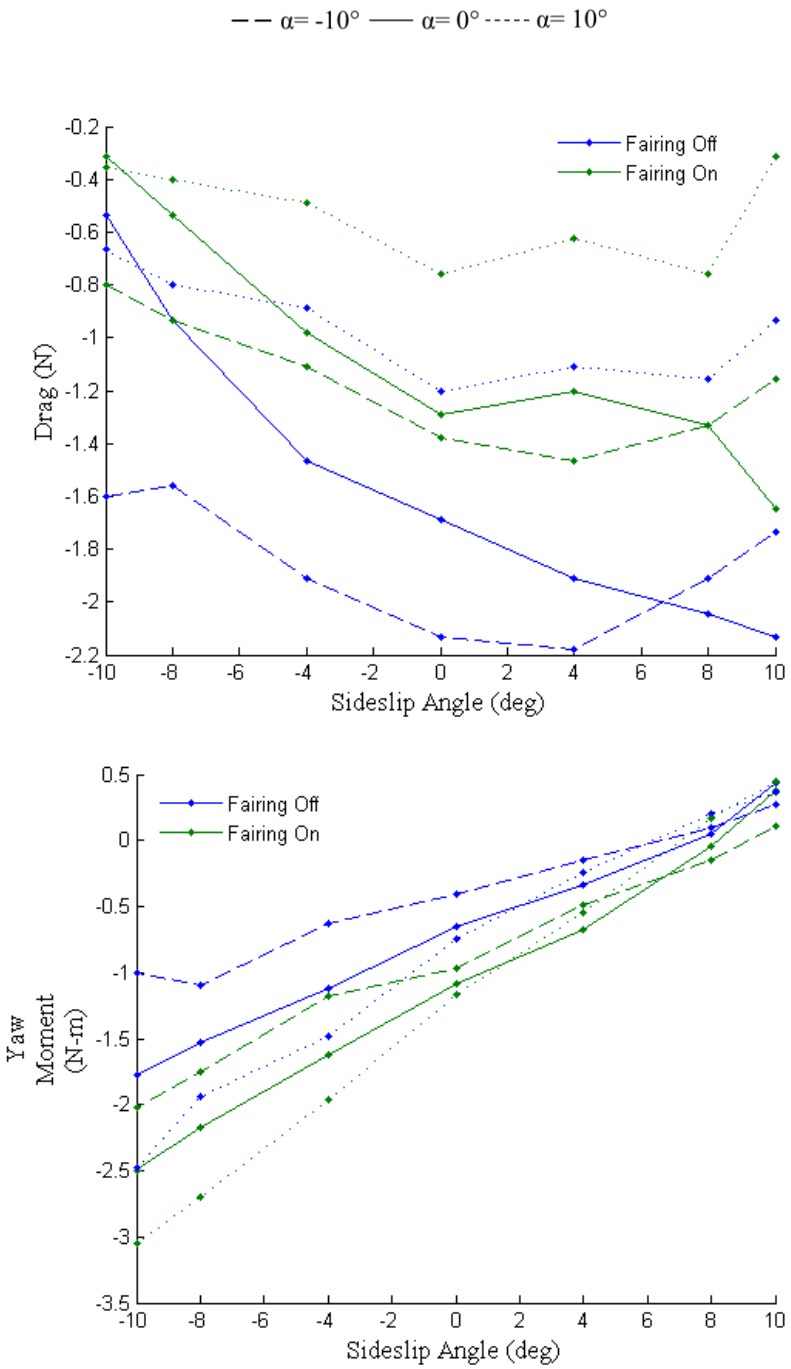

Figure 4.21. Comparison of drag and yaw moment between fairing on and fairing off tests

4.5.4.2 Drag Effect of Ventral Fin

The ventral fin is used to augment the lateral stability of the X-HALE in conjunction with the vertical tail. The tests detailed in this section demonstrate the effectiveness of the fin in counteracting unwanted lateral moments. These tests are conducted in the fairing-off

configuration. For the data shown in Figure 4.22, the line style indicates the pod's pitch angle of attack relative to the wind tunnel free stream. The solid line represents data from tests at angle of attack $\alpha = 0^{\circ}$, the dashed line represents $\alpha = -10^{\circ}$, and the dotted line represents $\alpha = +10^{\circ}$.

The effect of the ventral fin on the yaw moment is intuitive. As the sideslip angle changes, the fin, located behind the aerodynamic center of the wind tunnel model, offsets the yaw moment generated by the motor pod. In the fin-off configuration, the model does not reach yaw moment equilibrium until the sideslip angle is ~+8º. Figure 4.22 shows that with the fin, yaw moment equilibrium can be reached for β ~0-4º, depending on the pod angle of attack. This implies that the ventral fin will not only add add lateral damping to the aircraft, acting as as a stabilizer during maneuvers, but it will also improves the static trim behavior of the aircraft by reducing the left-yaw tendency of each motor pod.

4.5.4.3 Moment Effect of the Motor

The next set of tests compare the aerodynamic moments generated by the fairing-on configurations when the motor is at 100% power, and when the motor is at 0% power (propeller spinning freely). These tests were performed with the ventral fin in place, which corresponds to the configurations shown in Images B and C in Figure 4.20. The data is shown in Figure 4.23, and the line style indicates the pod's pitch angle of attack relative to the wind tunnel free stream. The solid line represents data from tests at angle of attack $\alpha = 0^{\circ}$, the dashed line represents $\alpha = -10^{\circ}$, and the dotted line represents $\alpha = +10^{\circ}$.

The powered motor introduces a significant offset to the pitching and rolling moment as the propeller slipstream interacts with the fairing and the tail. The additional down force on the tail results in an increased negative pitching moment at all sideslip angles. The torque of the motor contributes to the roll moment, but to a lesser extent. the presence of the propeller downwash intensifies the negative yaw moment acting on the pod assembly and increases the moment-slope with respect to sideslip angle. In fact, this result suggests that, due to the helical nature of the propeller wake, the propeller downwash is the source of the negative yaw moment that was noted in the previous tests and shown in Figure 4.21. A further examination of effect is conducted in Section 0.

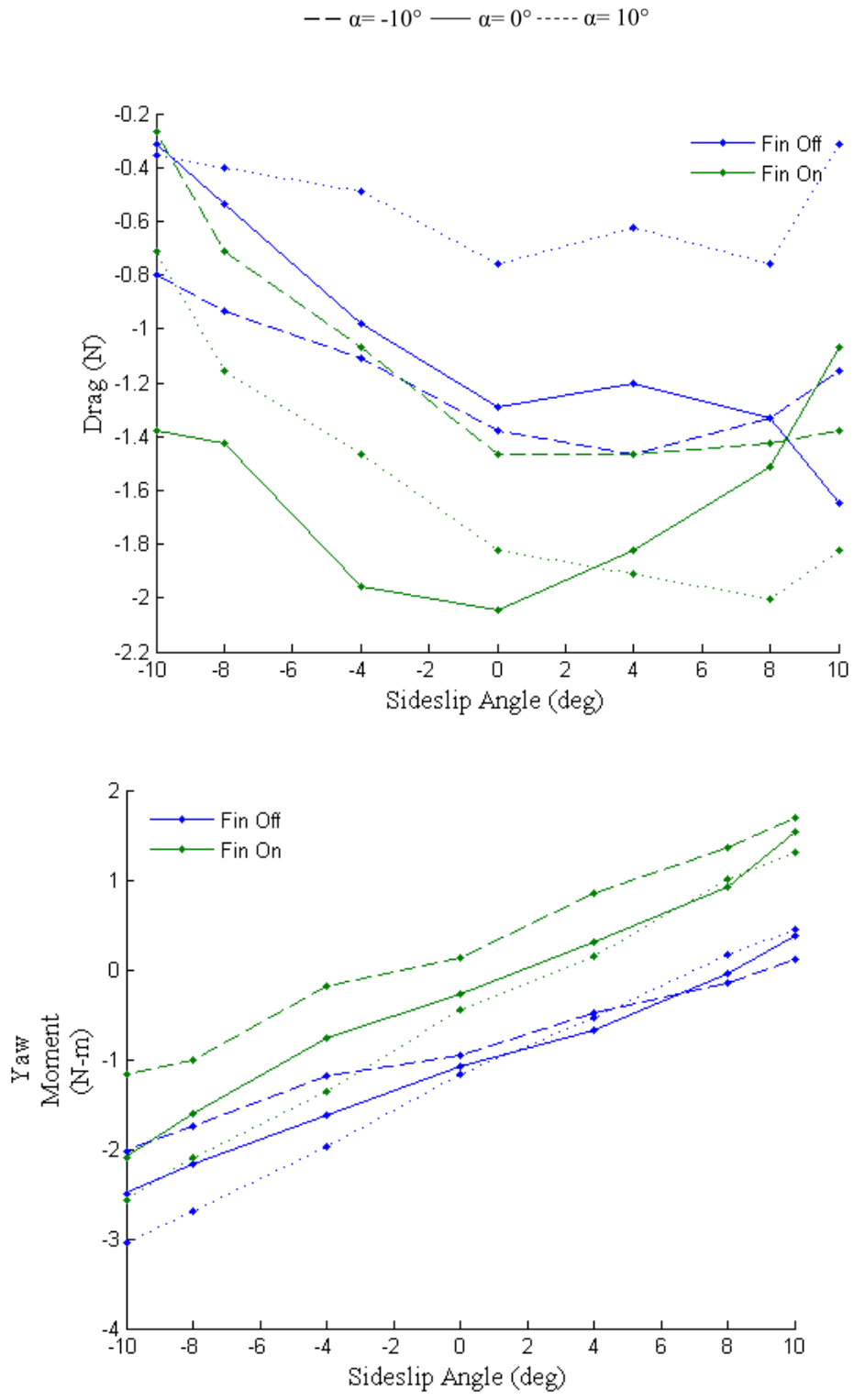

Figure 4.22. Comparison of drag and yaw moment between ventral fin-on and fin-off configurations

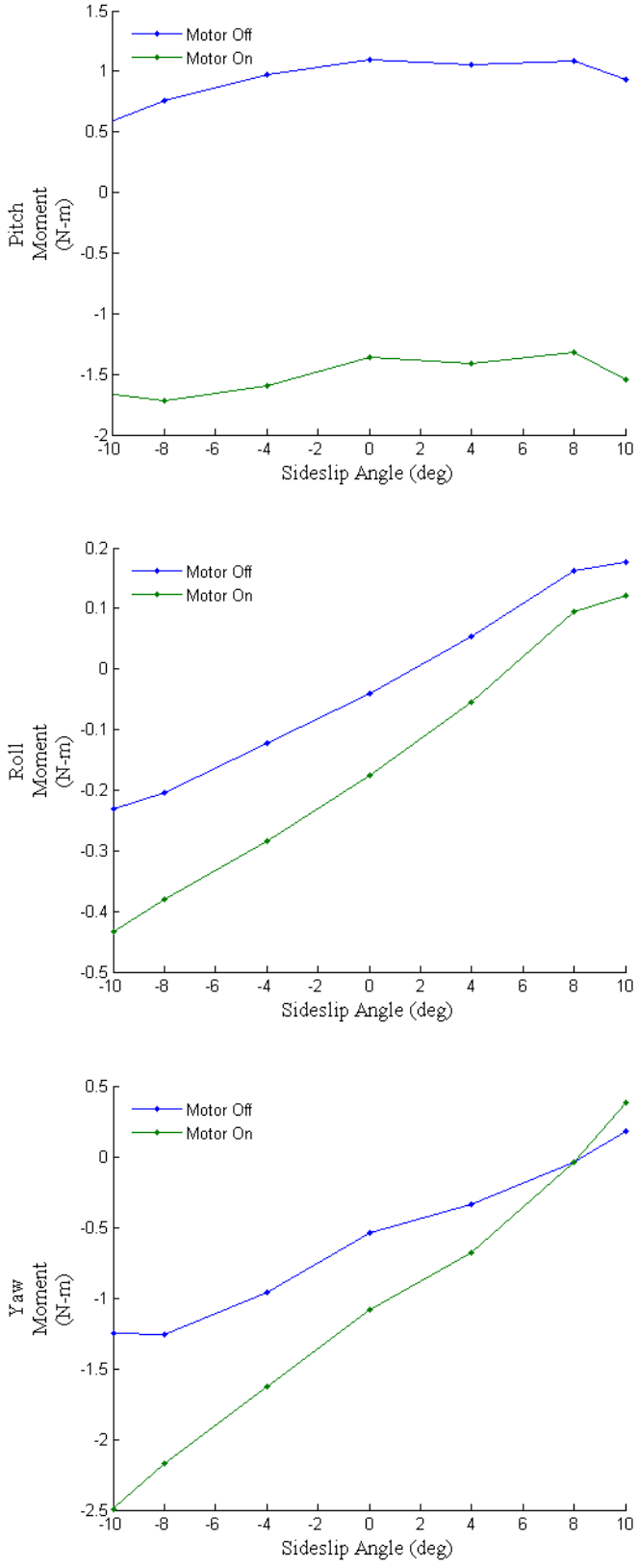

Figure 4.23. Comparison of yaw, pitch, and roll moments with motor on and motor off

4.5.5 Local Wing-Fairing Interference Effects

A second wind tunnel model was created to study the effects of the wing interference on the aerodynamic loads experienced by the fairing. The details of the model setup and wind tunnel calibration are given in the report by Hamilton and coworkers.[77] Figure 4.24 shows the wind tunnel model, which consists of two 0.5-meter wing segments, a single motor pod, and a horizontal tail. The configuration was tested with and without the aerodynamic fairing, and the motor is powered on during all tests. In the plots presented in Figure 4.26, data for the fairing off configuration is shown in blue, and data for the fairing on configuration is shown in green.

The data from these tests indicates that the presence of the fairing significantly alters the trends of the aerodynamic behavior. As seen in previous tests, the addition of the fairing introduces considerable drag at all angles of attack. The effect on the aerodynamic moments is strongest when the sideslip angle is varied, transitioning the fairing vent from the pressure side of the fairing to the suction side relative to the oncoming flow. Adding the fairing introduces a strong nose-down pitching moment, and increases the roll moment slope across all sideslip angles. These changes in the lateral aerodynamic coefficients at certain flight conditions can push the marginally stable lateral mode of the aircraft into fully unstable behavior.

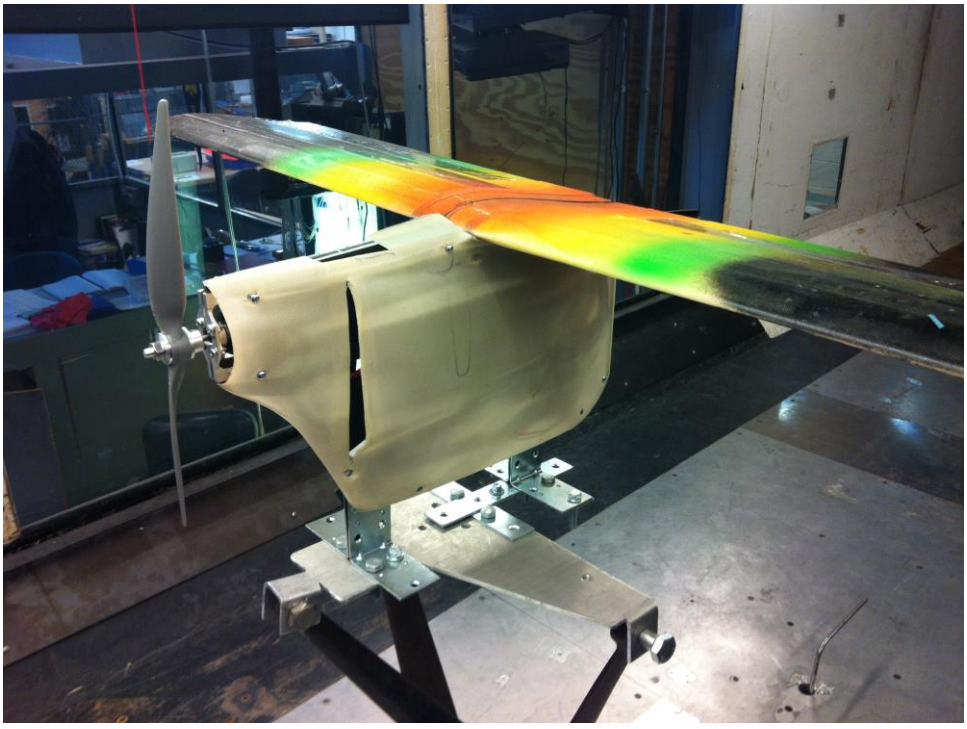

Figure 4.24. X-HALE wing-pod wind tunnel model: fairing on configuration

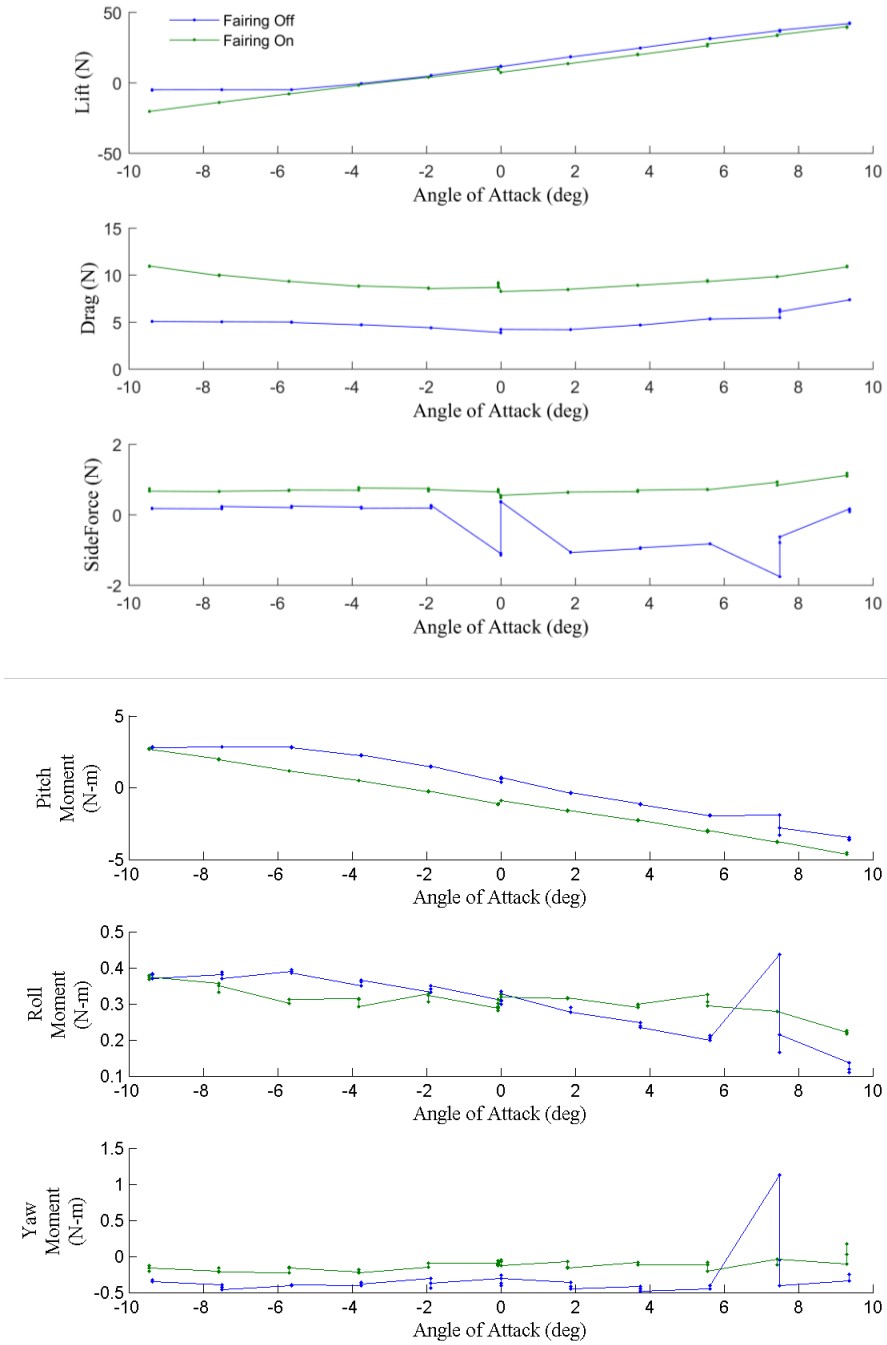

Figure 4.25. Forces and moments of the wing-pod-tail wind tunnel test with varying angle of attack

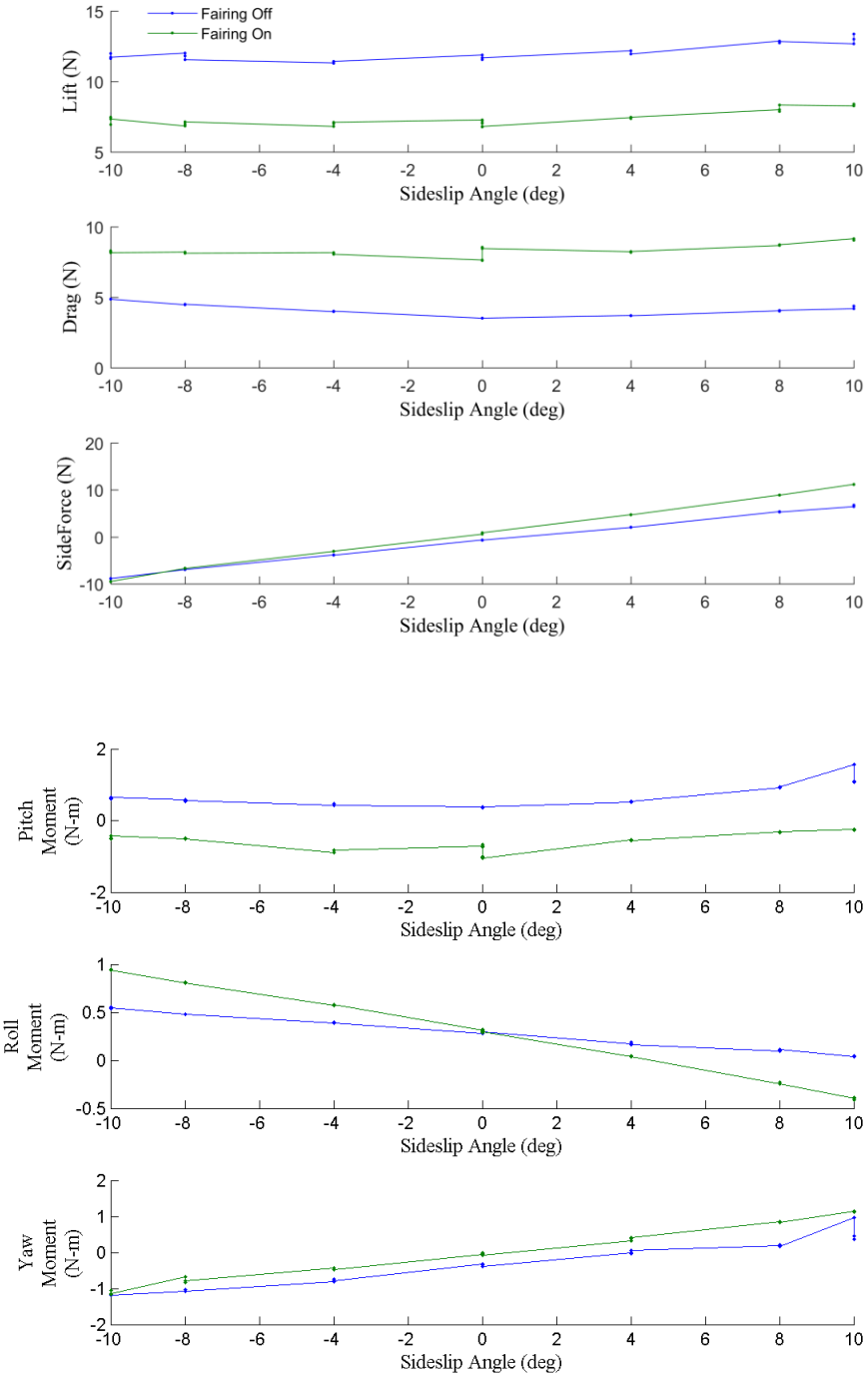

Figure 4.26. Forces and moments of the wing-pod-tail wind tunnel test with varying sideslip angles

4.5.6 Propeller Downwash Effects on the Motor Pod

Wind tunnel tests were performed on a motor pod by itself to evaluate the effect of various motor power levels on the drag and yaw moment.[78] The tests were conducted in the 2'x2' Stalker Wind Tunnel, the properties of which are given in Table 4.2. Unlike the larger 5x7 wind tunnel, the sting of the stalker tunnel only adjustment of the models angle of attack. As previous tests have shown, the sideslip angle of the motor pod relative to the oncoming flow is more impotant than angle of attack when investigating effects on drag and yaw moment. The pod was mounted with the wheels horizontal so that changes in the sting angle of attack resulting in orientations to the sideslip angle used in the other wind tunnel tests. Thus, the pitching moment described in this section is equivalent to yaw moment in the previous wind tunnel tests.

In these tests, the speed was varied from 12-20 m/s, which covers the entire range of flight speeds that will be experienced by the X-HALE cofigurations. At each speed, the motor was set at 0% (prop freely spinning), 80%, and 100% power, and the aerodynamic forces and moments were recorded. The drag and pitching moment from these tests is plotted in Figure 4.27 through Figure 4.30, and each color represents a different sideslip angle.

The data gathered in this test supports the conclusions drawn in previous wind tunnel tests. Figure 4.27 and Figure 4.28 show that the presence of the fairing imposes small changes in the aerodynamic loads, but does not significantly impact the overall trend of the behavior, In contrast, the prop wash interaction with the motor pod does have a significant effect on the aerodynamic loads, as evidenced by the increase in pitching moment with motor power and speed shown in Figure 4.29 and Figure 4.30. This prop wash interaction with the motor pod is present in both the fairing-off and fairing-on configurations, and may erode the handling qualities of a marginally-stable aircraft to the point of being unstable.

β= +8°, +5°, 0° , -5° , -8°

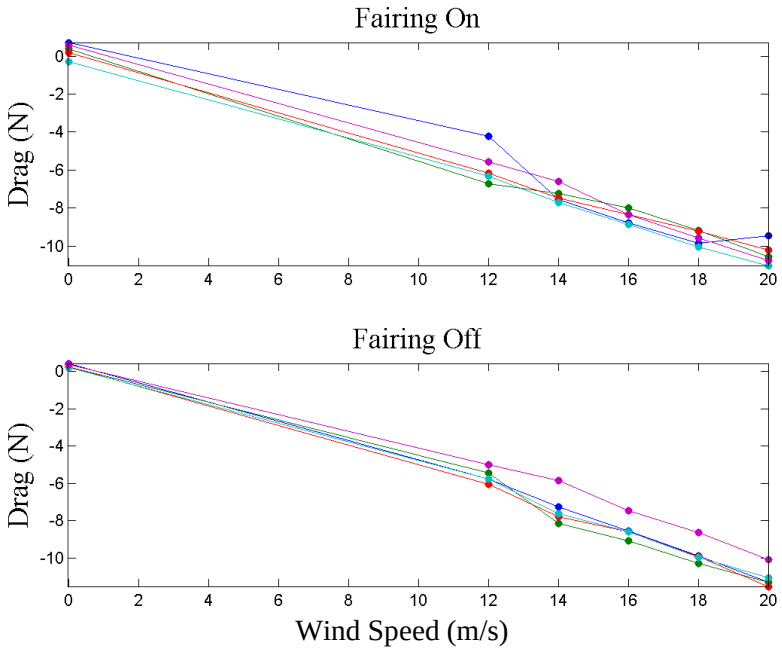

Figure 4.27. Drag of a fairing with motor at 100% power

β= +8°, +5°, 0° , -5° , -8°

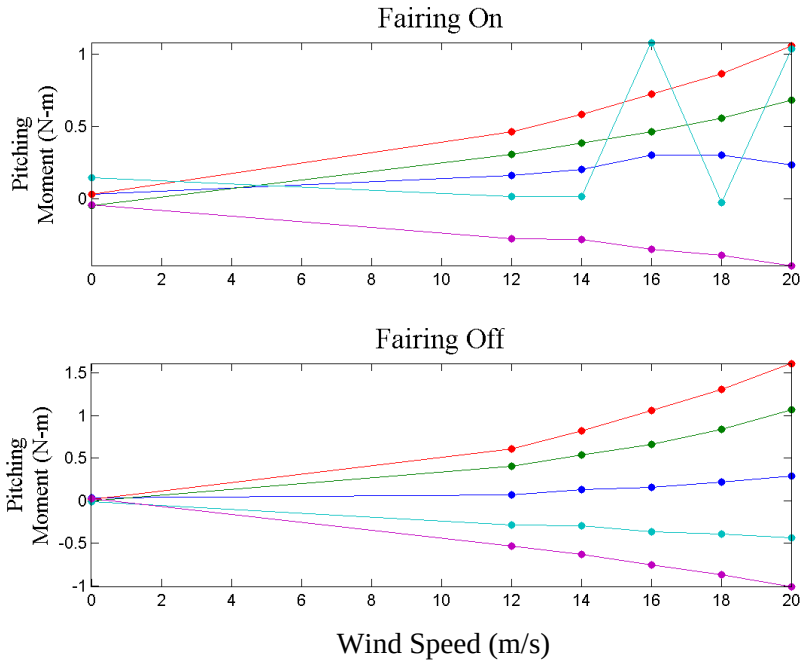

Figure 4.28. Pitching moment of fairing with motor at 100% power

β= +8°, +5°, 0° , -5° , -8°

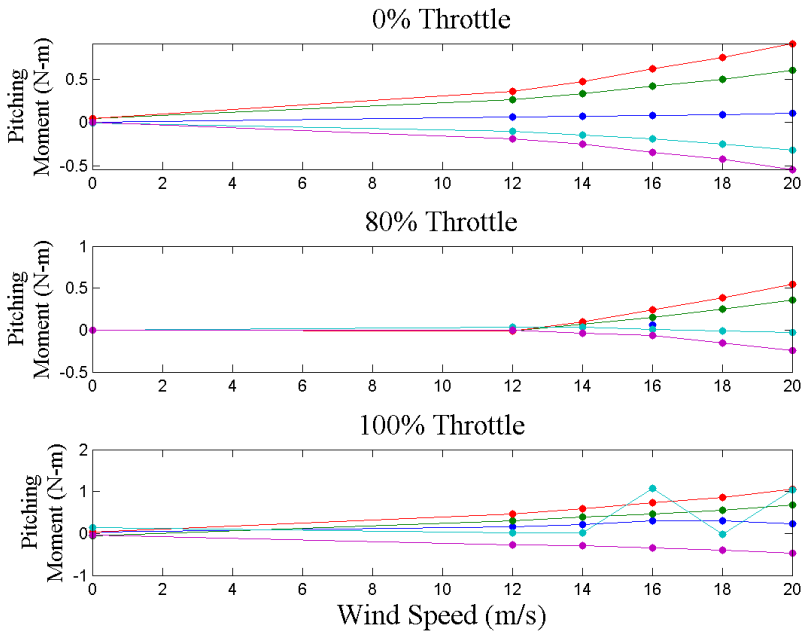

Figure 4.29. Prop wash effect with fairing off

β= +8°, +5°, 0° , -5° , -8°

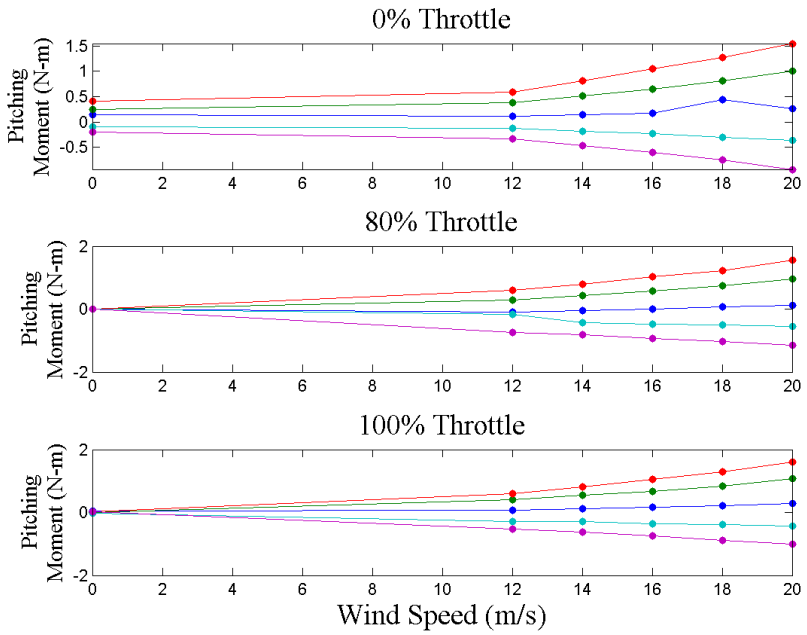

Figure 4.30. Prop wash effect with fairing on

4.6 X-HALE Configurations

As a risk reduction path for developing a fully instrumented X-HALE, multiple vehicles were conceived with various levels of instrumentation. The fully instrumented airframes are known as the X-HALE Aeroelastic Test Vehicles (ATV), and their lightly instrumented counterparts are known the X-HALE Risk Reduction Vehicles (RRV). The primary purpose of the RRV configurations is to assess the flight handling and verify the flight dynamic behavior of the X-HALE airframe design before the fully instrumented vehicles are flown. Thus, the X-HALE RRVs are identical to their fully instrumented counterparts, except that the instrumentation is replaced with representative ballast masses.

The original X-HALE Aeroelastic Test Vehicle (ATV-A) was proposed by Cesnik and coworkers[30,61] and was instrumented with strain gages for measurement of wing deformation during flight. The RRV-4 and RRV-6A are the risk reduction vehicles for this configuration. The second generation X-HALE ATV-B was outfitted with a marker-based stereovision wing shape measurement system developed by Pang et al.[60] The RRV-6B is the corresponding risk reduction vehicle for this configuration. A comparison of the main characteristics of the X-HALE configurations are summarized in . The remainder of this chapter presents tables of the airframe properties that were measured with the methods presented in the previous section. Numerical models were created using these properties, and UM/NAST was used to predict the aeroelastic response of each X-HALE configuration.

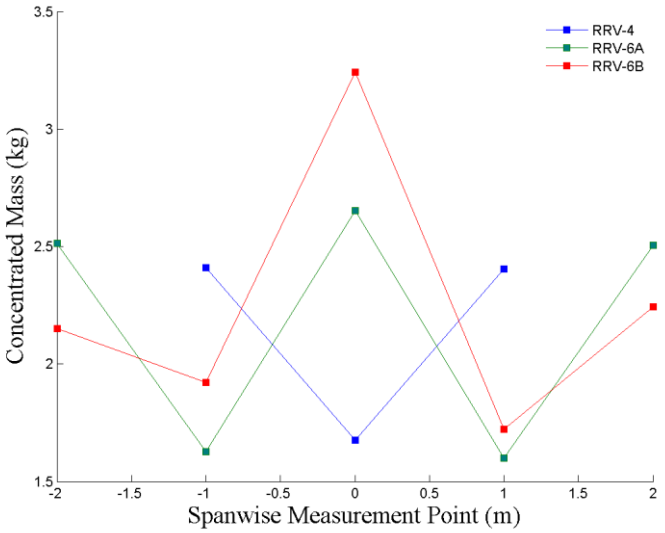

Figure 4.31. Weight distribution of the three X-HALE configurations

4.6.1 The X-HALE RRV-4

The X-HALE RRV-4 is a 4-meter span airframe intended to provide a training opportunity for the pilot before progressing to the higher aspect ratio, very flexible configurations.

Figure 4.32. The X-HALE RRV-4

4.6.1.1 Configuration Summary

This section summarizes the properties of the X-HALE components used in the RRV-4 configuration. Table 4.4 details the geometry and cross-sectional inertias of the primary aircraft structure, as well as the elements of the wing stiffness matrix. The origin of each local reference axes is given, and the positive *x,y,z* axes point towards the right wingtip, toward the wing leading edge, and vertically upward, respectively. Table 4.5 lists properties of the concentrated inertias used to model additional aircraft components. The values that are italicized correspond to values that are taken from the design,[30,61] and all other values were measured. Figure 4.3 illustrates the positioning footnotes used in Table 4.4 and Table 4.5.

4.6.1.2 Instrumentation

The RRV-4 is outfitted with a MIDG GPS/INS to measure the aircraft orientation and body rates. The GPS receiver also recorded the aircraft's GPS coordinates as well as the GPS speed and altitude. A Gumstix single board computer was used to establish record data onboard the aircraft. A Eagletree telemetry datalogger recorded the inputs to the servos, and Phoenix ICE Lite electronic speed controllers recorded the motor power, rpm, and battery voltage throughout

the flight. Go-Pro Hero 2 cameras were attached to the outboard spines in later flights. For a detailed description of the instrumentation used in each flight, refer to APPENDIX D.

4.6.1.3 Static Aeroelastic Trim

A model of the X-HALE RRV-4 was created for UM/NAST from the properties of the assembled aircraft and its components, described in Table 4.4 and Table 4.5. The wings were modeled as fully flexible members while the pods, tail booms, ventral fins, and tails were treated as rigid components. The thrust of each motor was modeled as a time-dependent, body-fixed force acting at the pod locations. The elevators and center tail were modeled as fully movable control surfaces with degrees of freedom in pitch and roll directions, respectively. The ailerons were modeled as traditional, trailing edge control surfaces. The trim solution of the model was generated using only motor thrust and elevator angle as control inputs, as the ailerons are not used for trimming the aircraft during flight. For this configuration the trim solution body angle of attack, elevator angle, and motor thrust were calculated in UM/NAST, and the corresponding trimmed static tip deflection is also calculated. The results are summarized in Table 4.6.

4.6.1.4 Dynamic Aeroelastic Response

The RRV-4 is meant to be a well-behaved, well-controlled aircraft to facilitate pilot training and familiarization with flying a multi-engine, turn-by-yaw aircraft. However, the aircraft is still quite flexible, and experiences a 5% wing tip deflection under trimmed flight conditions. A modal analysis of the aircraft was conducted to verify that the low frequency rigid-body and elastic mode coupling is still present in the lower-aspect ratio configuration. The first seven elastic frequencies and their mode shapes are presented in Table 4.7 and Figure 4.33, respectively. A root locus plot of the elastic and rigid body mode shapes are given in Figure 4.34.While all of the frequencies are stable under trimmed conditions, the lowest mode – corresponding to coupled first wing bending and dutch roll has a very low damping ratio equivalent to $\zeta\omega_n = -0.5$. This suggests that this mode may be susceptible to instability caused by pilot induced oscillation, gusty conditions, or configuration changes.

Table 4.3. Airframe characteristics of the X-HALE RRV configurations

	RRV-4	RRV-6A	RRV-6B	
Wing span	4	6	6	m
Wing Chord	0.2	0.2	0.2	m
Planform Area	0.8	1.2	1.2	m^2
Aspect Ratio	20	30	30	--
Length	0.96	0.96	0.96	m
Propeller diameter	0.30	0.30	0.30	m
Max Gross Takeoff Weight	6.9	10.8	11.2	kg
C.G. (w.r.t leading edge)	23.5	33.1	38	% wing chord
Power/Weight	10.0	10.73	10.34	W/kg
Airspeed Range	12-20	14-18	14-18	m/s

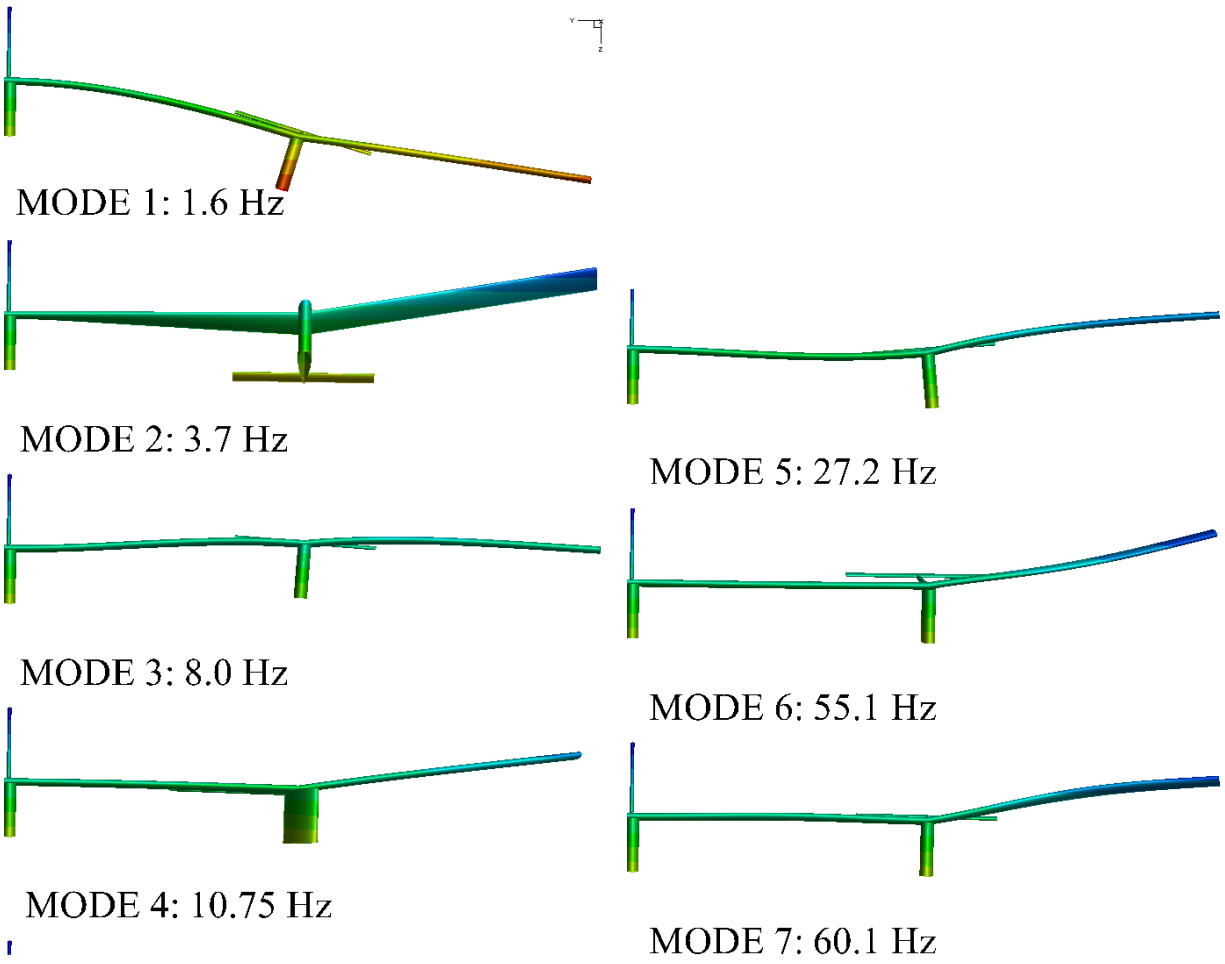

Figure 4.33. RRV-4 elastic half-span mode shapes

Table 4.4: List of the component properties of the X-HALE RRV-4 model[*]

	Wing	Boom	Tail	Pod	Units
Ref. axis location (from L.E.)	28.8	40.9	32.4	60.9	% chord
Center of gravity (from L.E.)	43.5 (m) 39.5 (d)[†]	40.9	25.0	25.0	% chord
Incidence Angle	5	n/a	0	0	deg.
Chord length / Diameter	0.20	0.024 (f) 0.013 (r)[‡]	0.11	0.37	m
Mass per unit span (m)	0.339 (m) 0.426 (d)	0.0429	0.2614	--	kg/m
Rotation Inertia (I_{xx})	5.74×10^{-4}	$2.91\times^{10\text{-}4}$	$1.60\times^{10\text{-}4}$	--	kg-m
Out-plane Bend. Inertia (I_{yy})	4.06×10^{-2}	1.46×10^{-9}	2.91×10^{-6}	--	kg-m
Out/In-plane Bend. Inertia (I_{yz})	*-6.49×10^{-4}*	*0*	*0*	--	kg-m
In-plane Bending Inertia (I_{zz})	3.94×10^{-2}	1.46×10^{-9}	1.57×10^{-4}	--	kg-m
Extensional Stiffness (k_{11})	*2.14×10^{6}*	--	--	--	N/m^2
Ext./Out-plane Bend. Stiffness (k_{13})	*1.54×10^{3}*	--	--	--	N/m^2
Ext./In-plane Bend. Stiffness (k_{14})	*-4.91×10^{4}*	--	--	--	N/m^2
Torsional Stiffness (k_{22})	56	--	--	--	N/m^2
Out-plane Bend.Stiffness (k_{33})	1.13×10^{2}	--	--	--	N/m^2
Out/In-plane Bend. Stiffness (k_{34})	*-46.34*	--	--	--	N/m^2
In-plane Bend. Stiffness (k_{44})	*6.35×10^{3}*	--	--	--	N/m^2

[*] The values that are italicized correspond to values that are taken from the design,[30,61] and all other values were measured.
[†] (m): main wing, (d): dihedral wing
[‡] (f): front, (r): rear

Table 4.5: List of the concentrated inertias of the X-HALE RRV-4 model*

	Inboard Pods		Center Pod		
	Payload	Pod Assembly	Payload	Pod Assembly	Units
mass	0.548	0.929	0.8046	1.046	kg
x_{cg}	0.01	2.14×10^{-3}	0	3.97×10^{-3}	m
y_{cg}	0.09	4.0×10^{-2}	0.1	6.12×10^{-2}	m
z_{cg}	0	7.81×10^{-2}	0	7.52×10^{-2}	m
I_{xx}	*9.13×10^{-4}*	*1.134×10^{-2}*	*6.24×10^{-4}*	*1.476×10^{-2}*	kg-m^2
I_{yy}	*4.57×10^{-4}*	*3.21×10^{-3}*	*3.12×10^{-4}*	*2.82×10^{-3}*	kg-m^2
I_{zz}	*4.57×10^{-4}*	*8.48×10^{-3}*	*3.12×10^{-4}*	*2.50×10^{-4}*	kg-m^2
I_{xy}	*0*	*-1.21×10^{-3}*	*0*	*2.32×10^{-4}*	kg-m^2
I_{xz}	*0*	*1.06×10^{-5}*	*0*	*2.27×10^{-3}*	kg-m^2
I_{yz}	*0*	*4.59×10^{-5}*	*0*	*4.50×10^{-4}*	kg-m^2

*The values that are italicized correspond to values that are taken from the design,[30,61] and all other values were measured.

Table 4.6.Trim parameters for the RRV-4

Trim Parameter	Trim Point	Unit
Speed	14.5	m/s
Angle of Attack	0.03	deg
Sideslip Angle	0.25	deg
Thrust/Motor	5.78	N
Elevator Deflection	1.26	degrees
Differential Thrust Offset	0.42	N
Wingtip Displacement	5	% semispan

Table 4.7. Elastic mode frequencies for the RRV-4

Mode #	Frequency (Hz)	Mode Shape
1	1.60	1 Out-of-Plane (OP) Bending
2	3.70	1 Torsion (T)
3	7.97	1 OP+1T
4	10.74	1 In-plane (IP) Bending
5	27.20	2 OP + 1T
6	55.14	2T
7	60.11	T+IP

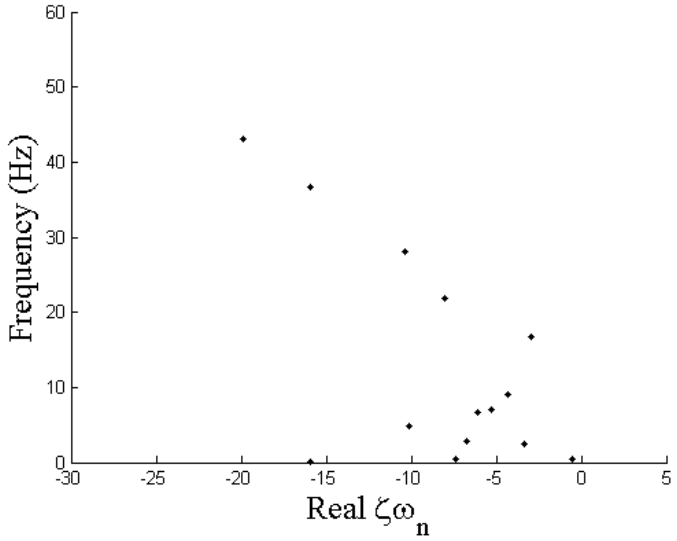

Figure 4.34. Root locus for RRV-4 elastic and rigid body modes

4.6.2 The X-HALE ATV-A (RRV-6A)

Following the successful flight tests of the RRV-4, two wing segments, motor pods, and horizontal tails were added to the aircraft to create the six-meter risk reduction configuration, the RRV-6A. This section details the airframe properties and instrumentation of this RRV configuration the fully instrumented counterpart, the ATV-A.

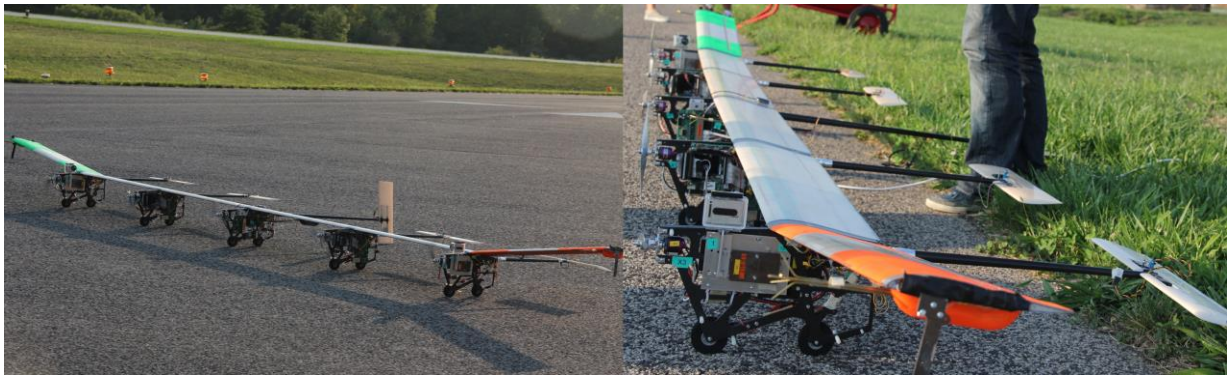

Figure 4.35. The X-HALE ATV-A

4.6.2.1 ATV-A Instrumentation

The instrumentation and design of the original X-HALE Aeroelastic Test Vehicle (ATV-A) is described in detail by Cesnik and Senatore[30]. A brief summary of that configuration is reviewed here.

The X-HALE ATV-A is equipped with a suite of sensors to measure its rigid body motion, including position, velocity, orientation, and angular velocity, as well as the wing deformation during flight. The orientation and angular velocity of the center pod is measured by a MIDG series INS/GPS system at 50 Hz. This measurement provides a reference body frame for all spanwise measurements. The MIDG also provides the aircraft's GPS location, velocity, and course heading. Three five-hole pressure probes measure the forward velocity, angle of attack, and sideslip angle relative to the oncoming wind at the center of the aircraft and each wingtip. The probe in the center of the aircraft is placed 0.5 meters to the left of the center motor pod to avoid flow disturbances from the propellers.

The wing deformation during flight is monitored by sets of strain gage bridges distributed along the wing. The strain gages are embedded in the foam core of the wing box, thus they are integral to the structure of the aircraft. At each measurement station along the wing, three strain gage bridges are used to measure out-of-plane (OP) bending, in-plane (IP) bending, and wing torsion.

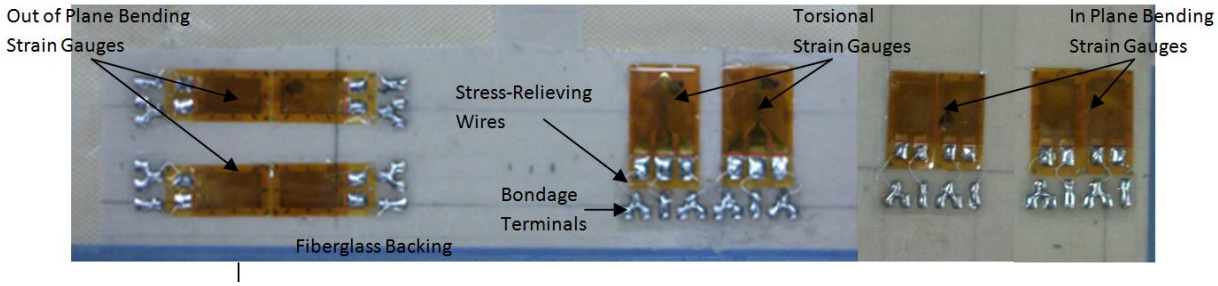

Figure 4.36. Strain gage orientation for X-HALE ATV-A

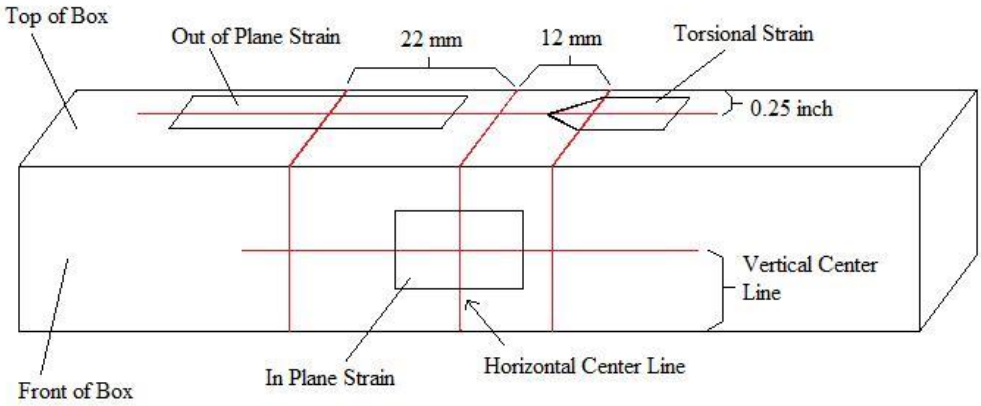

Figure 4.37. Strain gage bridge placement for X-HALE ATV-A

The OP strain gages are embedded on the top and bottom of the wing, and gages are oriented end-to-end as shown in Figure 4.36 with the centerline of the gages aligned with the centerline of the wingbox, which corresponds to the wing elastic axis. The IP strain gages are embedded on the leading edge and trailing edge of the wing box, and they are placed side-by-side, with center line aligned with the wing elastic axis. Torsional rosettes are also placed on the top and bottom of the wing box, with the centerline of each rosette aligned with the wing elastic axis.

Four 16-channel Diamond Systems Athena II PC104 augmented with a 16-channel input/output expansion cards are used for data acquisition. The Athena II syncs the timing of the analog and digital sensors and provides storage for the both types of data. There is no signal conditioning performed in the Athena II, so the outputs of the strain gage bridges, which measure in the millivolt range, are amplified before being transmitted for recording.

The ATV-A is radio-controlled using a 9-channel 2.4 GHz JR transmitter and receiver. The transmission and receipt of R/C signals are independent from the sensor data acquisition system. However, the servo commands, are transmitted and recorded at 50 Hz with the data from the science sensors. The ATV-A is also equipped with a 900MHz wireless modem which allows the status of the aircraft sensors and R/C system to be monitored via groundstation by the flight team. The wireless link also allows the flight team to remotely control the start, stop, and download of sensor data stored on the Athena II.

There are five independent control inputs to the aircraft: main throttle, differential thrust, ailerons, elevator, and center tail. Main throttle and differential thrust are provided by the five motors. The motors assigned as differential thrust provide the most authority for achieving and maintaining lateral and directional trim. Ailerons are used to provide additional roll authority and to excite lateral maneuvers. The four horizontal tails act as fully moveable elevons, and are used primarily for climb during takeoff. The aircraft's longitudinal balance is such that a neutral elevator input is enough to trim the aircraft angle of attack. The center tail also acts as a fixed elevator in its horizontal position, and it can also be rotated into a vertical configuration to augment the aircraft's recovery from lateral test maneuvers.

4.6.2.2 RRV-6A Instrumentation

The lightly instrumented X-HALE RRV-6A is also radio-controlled using a 9-channel 2.4 GHz transmitter and receiver system, and the control inputs are identical to the ATV-A. The aircraft is equipped with an Eagletree telemetry data logging system. This system records the servo pulse width modulation (PWM) commanded by the pilot, and the GPS position, speed, and aircraft heading. Selected sensor readings, including speed and altitude, are transmitted in real time to a handheld wireless display to aid the test team in decision-making during the flight.

In addition to the data recorded by the Eagletree system, the X-HALE RRV-6A is outfitted with two other sources of data capturing. Each motor is equipped with a 50-W Castlelink electronic speed controller that regulates and records motor shaft rpm, temperature, battery voltage, input current, and commanded power levels as a percentage of maximum motor output. Two center-facing GoPro Hero 2 cameras are installed in the outboard spines to record the motion of the aircraft during flight. Moreover, team members on the ground also record high definition video of the flight in an attempt to capture different aspects of vehicle flight behavior.

4.6.2.3 Configuration Summary

This section summarizes the properties of the X-HALE components used in the RRV-6A configuration. Table 4.8 details the geometry and cross-sectional inertias of the primary aircraft structure, as well as the elements of the wing stiffness matrix. The origin of each local reference axes is given, and the positive *x,y,z* axes point towards the right wingtip, toward the wing leading edge, and vertically upward, respectively. Table 4.9 lists properties of the concentrated inertias used to model additional aircraft components. The X-HALE RRV with elongated center tail and ventral fins is shown during takeoff in Figure 4.38. Figure 4.3 illustrates the positioning footnotes used in Table 4.4 and Table 4.5.

Figure 4.38: X-HALE RRV-6A with elongated center tail and ventral fins showing large wing deflections during takeoff

4.6.2.4 Static Aeroelastic Trim

A model of the X-HALE RRV-6A was created for UM/NAST from the properties of the assembled aircraft and its components, described previously in Table 4.8 and Table 4.9. The wings were modeled as fully flexible members while the pods, tail booms, ventral fins, and tails were treated as rigid components. The thrust of each motor was modeled as a time-dependent, body-fixed force acting at the pod locations. The elevators and center tail were modeled as fully movable control surfaces with degrees of freedom in pitch and roll directions, respectively. The ailerons were modeled as traditional, trailing edge control surfaces. The trim solution of the model was generated using only motor thrust and elevator angle as control inputs, as the ailerons are not used for trimming the aircraft during flight.

For this configuration the trimmed body angle of attack, elevator angle, and motor thrust were calculated in UM/NAST at the instantaneous flight speed immediately before the aileron inputs were applied. The corresponding trimmed static tip deflection is also calculated. The results are summarized in Table 4.10.

When trimmed at the same speeds, the larger aircraft produces more drag, thus the RRV-6A requires more thrust per motor compared to the RRV-4. The angle of attack is also adjusted to generate more lift for the heavier configuration. The resultant increased aerodynamic loading, combined with the longer, more flexible wing, results in a higher wingtip displacement when compared to the RRV-4.

4.6.2.5 Dynamic Aeroelastic Response

The X-HALE is designed to have a marginally stable, but controllable dutch roll within its flight envelope. The modal analysis of the aircraft, performed with a clamped boundary condition at the center, is shown in Figure 4.39. There is only one elastic mode below 1 Hz, and that mode is the first out-of-plane wing bending mode with little to no torsional component.

However, as Figure 4.40 shows, when free-flight conditions are considered and rigid body motion is allowed, there are two rigid body modes below 1-Hz, and both have significant levels of both bending and torsion. The mode with the lowest damping is a 0.4-Hz dutch roll-type mode, lightly coupled with wing bending and torsion. The phugoid mode occurs at 0.78-Hz and is strongly coupled with wing bending and a smaller torsion component. From this analysis, it is anticipated that flight tests of the RRV-6 will exhibit all of the desired behavior from the X-

HALE design, including large wing deformation during maneuvers, significant elastic-flight dynamic mode coupling, and a stable but controllable dutch roll.

Table 4.8: List of the component properties of the X-HALE RRV-6A model[§]

	Wing	Boom	Tail	Pod	Fin	Units
Ref. axis location (from L.E.)	28.8	40.9	32.4	60.9	50.0	% chord
Center of gravity (from L.E.)	25	40.9	25.0	25.0	50.0	% chord
Incidence Angle	5	n/a	0	0	0	deg.
Chord length / Diameter	0.20	0.024 (f) 0.013 (r)[**]	0.11	0.37	0.73(c) 0.485(o)[††]	m
Mass per unit span (m)	0.394	0.0429	0.2614	--	0.239	kg/m
Rotation Inertia (I_{xx})	8.09×10^{-4}	2.91×10^{-4}	1.60×10^{-4}	--	1.81×10^{-2}	kg-m
Out-plane Bend. Inertia (I_{yy})	1.22×10^{-5}	1.46×10^{-9}	2.91×10^{-6}	--	5.58×10^{-4}	kg-m
Out/In-plane Bend. Inertia (I_{yz})	*-6.49×10^{-4}*	*0*	*0*	--	*0*	kg-m
In-plane Bending Inertia (I_{zz})	7.97×10^{-4}	1.46×10^{-9}	1.57×10^{-4}	--	1.75×10^{-2}	kg-m
Extensional Stiffness (k_{11})	*2.14×10^{6}*	--	--	--	--	N/m^2
Ext./Out-plane Bend. Stiffness (k_{13})	*1.54×10^{3}*	--	--	--	--	N/m^2
Ext./In-plane Bend. Stiffness (k_{14})	*-4.91×10^{4}*	--	--	--	--	N/m^2
Torsional Stiffness (k_{22})	55.8	--	--	--	--	N/m^2
Out-plane Bend.Stiffness (k_{33})	1.04×10^{2}	--	--	--	--	N/m^2
Out/In-plane Bend. Stiffness (k_{34})	*-46.34*	--	--	--	--	N/m^2
In-plane Bend. Stiffness (k_{44})	*6.35×10^{3}*	--	--	--	--	N/m^2

[§] The values that are italicized correspond to values that are taken from the design,[30,61] and all other values were measured.
[**] (f): front, (r): rear
[††] (c): center, (o): outboard

Table 4.9: List of the concentrated inertias of the X-HALE RRV-6A model*

	Inboard Pods		Outboard Pods		Center Pod		
	Payload	Pod Assembly	Payload	Pod Assembly	Payload	Pod Assembly	Units
mass	0.548	0.929	0.571	1.046	0.375	1.046	kg
x_{cg}	0.01	2.14×10^{-3}	0.010	3.97×10^{-3}	0	3.97×10^{-3}	m
y_{cg}	0.09	4.0×10^{-2}	0.0941	6.12×10^{-2}	0.1	6.12×10^{-2}	m
z_{cg}	0	7.81×10^{-2}	0	7.52×10^{-2}	0	7.52×10^{-2}	m
I_{xx}	9.13×10^{-4}	1.134×10^{-2}	9.52×10^{-4}	1.134×10^{-2}	6.24×10^{-4}	1.476×10^{-2}	kg-m^2
I_{yy}	4.57×10^{-4}	3.21×10^{-3}	4.76×10^{-4}	3.21×10^{-3}	3.12×10^{-4}	2.82×10^{-3}	kg-m^2
I_{zz}	4.57×10^{-4}	8.48×10^{-3}	4.67×10^{-4}	8.48×10^{-3}	3.12×10^{-4}	2.50×10^{-4}	kg-m^2
I_{xy}	*0*	*-1.21×10^{-3}*	*0*	*-1.21×10^{-3}*	*0*	*2.32×10^{-4}*	kg-m^2
I_{xz}	*0*	*1.06×10^{-5}*	*0*	*1.06×10^{-5}*	*0*	*2.27×10^{-3}*	kg-m^2
I_{yz}	*0*	*4.59×10^{-5}*	*0*	*4.59×10^{-5}*	*0*	*4.50×10^{-4}*	kg-m^2

*The values that are italicized correspond to values that are taken from the design,[30,61] and all other values were measured.

Table 4.10. Trim parameters of the X-HALE RRV-6A

Trimmed Parameter	Trim Point 1	Trim Point 2	Unit
Flight Speed	16	17.6	m/s
Body Angle of Attack	-0.47	-1.51	deg
Sideslip Angle	0.19	0.19	deg
Motor Thrust	6.96	8.37	N
Elevator Deflection Angle	-0.74	-1.68	degrees
Differential Thrust Offset	0.47	0.59	N
Static Tip Deflection	9.11	9.28	% semispan

Table 4.11. Mode shapes and frequencies of the RRV-6A

Mode #	Frequency (Hz)	Mode Shape
1	0.59	1 Out-of-Plane (OP) Bending
2	2.39	1 Torsion (T)
3	3.63	2 OP+2T
4	4.06	2 OP+2T + 1 In-plane (IP) Bending
5	6.11	3 OP + 2T
6	8.17	3 OP+ 3T
7	23.71	4 OP + 4T

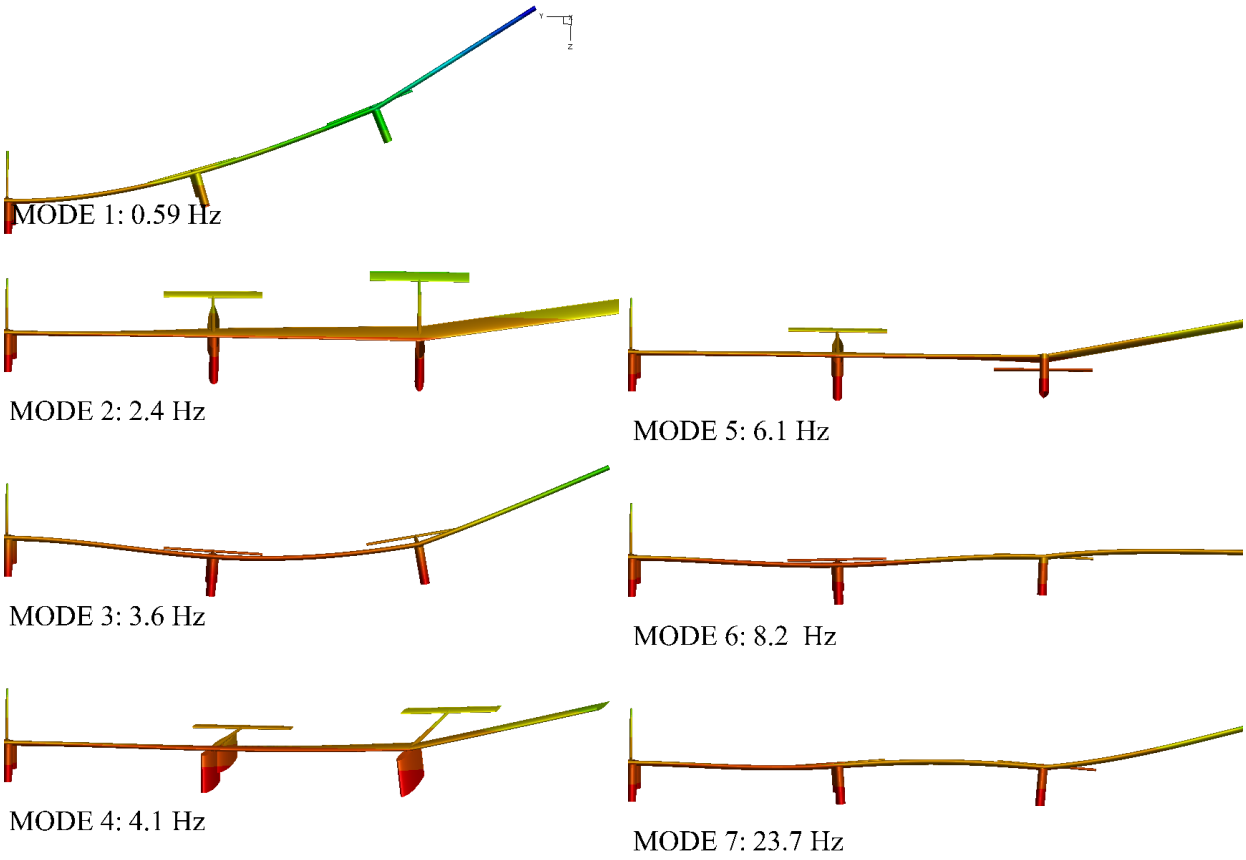

Figure 4.39. RRV-6A elastic half-span mode shapes

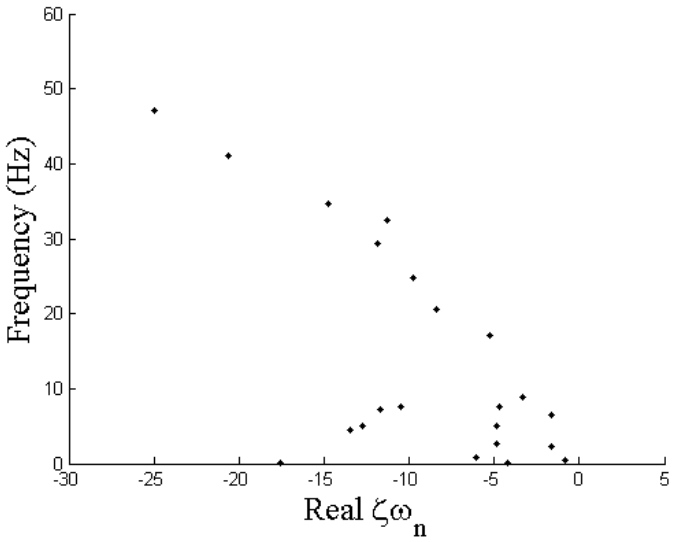

Figure 4.40. Root locus of the RRV-6A elastic and rigid body modes

4.6.3 The X-HALE ATV-B (RRV-6B)

The design of the second generation X-HALE ATV-B was motivated by the operational challenges encountered during ground tests of the X-HALE RRV-6B and ATV-A configurations. The ATV-A wings were constructed with strain gage bridges embedded along the wingbox to measure the in-plane, out-of-plane, and torsional deformation of the wing during flight. This strain gage setup worked well within the lab environtment, however, each bridge needed to be balanced by hand before flight. Additionally, the heat sensitivity of the strain gages became a significant factor during flight tests. Half of the strain gages that composed the out-of-plane bending and torsion bridges were installed on the top of the wing box, thus exposed to direct sunlight. However, the other half of the of the strain gage bridge was installed on the underside of the wingbox, which remained in shade and considerably cooler than the upper side. Although the changes due to temperature would be very small, it would introduce significant noise into the system that would possibly alter or even obscure completely the microstrain measurements due to wing bending. These issues led to the decommissioning of the X-HALE ATV-A after ground and taxi testing, and a more robust wing shape measurement system was sought. The redesigned X-HALE aircraft is known as the X-HALE ATV-B, and the instrumentation and updated airframe parameters are described in this section.

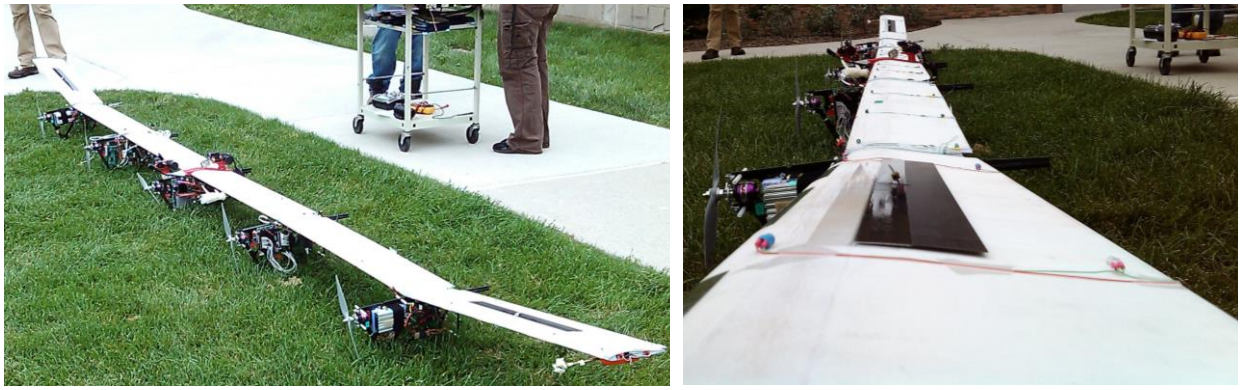

Figure 4.41. The second generation X-HALE ATV-B (shown without tails)

4.6.3.1 ATV-B Instrumentation

The X-HALE ATV-B rigid body states, consisting of position, velocity, orientation, and angular velocity are measured using a diverse set of sensors. The orientation and angular velocity of the center pod, assumed to correspond to the aircraft's rigid body motion, is measured by a

MIDG series INS/GPS system at 50 Hz. The MIDG also provides the aircraft's GPS location, velocity, and course heading. Four VectorNav VN-100 Rugged IMUs, mounted in each outboard motor pod, provide local measurements of linear acceleration, angular orientation, and angular rate. The output frequency is set to 50 Hz. Three five-hole pressure probes measure the forward velocity, angle of attack, and sideslip angle relative to the oncoming wind at the center of the aircraft and each wingtip. The probe in the center of the aircraft is placed 0.5 meters to the left of the center motor pod to avoid flow disturbances from the propellers. One 16-channel Diamond Systems Athena II PC104 is used for data acquisition. The Athena II syncs the timing of the analog and digital sensors and provides storage for the both types of data.

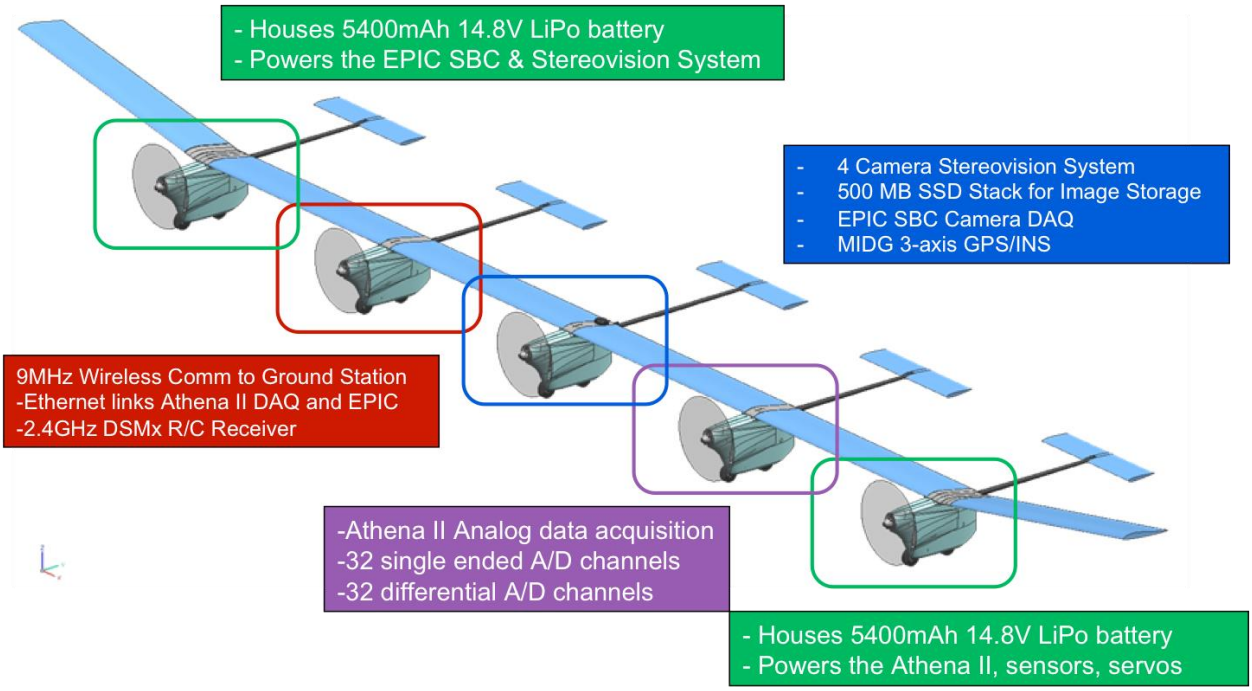

Figure 4.42. Instrumentation diagram of the X-HALE ATV-B

As with previous X-HALE configurations, the ATV-B is radio-controlled using a 9-channel 2.4 GHz JR transmitter and receiver. The transmission and receipt of R/C signals is independent from the sensor data acquisition system. However, the servo commands, are transmitted and recorded at 50 Hz with the data from the science sensors. The ATV-B is also equipped with a 900MHz wireless modem which allows the status of the aircraft sensors and R/C system to be monitored via groundstation by the flight team. The wireless link also allows the flight team to remotely control the start, stop, and download of some sensor data stored on the Athena II.

There are five independent control inputs to the aircraft: main throttle, differential thrust, differential roll spoiler, elevator, and center rudder. Main throttle and differential thrust are provided by the five motors, with the combination of programmed for each flight depending on the needs for planned maneuvers. The motors assigned as differential thrust provide the most authority for achieving and maintaining lateral and directional trim. Rather than traditional ailerons, roll spoilers located in the center of the dihedral wingtip segments dump lift when actuated, reducing the probability of wing twist resulting in control surface reversal and adverse yaw. The roll spoilers provide roll authority for coordinated turns and excitation of unstable lateral dynamic modes. The four horizontal tails act as fully moveable elevons, and are used for climb. The center tail is used to augment the aircraft's lateral damping during recover from test maneuvers.

Measurements of wing bending and twist during flight are crucial to validating the aeroelastic modeling capabilities of UM/NAST. Several methods of measuring the wing shape were considered and a tradeoff analysis showed that a stereovision-based wing shape measurement system was the best option for this application. Two pairs of high-resolution Flea3 camera were stationed in the center of the aircraft facing the wingtips. These cameras record the locations of eighteen sets of LEDs distributed along the span of the aircraft during flight. The cameras are synchronized using a hardware trigger, where the triggering TTL signal is generated by the Athena II. An EPIC single board computer coordinates the high-bandwidth download of the images from the cameras to two 256 GB solid-state hard drives. Status updates for each camera are transmitted from the EPIC to the groundstation via the Athena II and wireless modem. For additional details on the sterovision system design and calibration, refer to the workd by Pang et al.[60]

4.6.3.2 RRV-6B Instrumentation

The addition of the stereovision measurement system resulted in a significant change to the aircraft weight distribution when compared to the previous configurations, so a second set of flight tests with a lightly instrumented airframe were conducted to assess the flight handling qualities of this updated aircraft configuration. This configuration, known as the RRV-6B, is equipped with a Pixhawk autopilot and telemetry system located in the center motor pod. The Pixhawk system records the GPS position and speed as well as the aircraft orientation and body

rates and transmits the information in real time to a monitored ground station. The autopilot function is used to record the pilot commands as well as execute testing maneuvers via pre-determined servo actuation. Two Go-Pro Hero 2 cameras mounted on the outboard motor pods allow visual observation of the wing deformation during flight.

4.6.3.3 Configuration Summary

The RRV-6B is designed to be aeroelastically representative of the X-HALE ATV-B. This section summarizes the properties of the X-HALE components used in the RRV-6B configuration. The geometry of the airframe is identical to the RRV-6A, and shown in APPENDIX B. Table 4.12 details the geometry and cross-sectional inertias of the primary aircraft structure, as well as the elements of the wing stiffness matrix. The origin of each local reference axes is given, and the positive *x,y,z* axes point towards the right wingtip, toward the wing leading edge, and vertically upward, respectively.

Table 4.13 lists properties of the concentrated inertias used to model additional aircraft components. Figure 4.3 illustrates the definition of the positioning footnotes used in Table 4.12 and Table 4.13.

4.6.3.4 Static Aeroelastic Trim

A model of the X-HALE RRV-6B was created for UM/NAST from the properties of the assembled aircraft and its components, described in Table 4.12 and Table 4.13. The wings were modeled as fully flexible members while the pods, tail booms, ventral fins, and tails were treated as rigid components. The thrust of each motor was modeled as a time-dependent, body-fixed force acting at the pod locations. The elevators and center tail were modeled as fully movable control surfaces with degrees of freedom in pitch and roll directions, respectively. The roll spoilers were modeled as control surfaces with 100% differential deflection, meaning that only one spoiler deployed at a time, and only in the upward direction. The trim solution of the model was generated using only motor thrust and elevator angle as control inputs, as the roll spoilers are not used for trimming the aircraft during flight. Lateral trim is achieved by introducing a differential thrust offset value to the outboard motors.

For this configuration, the trim solution body angle of attack, elevator angle, and motor thrust were calculated in UM/NAST at three different flight speeds. The corresponding trimmed static tip deflection is also calculated. The results are summarized in Table 4.14.

4.6.3.5 Dynamic Aeroelastic Response

The updated instrumentation package of the ATV-B resulted in a heavier vehicle with a center of gravity that is shifted over 6% toward the rear of the aircraft. The stereovision system in the center pod also changed the weight distribution from relatively symmetric and span-loaded in the ATV-A/RRV-6A to asymmetric and more concentrated in the center of the vehicle (ATV-B/RRV-6B). This configuration is similar in a sense to the final configuration of the Helios, which had a slow, but unstable Phugoid mode that, when left to develop, resulted in structural failure and the loss of the vehicle.

The X-HALE RRV-6B is very flexible, and experiences ~18.5% wing tip deflection under trimmed flight conditions. A modal analysis of the aircraft was conducted to determine the new elastic frequencies and to evaluate how the change in mass distribution affected the elastic and flight dynamic mode coupling. The first seven elastic frequencies and their mode shapes are presented in Table 4.15 and Figure 4.44, respectively. A root locus plot of the elastic and rigid body mode shapes are given in Figure 4.45.

As expected, the increased mass of the aircraft significantly lowered the elastic mode frequencies, however it did not destabilize the aircraft. All of the modes are stable, and the lowest mode, corresponding to coupled first wing bending and phugoid, has a very low damping ratio equivalent to $\zeta\omega_n$ = -0.5. This suggests that, like the RRV-6A, this model may be susceptible to instability caused by pilot induced oscillation, gusty conditions, or configuration changes.

Figure 4.43. X-HALE ATV-B LED markers for the stereovision wing shape measurement system

Table 4.12: List of the component properties of the X-HALE RRV-6B model[‡‡]

	Wing[§§,***]	Boom	Tail	Pod	Fin	Units
Ref. axis location (from L.E.)	28.8	50	25	60.9	50.0	% chord
Center of gravity (from L.E.)	43.5($m_{i/o}$) 39.5(d)	34(i/o) 44(c)	25	25.0	50.0	% chord
Incidence Angle	5	0	0	0	0	deg.
Chord length / Diameter	0.20	0.024 (f) 0.013 (r)	0.11	0.37	0.76 (c) 0.485 (i)	m
Mass per unit span (m)	0.438 (m_i) 0.361 (m_o) 0.428 (dih)	0.07	0.24	--	0.1 (c) 0.09 (i)	kg/m
Rotation Inertia (I_{xx})	6.54×10^{-4} 5.81×10^{-4} 6.4×10^{-6}	2.17×10^{-5}	1.71×10^{-4}	--	4.01×10^{-4} 1.63×10^{-4}	kg-m
Out-plane Bend. Inertia (I_{yy})	1.34×10^{-2} 1.19×10^{-2} 1.31×10^{-2}	1.79×10^{-3}	1.10×10^{-4}	--	5.98×10^{-3} 2.43×10^{-3}	kg-m
In-plane Bending Inertia (I_{zz})	2.07×10^{-2} 1.84×10^{-2} 2.02×10^{-2}	1.79×10^{-3}	5.97×10^{-3}	--	1.27×10^{-2} 2.27×10^{-3}	kg-m
Extensional Stiffness (k_{11})	*2.14×10^{6}*	--	--	--	--	N/m^2
Torsional Stiffness (k_{22})	57 ($m_{i/o}$) 54 (d)	--	--	--	--	N/m^2
Out-plane Bend.Stiffness (k_{33})	1.05×10^{2} 0.79×10^{2}	--	--	--	--	N/m^2
In-plane Bend. Stiffness (k_{44})	*6.35×10^{3}*	--	--	--	--	N/m^2

[‡‡] The values that are italicized correspond to values that are taken from the original design,[30,61] and all other values were measured.
[§§] (m): main wing, (dih): dihedral wing
[***] (c): center , (o): outboard, (i): inboard, (f): front, (r): rear

Table 4.13: List of the concentrated inertias of the X-HALE RRV-6B motor pods*

	Inboard Pods		Outboard Pods		Center	
	Left	Right	Left	Right	Pod	Units
mass	0.989	0.959	1.265	1.324	3.29	kg
x_{cg}	3.55×10^{-3}	5.95×10^{-3}	4.51×10^{-3}	4.51×10^{-3}	-6.7×10^{-4}	m
y_{cg}	6.9×10^{-2}	7.0×10^{-2}	8.40×10^{-2}	8.70×10^{-2}	5.4×10^{-2}	m
z_{cg}	-4.45×10^{-2}	-5.15×10^{-2}	-4.25×10^{-2}	-2.85×10^{-2}	-8.15×10^{-2}	m
I_{xx}	1.34×10^{-2}	1.30×10^{-2}	1.73×10^{-2}	1.17×10^{-2}	2.02×10^{-2}	kg-m^2
I_{yy}	2.61×10^{-3}	1.56×10^{-3}	3.81×10^{-3}	3.61×10^{-3}	3.27×10^{-3}	kg-m^2
I_{zz}	1.35×10^{-2}	1.02×10^{-2}	8.91×10^{-3}	9.22×10^{-3}	1.46×10^{-2}	kg-m^2
I_{xy}	*-1.21×10^{-3}*	*-1.21×10^{-3}*	*-1.21×10^{-3}*	*-1.21×10^{-3}*	*2.32×10^{-4}*	kg-m^2
I_{xz}	*1.06×10^{-5}*	*1.06×10^{-5}*	*1.06×10^{-5}*	*1.06×10^{-5}*	*2.27×10^{-3}*	kg-m^2
I_{yz}	*4.59×10^{-5}*	*4.59×10^{-5}*	*4.59×10^{-5}*	*4.59×10^{-5}*	*4.50×10^{-4}*	kg-m^2

*The values that are italicized correspond to values that are taken from the design,[30,61] and all other values were measured.

Table 4.14. Trim parameters of the RRV-6B

Trimmed Parameter	Trim Point 1	Trim Point 2	Trim Point 3	
Flight Speed	14	15	16	m/s
Body Angle of Attack	1.74	0.65	-0.22	deg
Sideslip Angle	0.31	0.31	0.30	deg
Motor Thrust	5.82	6.65	7.54	N
Elevator Deflection Angle	2.31	1.02	0.04	degrees
Differential Thrust Offset	0.38	0.45	0.53	N
Static Tip Deflection	18.57	18.50	18.46	% semispan

Table 4.15. Elastic frequencies of the RRV-6B

Mode #	Frequency (Hz)	Mode Shapes
1	0.60	1 Out-of-Plane (OP) Bending
2	1.60	1 Torsion (T)
3	3.52	2 OP+2T
4	4.30	2 OP+2T + 1 In-plane (IP) Bending
5	4.73	3 OP + 2T + 1IP
6	7.81	3 OP+ 3T
7	10.90	4 OP + 3T

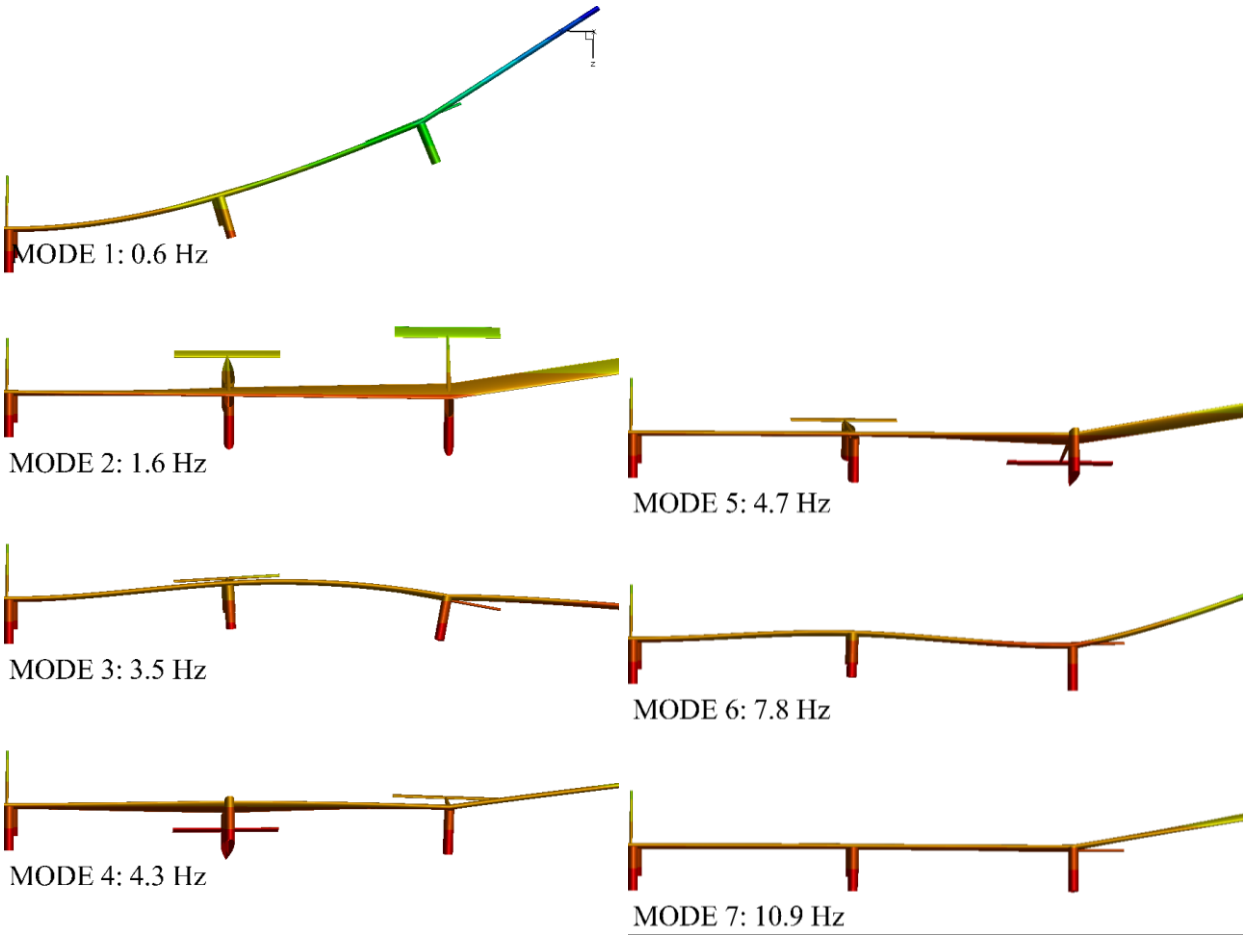

Figure 4.44. RRV-6B elastic half-span mode shapes

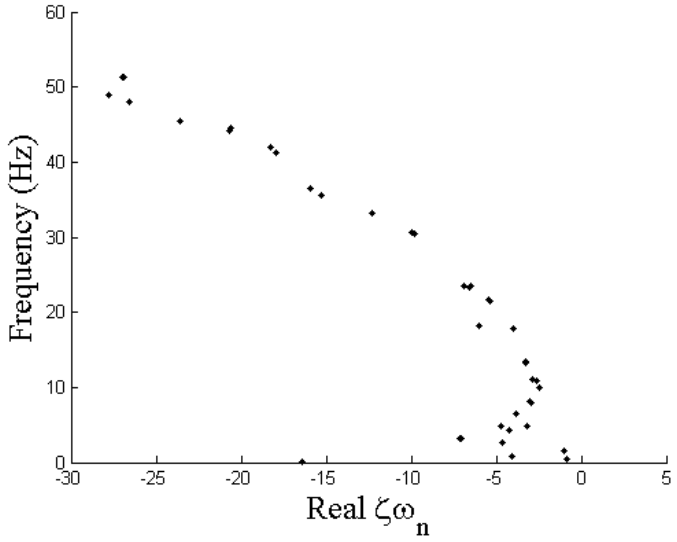

Figure 4.45. Root locus for RRV-6B elastic and rigid body modes

4.7 Concluding Remarks

This chapter presented the design and characterization of three X-HALE configurations. Each configuration has similar structural and aerodynamic parameters, but the mass and inertia distributions varies between configurations due to the instrumentation payload used on each. Aeroelastic simulations of the trim response of each configuration confirms that they exhibit considerable deformation in trim, ranging from 5% of the semispan in the 4-m span configuration to 18% in the heaviest 6-m configuration. All three configurations are expected to be stable during trimmed flight, and all possess a lightly damped low frequency elastic-coupled rigid body mode that can be excited during flight.

There was no characterization of structural damping presented in the data from this chapter. The UM/NAST models use an arbitrarily chosen 2% stiffness-proportional damping. A ground vibration test of the aircraft is required to determine if this level of damping is sufficient to accurately capture the aircraft structural dynamics. The work in progress for this GVT is discussed in the future work recommendations of CHAPTER 7.

CHAPTER 5. Flight Test Data of the X-HALE Aeroelastic Testbed

This chapter presents the data gathered during flight tests of the X-HALE Aeroelastic Testbed. Three X-HALE configurations that have been flown: the RRV-4, RRV-6A, and RRV-6B. An overview of the activities undertaken during a typical flight test day is presented. Observations and lessons learned from each configuration are discussed, and data from a representative flight test of each is presented. These RRV configurations are lightly instrumented, and varying quality of in-flight data was gathered. The data, when available, is used to confirm the presence of designed flight dynamic behavior.

5.1 Overview of Flight Tests

In a typical test flight day, the aircraft is partially assembled before transporting it to the field. In the four-meter long configuration, each half of the aircraft is assembled in the lab. In the six-meter configurations, the two inboard wings are assembled with center and inboard motor pods, and the outboard and dihedral wings are assembled with the outboard motor pods. The two-meter long aircraft sections are then transported to the field for full aircraft assembly before flight. Once the sections are reattached, the tails are added and all wiring is connected. Servo and motor rpm tests are performed to verify each system's operation, and all data logging systems are cleared. The aircraft is carried into position on the runway, and the takeoff direction is chosen to minimize cross-wind.

Flights are all conducted outdoors on very calm days, with winds less than 7 mph (25% of airplane stall speed). Test flights were attempted in higher wind conditions, but, as seen with other VFA class aircraft, the atmospheric disturbance excited the marginally stable flight dynamic modes (roll-coupled yaw) and reduced the pilot's ability to control the aircraft response. The temperatures are also restricted to days above 40 degrees Fahrenheit so that pilot had full dexterity and the LiPo batteries discharged at full capacity.

Before takeoff, the aircraft is held by hand at the center leading edge, and the motors are brought to 100% power in this holding position. The motors are commanded together but actuated separately, each with its own battery and speed controller, so each motor reaches full throttle at slightly different times. This is a known characteristic of multi-engine aircraft. However, since X-HALE is a yaw-marginal aircraft and differential thrust provides the main yaw authority, the aircraft is held during takeoff to avoid exciting any unstable modes. Once the motors reach full power, the aircraft is released for takeoff. The aircraft's nominal testing altitude is 100-250 feet, which is high enough to allow recovery in the event of unexpected responses, but still within visible range of the pilot and flight crew. The aircraft field is bounded, so, once the aircraft reaches its testing altitude, racetrack loops or figure-eight patterns are flown for the duration of the flight test. When landing, similar wind conditions to take-off are desired. Once the aircraft is on the ground, the data is downloaded from its onboard instrumentation onto the ground station. If additional flights are scheduled, the motor batteries are swapped out and the aircraft is prepared for the next flight. If flight testing is completed for the day, the aircraft is disassembled into its transportable configuration and taken back to its storage location.

5.2 Flight Test Data from the RRV-4

The primary objective of the RRV-4 configuration was to provide a training opportunity for the pilot before progressing to the high-aspect-ratio, higher flexibility 6-m configurations. The wing cross-sectional stiffness was the same in all of the configurations, however, the RRV-4 had an aspect ratio closer to conventional aircraft rather than very flexible HALE aircraft. This aircraft was not expected to exhibit very large wing deformations during flight, but the excitable dutch-roll instability coupled with wing bending was anticipated to be present.

The data recorded during one RRV-4 flight is presented in Figure 5.1 through Figure 5.6.[*] The R/C pulse-width-modulation (PWM) commands to the aileron, elevator, and throttle are shown in Figure 5.1. These are the pilot commands used to to fly figure-eight loops around the flight field, and they were recorded using the Eagletree Datalogger. The GPS trajectory of the entire flight is shown in Figure 5.2. The red triangle indicates the starting position of the takeoff roll, and the blue square indicates the touchdown point. The body orientation and rates are given

[*] Data from X-HALE Flight #6 conducted on Oct 18, 2011

in Figure 5.4 through Figure 5.6. The GPS parameters, body orientation, and body rates were measured with a MIDG II GPS/INS system.

Table 5.1: Flight conditions at airfield for X-HALE RRV-4 test flight.

Temperature	65°F
Wind Direction and Speed	270,3-5 mph
Precipitation	None
Cloud Cover	Overcast

The takeoff roll begins at t~80 seconds, indicated by the increase in GPS speed and throttle shown in Figure 5.1 and Figure 5.3, respectively. The elevator is deployed a few seconds later to induce a nose-up pitching moment and the aircraft lifts off. After liftoff, a positive aileron command is given, which results in a roll to the left. The ailerons in this flight were programmed with 100% differential, where the ailerons were only allowed to deflect upward to initiate a roll. In previous flights, the RRV-4 experienced a strong adverse yaw. Any attempt to use the aileron to initiate the turn resulted in a very small roll response, followed by a strong opposite yaw tendency. Attempts were made to mitigate this effect by reducing the aileron throw, and finally moving to 100% differential.

Beyond this first turn, the ailerons are used minimally and turning authority is handled primarily by differential thrust, using the yaw-roll coupling to execute these maneuvers. Turns using differential thrust involved very high bank angles and considerable sideslipping, and yaw oscillations developed as a result. Increasing the flight speed helped to damp out these oscillations, however, power needed to be reduced to 80-90% in order to regain enough differential thrust authority to initiate another turn. This is due to the fact that at 100% motor power, a differential thrust command results in the inboard motor reducing in power, but no change in the other motors. When a turn is commanded at lower power, the outboard motor increases to its full authority (20% higher than sat. thrust) while the inboard motor reduces further, allowing greater authority during turns.

The cyclical response of the body rates shows the repeated turns that correspond to the GPS trajectory shown in Figure 5.2. The yaw-roll coupling is also evident in Figure 5.6, where the sinusoidal yaw motion is echoed in the roll angle response.

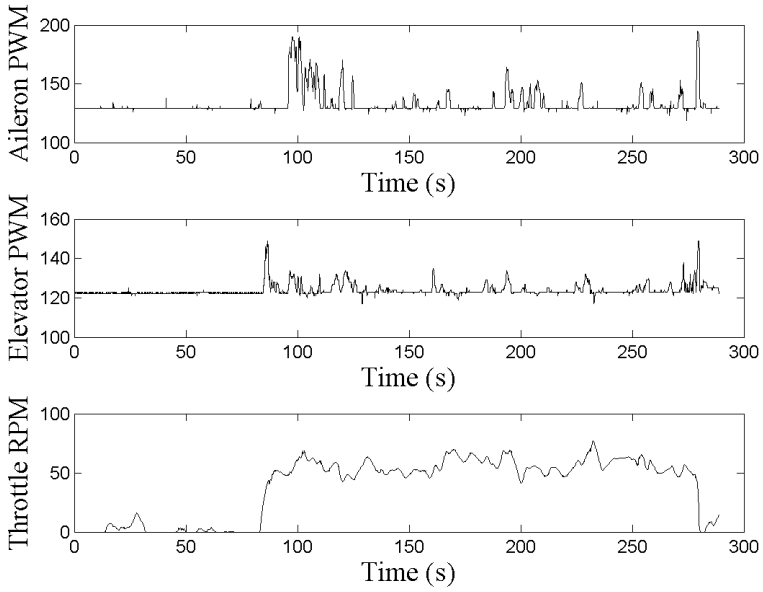

Figure 5.1. RRV-4 flight test: control inputs

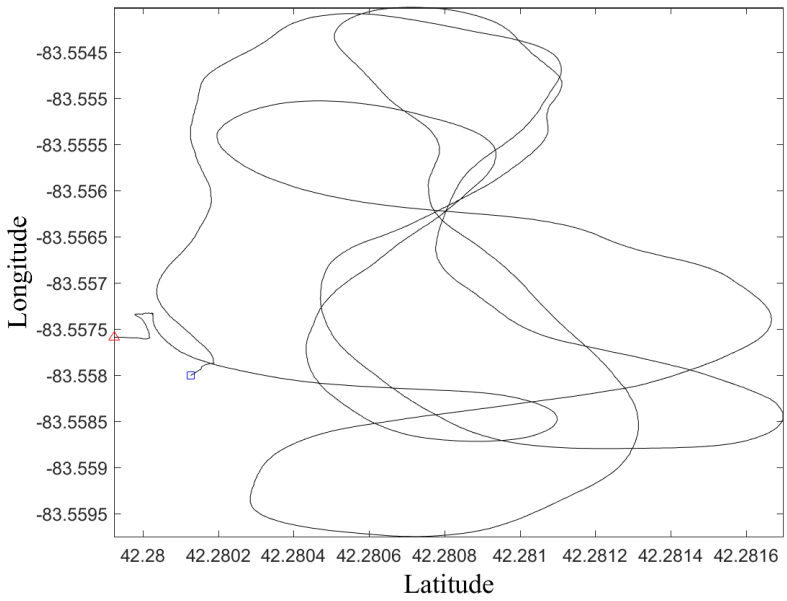

Figure 5.2. RRV-4 flight test: GPS trajectory

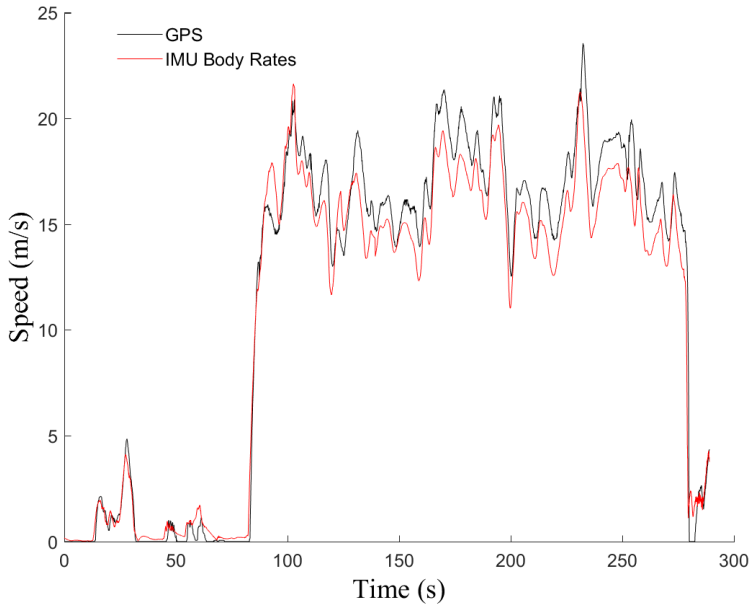

Figure 5.3. RRV-4 flight test: speed

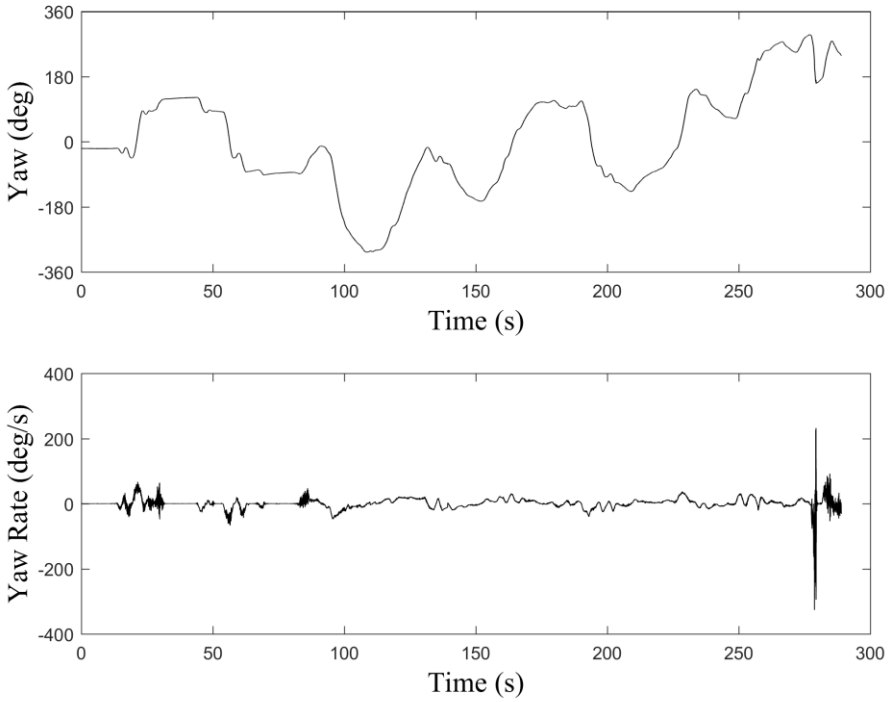

Figure 5.4. RRV-4 flight test: heading angle

The yaw rate is sinusoidal, as expected from a figure-eight trajectory. The roll rate also contains a low frequency sinusoidal response that corresponds to the yaw-roll coupling induced to turn, but there is also a higher frequency roll motion that corresponds to the marginally stable dutch roll identified in aeroelastic analysis. The low frequency turns also appear in the pitch angle, but the pitch response is a result of coupling between the degrees of freedom rather than a direct command.

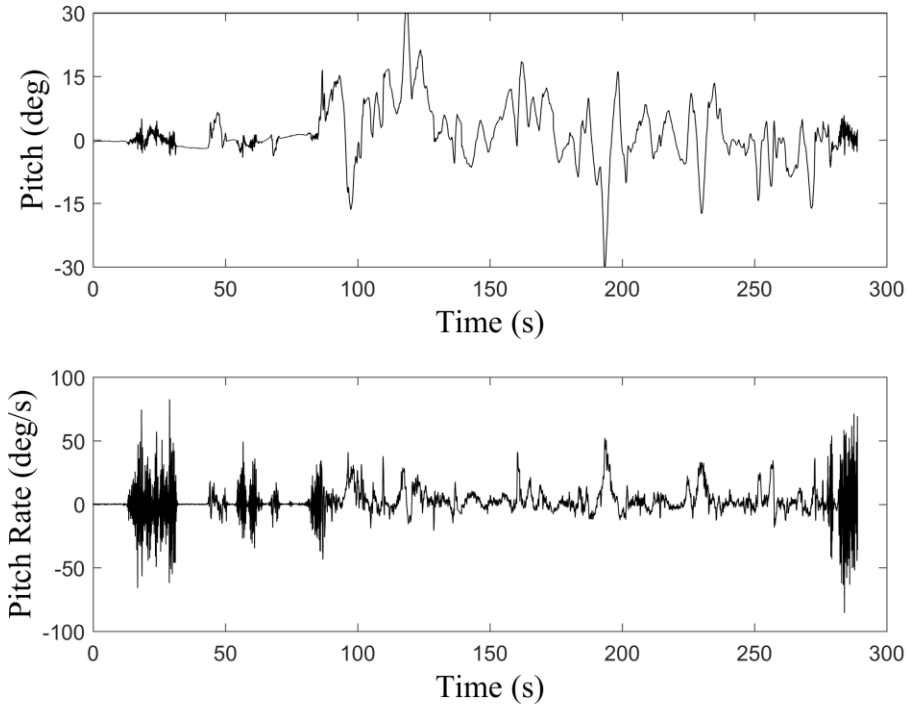

Figure 5.5. RRV-4 flight test: pitch angle

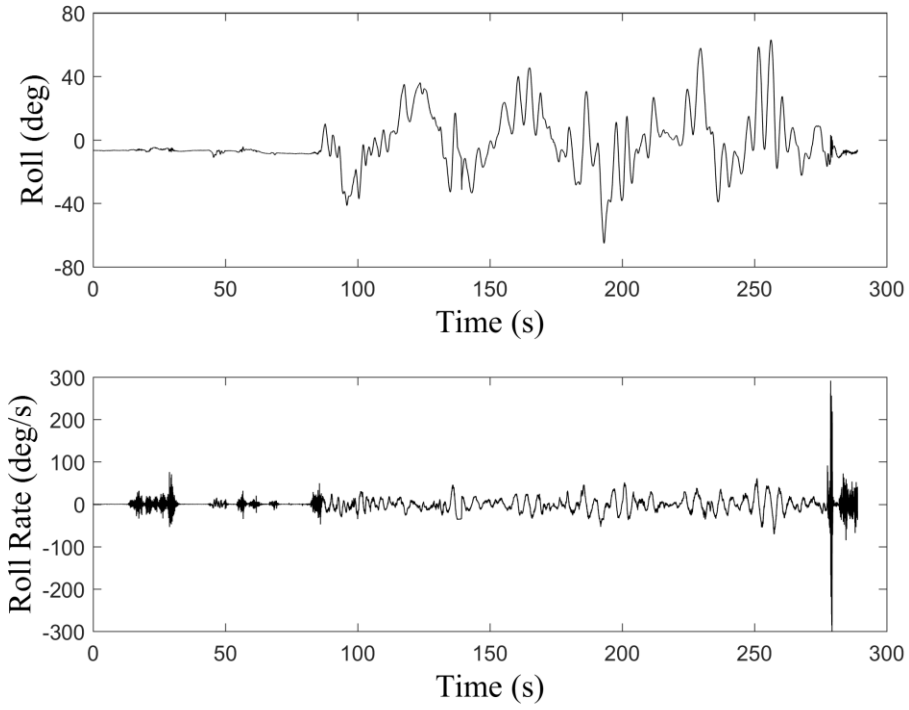

Figure 5.6. RRV-4 flight test: roll angle

5.3 Flight Test Data from the RRV-6A

Figure 5.7. RRV-6A during takeoff demonstrating large wing deformation

The X-HALE RRV-6A flight tests are the next step in the progression towards the test flights of the X-HALE ATV-A. The initial flight tests of the RRV-6A experienced the same challenges as the RRV-4 including aileron adverse yaw and rigid body oscillations when making a turn using differential thrust. However, the increased aspect ratio and flexibility of the aircraft exacerbated these effects.

In the RRV-4, the yaw oscillations were only present when excited by a turn or during the reduced velocity descent into landing. In the RRV-6A, the yaw oscillations were present throughout the flight, and much of the pilot's effort was devoted to damping out the oscillations

to maintain control of the aircraft. While these oscillations were manageable during flight, they became uncontrollable during the descent into landing.

As seen with the RRV-4, the aerodynamic damping available at full speed, combined with continuous pilot input, were needed to maintain a semblance of steady flight. When the speed is reduced, the associated aerodynamic damping is reduced, and the aircraft becomes uncontrollable. Pilot commands alone are not sufficient to stabilize the aircraft, and slight anticipations of delay in pilot input actually serve to intensitify the unstable response as they turn into pilot-induced oscillations. The RRV-6A was stable and controllable during flight, as expected, however, this configuration was un-landable. This was an unacceptable behavior for the ATV-A, as a hard landing would compromise the testbed capabilities of the aircraft. Any damage to the wings would likely damage the strain gages embedded in the wingbox, making them unusable for measuring deformation. A hard impact or roll-over during touchdown could also damage the computers used for data acquisition and result in the loss of the data gathered during flight.

A change to the configuration was made as a result of these findings. A longer center tail boom was added to increase the moment arm and thus, the effectiveness of the vertical tail[†]. This longer tail successfully eliminated most of the yaw oscillations experienced during flight. Flipping the tail to its horizontal position removed that source of damping so that they would not affect portions of the flight tests where measuring the unstable lateral modes was desired. The long tail was not able to reduce the oscillations during descent and landing to a manageable level, so an additional source of yaw damping was sought.

Increasing the vertical surface area was the most straightforward way to improve the aircraft's lateral stability. Conventional aircraft design suggests that increasing the wing dihedral will provide additional lateral stability. To achieve this higher dihedral, the ballast masses on the two outboard spines were removed and transferred to the inboard spines, keeping the mass and c.g. of the aircraft the same but creating a more center-loaded mass distribution[‡]. The increase in wing deformation was visually apparent to the pilot and observers on the ground, however, the increased dihedral had the opposite effect intended. The high dihedral introduced strong roll oscillations to the point where they eroded all remaining yaw authority from the plane. These

[†] X-HALE Flight #16 conducted on July 27, 2012
[‡‡] X-HALE Flight #17 conducted on August 28, 2012

oscillations were not only uncontrollable, but they made it impossible to execute a turn using differential thrust or aileron inputs. Instead, the pilot used the elevators to push the plane into a turn during the extreme bank angles of the yaw oscillations. Due to the extreme instability, trying to increase the wing dihedral was deemed an unsuitable method to improving the lateral stability.

In the next configuration, a ventral fin was added to the long center tail as well as the two inboard tails.[§] These fins were constructed of simple flat plate foam board, and spanned the entire distance from the rear of the pod to the leading edge of the tail. As expected the increased vertical surface area markedly improved the aircraft stability, eliminating all of the yaw oscillations during cruise flight. The Dutch roll coupled with first wing bending mode, when intentionally excited by aileron inputs, damped out within 2-3 cyles without any intervention with the pilot when the center tail was vertical. When the center tail was flipped to the horizontal position, removing that source of damping, the dutch roll-bending oscillations persisted for a longer period of time but still decayed back an equilibrium orientation with minimal pilot intervention. Most notably, the dutch roll-bending oscillations during descent were entirely controllable, and the pilot was able to execute a landing, making this configuration suitable for the further studies.

A final configuration change was made to the RRV-6A. As mentioned previously, all flight tests were conducted with "bare" spines; the aerodynamic fairing for the motor pod was not used so that the fiberglass shells wouldn't be damaged by the repeated hard landings. These fairings are necessary for the ATV-A since they not only streamline the flow around the bulky payload components, but they also protect the instrumentation from wind battering, airborne debris, and ground detritus during takeoff and landing. The numerical study of the effect of propeller downwash on the aircraft stability was presented in Chapter 2, and the results of an experimental investigation of the propwash over the motor pod was given in Chapter 3. Both studies concluded that the motor pods would be a destabilizing feature of the airplane, introducing a strong yaw tendency that the pilot may not have the control authority to trim for or eliminate. As predicted, the presence of the fairing surface in front of the wing reduced the effect of the ventral fins in the rear of the aircraft.[**] The dutch roll-bending oscillations returned to their pre-fin intensity – unstable but controllable with pilot intervention. The pilot was able to

[§] X-HALE Flight #18 and #19 conducted on August 29, 2012, and subsequent flights
[**] X-HALE Flight #22 conducted on August 30, 2012

successfully damp out these oscillatinos during flight, however the oscillations grew in amplitude during the descent and the aircraft could not be landed without incurring significant damage to the wings.

Figure 5.8. X-HALE RRV-6A at takeoff, shown with long center tail, ventral fins, and motor pod fairings

A representative segment of data from the most successful flight test (ventral fins, long center tail, no fairings) was extracted for the purposes of simulation correlation[††]. The process of gathering and post-processing the flight data for simulation comparison is detailed in the next section.

5.3.1 Determining Aircraft Euler Angle Response from Wing Mounted Cameras

As discussed previously, the X-HALE RRV airframes were not intended for aeroelastic tests, and, therefore, were not outfitted the instrumentation needed to directly collect flight mechanics and/or aeroelastic data. However, an attempt to estimate attitude of the RRV-6A is made here with the available collected data. The post-processing of the onboard camera footage provides close estimates of the roll angle relative to the horizon and the aircraft body angle of attack. Figure 5.9 shows the geometry of the horizon relative to the aircraft location. The location of the horizon in the image recorded by the onboard cameras is known as the apparent horizon. If R is the radius of the earth, and h is the altitude of the aircraft above the earth's surface, then :

$$d = \sqrt{(R+h)^2 - R^2} \tag{5.1}$$

[††] Data from X-HALE Flight #20 conducted on Aug. 29, 2012

$$\theta = \tan^{-1}(d/R) \qquad (5.2)$$

where d is the horizon distance and θ is the angle of the apparent horizon below the camera's true horizon.

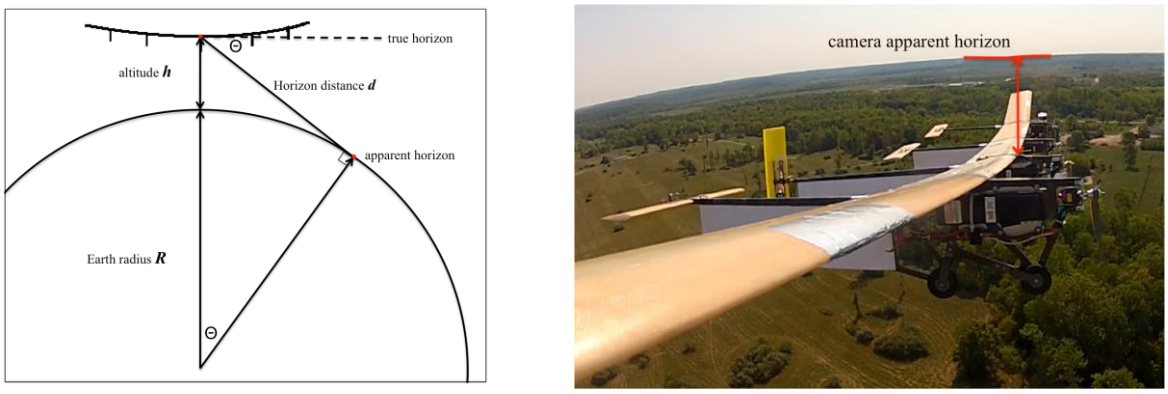

Figure 5.9: Diagram of aircraft-horizon geometry from RRV-6A onboard camera

Using an image captured at the altitude of interest when the aircraft is flying with wings level, the position of the horizon in the camera field of view (FOV) can also be measured in pixels. From this measurement, the ratio of horizon angle θ to image pixels for the camera can be calculated. Using this ratio, the position of the horizon in each camera frame can be used to approximate the aircraft roll angle. The aircraft pitch angle can be approximated by comparing the angle of the apparent horizon in the camera FOV with a horizontal reference. Vertical wingtip displacement is approximated by measuring the wingtip position in pixels relative to the center of the aircraft for each camera frame. This measurement is then normalized against the wing position within the initial frame.

5.3.2 Aircraft Rigid Body Data

The first objective of the flights of the RRV-6A was to establish the controllability and handling qualities of the designed airframe.The X-HALE RRV-6A flight tests presented here were conducted when conditions at the field were as given in Table 5.2.

Table 5.2: Flight conditions at airfield for X-HALE RRV-6A test flight.

Temperature	78°F
Wind Direction and Speed	090 at 5 mph
Precipitation	None
Cloud Cover	Clear

The second objective of these flights was to confirm that the airframe exhibited the predicted aeroelastic characteristics, including large tip deflection and coupled structural and flight dynamic behavior. The data recorded for the duration of the flight test by the Eagletree Datalogger is shown in Figure 5.10 through Figure 5.14. At time t~0 seconds, the aircraft begins its takeoff roll before lifting off and climbing to its testing altitude. The control surface inputs recorded throughout the test are shown in Figure 5.10. The aileron's main purpose during this test was to provide doublet excitation tests, which will be discussed in more detail in Section 6.2. The center tail was in its vertical (high PWM) position for takeoff and landing, and it was flipped to horizontal (the low PWM setting) during select maneuvers. The motor rpm of each motor is shown in Figure 5.11. The motors are labeled according to their location left or right of the center and whether they are at the outboard or inboard position. The altitude during the tests, shown in Figure 5.12, varied between widely throughout the test due to the maneuvers being flown. The speed, shown in Figure 5.14, ranged between 10 and 25 m/s, with the average testing speed being ~16 m/s. During this test several aileron doublets were commanded to excite the unstable Dutch roll coupled with wing bending mode. An elongated center tail and ventral fins were necessary to successfully dampen the lateral instability present in exploratory flight trials, allowing the pilot to complete several right-handed racetrack maneuvers, shown in Figure 5.13, with minimal retrimming using differential thrust. The flight concluded with a successful runway landing.

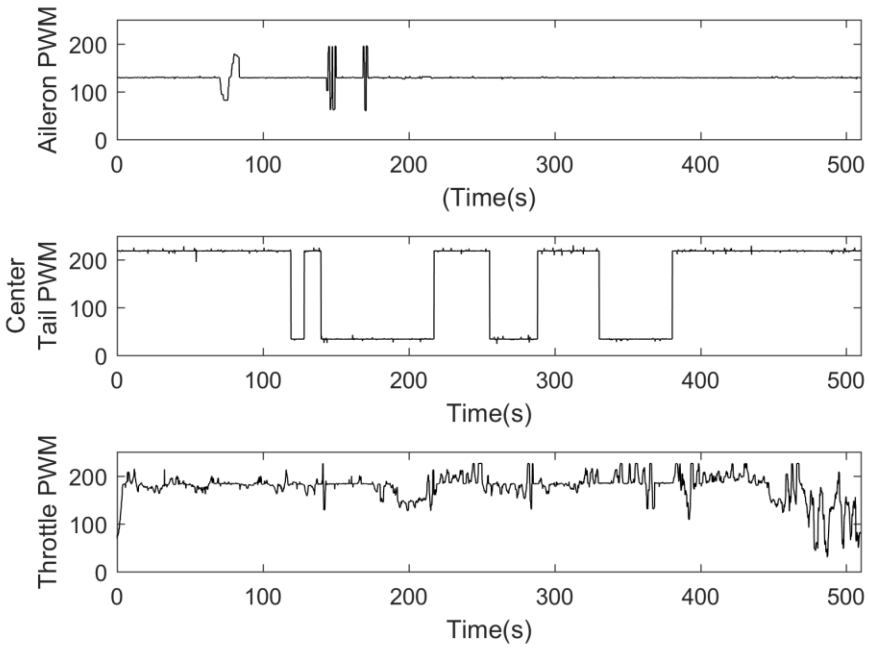

Figure 5.10. RRV-6A flight test: control inputs

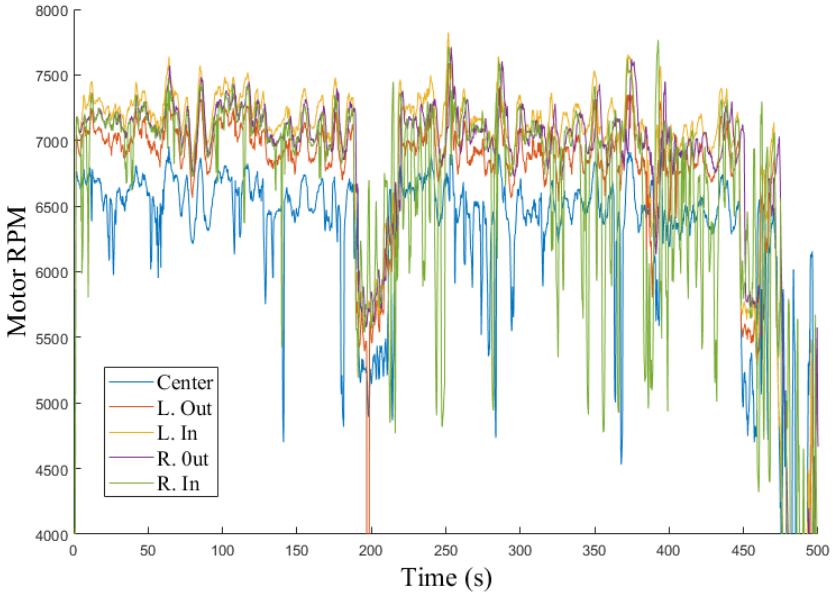

Figure 5.11. RRV-6A flight test: motor rpm

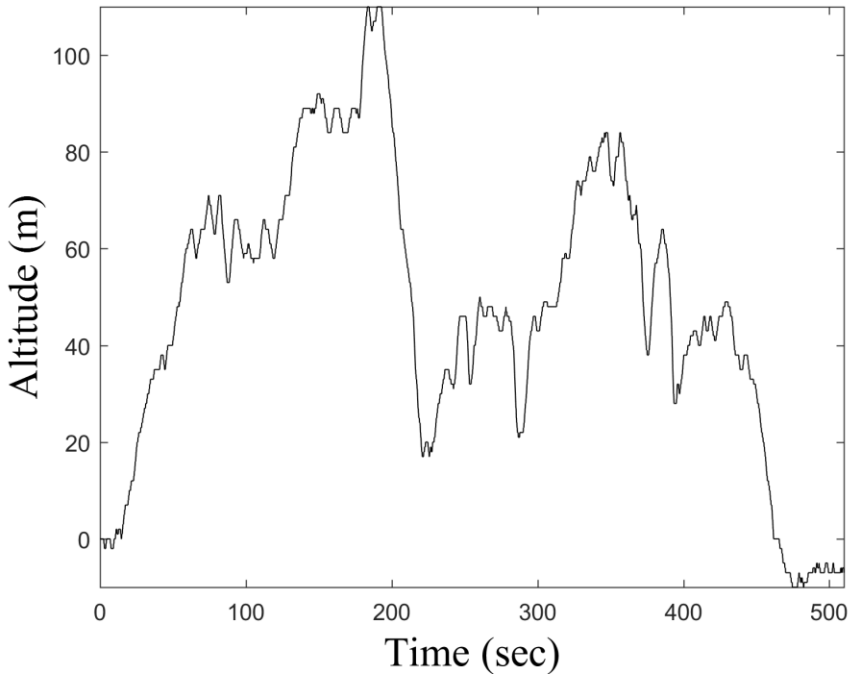

Figure 5.12. RRV-6A flight test: GPS altitude

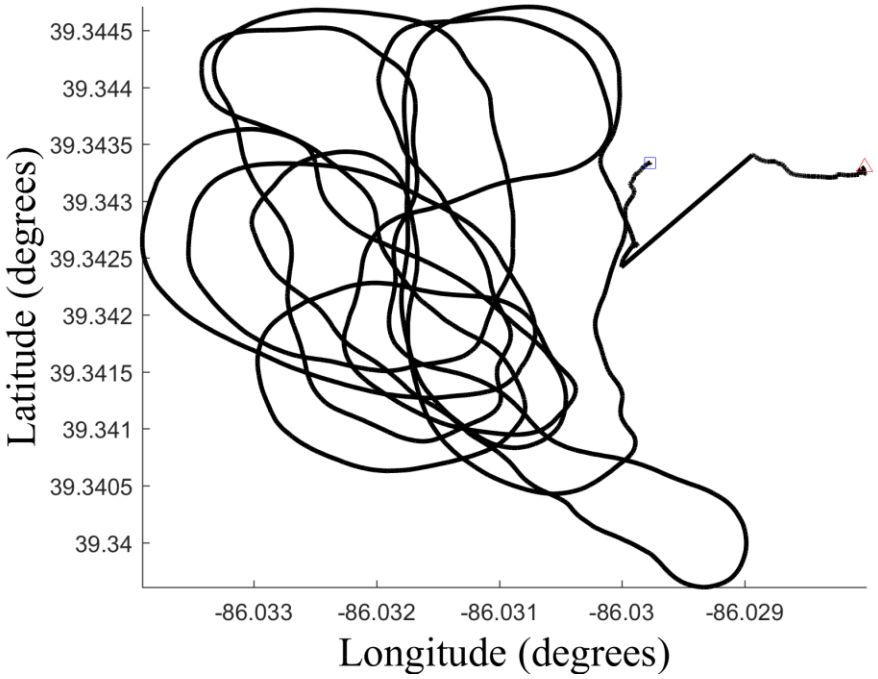

Figure 5.13. RRV-6A flight test: GPS trajectory

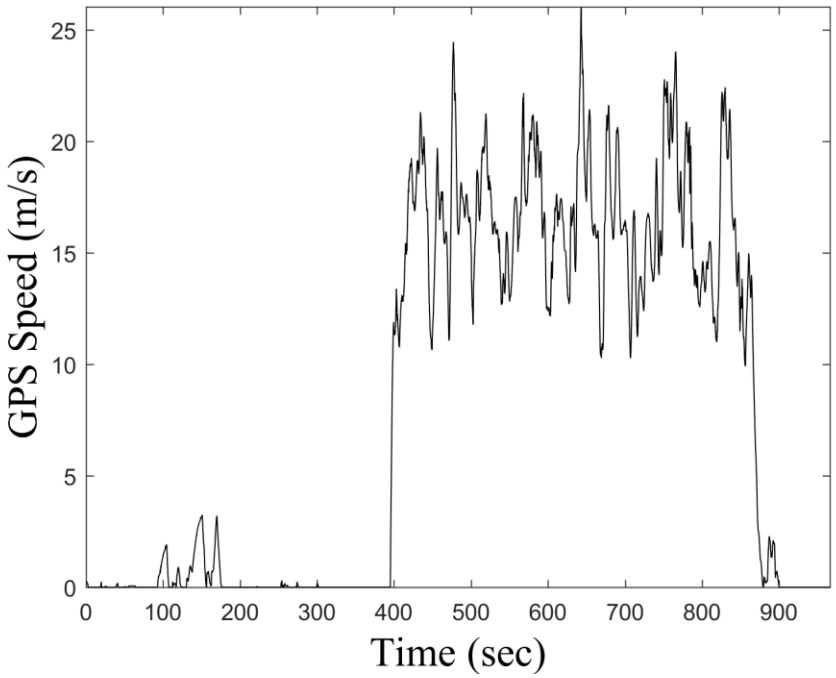

Figure 5.14. RRV-6A flight test: speed

5.4 Flight Test Data from the RRV-6B

The RRV-6B is the risk reduction airframe of the X-HALE ATV-B, which was outfitted with a sterevosion measurement system to address the issues with strain gages seen in the X-HALE ATV-A. Based on the simulations results presented in Section 4.6.3, the RRV-6B was expected to exhibit very similar behavior to the RRV-6A, despite the change in mass distribution and backwards shift of the center of gravity. A series of flight tests were performed to verify this behavior and gather system identification data for future control law studies. The data from the most successful flight test is presented here.[‡‡]

Table 5.3: Flight conditions at airfield for X-HALE RRV-6A test flight.

Temperature	65°F
Wind Direction and Speed	negligible
Precipitation	None
Cloud Cover	Scattered

[‡‡] X-HALE Flight #32, conducted June 2, 2017

Figure 5.15. X-HALE RRV-6B on the runway (top) and during takeoff (bottom)

The pilot commands for the duration of the flight test were recorded by the Pixhawk autopilot system and are given in Figure 5.16. Figure 5.17 gives the GPS speed throughout the flight. The ground roll begins at time t=0, as shown by the increase in throttle command and speed, and the elevators are deployed once the aircraft reaches takeoff speed. The takeoff climb rate was slower than the RRV-6A, due the decreased thrust to weight ratio of the heavier configuration. No significant yaw oscillations were seen during the takeoff or cruise phase, however, the aircraft had a pronounced left yaw tendency, much like the RRV-4. The pilot uses roll spoilers and differential thrust directly after takeoff in order to maneuver into testing position above the field and level the aircraft wings before each test segment. The aircraft follows a left-hand circular trajectory, shown in Figure 5.18, for the duration of the flight, but these loops are largely driven by the aircraft's yaw tendency, not pilot commands. Approximately two minutes

are used for to gain altitude and stabilize the aircraft before beginning the system identification tests.

For the system identification tests, a series of pre-determined commands were fed to the control surfaces using the Pixhawk's autopilot functionality. Each command consisted of a 10-second sinusoidal chirp signal, with a frequency range from 0 to 3 Hz. The chirp commands were fed to one control surface at a time, and the other control surfaces remained fixed at the setting at the beginning of the chirp. The "elevator" chirp commanded all of the horizontal tails simultaneously. The "roll spoiler" chirp is a doublet command, where positive signal indicates that the right spoiler is deployed into the flow, and a negative signal corresponds to left spoiler deployment. The "differential thrust" chirp is also a doublet command, where positive signal (above the thrust setting at the beginning of the chirp) indicates an increased power on the right motors, and a corresponding decrease on the left. A throttle chirp was also commanded, but that test was incomplete, and the data is not presented here.

The pilot allowed the aircraft to respond without interference, retaking control of the aircraft only after the chirp was complete or to aid the aircraft recovery from an unstable response. The cycle of chirp command→response→ pilot recovery was repeated three times for each control surface, and the sequence of chirps are clearly seen in the control surface plots in Figure 5.16. The amplitude of each control surface input is given in Table 5.4 and a closer view of the chirps are shown in Figure 5.22, Figure 5.32, and Figure 5.42.

The aircraft orientation and body rates throughout the flight is given in Figure 5.19 through Figure 5.21. The roll motion, given in Figure 5.19 shows a ~0.2Hz oscillatory mode excited by the pilot's attempts to level the aircraft after each turn. The mode persists throughout the flight, so the chirp responses are superimposed onto this roll motion. Similarly, heading angle of the aircraft, shown in Figure 5.21, changes constantly as the aircraft follows its circular trajectory. The large amplitude 0.2Hz roll mode is also coupled with the yaw motion, as seen in the small disturbances in the yaw angle trend and corresponding increases in the yaw rate amplitude. There does not appear to be significant coupling between the longitudinal pitch motion and the lateral roll and yaw motions, which is consistent with the behavior seen in the RRV-4 and RRV-6A test flights.

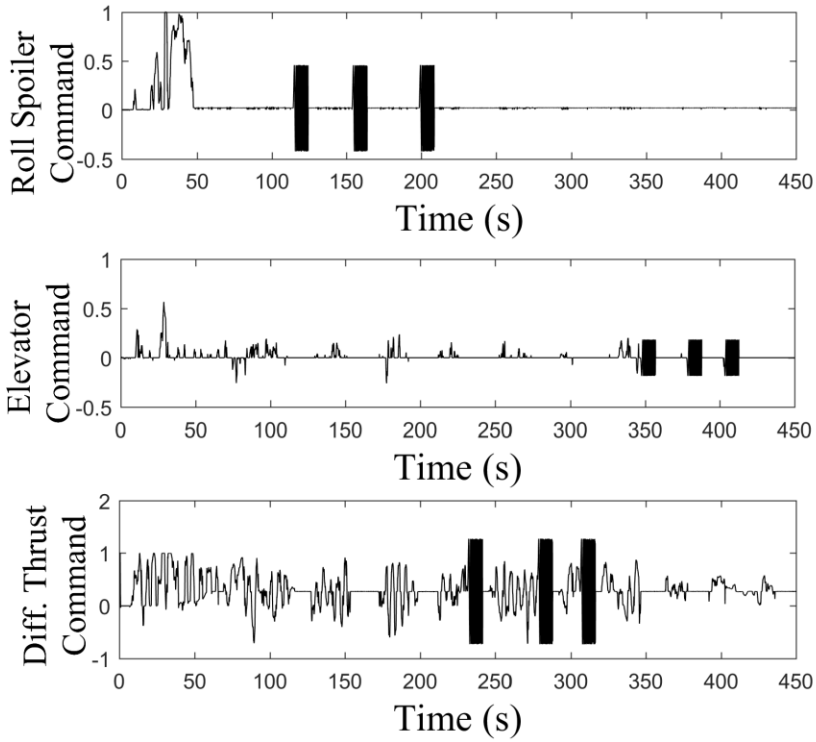

Figure 5.16. RRV-6B flight test: control inputs

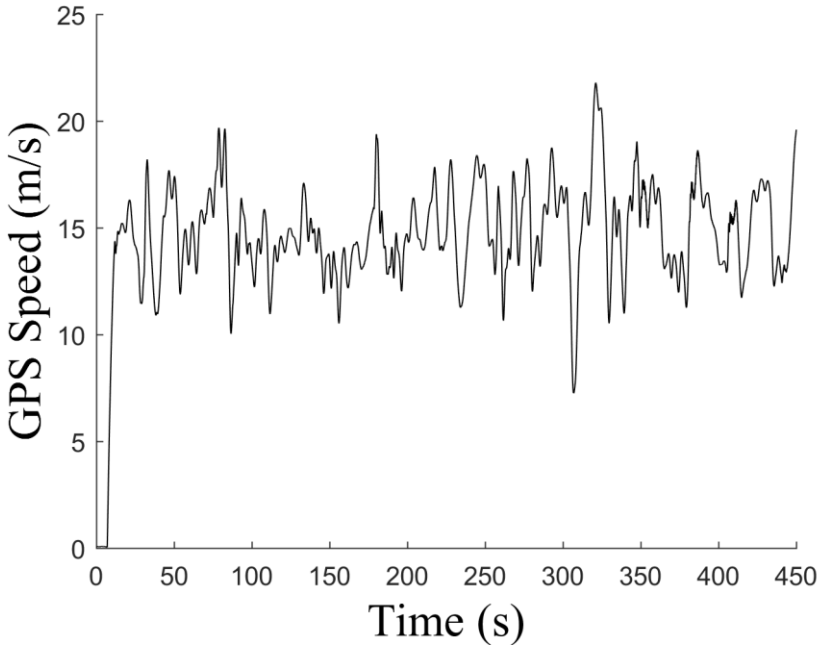

Figure 5.17. RRV-6B flight test: speed

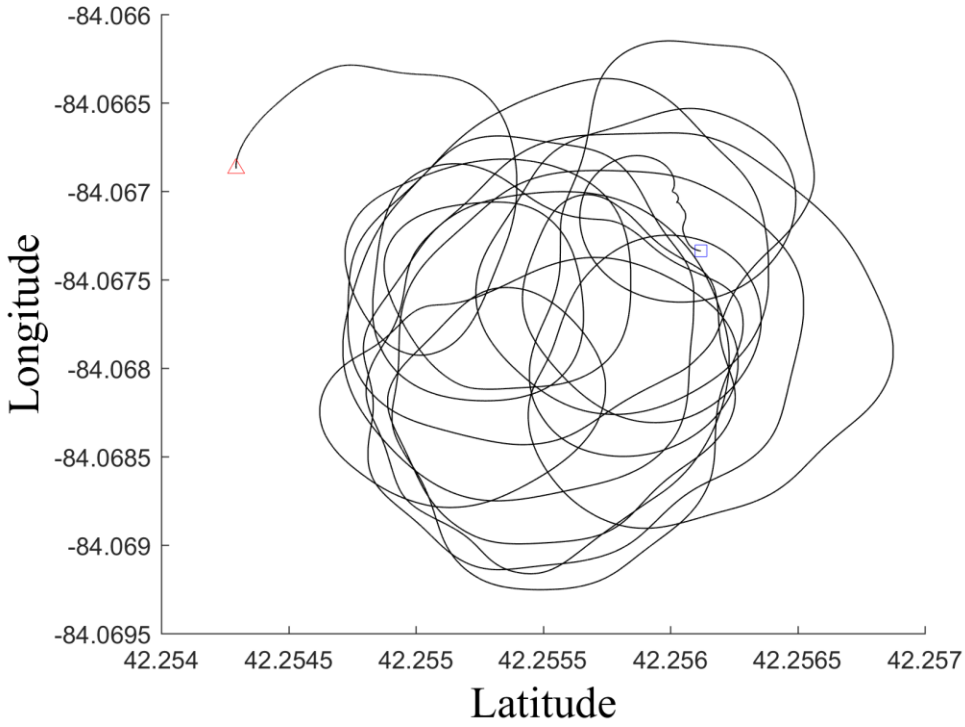

Figure 5.18. RRV-6B flight test: GPS Trajectory

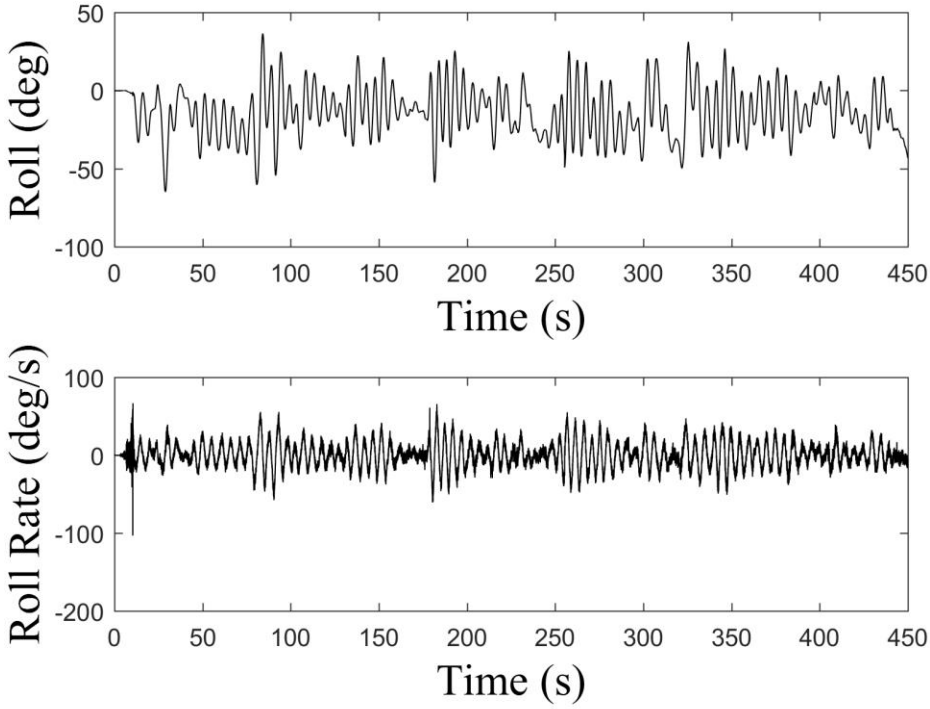

Figure 5.19. RRV-6B flight test: roll angle and roll rate

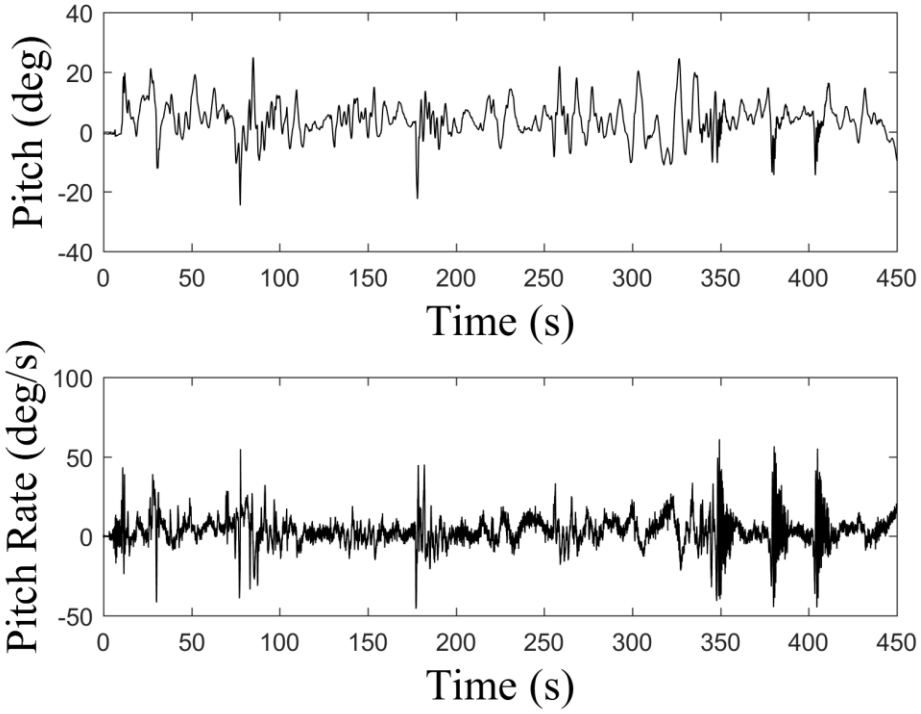

Figure 5.20. RRV-6B flight test: pitch angle and pitch rate

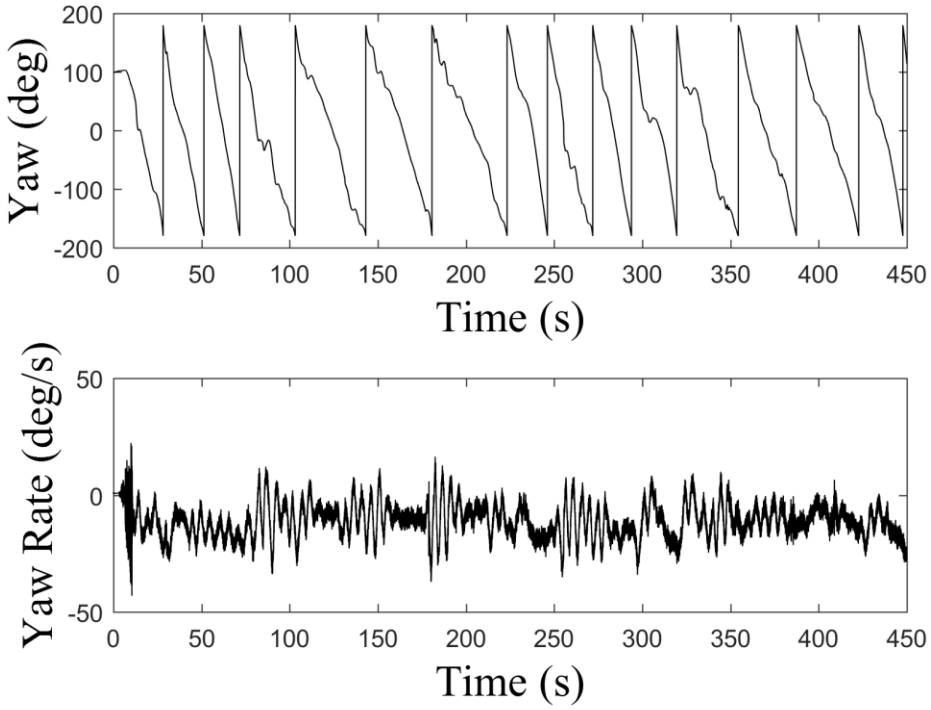

Figure 5.21. RRV-6B flight test: heading angle and yaw rate

Table 5.4. Control surface chirp parameters

Control Input	Maximum Value
Elevator Angle	± 45 deg.
Roll Spoiler	± 60 deg.
Motor Thrust (@ 15m/s)	4 N at 100% power 3.75N at 80% power

5.4.1 Roll Spoiler Chirp Tests

The roll spoiler chirps were conducted at an average speed of 13.8 m/s. The pilot attempted to bring the aircraft as close to steady level trim as possible before the chirp commands were given, however, due to the roll oscillations and strong yaw tendency, this trim was very difficult to achieve. Instead, the aircraft states at the beginning of each roll spoiler chirp sequence is given in Table 5.5. The heading angle varied between chirps, as the commands were not given at the same poinst in the aircraft's circular trajectory. The body angular rates are smallest overall in the first chrip, with the yaw rate increasing in the second and third chirp segments. The pitch rate decreased between chirp segments, while roll rate stayed relatively consistently throughout the chirps. Although the roll rate is consistent, the fact that it is nonzero means that the aircraft response measured during and after the chirp consisted of the chirp response superimposed over the existing motion of the aircraft.

The aircraft response during and immediately after the roll spoiler chirp commands are plotted in Figure 5.23 through Figure 5.31. In all three chirp responses, the 0.2Hz oscillatory roll mode is present. The roll mode persists throughout chirp 1, but the amplitude of this motion begins to decay during chirps 2 and 3, trending toward a steady state near $\varphi \sim 20$ degrees. This amplitude decay is due to the lack of pilot input during the chirps, as the roll mode reasserts itself once the pilot takes back control at the conclusion of the roll spoiler chirp segment. From Figure 5.19, it can be seen that the majority of the roll motion during flight occurs around this steady state value of $\varphi \sim 20$ degrees, suggesting that it is due to the yaw-roll coupling of the circular trajectory. The pitch angle, speed, and altitude also demonstrates some oscillation in response to very large roll angle. The low frequency content of the roll spoiler chirp is not present in the pitch rate, indicating tha that the changes in pitch angle are an indirect result of the roll response rather than a direct response to the roll spoiler input. Similarly, the changes in lift and drag

caused by the roll spoiler chirps occur too quickly to affect the speed and altitude significantly. Instead, the bump in speed and drop in altitude are due to sideslipping at the high bank angles experienced during the chirp segments.

Table 5.5. RRV-6B initial conditions for roll spoiler chirps

Aircraft State	Chirp 1	Chirp 2	Chirp 3	Units
Velocity	13.55	13.68	14.19	m/s
Thrust per Motor	2.74	2.86	2.86	N
Yaw Angle	82.79	-1.14	7.59	deg
Pitch Angle	90.34	10.94	19.24	deg
Roll Angle	49.22	1.06	14.07	deg
Yaw Rate	-9.2	-18	-15.73	deg /s
Pitch Rate	6.85	3.65	2.61	deg /s
Roll Rate	-7.39	-9.24	-9.88	deg /s

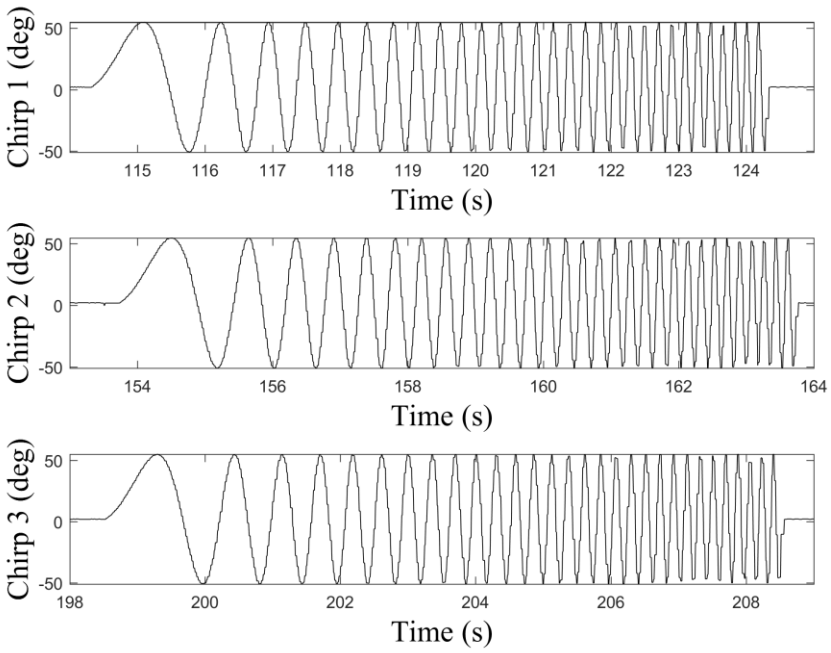

Figure 5.22. Sinusoidal chirp commands supplied to roll spoiler

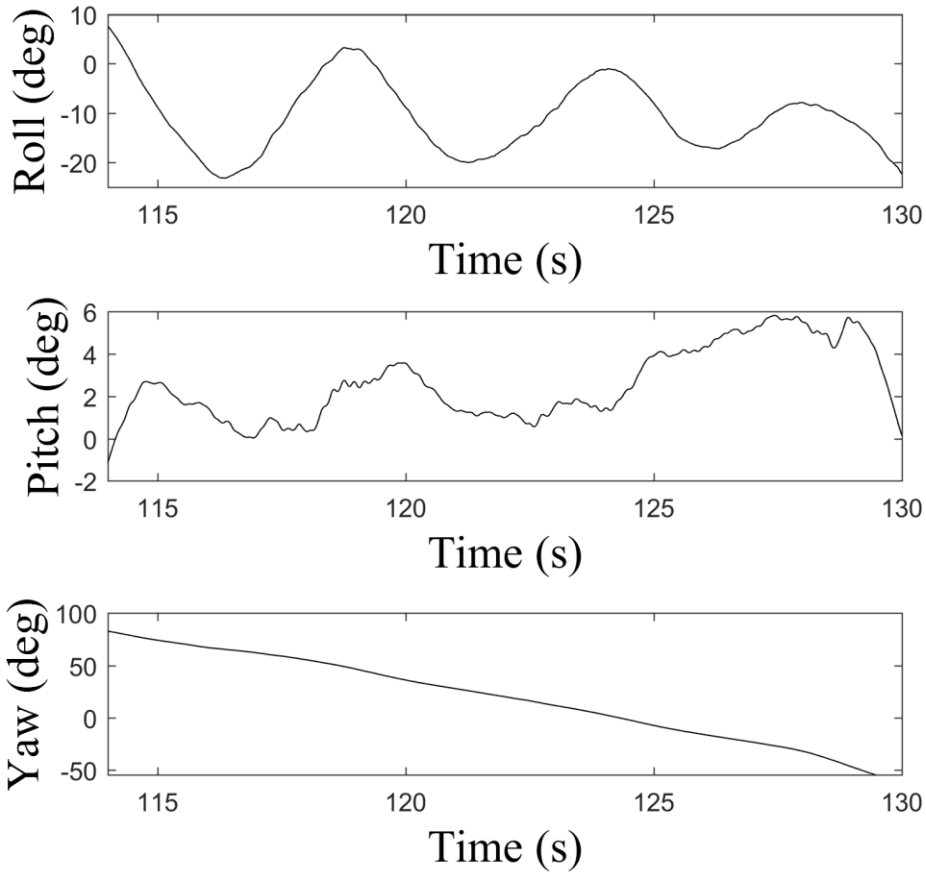

Figure 5.23. RRV-6B body orientation response to roll spoiler chirp input 1

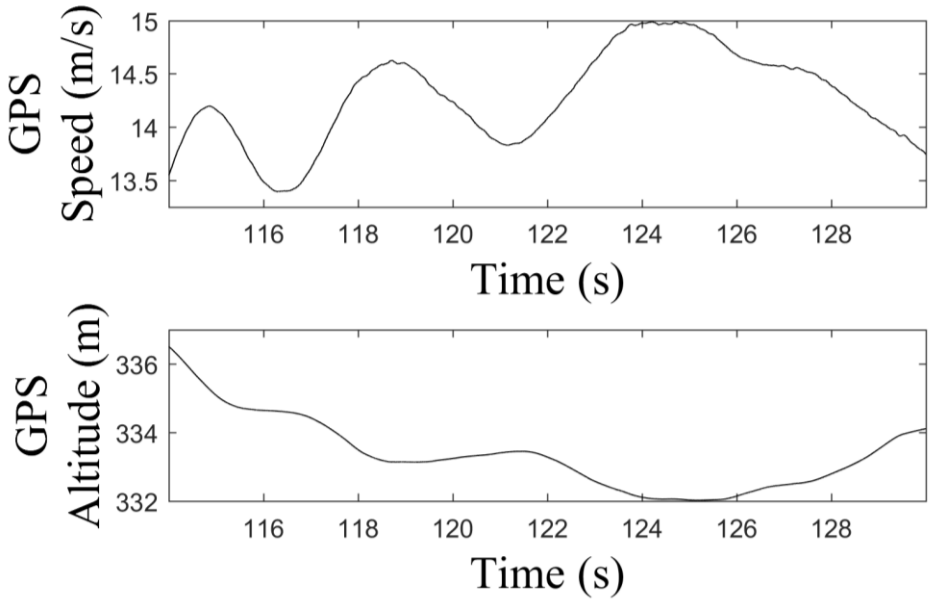

Figure 5.24. RRV-6B body position response to roll spoiler chirp input 1

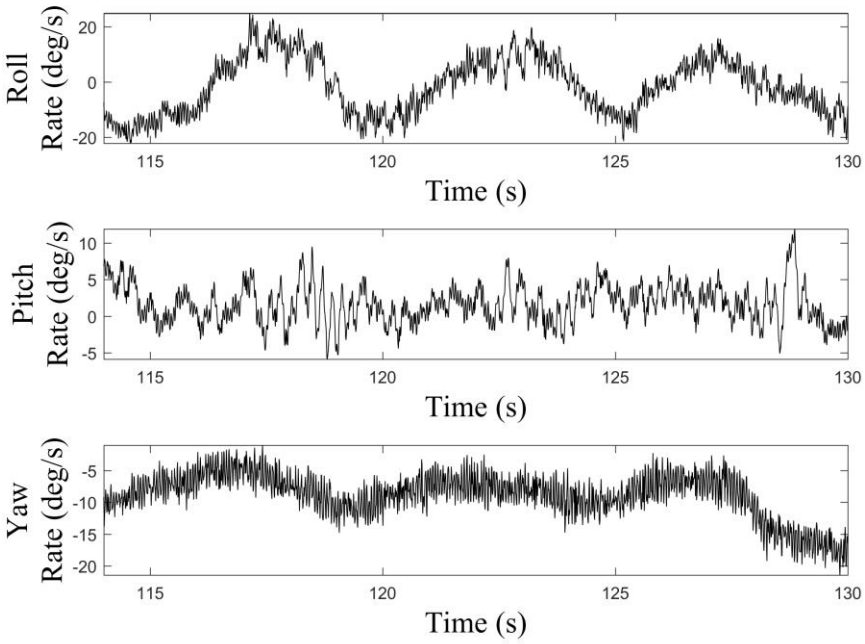

Figure 5.25. RRV-6B body rate response to roll spoiler chirp input 1

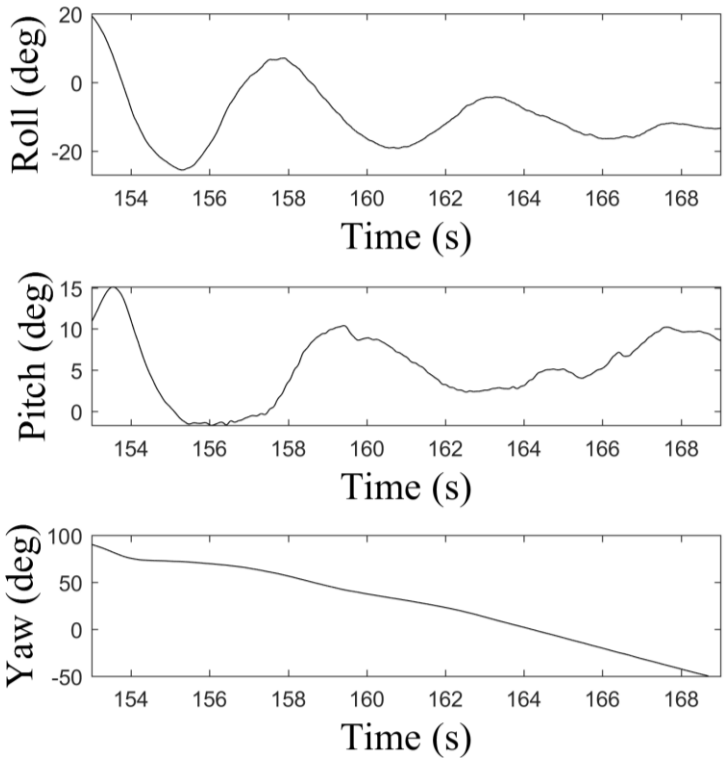

Figure 5.26. RRV-6B body orientation response to roll spoiler chirp input 2

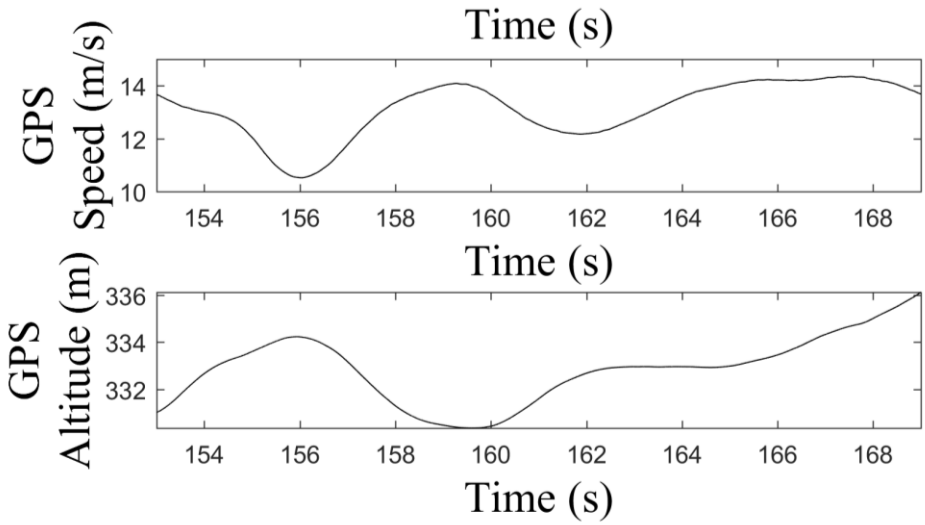

Figure 5.27. RRV-6B body position response to roll spoiler chirp input 2

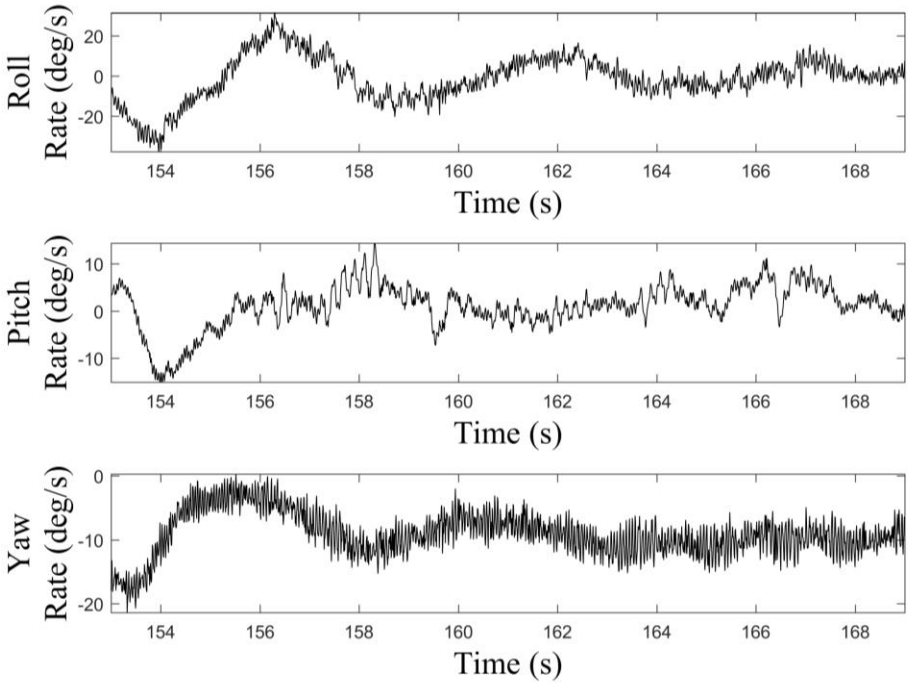

Figure 5.28. RRV-6B body rate response to roll spoiler chirp input 2

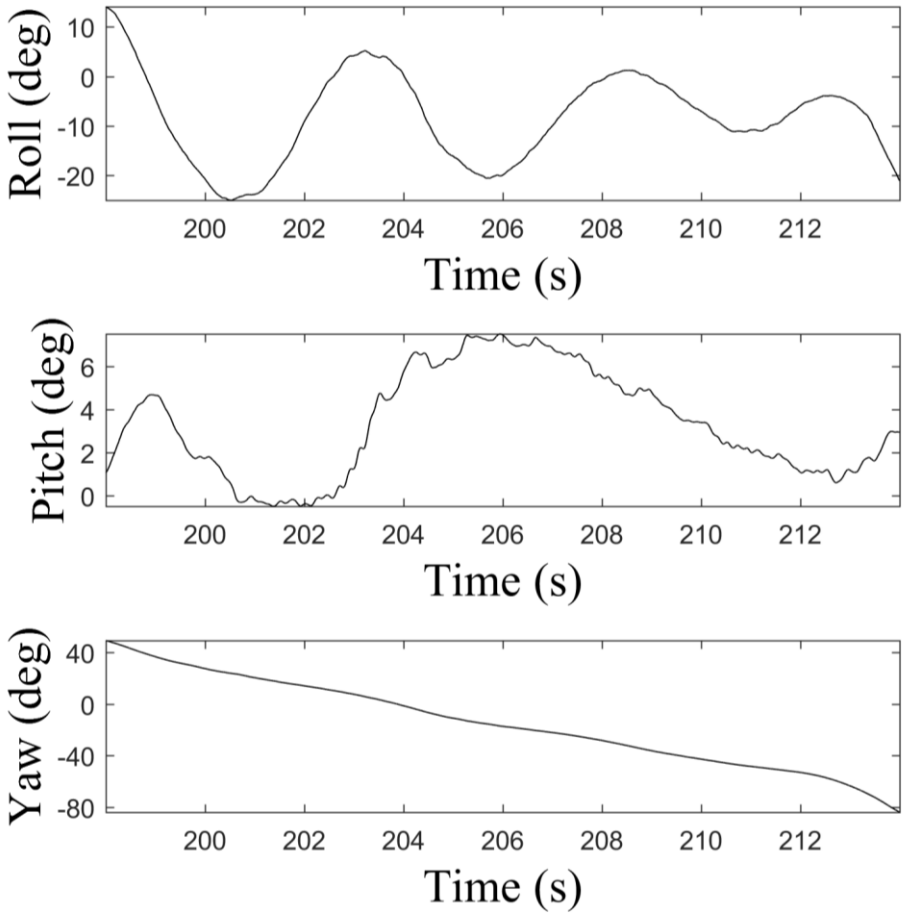

Figure 5.29. RRV-6B body orientation response to roll spoiler chirp input 3

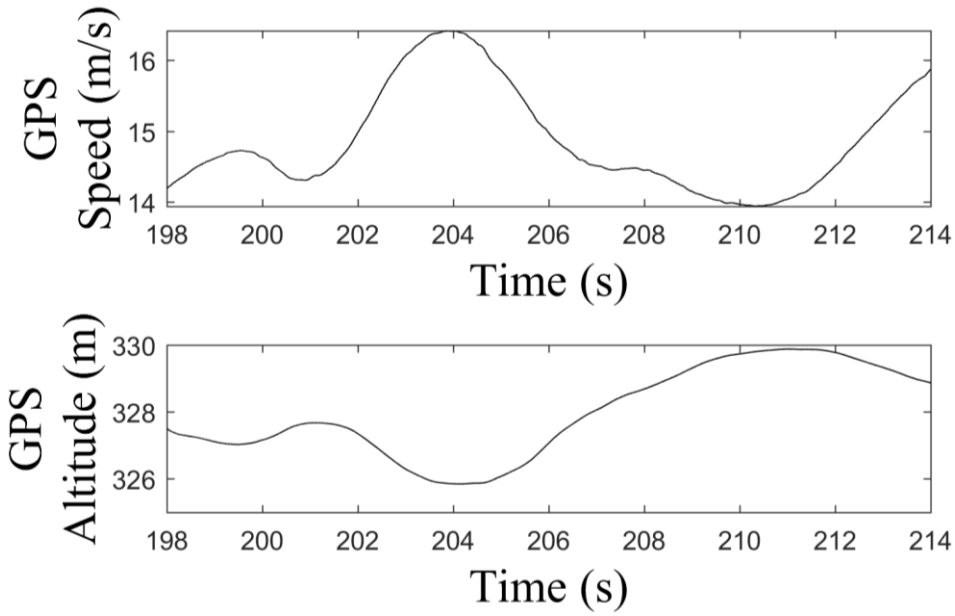

Figure 5.30. RRV-6B body position response to roll spoiler chirp input 3

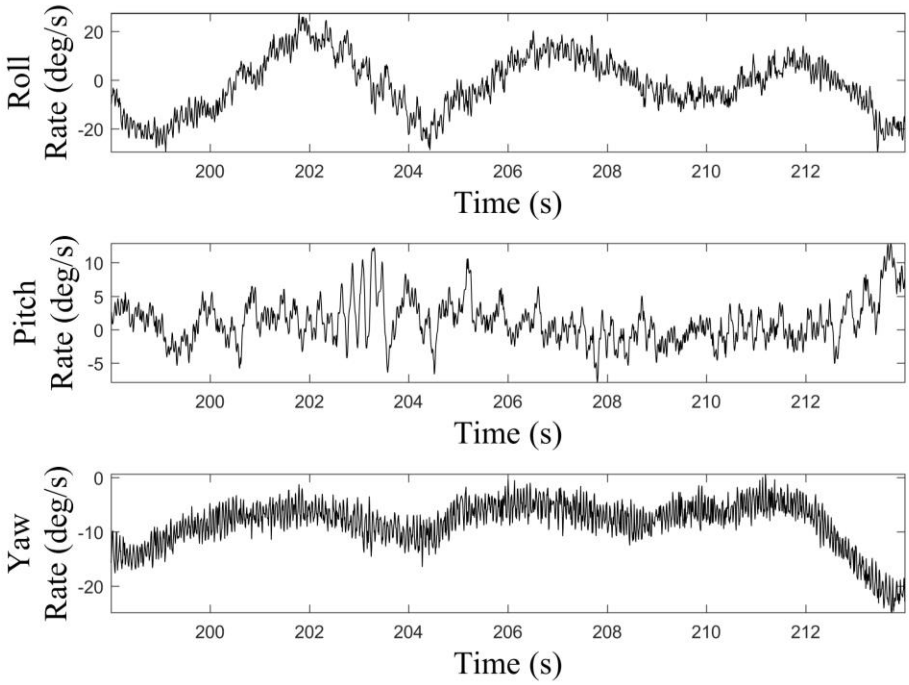

Figure 5.31. RRV-6B body rate response to roll spoiler chirp input 3

5.4.2 Elevator Chirp Tests

Prior to the elevator tests, the pilot once again attempted to bring the aircraft as close to steady level trim as possible. The measured aircraft states at the beginning of each elevator chirp sequence is given in Table 5.6. The first elevator chirp was given at a significantly higher speed than chirps 2 and 3, and the yaw and pitch rates were very large at the start of this chirp.The rates for chirps 2 and 3 were smaller, with chirp 2 having the smallest pitch rate and chirp 3 being closest to trim overall.

The wing is much less flexibile in the chordwise direction, and the aircraft overall is very stiff along its longitudinal axis. Because of the high stiffness along the longitudinal degrees of freedom, the high frequency content of the elevator chirp is translated directly into rigid body motion, rather than being dampened and absorbed by elastic motion. The full range of frequencies contained in each chirp is clearly seen in the pitchrate responses, shown in Figure 5.35, Figure 5.38, and Figure 5.41. The pitching angle also contains the same frequency content, although it superimposed on top of the pitching angle induced by the roll oscillations. As expected, there is no evidence of direct coupling between the elevator input and lateral degrees of freedom. The roll response contains none of the high frequency content seen in the pitch response, however, the the lower frequency, high amplitude pitch oscillations do induce

oscillations in the yaw rate. This is clearest in the first 12 seconds of the yaw rate response to chirps 1 and 2, given in Figure 5.33 and Figure 5.36. This behavior is absent from the response of the third chirp, but the yaw rate at the beginning of the third chirp excitation was also much smaller, which may have been a factor. As with the roll spoiler input, the changes in speed and altitude of the aircraft is driven primarily by the roll mode, with the elevator chirp response being seen as a superposition of small amplitude, high frequency oscillations over the ongoing rolling motion of the aircraft.

Table 5.6. RRV-6B initial conditions for elevator chirps

Aircraft State	Chirp 1	Chirp 2	Chirp 3	Units
Velocity	18.46	13.53	13.28	m/s
Thrust per Motor	3.1	3.1	3.09	N
Yaw Angle	-126.06	-65.9	30.98	deg
Pitch Angle	13.62	14.87	6.44	deg
Roll Angle	8.17	1.26	-4.05	deg
Yaw Rate	-20.69	-14.73	-8.18	deg /s
Pitch Rate	-3.51	-0.81	3.04	deg /s
Roll Rate	-42.93	-18.19	-3.41	deg /s

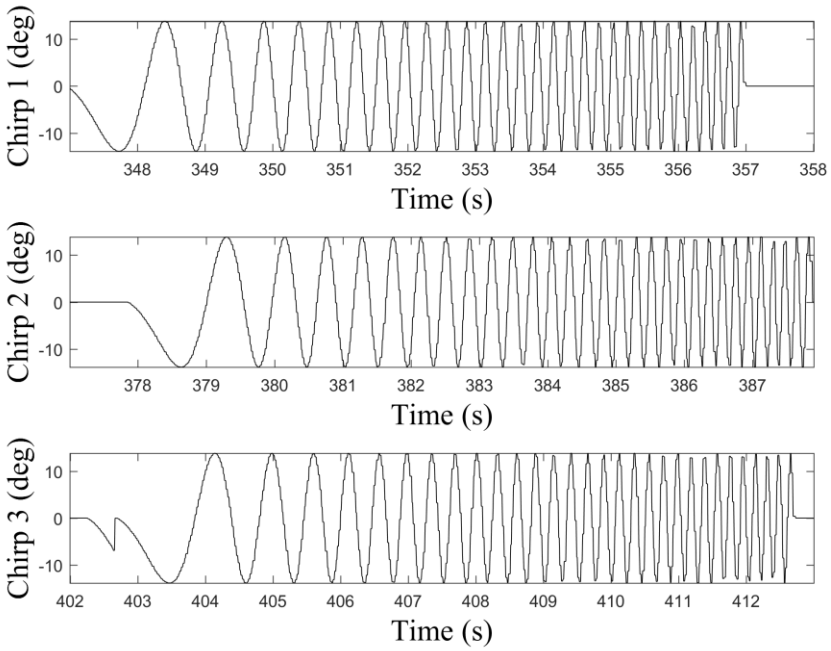

Figure 5.32. Sinusoidal chirp commands supplied to elevator

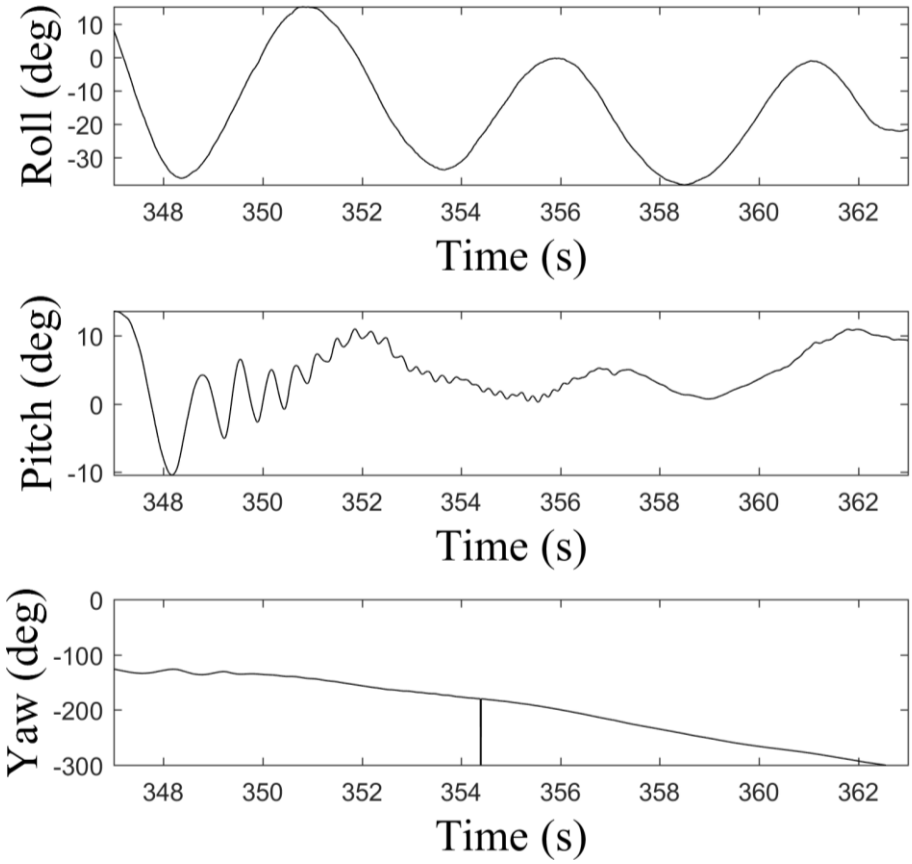

Figure 5.33. RRV-6B body orientation response to elevator chirp input 1

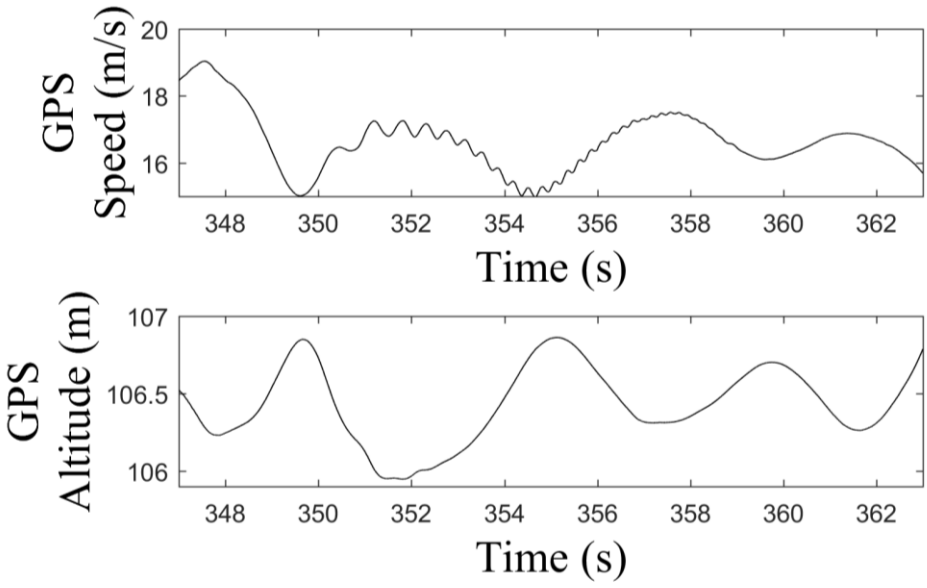

Figure 5.34. RRV-6B body position response to elevator chirp input 1

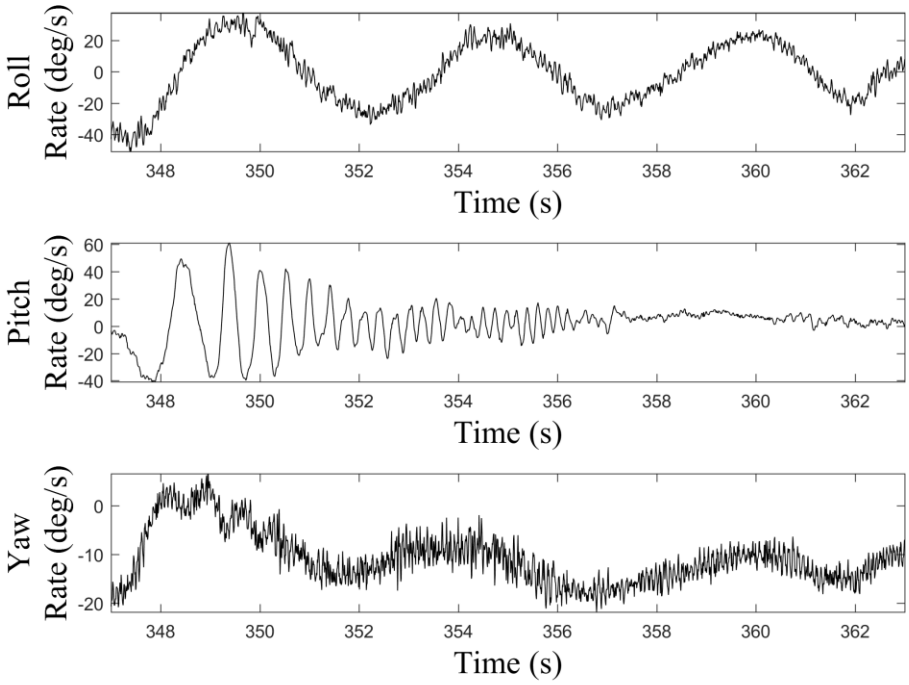

Figure 5.35. RRV-6B body rate response to elevator chirp input 1

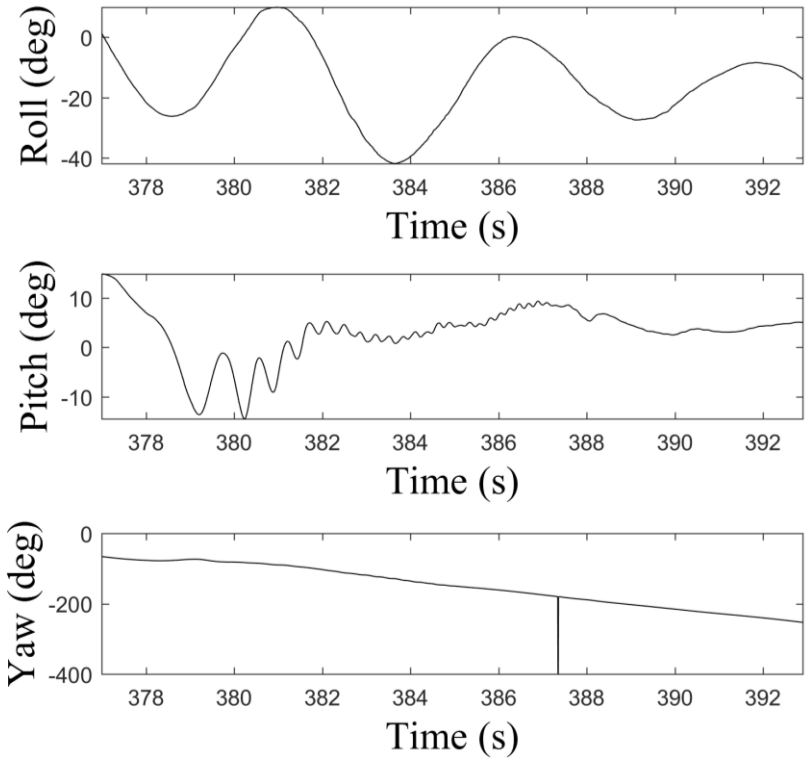

Figure 5.36. RRV-6B body orientation response to elevator chirp input 2

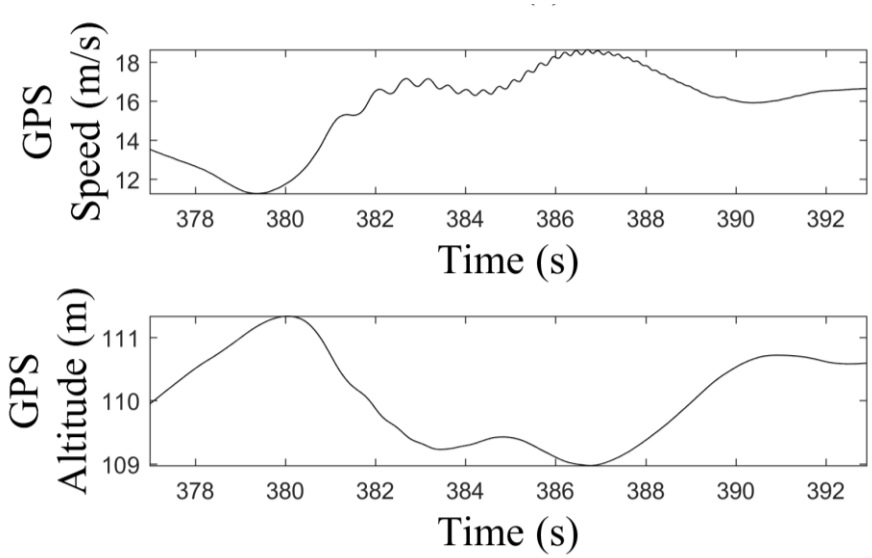

Figure 5.37. RRV-6B body position response to elevator chirp input 2

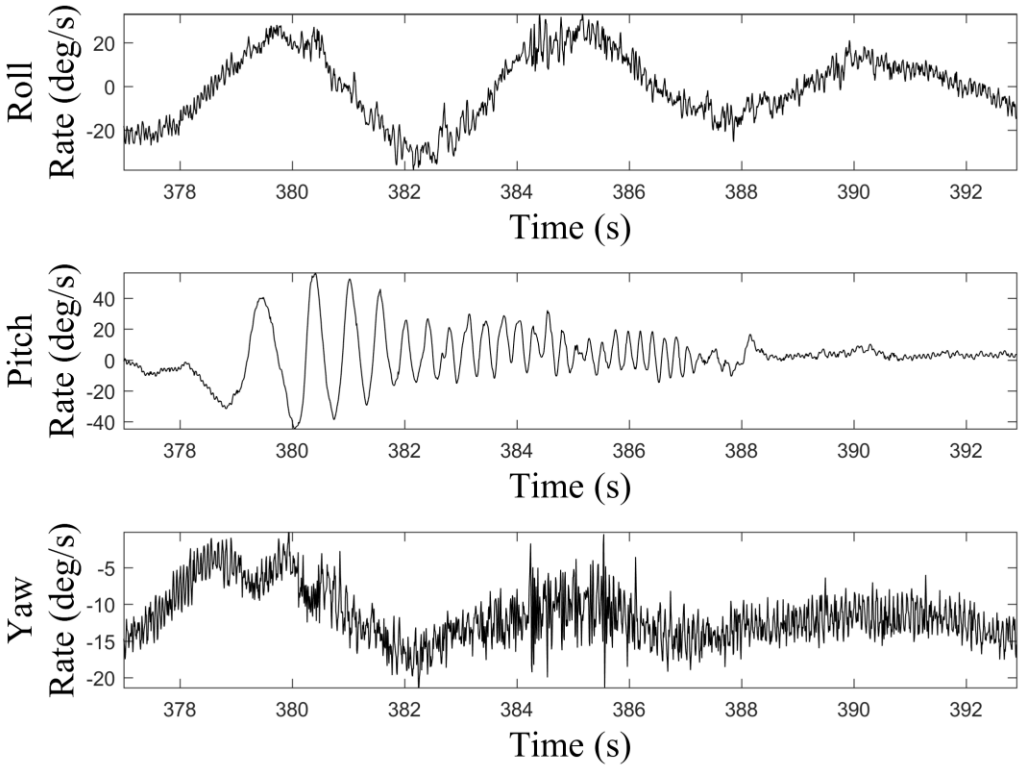

Figure 5.38. RRV-6B body rate response to elevator chirp input 2

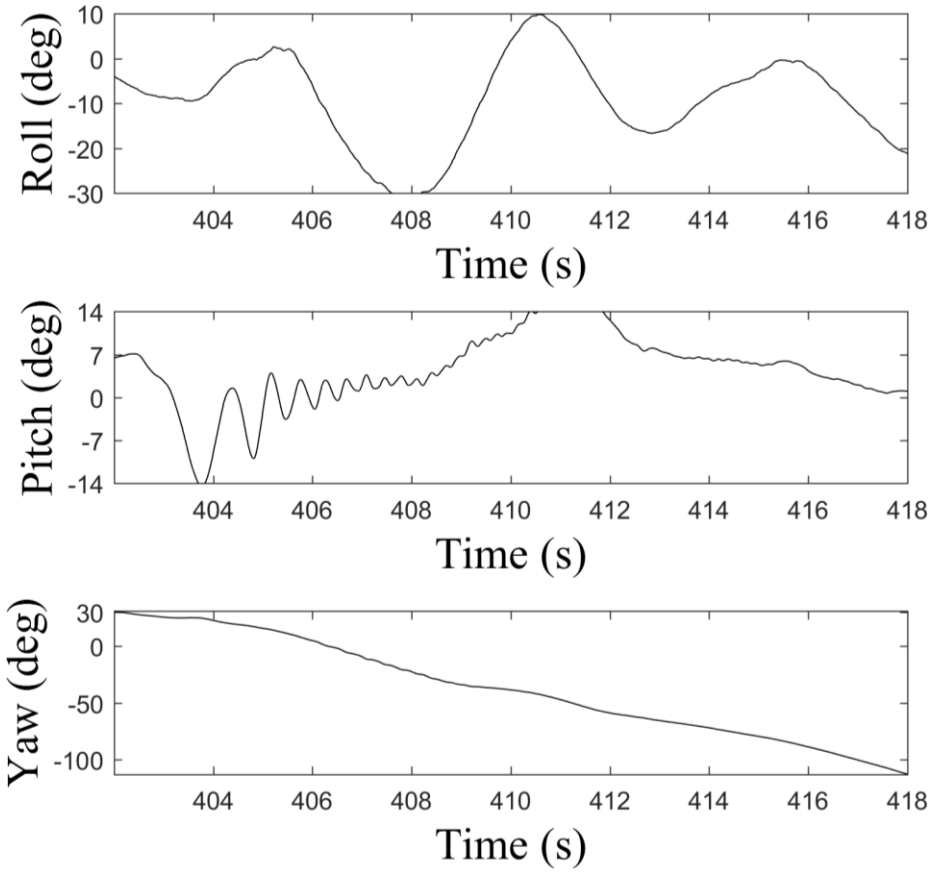

Figure 5.39. RRV-6B body orientation response to elevator chirp input 3

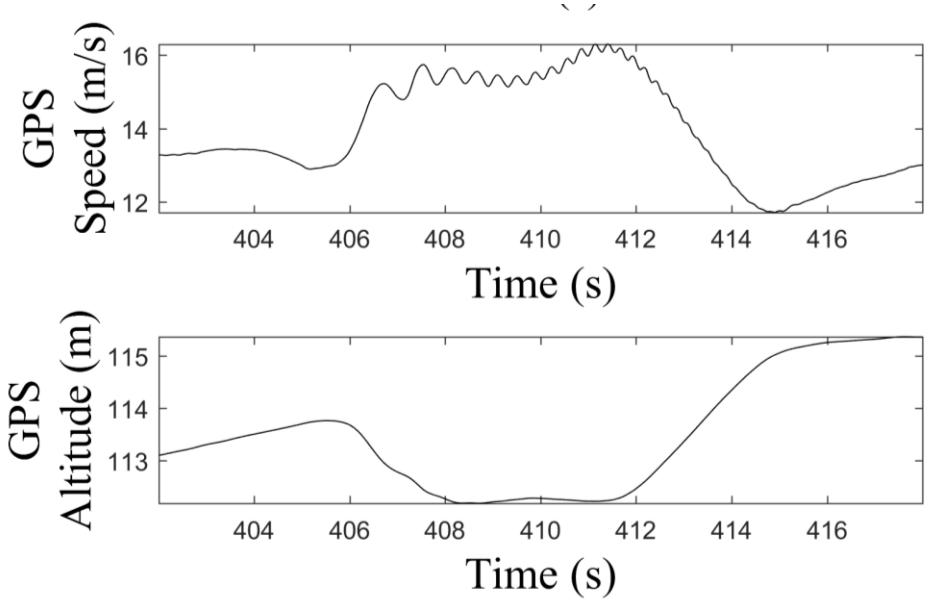

Figure 5.40. RRV-6B body position response to elevator chirp input 3

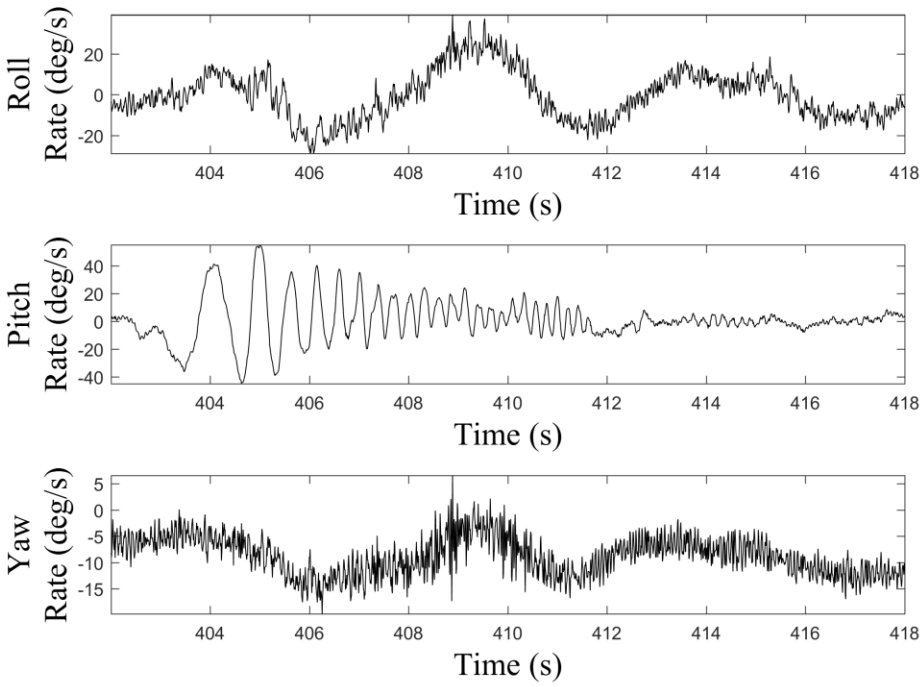

Figure 5.41. RRV-6B body rate response to elevator chirp input 3

5.4.3 Differential Thrust Chirp Test

The initial conditions for the differential thrust chirps are listed in Table 5.7. The steady state throttle level was consistent for all three chirp sequences, and the differential thrust chirps resulted in an offset to this steady state thrust. The body rate responses to each chirp are given in Figure 5.45, Figure 5.48, and Figure 5.51. The roll rates were very high at the beginning of each chirp. However, this roll rate amplitude decays towards the end of each response. In chirps 1 and 3, the roll angle is oscillating around a diverging steady state. These two chirps had an initially positive roll rate, while the roll rate during chirp 2 was similar magnitude but initially negative. The steady state value of the roll angle in chirp 2 remained relatively constant throughout the response, thus the divergent response seen during chirp 1 and 3 is a result of the aircraft being pushed outside of its stabililty boundary. The pilot input after each chirp, given in Figure 5.16, shows that the pilot had to work much harder to recover the aircraft after chirps 1 and 3, while the recovery inputs after chirp 2 were minimal.

Similar to the roll spoiler response, the high amplitude, low frequency differential thrust inputs have an observable effect on the yaw response. The oscillatory input is seen clearly in the yaw rate, however the differential thrust inputs are not large enough to overcome the yawing

tendency of the aircraft. The differential thrust chirps do not significantly change the yaw motion of the circular turns, as shown by the plots of the body orientation in Figure 5.43, Figure 5.46, and Figure 5.49.

Bench tests demonstrated that the motors were fully capable of being actuated at the frequency range of these chirps, and differential thrust is the primary control surface used for lateral control. However, the aircraft shows the least response to the differential thrust inputs compared to the roll spoiler and elevator response. Since the aircraft is not insensitive to differential thrust commands, these results indicate that the commands occurred too quickly for the low frequency roll or yaw modes to respond.

Table 5.7. RRV-6B initial conditions for differential thrust chirps

Aircraft State	Input 1	Input 2	Input 3	Units
Velocity	14.54	18.24	8.56	m/s
Thrust per Motor	3.1	3.09	3.1	N
Yaw Angle	67.27	89.01	21.99	deg
Pitch Angle	14.16	14.93	6.06	deg
Roll Angle	3.18	-4.1	-0.48	deg
Yaw Rate	-3.75	-27.95	4.9	deg /s
Pitch Rate	-0.54	5.78	-12.2	deg /s
Roll Rate	24.66	-24.27	30.57	deg /s

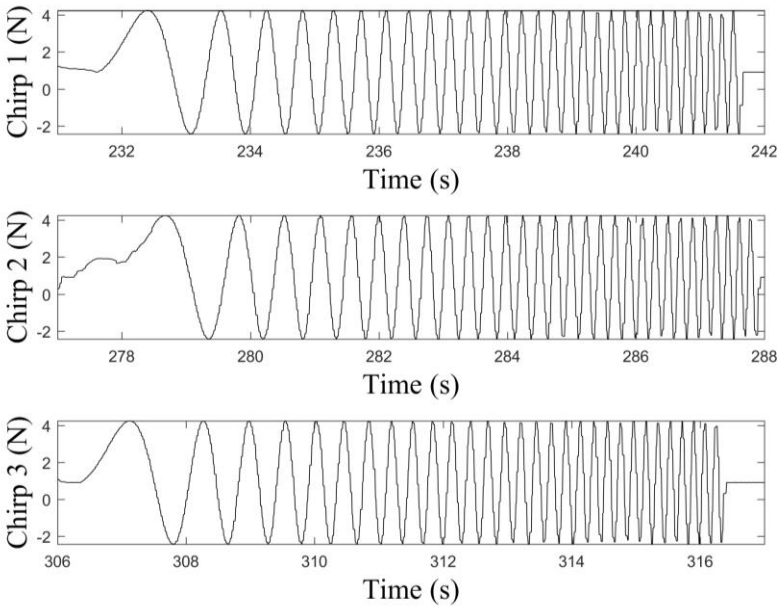

Figure 5.42. Sinusoidal chirp commands supplied to differential thrust

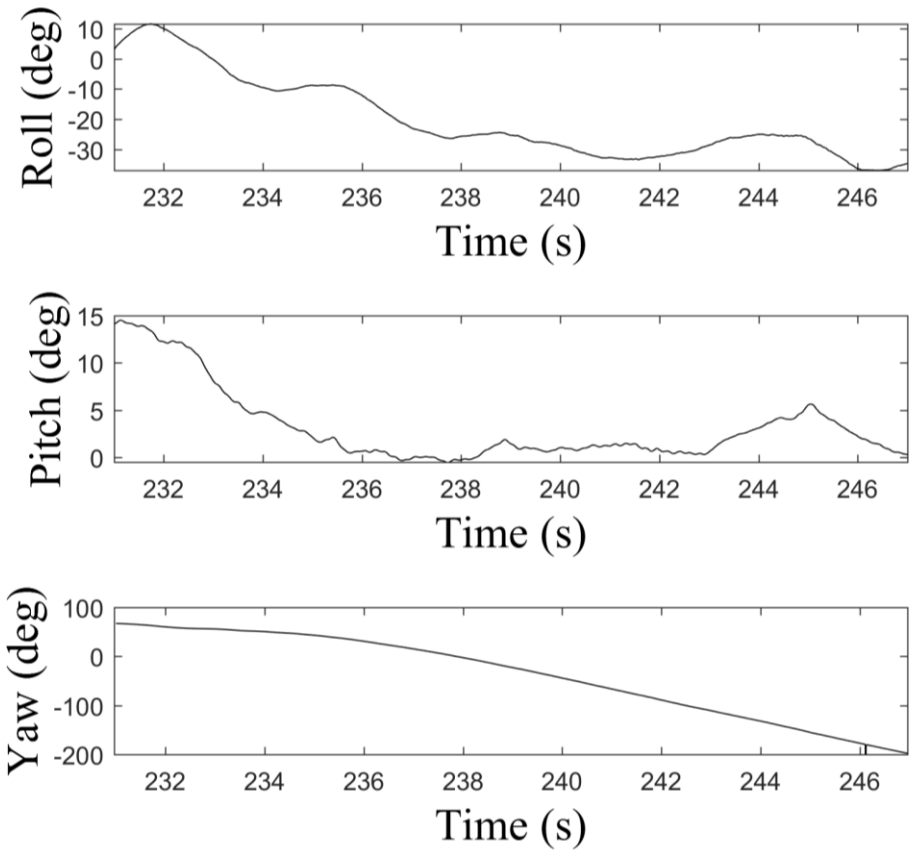

Figure 5.43. RRV-6B body orientation response to differential thrust chirp input 1

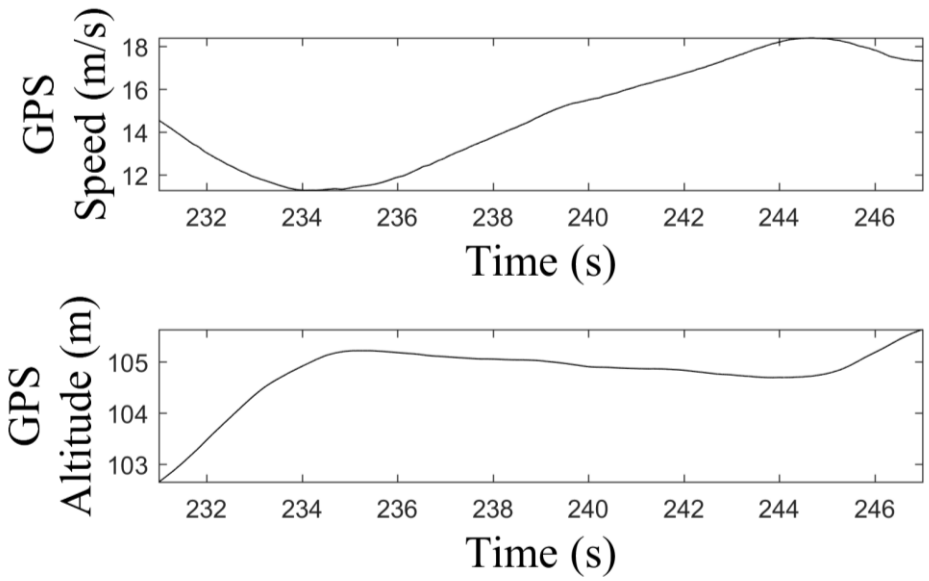

Figure 5.44. RRV-6B body position response to differential thrust chirp input 1

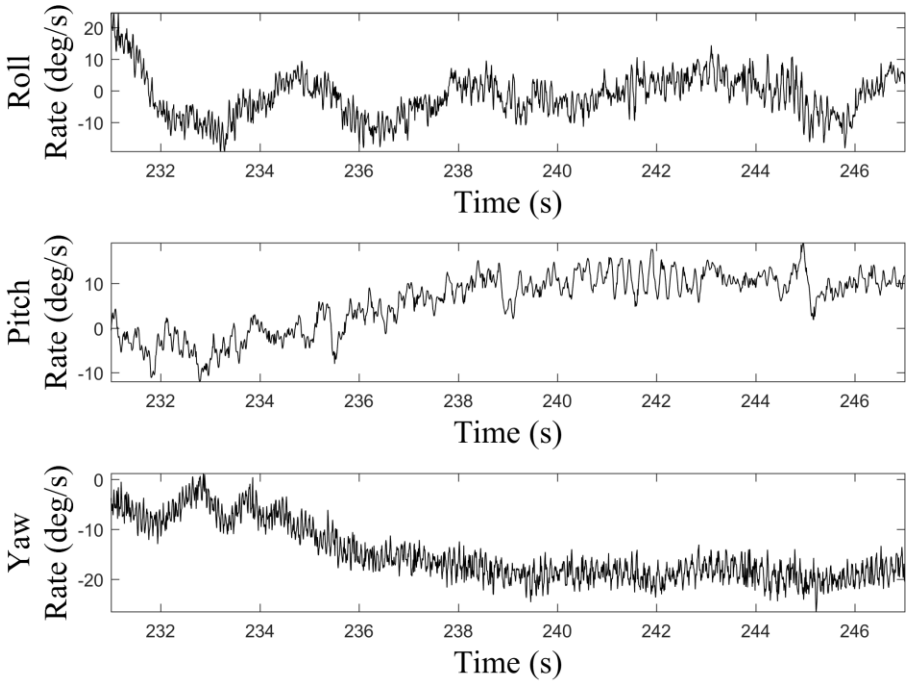

Figure 5.45. RRV-6B body rate response to differential thrust chirp input 1

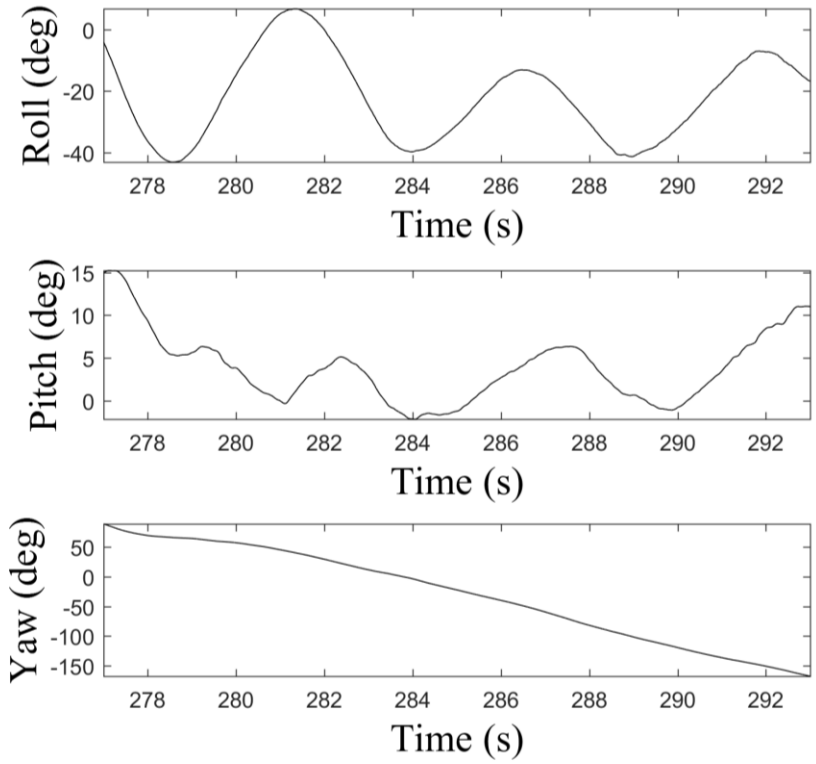

Figure 5.46. RRV-6B body orientation response to differential thrust chirp input 2

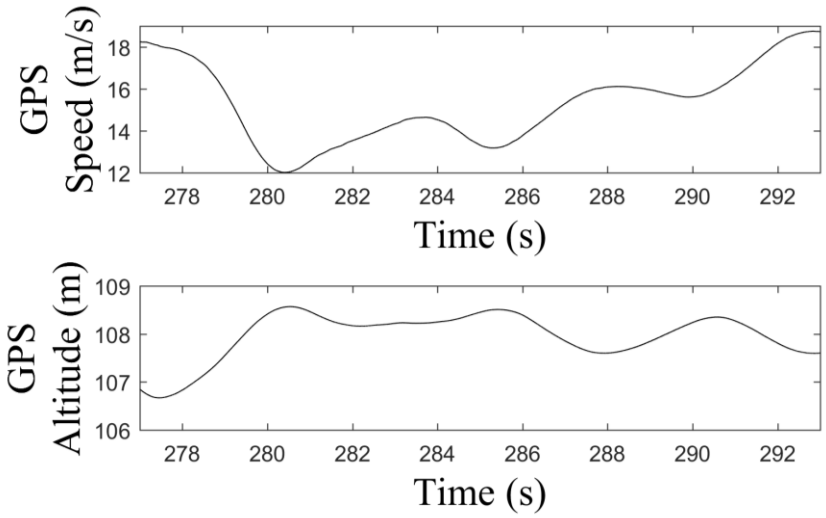

Figure 5.47. RRV-6B body position response to differential thrust chirp input 2

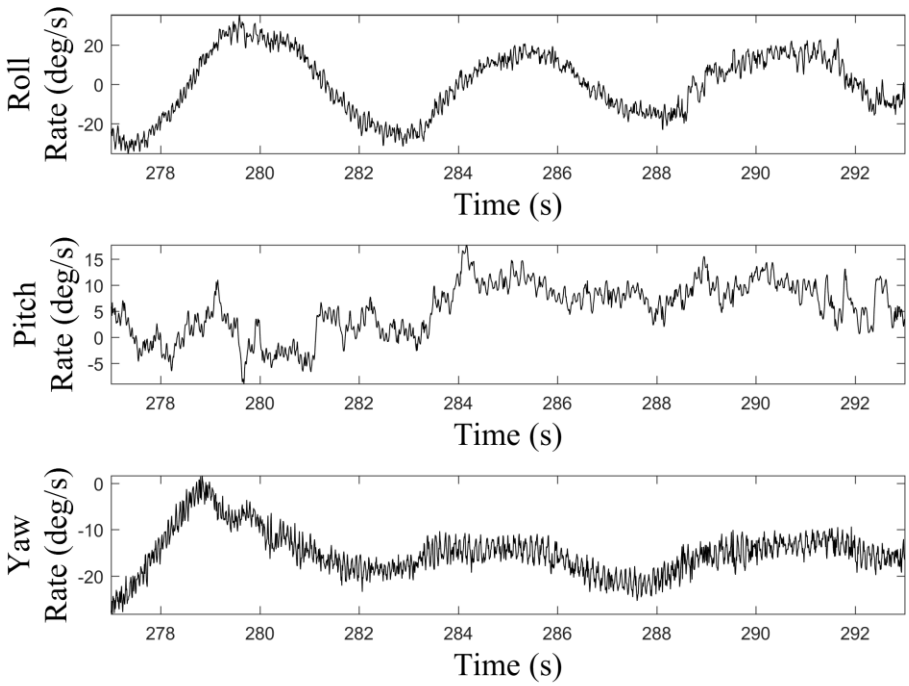

Figure 5.48. RRV-6B body rate response to differential thrust chirp input 2

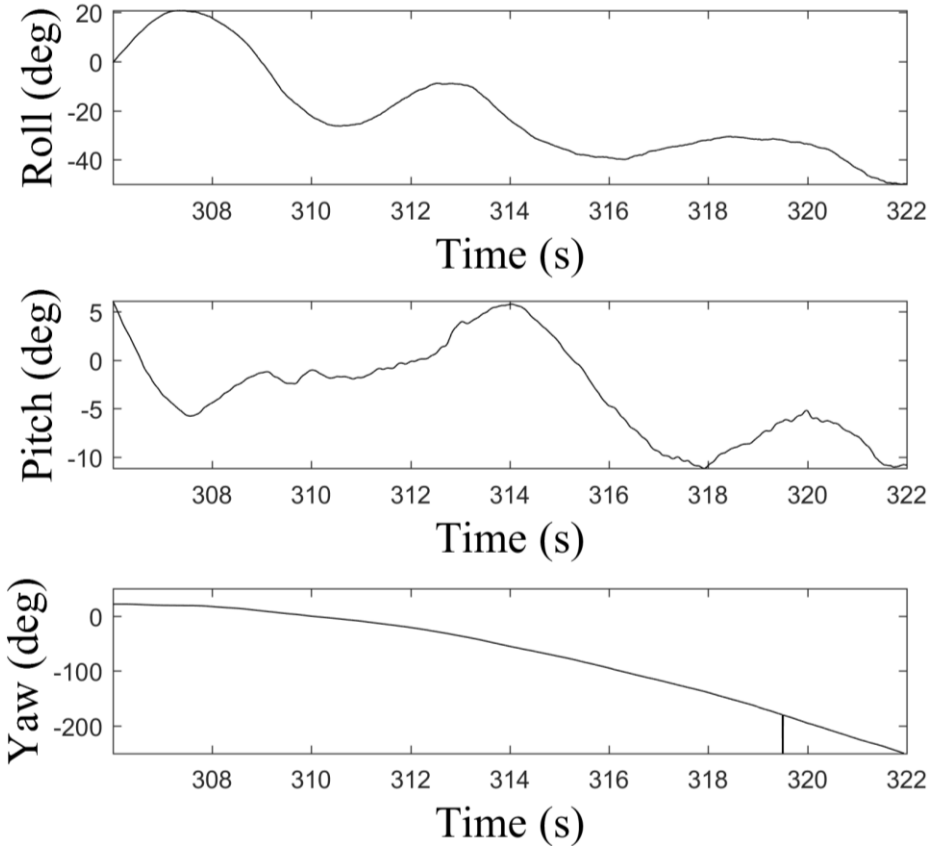

Figure 5.49. RRV-6B body orientation response to differential thrust chirp input 3

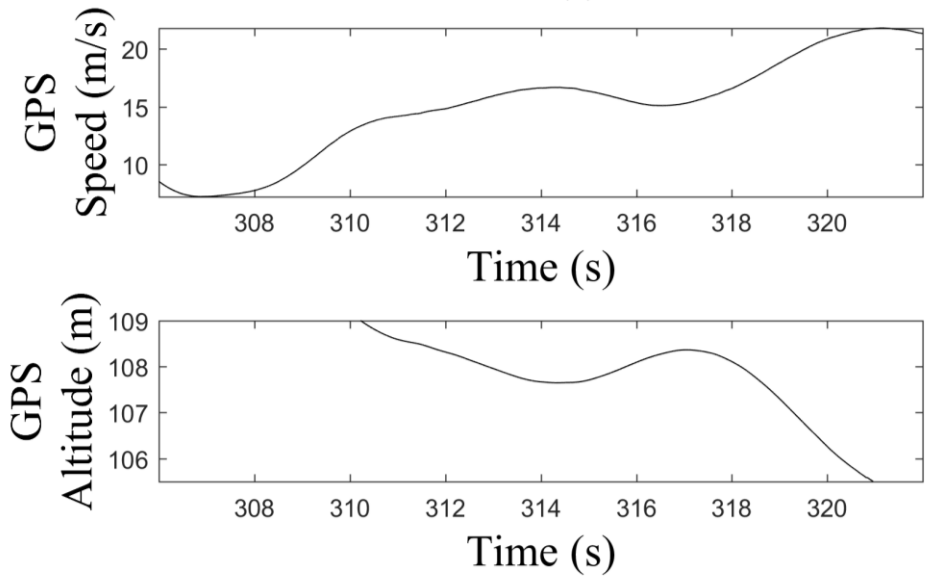

Figure 5.50. RRV-6B body position response to differential thrust chrip input 3

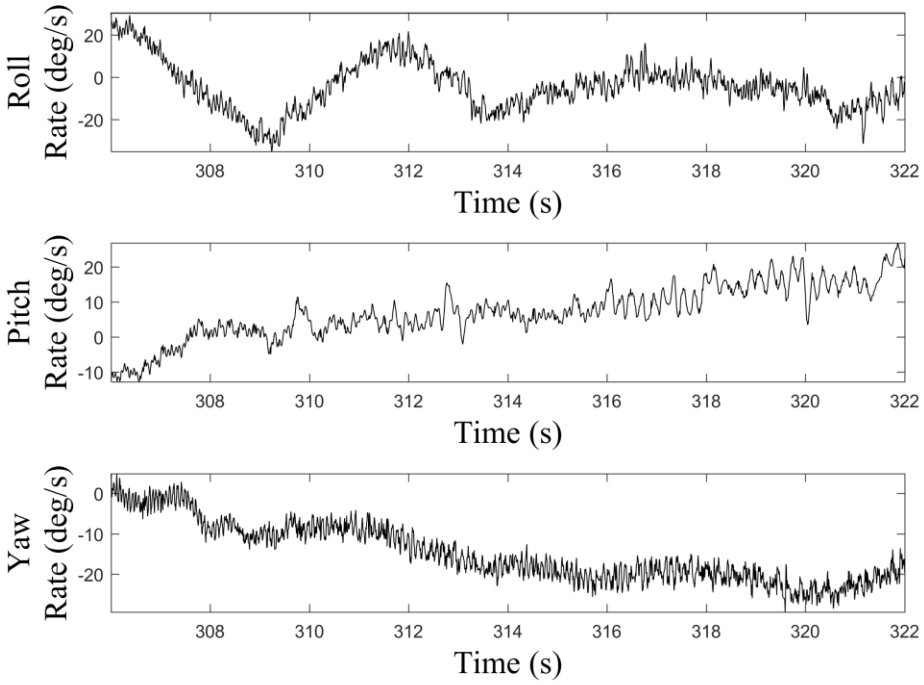

Figure 5.51. RRV-6B body rate response to differential thrust chirp input 3

Due to the high flexibility of the aircraft, the elastic-coupled rigid body modes are very low frequency and the lateral degrees of freedom in the aircraft respond slowly to the control surface inputs. The low frequency portion of the roll spoiler and differential thrust chirps resulted in changes in roll and yaw rates as expected, however the high frequency content of these chirps are largely absent from the aircraft response. The opposite is true for the longitudinal degree of freedom, as the full frequency range of the elevator input was seen in both the pitch angle and pitch rate response.

Althought it was not measured directly, large dynamic wing bending was observed in response to the elevator chirp commands. An subsequent chirp test in the throttle input was performed during this flight, but the test was incomplete. The data is not presented here, but is available in the supplementary files listed in 0. During this test, the aircraft experienced large pitching oscillations coupled with very high dihedral. These high stress manuevuers resulted in the full structural failure of the center aluminum joiner during the flight. The aircraft separated into two parts during the throttle test and crashed. It is possible that the joiner failed partially during the earlier maneuvers, and the aluminum L-brackets prevented the aircraft from

separating until the loads generated by the throttle test exceed their structural limit. However, post-flight analysis of the airframe, flight videos, and the available data was unable to pinpoint the exact time or nature of the failure.

5.5 Summary of Flight Tests

The flight tests of the RRV configurations confirmed several behaviors of HALE-class aircraft. Adverse yaw was present in the RRV-4 and RRV-6A configurations, rendering the ailerons ineffective when attempting to trim the aircraft. However, when 100% differential was implemented to attenuate the adverse yaw, the ailerons were suitable for roll authority augmentation and implementing gust-like disturbances. Differential thrust was used for turning maneuvers, taking advantage of the aircraft's strong yaw-roll coupling. If rudder/differential thrust does not provide enough yaw authority for controlled turning, as is the case when an aircraft requires a significant yaw trim or when 100% motor power is needed to maintain level flight, roll spoilers are an effective replacement for ailerons.

The large bank angles that result from differential thrust or rudder-induced turns incur significant sideslipping as penalty, but this can be mitigated by using the elevator to level out the turn. However, care must be taken that the attempts to recover equilibrium orientations do not induce additional oscillations that cannot be stabilized.

A center-loaded configuration does not necessarily have different flight-dynamic modes when compared to a span-loaded configuration with the same geometry. As mentioned in Section 5.3, flight tests of the span-loaded and high dihedral versions of the RRV-6A were conducted, and the dutch-roll coupled with the first wing bending mode was the dominant flight behavior in both configurations. Similarly, the shift from the span-loaded RRV-6A to the center-loaded RRV-6B did not change the dominant flight behavior. The wing deformation during takeoff and other high-g maneuvers was noticeably higher in the RRV-6B, and the high dihedral that resulted from the center-loaded configurations was correlated with a loss of lateral damping and and increased sensitivity to disturbance. However, the dominant flight mode was still dutch roll coupled with symmetric wing bending. This result suggests that the flexibility of the aircraft (which was nearly identical between all of the six-meter configurations) is the primary driver for determining the identity of the elastic-rigid body coupled modes while the total mass and mass

distribution will have a significant effect on the stability of that mode. Thus, if a center-loaded configuration is unavoidable, then a method of monitoring and/or controlling wing deformation is desirable. Again, roll spoilers are an effective tool for altering wing deformation as they result in an immediate drop in lift without the wing-twisting moment that could cause control surface reversal.

Additional flight tests with a repaired RRV-6B and the final ATV-B configuration are planned, but not yet completed as of this writing.

CHAPTER 6. Experimental Validation of the X-HALE Model

Several numerical studies of the X-HALE aircraft were conducted prior to the flight tests using the University of Michigan Nonlinear Aeroelastic Simulation Toolbox (UM/NAST). These initial design studies were conducted on an 8-meter span configuration. This design exhibited stable flight when trimmed, and possessed an unstable Dutch roll coupled with wing bending that could be excited using aileron inputs or gust excitation.[30] A center tail that could rotate from horizontal to vertical was added in order to augment the lateral stability to return the flight to stable trimmed flight after exciting this unstable mode.[61] The flight tests detailed in CHAPTER 5 successfully demonstrated the aeroelastic behaviors sought in the design of the X-HALE.

This chapter details numerical studies of the 4- and 6-meter span X-HALE configurations that were built and flight tested. UM/NAST was used to simulate the aircraft response to the recorded control surface inputs during flight, and the simulated results were compared to the available flight data. Through study of the correlations between the numerical and experimental data, further understanding of the aircraft behavior was achieved in support of validation of the UM/NAST formulation.

6.1 Simulation Correlations with the RRV-4 Flight Tests

Figure 6.1. The RRV-4 in flight

6.1.1 Flight Test Data

A subset of the flight test data was extracted in order to determine the correlation between behavior seen in flight tests and the predictions of the numerical model. The aircraft state measured at the start of the extracted flight test data and the initial conditions of the simulation are given in Table 6.1. The starting thrust value used for the simulation model corresponds to the trimmed condition at this speed, originally presented in Table 4.6. The time-marching simulation in UM/NAST allows specification of the initial velocity, thrust per motor, body angle of attack (pitch) and body sideslip angle. Thus, body roll angle and body rates were not used as starting values to the numerical study. The flight test data showing the aircraft inputs and response during a thirty second window of time is plotted in Figure 6.2 through Figure 6.3.

Table 6.1. RRV-4 aileron response starting conditions

Aircraft State	Flight Test	Simulation	Units
Velocity	14.51	14.51	m/s
Thrust per Motor	4.0	5.78	N
Yaw Angle	-43.60	0	deg
Pitch Angle	5.36	0	deg
Roll Angle	-32.4	0	deg
Yaw Rate	-29.70	0	deg /s
Pitch Rate	5.47	0	deg /s
Roll Rate	2.69	0	deg /s

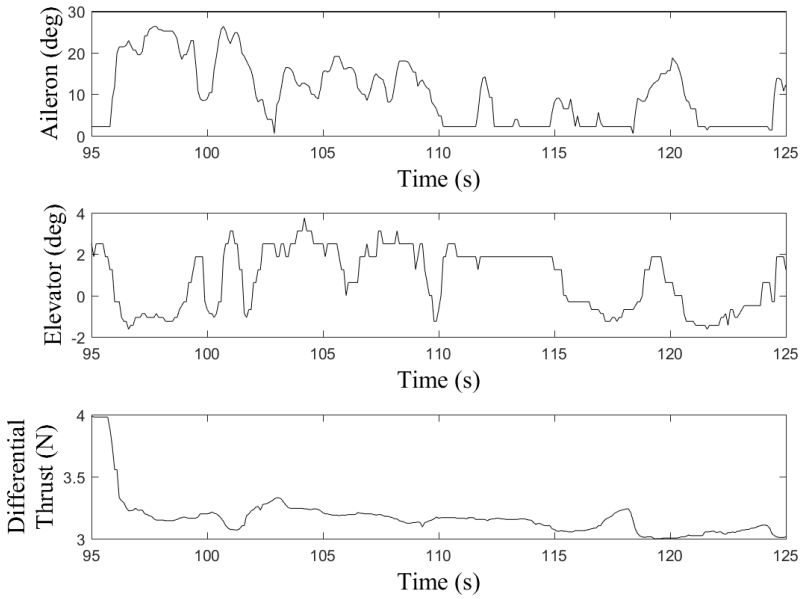

Figure 6.2. RRV-4 flight test: control surface inputs during turn

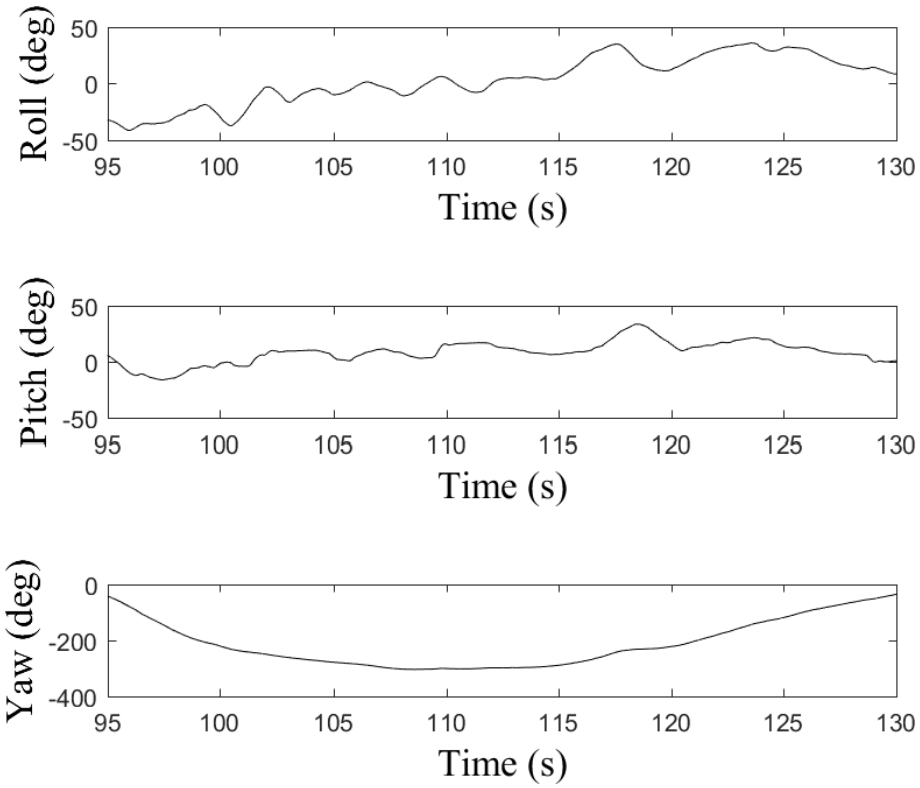

Figure 6.3. RRV-4 flight test: body orientation during turn

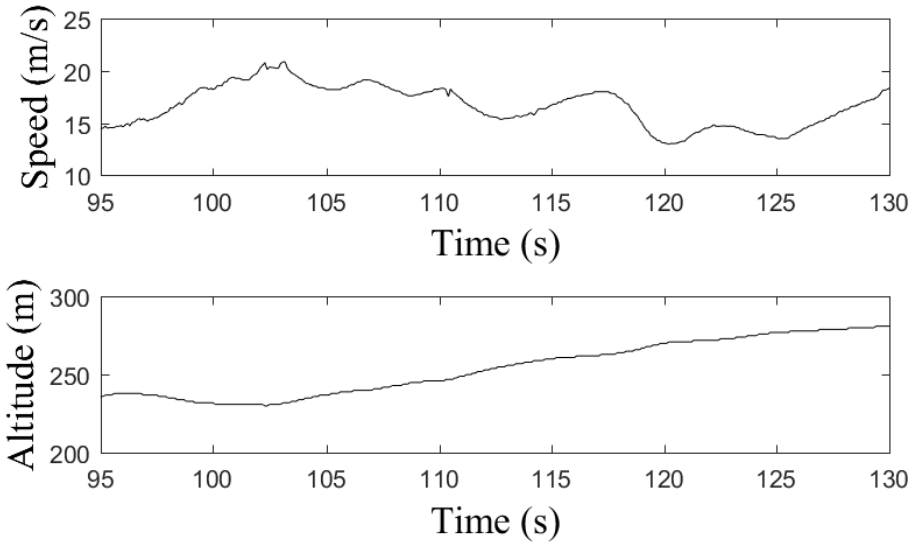

Figure 6.4. RRV-4 flight test: speed and altitude during turn

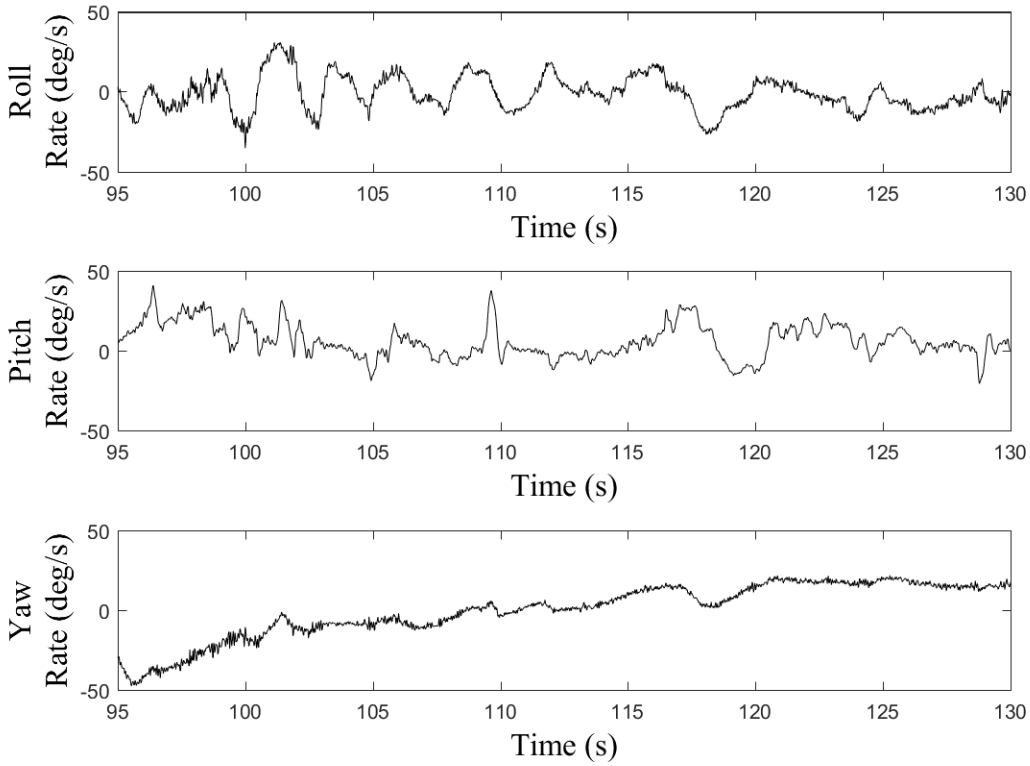

Figure 6.5. RRV-4 flight test: aircraft body rates during turn

The maneuver commanded by the control surface inputs shown in Figure 6.2 was a left-hand turn that was part of the continuous figure-eight pattern the pilot was flying around the field. The inputs during this turn were bang-bang style commands, with a large aileron and elevator deflection used to initiate the turn. The ailerons were programmed with 100% differential to avoid adverse yaw, i.e. the positive aileron command corresponds to the left aileron deflecting upward, and the right aileron remaining at its zero-deflected condition. The negative elevator command corresponds to the horizontal tails rotating trailing edge down. A positive differential thrust commands the right side motor to increase in power, while the left motor reduces in power. The commands for this maneuver lasts for roughly four seconds before the command to return to equilibrium.

6.1.2 Comparison of Simulation with Flight Test Data

In order to simulate this turn, the control surface commands used during flight were replicated as a lookup table in UM/NAST, and the resulting simulation inputs are shown in Figure 6.6. The

simulation was started at at time *t=0* with the initial conditions given in Table 6.1, and the inputs were applied starting from the first timestep. The differential thrust offset used for lateral trim was removed from this simulation to replicate the differential thrust command. The flight test data was zeroed to the start of the maneuver for an improved visualization of the response, and the comparison to the simulated flight behavior is presented in Figure 6.7.

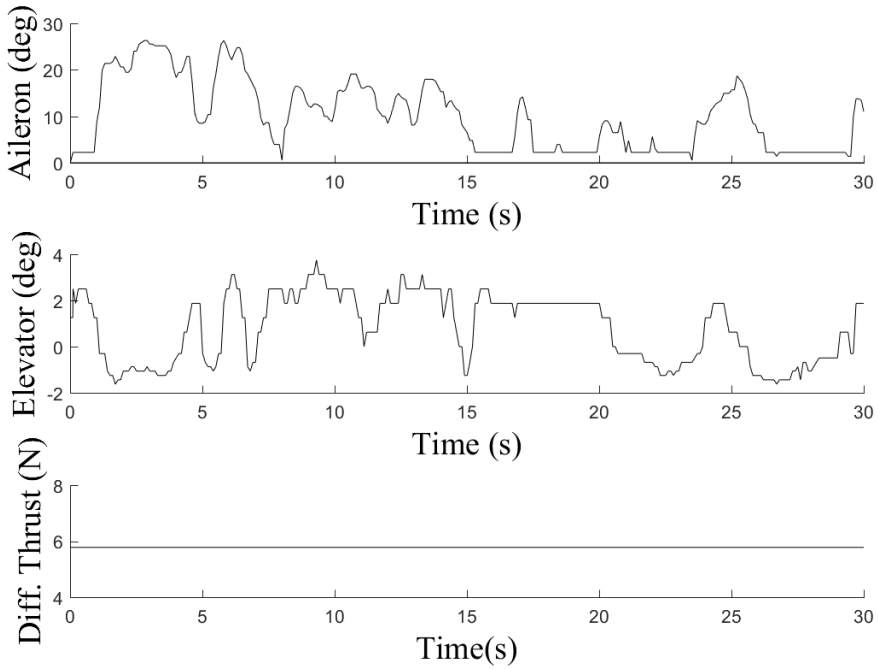

Figure 6.6. RRV-4 simulated control surface inputs for turn maneuver

The flight test data shows that the aircraft had an initial yaw rate as well as a nonzero heading angle, and this is evident in the plot of the yaw angle. This initial yaw rate can't be replicated within the UM/NAST framework, however in both the simulation and the flight test, the response to this aileron input is a left handed turn. The pitch angle shows particularly good agreement during the 4-second turn, with the pitch angle amplitudes diverging around 8 seconds into the maneuver. During the flight, the body angle of attack oscillated between ±10 degrees following the turn as the pilot continued the figure-eight pattern. The behavior simulation correlates very well with the flight data, however the body angle is offset by approximately 10 degrees, oscillating between –20 and 0 degrees. The simulated roll behavior also follows the general trend of the flight test, however the high frequency content of the roll response is missing from the simulation. This high frequency is likely due to the fact that the differential thrust and throttle were being commanded continuously throughout the turn and afterward, but these inputs

were assumed constant in this simulation. The speed shows similar results, where the trend to the flight test correlates relatively well, but the high frequency content of the response is missing. During a maneuver with such large roll angles, the aircraft lift vector is not oriented vertically, so the aircraft tends to lose altitude, sideslipping until it returns to equilibrium. This effect is shown in the simulation, however the measurd data indicates the opposite occurred during the flight test. The GPS data shows that the aircraft climbed 50 meters during this 25 second time period, while the simulation indicates that the aircraft lost altitude at the same rate.

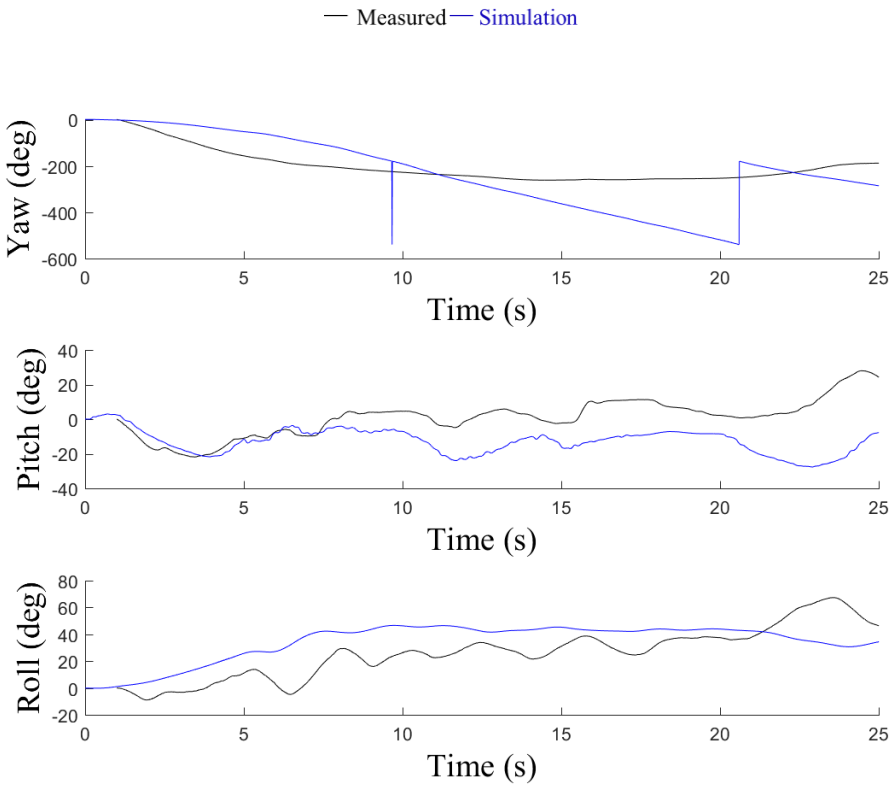

Figure 6.7. RRV-4 simulated vs measured rigid body motion during turn maneuver

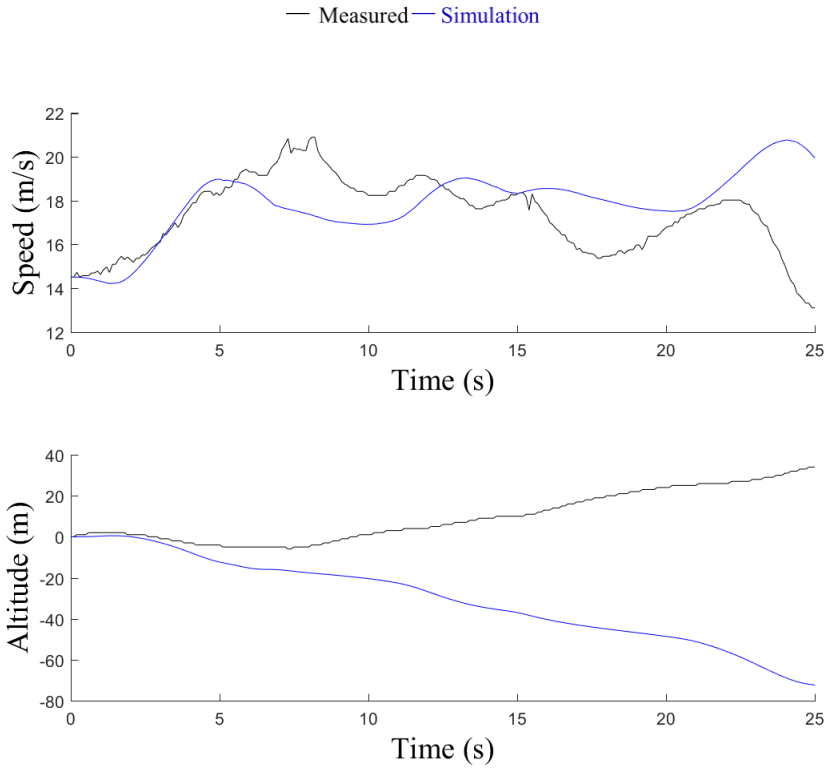

Figure 6.8. RRV-4 simulated vs measured altitude and speed during turn maneuver

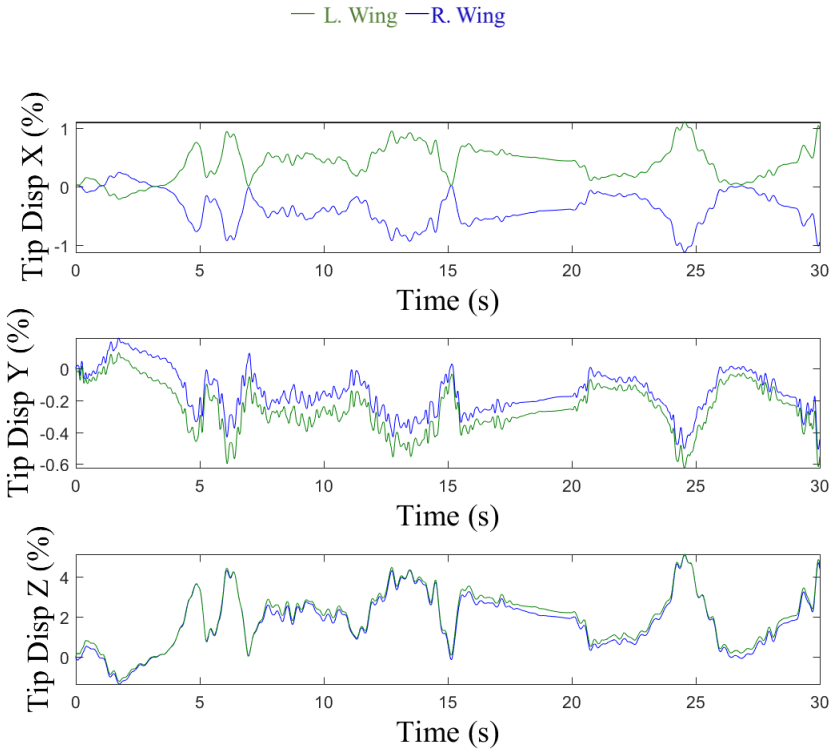

Figure 6.9. RRV-4 simulated wingtip displacement during turn maneuver

6.2 Simulation Correlations with the RRV-6A Flight Tests

Figure 6.10. RRV-6A during flight

During this flight, two aileron inputs were given to the aircraft to simulate gust-like excitations. The first aileron input (A1), shown in Figure 6.11, was commanded while the aircraft was in a vertical center tail configuration. A polynomial (cubic) curve fit of aileron input A1 was used in Figure 6.11 for the UM/NAST simulation to avoid higher frequency excitation as result of the low resolution in the recorded servo signal. A second aileron input (A2), shown in Figure 6.12, was commanded with the aircraft in the marginally stable horizontal center-tail configuration. This higher frequency input was an attempt to excite the unstable dutch roll coupled with the first wing bending mode observed in simulations and in exploratory flight trials. Llinear interpolation was used to represent aileron input A2 before applying it to the simulation.

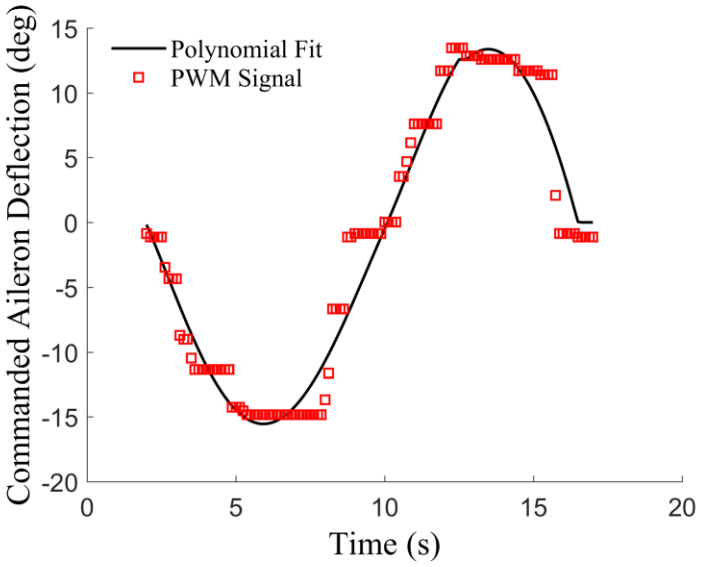

Figure 6.11: RRV-6A simulated vs measured aileron input A1

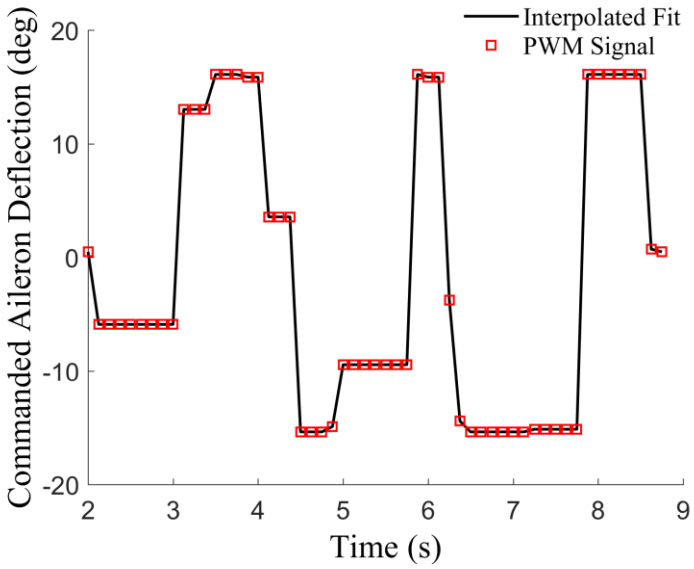

Figure 6.12: RRV-6A simulated vs measured aileron input A2

For the dynamic, time-marching simulation, the motors and elevators were set to their trimmed value, given in Table 4.10, and did not change from this constant setting during the aileron excitation. This section describes the results of these simulations and compares them to the data gathered during the test flights.

6.2.1 Aircraft Rigid Body Response to Disturbance Input

The simulated vertical displacement of the aircraft body frame from its initial position is compared to the measured GPS altitude. The magnitude of the body frame speed is compared to the measured GPS speed. The UM/NAST simulation assumes zero wind-speed, so the UM/NAST modeled airspeed and ground speed are identical, and direct comparison to the GPS speed are made without correcting for wind effects. The simulated yaw angle of the aircraft body frame relative to its initial orientation is compared to the measured GPS heading angle. The simulated roll and pitch angles are compared against estimates of the aircraft roll angle and pitch angle made from post-processing of the onboard camera data. The simulated and estimated wingtip displacement are normalized with respect to the initial wingtip positions.

Comparisons between the simulation results and experimental data for input A1 are shown in Figure 6.13 through Figure 6.18. The aircraft is modeled in the vertical center tail configuration using the parameters described previously.

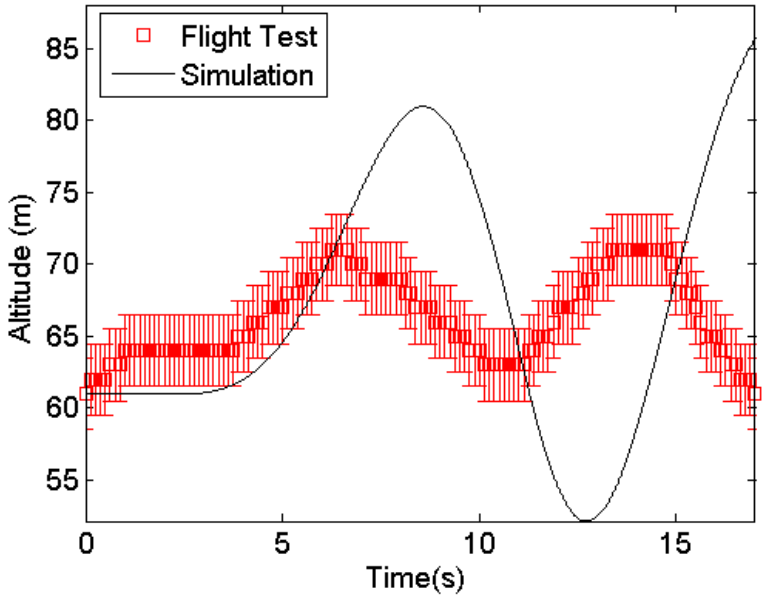

Figure 6.13. RRV-6A simulated vs measured altitude for aileron input A1.

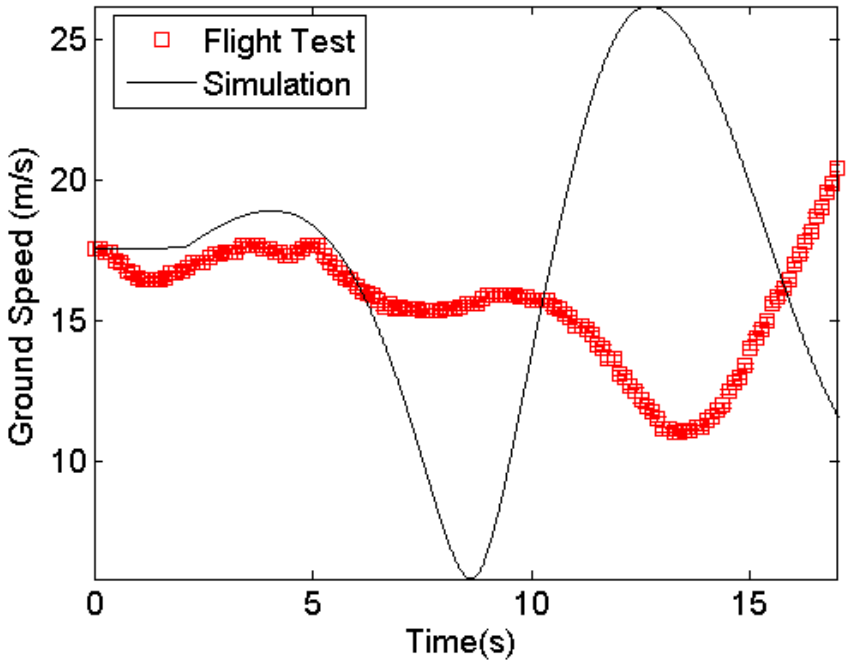

Figure 6.14. RRV-6A simulated vs measured speed for aileron input A1

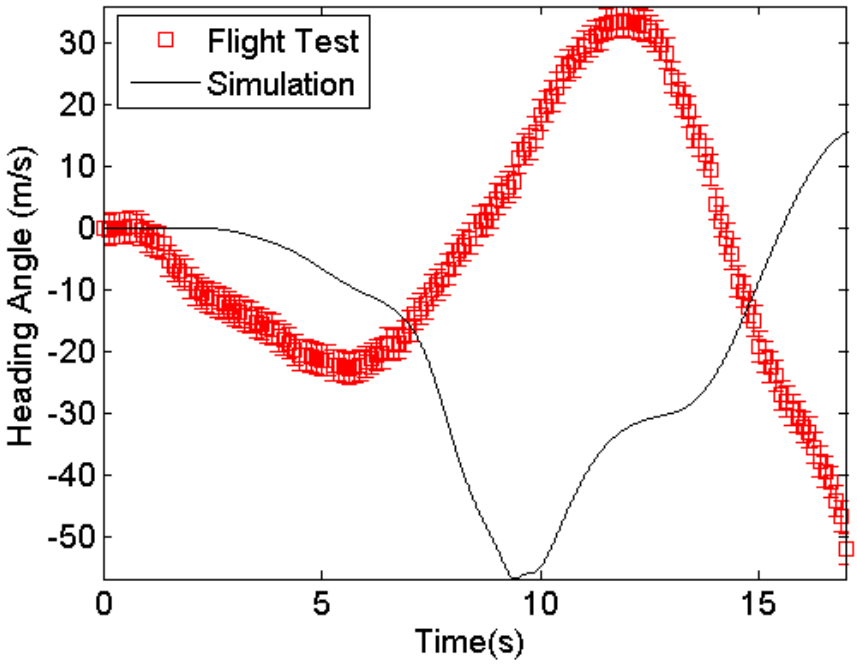

Figure 6.15. RRV-6A simulated vs measured heading angle for aileron input A1

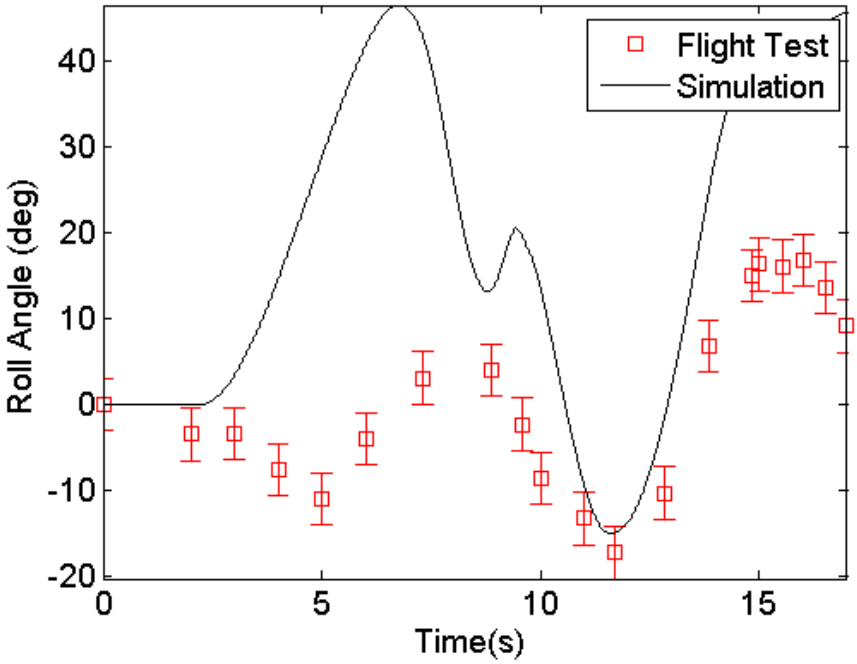

Figure 6.16. RRV-6A simulated vs measured roll angle for aileron input A1

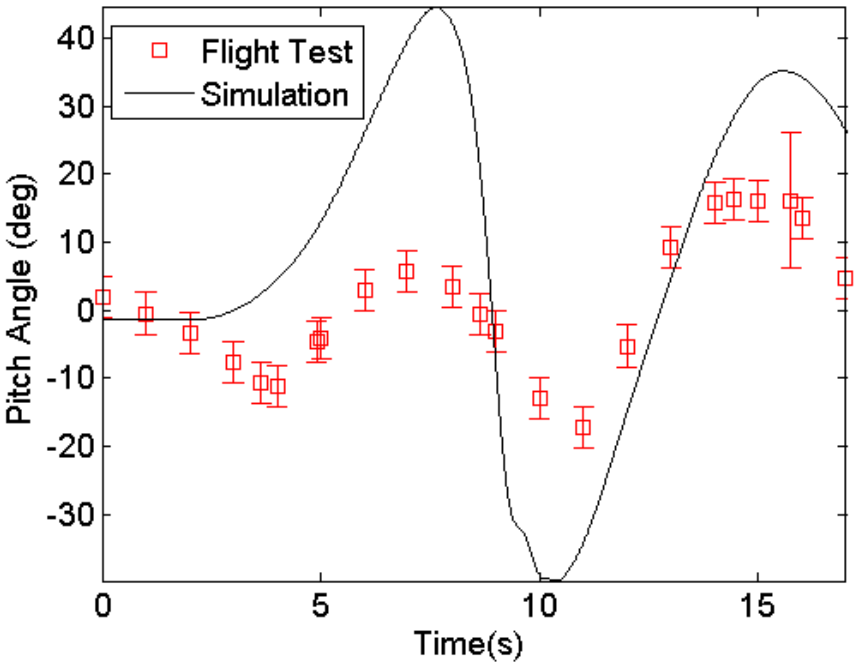

Figure 6.17. RRV-6A simulated vs measured pitch angle for aileron input A1

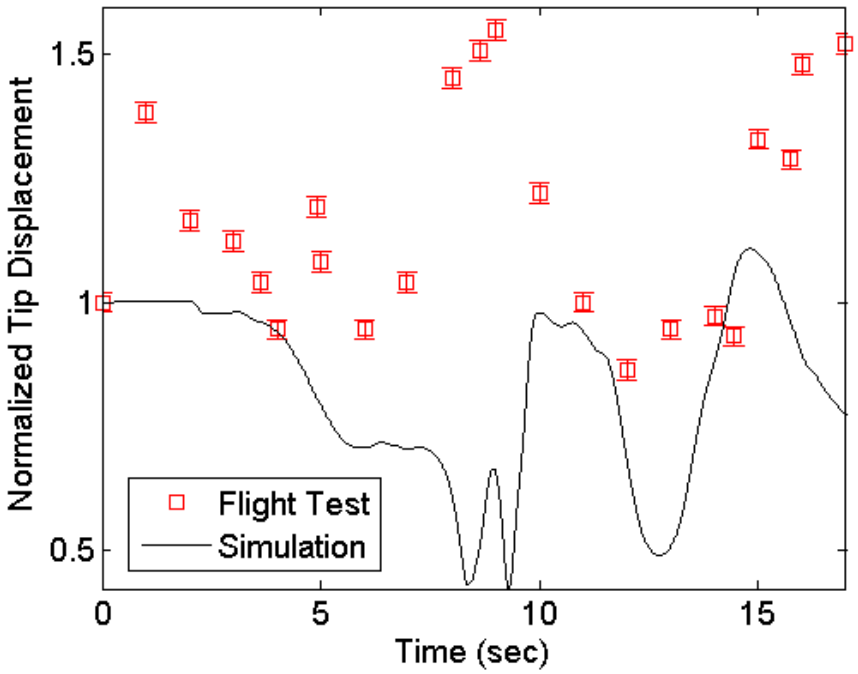

Figure 6.18. RRV-6A simulated vs measured tip displacement for aileron input A1

The simulated RRV response to input A1 is more pronounced than the response seen in flight. In particular, the duration of the input yields an extremely high amplitude roll (Figure 6.16)

and pitch (Figure 6.17) responses in the simulation. The actual aircraft exhibited much calmer Dutch-roll-like behavior that was observed to damp out within two cycles without pilot intervention due to the combined restoring forces of the ventral fins and vertically positioned center tail. Conversely, the simulated wingtip deflection (Figure 6.18) decreases from the initial value for the majority of the input, while the wingtip displacement measured during actual flight oscillated between the initial position and a high-dihedral configuration. When comparing the basic trends of altitude (Figure 6.13) and speed (Figure 6.14) between the simulation and actual flight, there are significant discrepancies, showing opposite behavior in some of the time segments. This clearly indicates that some of the input parameters in the simulation are not representative of the experiment. Unfortunately, due to the limited instrumentation, no further improvement can be made for this case.

Comparisons between the simulation results and experimental data for input A2 are shown in Figure 6.19 through Figure 6.23. For this maneuver, the aircraft is modeled with the center tail in its horizontal position.

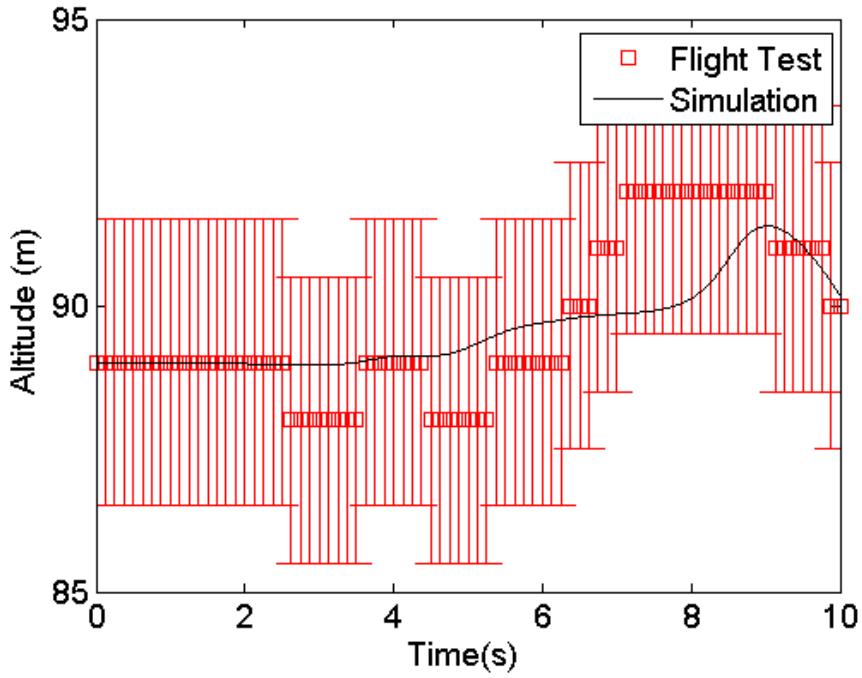

Figure 6.19. RRV-6A simulated vs measured altitude for aileron input A2

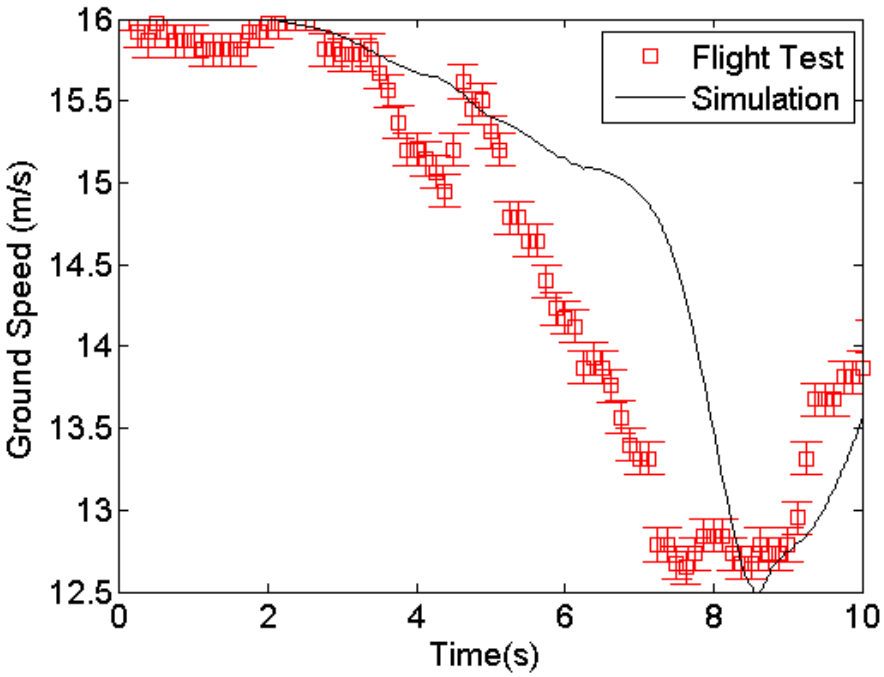

Figure 6.20. RRV-6A simulated vs measured speed for aileron input A2

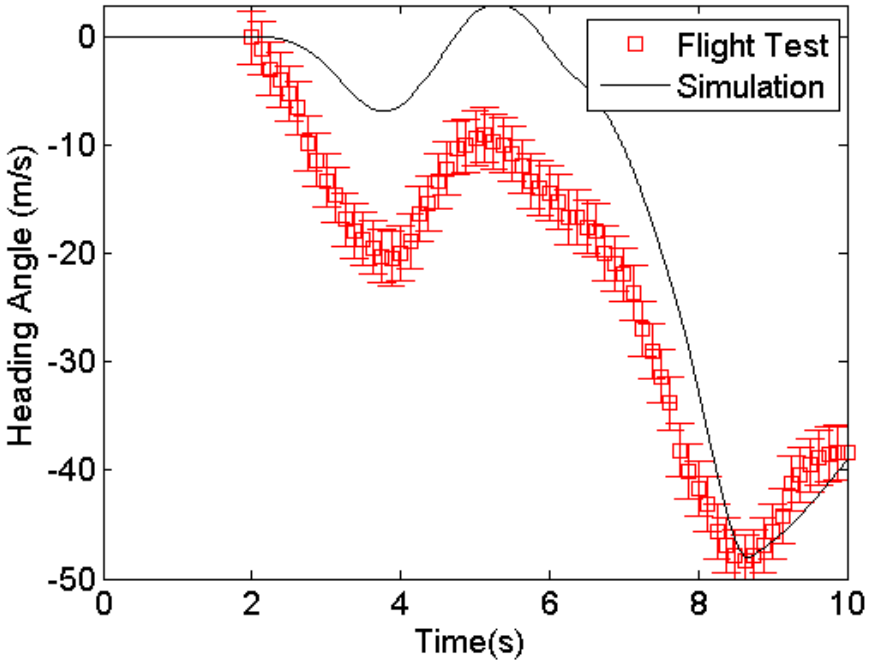

Figure 6.21. RRV-6A simulated vs measured heading angle for aileron input A2

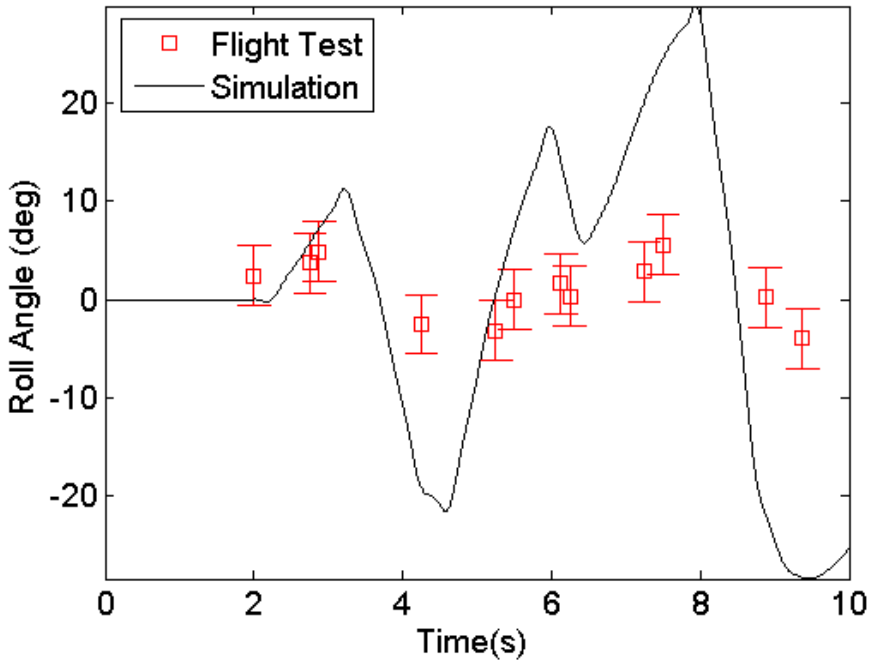

Figure 6.22. RRV-6A simulated vs measured roll angle for aileron input A2

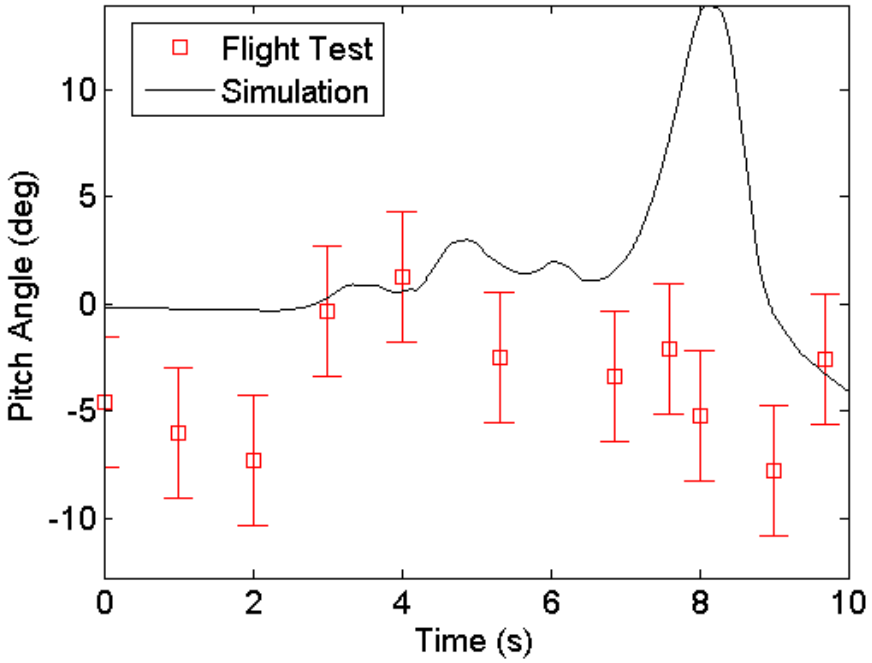

Figure 6.23 RRV-6A simulated vs measured pitch angle for aileron input A2

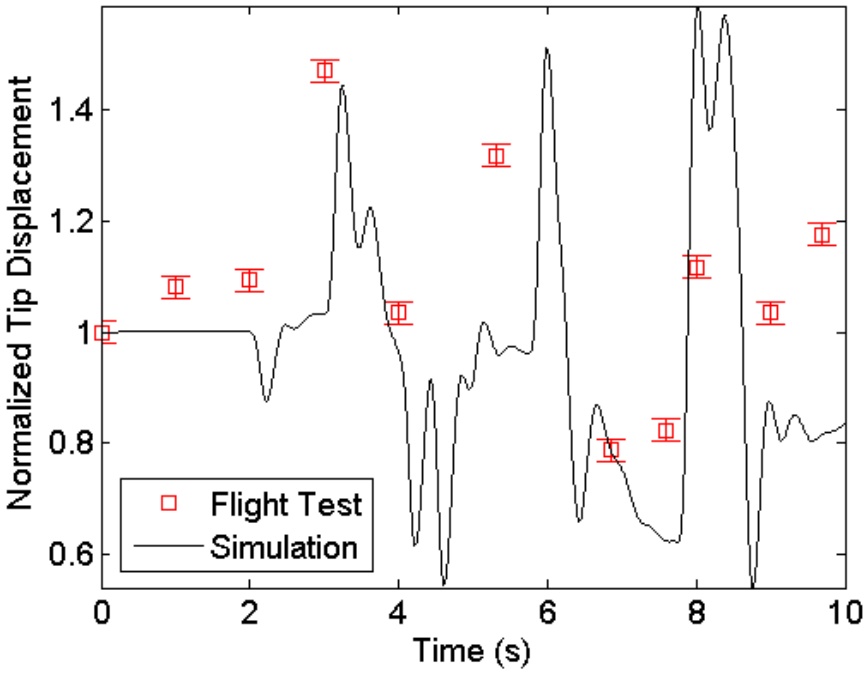

Figure 6.24. RRV-6A simulated vs measured tip displacement for aileron input A2

The RRV's altitude and speed responses to aileron input A2, shown in Figure 6.19 and Figure 6.20, are very close to the corresponding simulated ones. After the input, the RRV began to exhibit Dutch-roll-like coupling between the yaw angle and excited roll motion. After several seconds, the pilot had to inititate a turn to avoid crossing an airfield boundary. The pilot flipped the tail to its vertical position, and the immediate increase in the lateral stability of the aircraft arrested the coupled oscillatory motion. Both simulation and experiment reinforce this behavior: in the absence of additional inputs, strong but rapid aileron disturbance caused a small, fast-settling increase in altitude and a significant drop in speed. This input also induced negative yaw, shown in Figure 6.21, and if left without pilot input, the aircraft would continue to travel in a circular path as the roll angle settled back to its trimmed, wings level state. The simulated roll and pitch angle responses, shown in Figure 6.22 and Figure 6.23, are significantly more pronounced than their corresponding measured ones to input A2. This is most evident for the roll angle response (Figure 6.22). Previous attempts to excite a roll response during the same test flight using smaller amplitude inputs resulted in a negligible roll response.

Overall, the measured aircraft response after input A2 shows much better correlation to the simulation than the response after input A1. The control input frequency has a significant effect on the low frequency response of the aircraft that is not captured with the current simulation parameters. From the wingtip deflection correlation, shown in Figure 6.24, it can be seen that the simulation closely predicts the initial peak in tip displacement after the aileron input. However, the simulation fails to capture the decaying amplitude of structural response, suggesting that there is a significant source of damping in the experiment that is not adequately modelled in the simulation. Further analysis to determine the vehicle roll response, its relationship to wingtip deflection, and correlations with future flight test measurements are needed to understand this behavior, and direct measurements of wing shape and wingtip displacement will be required before more detailed correlation can be completed.

The results of the flight tests showed that the aircraft did exhibit the expected aeroelastic behavior, including the capability of developing a large, sustained wingtip displacement during flight, and an unstable dynamic flight mode that was excited using the aircraft's ailerons. The goal of the next phase of flight tests was to conduct more detailed studies of the in-flight behavior to develop controllers to aid the pilot in the operation of the fully-instrumented ATV configurations.

6.2.2 Discussion of Error and Uncertainty in RRV-6A Flight Test Data

Regarding uncertainties in the data, several sources must be considered in the analysis of the results shown in the previous section. The error inherent in the various sensors as well as uncertainty in the test conditions and post-processing contributed to the overall error in the correlation study. The primary sources of uncertainty in the flight data are described below as well as brief recommendations for future test flights.

As mentioned previously, the aircraft rigid-body and structural response, specifically roll angle, pitch angle, and wing-tip displacement, were not measured directly during the test. This data was estimated from post-processing of the onboard video. The cameras use a fish-eye lens, which captures a field of view of nearly 170 degrees, but also distorts objects near its edges. The camera is mounted such that the aircraft is always in the center of the frame, as shown in Figure 6.10. However, during very large deformation, the wing can extend into the distorted region. Furthermore, while the images themselves measured 1920 x 1080 pixels, the aircraft occupies a very small percentage of the overall frame, so a single pixel corresponds to a significant portion

of the overall motion of the aircraft within the frame. Thus, the amplitudes of the roll angle, pitch angle, and wingtip displacement estimated from those images have considerable uncertainty.

The finite measurement accuracy of the sensors used in the X-HALE RRV are listed in Table 6.2. The accuracy of the rigid body orientation and wingtip displacement measurements taken from the onboard cameras are indicated in the plots above as error bars. These values were based on the camera resolution. It is important to note that the actual error in measured speed is worsened by the fact that the aircraft was not flying in a constant plane parallel to the ground. The difference between the aircraft speed and its ground (projected) speed was not accounted for in the accuracy presented in Table 6.2 or in results above.

Table 6.2. List of RRV-6A instrumentation measurement accuracies

Sensor	Measurement Accuracy
GPS Position	2.5 m
GPS Speed	0.1 m/s
Aileron Angle	1 deg
Motor RPM	200 rpm
GPS Course	2.5 deg
Roll Angle (camera)	3.036 deg
Pitch Angle (camera)	3.036 deg
Wingtip displacement (camera)	0.06 m

Finally, considerable error was introduced into the simulation by the use of parameters that were not measured during flight. Due to malfunctions in the data logging system, the elevator servo commands were not recorded during the test flight, and the simulated elevator deflections were assumed to be equal to the trimmed values. The simulated thrust inputs were also set to their calculated trimmed values. However, during the flight, the motors experienced individual variations in current draw and rpm, which resulted in variations in thrust during the test period. Finally, although the airfield conditions were nearly ideal, the wind speed gradient, temperature variation, and random excitations (e.g., thermals) are experimental conditions that influence the flight results but are not modeled within the simulation and must be considered in the final analysis.

6.3 Simulation Correlations with the RRV-6B Flight Tests

During the flight tests of the RRV-6B, a sinusoidal chirp signal was supplied to each control surface in turns and the aircraft response to the chirp was recorded. The chirp frequencies ranged

from 0.1 to 3 Hz. UM/NAST is used to calculate the trim condition at the start of the chirp input, and simulations of the response to this chirp starting from trimmed conditions are compared with flight test data.

6.3.1 Response to Roll Spoiler Input

For the simulated roll spoiler chirp response, the RRV-6B model is trimmed at 13.5 m/s. During the flight test, no inputs other than roll spoiler were applied during the chirp, so this trim does not use differential thrust offsets to balance model's negative yaw tendency. The roll spoiler inputs are applied starting at 0.5 seconds. The flight test data is referenced to its initial value to allow the trends to be seen more easily. The comparison is given in Figure 6.25, where the simulated response is shown in black, and the responses from three independent chirp excitations during flight are shown in blue, green, and red.

Both the numerical model and the actual RRV-6B demonstrate a strong negative yaw tendency when differential thrust is not actively applied to remove it. The model also captures the strong coupling that occurs with the pitch degree of freedom when the roll angle amplitude is large. The model responds quickly, and the high frequency content of the chirp is present in the simulated response. Once the simulated chirp ends at 12 seconds, the pitch and roll angles settle to an equilibrium. Actually, the flexibility of the RRV-6B's wings acted as a low-pass filter, absorbing the energy of the chirp into wingtip vibration so that there is little response from the rigid body motion. The roll response of the RRV-6B during the chirp is roughly equivalent to the response of the model to the first 1.5 seconds of the chirp. The large amplitude of the RRV-6B response relative to the model's response is due to the lack of trim in the aircraft at the beginning of the chirp input. Yaw and roll are coupled, so the negative yaw tendency of the RRV-6B also resuls in a negative roll. Before each chirp was applied, the pilot attempted to level the wings, but this excited roll oscillations that carried over into the chirp response. Thus, response of the aircraft during flight is the combination of the chirp response with the existing roll oscillations. Despite this poor match in the initial conditions of the chirp, the model tracks the rigid body response of the RRV-6B quite well. The speed and altitude trends are shown here to provide a reference for how the aircraft was moving in space during the tests.

Table 6.3. RRV-6B Roll Spoiler Chirp Starting Conditions

Aircraft State	Simulation	Units
Velocity	13.5	m/s
Thrust per Motor	4.0	N
Yaw Angle	0	deg
Pitch Angle	2.4	deg
Roll Angle	0	deg
Yaw Rate	0	deg /s
Pitch Rate	0	deg /s
Roll Rate	0	deg /s

Table 6.4. RRV-6B Elevator Chirp Starting Conditions

Aircraft State	Simulation	Units
Velocity	18.5	m/s
Thrust per Motor	9.5	N
Yaw Angle	0	deg
Pitch Angle	0	deg
Roll Angle	0	deg
Yaw Rate	0	deg /s
Pitch Rate	0	deg /s
Roll Rate	0	deg /s

6.3.2 Response to Elevator Input

For the simulated elevator chirp response, the model was trimmed at 18.5 m/s to match the starting conditions of the first chirp. There is a one-second delay in the applications of chirp 2 and 3, so these measured chirp responses are offset from the first for equivalent timescales. As mentioned previously, there are ongoing roll oscillations present in the RRV-6B response that are not due to the chirp, but are the result of pilot input just before the chirp. The frequency of that roll response remains the same across all inputs and chirps.

Both the numerical model and the RRV-6B are quick to respond in the longitudinal degrees of freedom, so the high frequency content of the elevator excitation is present in the response. The model exhibits a higher pitch rate in its response, however, resulting in a response that is higher amplitude than seen in flight.

The model demonstrated coupling between the roll and pitch degrees of freedom in the roll spoiler chirp response, however, that coupling is absent in the elevator response. This is due to the fact that the roll spoiler is an asymmetric excitation, with only one spoiler deploying at a time. The effect of spoiler deployment on the wingtip displacement can be seen in Figure 6.28.

When the left spoiler is deployed, the loss of lift and increase in drag on the wingtip segment result in larger displacements than those seen on the right wingtip, where the spoiler is not deployed. This larger displacement corresponds to an asymmetric aerodynamic load and moments that excite oscillations in the body angle of attack until the chirp ends and the model regains equilibrium. Contrast this with the elevator deflection, where the excitation is symmetric about the aircraft center. The only moments being applied by this excitation are in the pitch direction, so the model experiences no roll oscillations. The large induced roll oscillations experienced by the RRV-6B make it difficult to decisively conclude whether pitch-roll coupling is present during the elevator chirp. However, the model accurately predicts the coupling trend that is seen during the roll spoiler response.

Additionally, the simulations indicate the aircraft's yaw tendency increases a function of speed. This supports the conclusion that the propeller downwash is a primary driver of the yaw tendency, as the propeller velocity increment increases with oncoming flow velocity. Since airspeed was not captured during flight, only GPS speed, it is unclear which model speed is most accurate, however the simulation correlation suggests that the airspeed of the aircraft is higher than the relative ground speed being measured by the GPS.

6.4 **Conclusions**

This chapter presented the results from the flight tests of three different configurations of the X-HALE Risk Reduction Vehicle. The goal of these test flights was to assess the X-HALE airframe's handling qualities and stability as well as verify that the configuration exhibits large deformations and elastic-rigid body mode coupling. A secondary objective was to use whatever data could be extracted from those flights for correlation with aeroelastic simulations performed using UM/NAST. To this end, the X-HALE RRV carried a limited sensor payload consisting of an RC-type data acquisition system and onboard cameras to record the aircraft response.

The expected coupled structural and flight dynamic response was observed in all configurations with varying degrees of intensity, including large sustained wingtip displacement during flight, and an unstable lateral dynamic mode that can be excited using the aircraft control surfaces. The aircraft was controllable throughout the tests although it presented a strong left yaw tendency that degraded handling qualities during landing.

There is good agreement between the aircraft flight test and UM/NAST predictions in the rigid body responses. Despite significant differences in initial conditions, the UM/NAST model is able to capture the overall trend of the responses. The rigid body responses of each aircraft configuration include the effects of elastic coupling, so the positive correlations made for rigid body responses also suggest that the structural response coupling is also well captured. However, the wing deformation data from the fully instrumented aircraft is required to definitively validate the structural coupling.

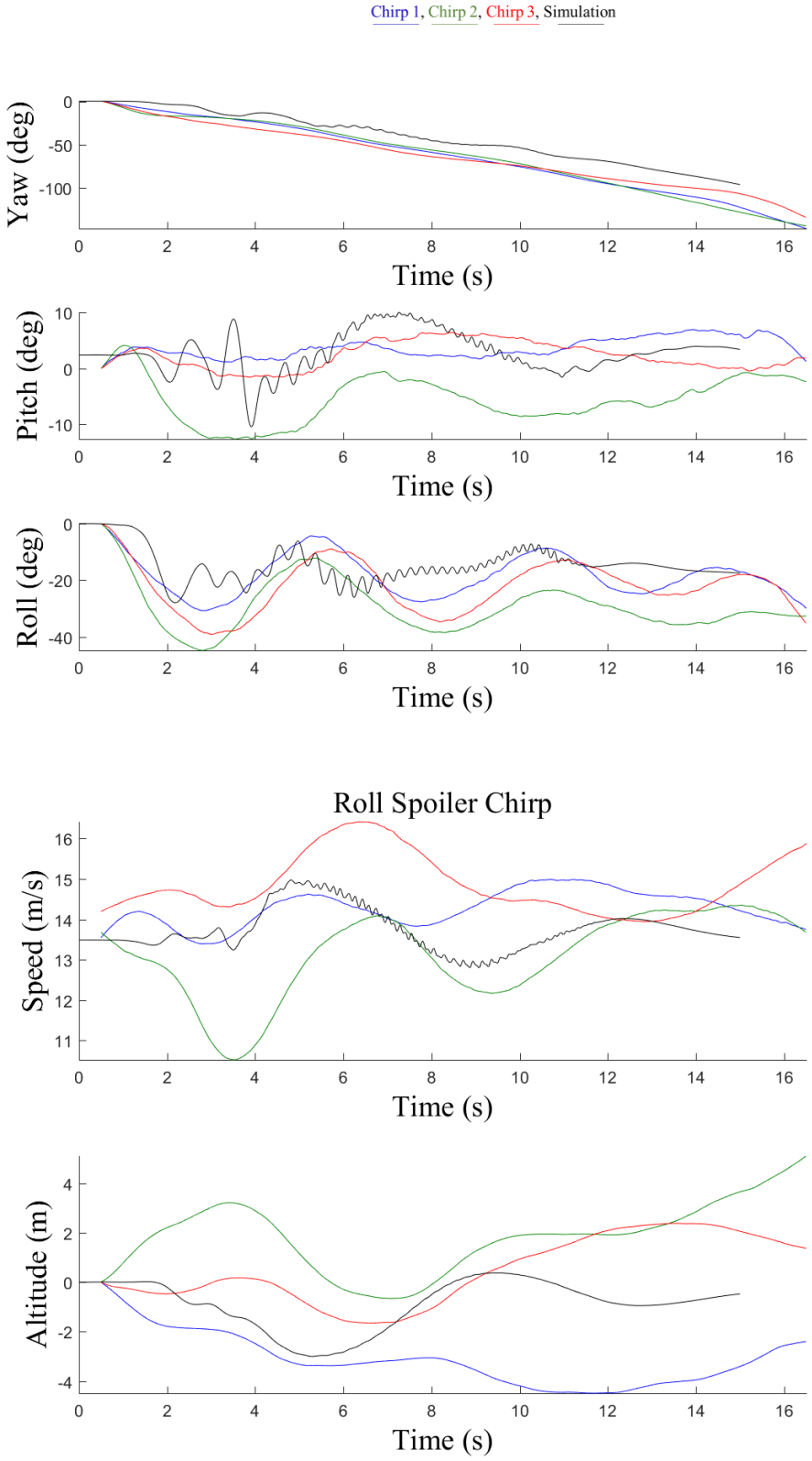

Figure 6.25. RRV-6B simulated vs measured roll spoiler chirp response

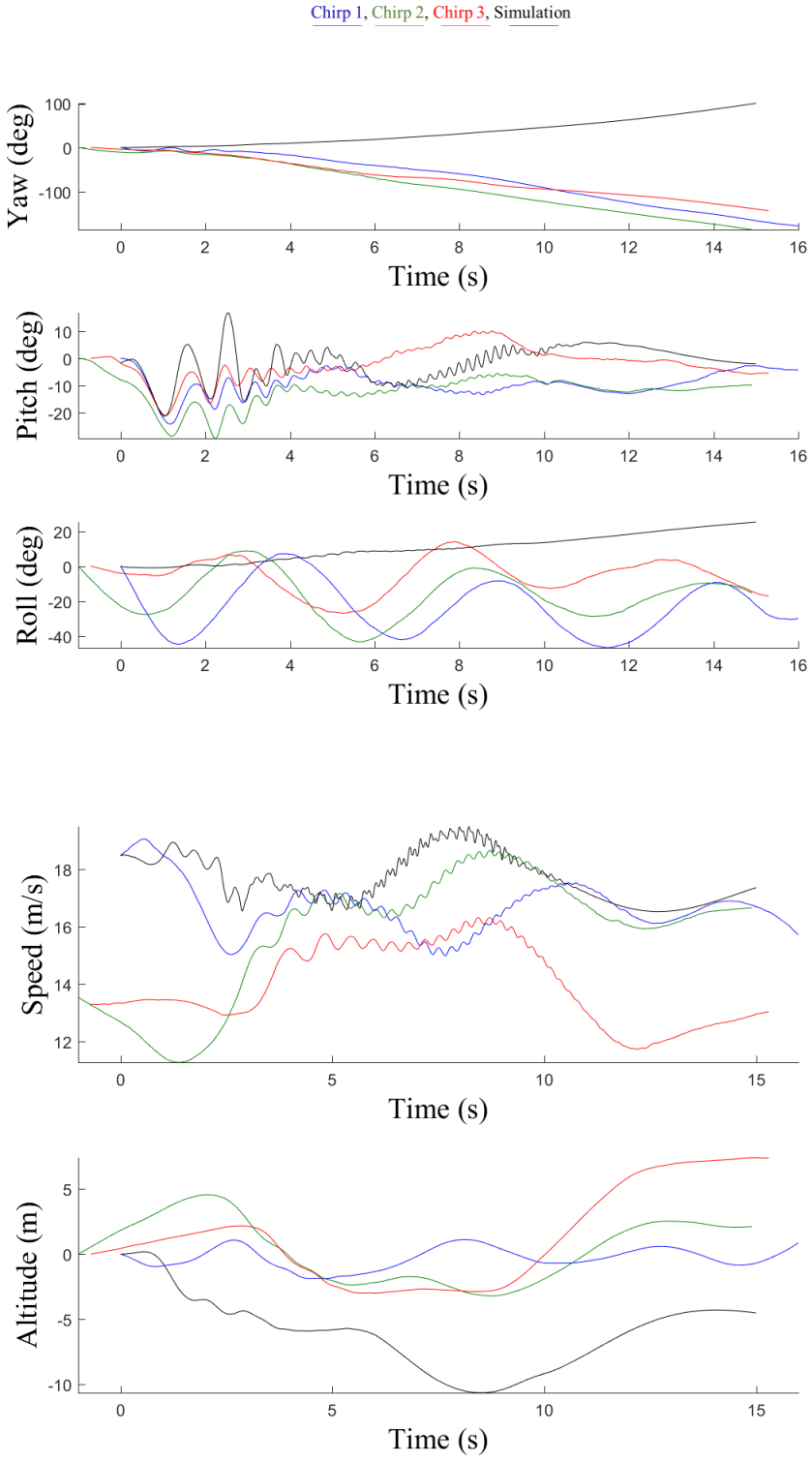

Figure 6.26. RRV-6B simulated vs measured elevator chirp response

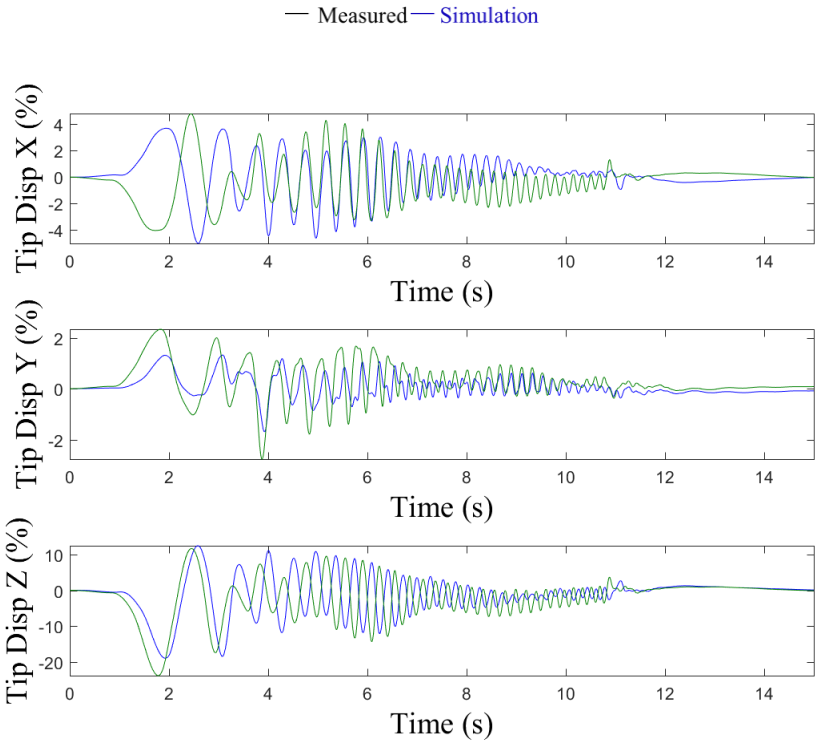

Figure 6.27. RRV-6B simulated wingtip displacement during roll spoiler chirp

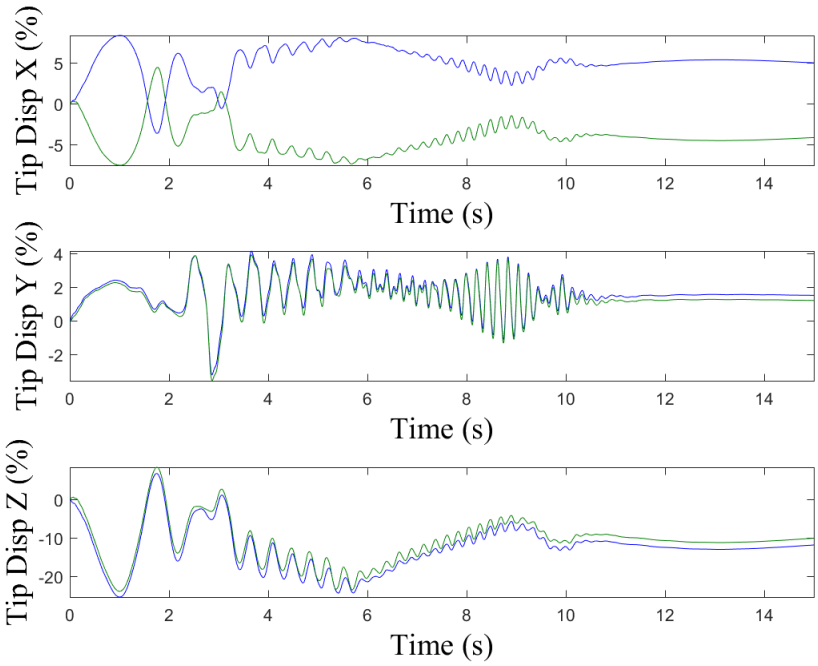

Figure 6.28. RRV-6B simulated wingtip displacement during elevator chirp

.

CHAPTER 7. Conclusions and Recommendations

This chapter summarizes the main contributions of this work, including the implementation improvements made to UM/NAST and the development and experiments performed with the X-HALE testbed. Some conclusions regarding the UM/NAST validation are presented, and recommendations for future work in this area are given.

7.1 Key Contributions of this Dissertation

The main goal of this work was the development, characterization, and flight testing of a flexible aircraft testbed. Three configurations of the X-HALE high altitude long endurance aeroelastic testbed were developed. The first model, known as the RRV-4, is a medium aspect ratio HALE-type aircraft used to provide initial verification of flight handling and stability characteristics of the X-HALE design before the more flexible 6-m configurations were flown. The first-generation X-HALE Aeroelastic Test Vehicle (ATV-A) was designed with a strain-gage based wing deformation measurement system. This was later replaced by the second generation X-HALE (ATV-B) with a stereovision wing shape measurement system to address the operational deficiencies of the strain gage instrumentation.

The elastic and inertia properties of the aircraft were measured and the properties of the components and the assembled configurations are provided. Wind tunnel tests were performed on the representative sections of the aircraft to experimentally assess its aerodynamic properties. The characterization data gathered facilitated the creation of flexible aircraft models that exhibit geometric nonlinearity through large deformation and coupled rigid-body and elastic behavior.

Flight tests of risk reduction versions of the X-HALE configurations– the RRV-4, RRV-6A, and RRV-6B– were conducted. The flight tests involved a variety of maneuevers, including takeoff, climb, turns, and control surface responses, and the control surface inputs and rigid body responses during these maneuvers were recorded with onboard sensors. Video of the wing deformation was recorded during these flights for a full evaluation of the aeroelastic behavior of

the aircraft. These initial flight test data, combined with the detailed airframe characterization provides a preliminary dataset in response to the need for publicly available in-flight data of a very flexible aircraft, particularly for use in validation of the static, dynamic, and free-flight solutions of nonlinear aeroelastic solvers.

In parallel with the X-HALE development and flight testing, several improvements to the University of Michigan Nonlinear Aeroelastic Simulation Toolbox were implemented. The formulation for absolute and relative nodal constraints was expanded to allow multiple constraints to be defined within a single model. Using Lagrange multipliers, the position of an arbitrary number of the nodes may be defined using absolute, body-fixed constraints or relative node-to-node constraints. These constraints may be applied to the position of the node to create a pinned condition, or the constraint may be applied to the position and rotation of the node to create a 6-dof clamped condition. This expanded implementation improves UM/NAST's capability to model flexible structures with inter-member linkages and support types.

A propeller downwash module was developed to incorporate propeller downwash and wake effects into the UM/NAST's 2-D aerodynamic model. This module takes user-defined propeller parameters and applies an axial and transverse velocity increment to the model lifting surfaces within the propeller wake. A study on a multi-engine 4-m span flying wing model showed that considerable changes to aircraft stability may result from the use of propeller-driven engines on very flexible aircraft. This propeller downwash module provides a computationally efficient way to assess the aerodynamic effect of propeller engines on the flexible vehicle performance and stability before creating a higher fidelity model in a panel or CFD code.

An approach to creating a simplified, nonlinear aeroelastic model from experimentally validated FEM and CFD data was developed. This approach was used to develop a simplified UM/NAST model of the X-56A Multi-Utility Aeroelastic Demonstrator. The X-56A is an unmanned blended wing-body aircraft used for in-flight studies of flutter and flutter suppression techniques. This model was used to investigate the impact of wing flexibility and payload configuration on the X-56A flutter boundary. The performance of this simplified model was verified using flutter boundary predictions made by other researchers using higher fidelity methods. As an aircraft progresses through its design cycle, the cost of design modifications becomes increasingly expensive, particularly in time and computational resources. These results illustrate the efficacy of using UM/NAST and similar solvers to perform low-cost targeted

investigations of configuration changes in the detail design and flight testing phase of aircraft development.

Simplified models of the three X-HALE RRV configurations were developed using the characterized aircraft properties. A series of numerical studies were performed to assess the correlation between the solutions of UM/NAST with the X-HALE flight tests. Wing deformation was not measured during this set of flight tests, but the rigid body motion incorporates effects of wing flexibility. These effects were mostly captured in the UM/NAST predictions, however high quality measurements of the wing deformation during flight is needed before the UM/NAST formulation can be fully validated.

7.2 Recommendations for Future Work

The numerical framework of UM/NAST may be used for aeroelastic analysis of flexible vehicles from conceptual design through detail design and flight testing. Efforts to improve the aerodynamic modeling capability are ongoing, including the development of a UVLM-based aerodynamic module and a viscous particle vortex method-based propeller downwash module to incorporate lifting surface interference effects.

Improvements can also be made to the modeling of control surfaces within UM/NAST. The current formulation does not include aeroservoelastic effects, which have been shown to be particularly important in very flexible aircraft. The specification of initial body rates in time-marching simulations is also a desirable feature for correlating experimental and numerical experiments.

Flight tests with the X-HALE testbed are also an ongoing effort, and there are a number of aeroelastic experiments that may be conducted with this testbed. The X-HALE simulation model may be used to evaluate controller design methodologies, and the testbed aircraft can be used to validate these results. The X-HALE can be used to evaluate shape-based control methodologies, as it is already instrumented with a camera-based measurement system. However, additional integration of these camera measurements to the control system of the aircraft would be required. With an adequate controller, the X-HALE can also be used to study gust response alleviation techniques, which is a currently a topic of intense interest. Additionally, the X-HALE modular design allows for the installation of morphing wing segments to evaluate their effectiveness in actuating maneuvers.

APPENDIX A. X-HALE Materials

This appendix gives a summary of the materials used in the construction of the composite elements of the X-HALE testbed. The constructed components are the wing, tail, and spine. The first section details the source and properites of the materials used throughout the X-HALE construction. The second section details the dimensions of the materials used in the layup of each composite component.

A.1 Material Properties

Table A.1 lists the manufacturer and properties of the foam core used in the wing segments and tail. Table A.2 lists the manufacturer and properties of the fiberglass composite used for the skin of the wing and tail and the motor pod's aerodynamic fairing. Table A.3 lists the manufacturer and properties for the graphite-epoxy composite used to build the motor pod spines and tail connectors. Table A.4 lists the manufacturer and properties of the adhesive film used to bond together the components of the wing and tail prior to curing. The properties listed are all publicly available on the material data sheets provided by the manufacturer unless otherwise indicated.

Table A.1. Foam core material properties

Foam Core	Density	Elastic Modulus	Shear Modulus
Rohacell 31-IG Hi-Temp Foam	23 kg/m^3	36 MPa	13 MPa

Table A.2. Fiberglass-epoxy material properties

Pre-preg Epoxy-glass	Cured Ply Thickness	Compression Modulus	Tensile Modulus	Fiber Areal Weight	Resin Spec. Gravity	Resin Tensile Modulus
Henkel 120/F155	0.12 mm	20.7 Gpa @24C	20.7 Gpa @24C	115 g/m^2	1.335	3.24 GPa

Table A.3. Graphite-epoxy material properties

Carbon-Epoxy Prepreg	Cured Ply Thickness	Compression Modulus	Tensile Modulus	Fiber Areal Weight	Cured Resin Density	Fiber Modulus
Cytec 7714A/G30-500	0.18mm*	97-117 GPa @ Room Temp	110-145GPa @ Room Temp	--†	1.25-1.26 g/cc	228 GPa

Table A.4. Adhesive film material properties

Epoxy Film Adhesive	Flatwise Tensile Strength	Cured Tensile Lap Shear Strength	Areal Weight
Hysol EA 9696	8.3 MPa @ 25C	43.4 @25C	293 g/m^2

A.2 Material Quantities

This section details the amounts and dimensions of materials used to construct the wing, tail, and carbon fiber spine layups.Table A.5 and Table A.6 detail the materials and layup details of the wingbox. The foam core is 7.6cm shorter than than the wing box itself. The additional length is used to create a cavity for the aluminum wing joiner to fit into. This cavity is made by wrapping the carbon fiber edges of the wingbox over a polished aluminum mold in the shape of the joiner, shown in Figure A.1 before attaching the aluminum mold to the foam core using adhesive film, as shown in Figure A.2.

Table A.5. Wing box layup materials

Wing Box	Quantity	Length	Width	Height
Foam Core	1	9.37x10^2	30	25.4
Fiberglass	1	1.02x10^3	5.40	--
Carbon Fiber	2	4.30x10^2	38.1	--
	8	38.1	22.86	--
Adhesive Film	2	90	38.1	--
Adhesive Film	2	9.37 x10^2	30	--
Adhesive Film	2	9.37 x10^2	20	--

* Ply thickness taken from Feraboli[79]

† Areal weight is the weight of the composite fiber reinforcement per unit area. There is no publicly available information on the carbon fiber used in this pre-preg or its weight or density.

Table A.6. Wing box layup order

Label	Plies	Material	Thickness (mm)	Orientation
1	5	E-Glass 120/F155	0.12	90/90/90/90/90
2	n/a	IM7/977-3 Dowel	1.0(diameter)	0
3	5	E-Glass 120/F155	0.12	0/0/0/0/0
4	2	IM7/977-3 Tape	0.137	0/0
5	1	E-Glass 120/F155	0.12	0
6	5	E-Glass 120/F155	0.12	0/0/0/0/0
7	1	E-Glass 120/F155	0.12	0

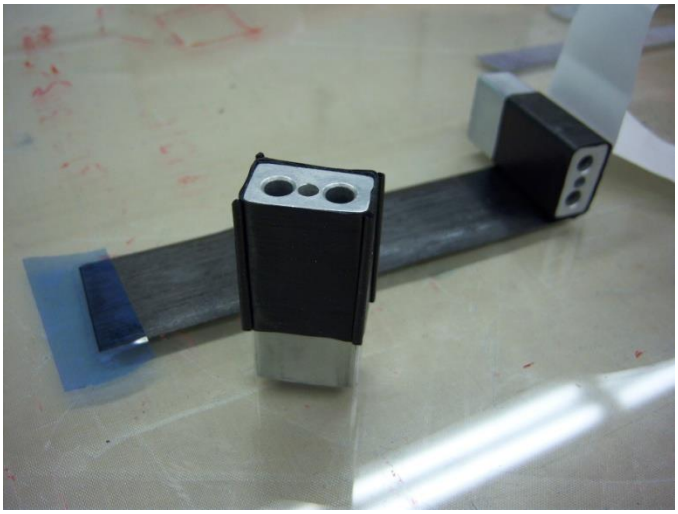

Figure A.1.Carbon fiber layup for wing box joiner recess

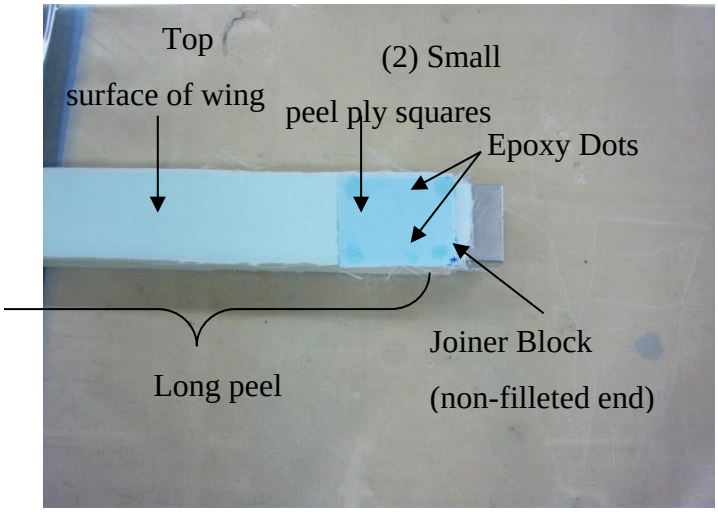

Figure A.2. Completed wing box layup

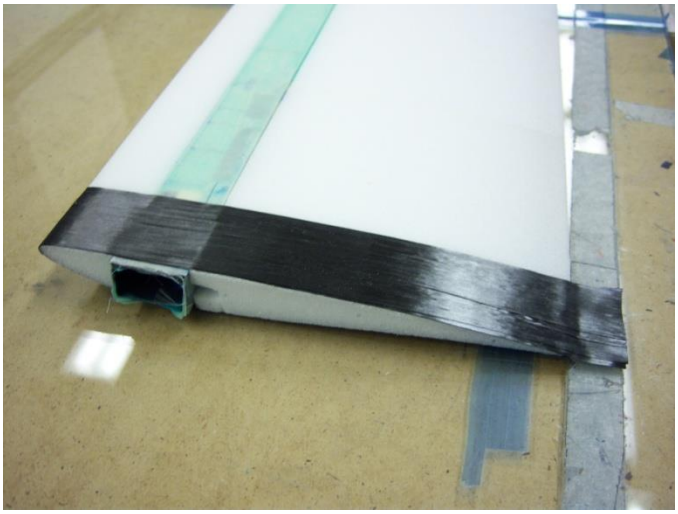

Figure A.3. Full wing layup around the cured wingbox

Once the wingbox is cured, the full wing is created by shaping foam around it to create the leading and trailing edge of the airfoil. The wingbox and foam shape is held together by strips of carbon fiber on the edges and the fiberglass skin is wrapped around the entire layup. The materials used in the wing layup are given in Table A.7 and the layup is shown without the final fiberglass skin in Figure A.3.

The tail requires only a single layup. The foam blocks are arranged around an aluminum mold, and the mold creates a cavity for the servo to be placed in during final assembly. The materials used in the tail layup are given in Table A.8 and a picture of the tail layup in progress is shown in Figure A.4.

Table A.7. Full wing layup materials

Material	Quantity	Length (mm)	Width (mm)	Height (mm)
Foam: Leading Edge	1	1.01×10^3	32	25.4
Foam: Trailing Edge	1	1.01×10^3	1.38×10^2	25.4
Fiberglass	1	1.02×10^3	425×10^2	--
Carbon Fiber	4	4.50×10^2	38.1	--
Adhesive Film	1	1.00×10^3	15	--
Adhesive Film	1	1.00×10^3	20	--
Adhesive Film	1	35	38.1	--

Table A.8. Tail layup materials

Material	Quantity	Length (mm)	Width (mm)	Height (mm)
Foam: Full Airfoil	2	1.65 x10^2	1.143 x10^2	25.4
Foam: Trailing Edge Large	1	1.27 x10^2	76.2	25.4
Foam: Trailing Edge Small	1	50.8	57.15	25.4
Foam: Leading Edge	1	1.78 x10^2	25.4	25.4
Fiberglass	1	2.54 x10^2	49.5	--
Fiberglass	1	2.92 x10^2	1.778 x10^2	--

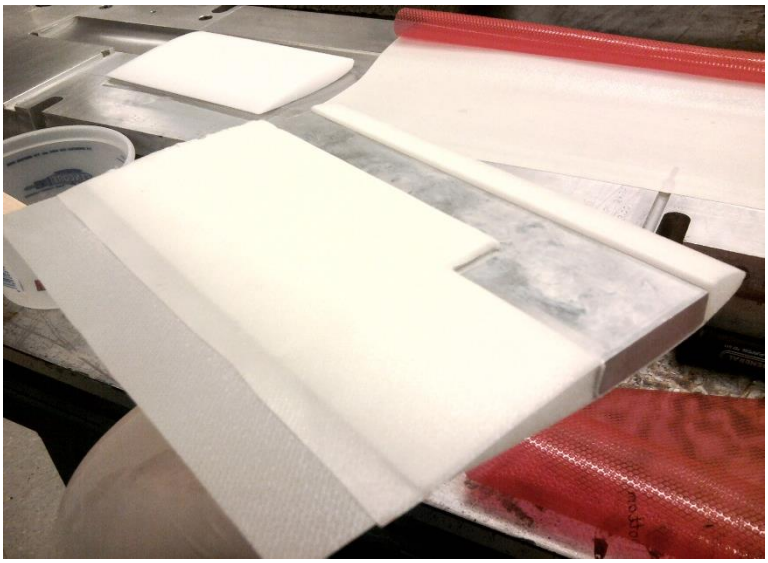

Figure A.4. Foam block placement in single ply tail layup

For each motor pod, the spine and tail connector are cut from a single 0.5m x 0.5m carbon fiber plate. The materials and layup of this plate is given in

Table A.9. Spine materials and layup

Spine Plate	Quantity	Length (mm)	Width (mm)	Height (mm)	Ply Orientation
Carbon Fiber	21	5.0 x10^2	5.0 x10^2	3	0/+45/-45/90/0/90/-45/+45/0

APPENDIX B. X-HALE Dimensions

The X-HALE aeroelastic testbed aircraft consists of a high aspect ratio wing broken in meter long segments. A motor pod is attached between each wing segment, and a tail boom extends aft of the aircraft from each motor pod. This appendix presents dimensioned drawings for the aircraft assembly and its key components.

Figure B.1 gives the planform view of the X-HALE aircraft. The drawing shows the six-meter configuration of X-HALE with the long center tail. This corresponds to the RRV-6A and RRV-6B configuration that were flown in X-HALE Flights #16-32. Further details of these flights are given in 0. Figure B.2 gives a dimensioned cross-section of the wing. The location of the reference axis used in the the UM/NAST model is shown by the red cross.

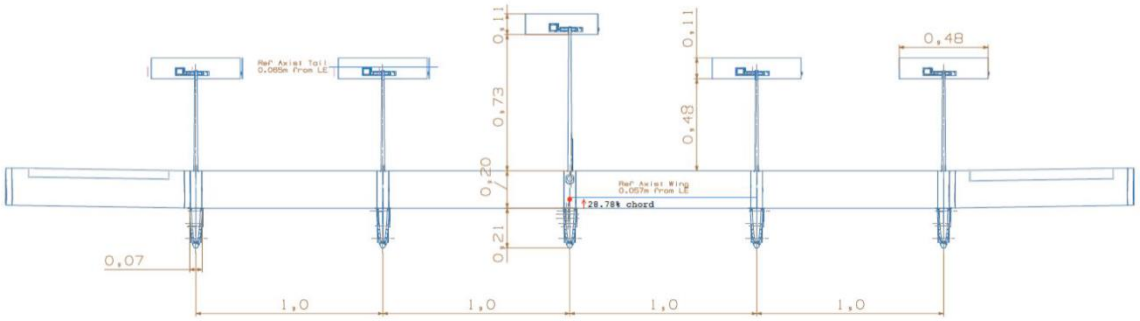

Figure B.1. Dimensioned layout of the X-HALE, units in meters

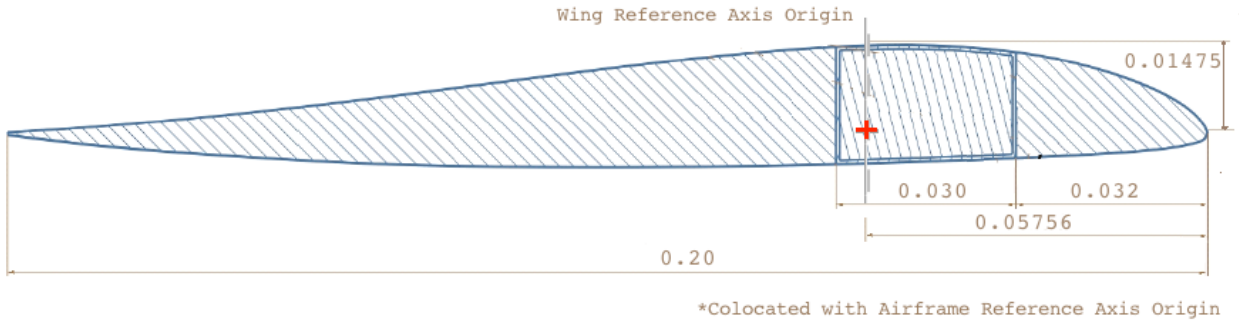

Figure B.2. Dimensioned cross-section of the wing, units in meters

Figure B.3 gives the dimensions of the motor pod and attached tail boom, ventral fin, and tail. This motor pod configuration is used at all positions on the RRV-4 and RRV-6A. On the RRV-6B, the center motor pod is modified to accommodate the stereovision camera system. This pod design is shown in Figure B.4.

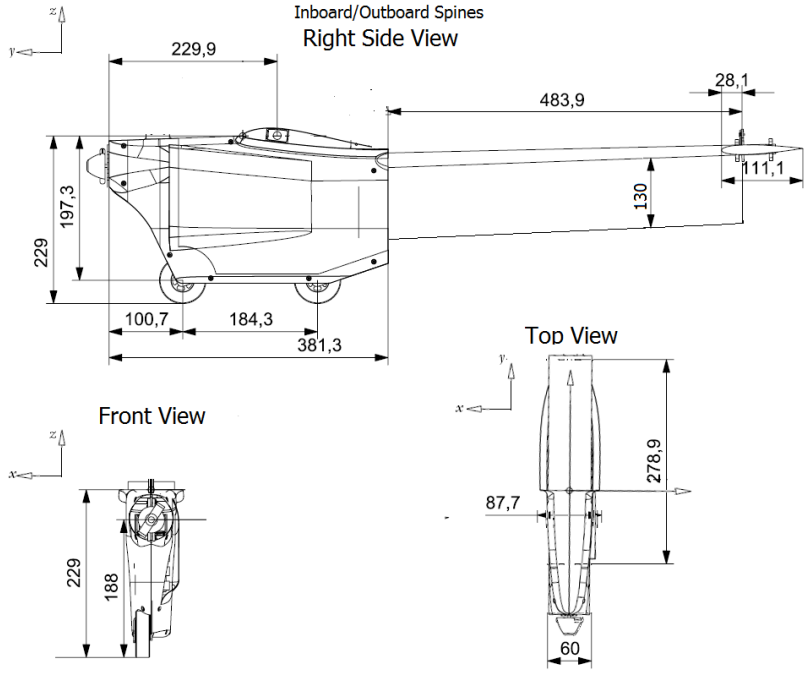

Figure B.3: Dimensioned layout of the X-HALE ATV-B outboard spines, units in mm

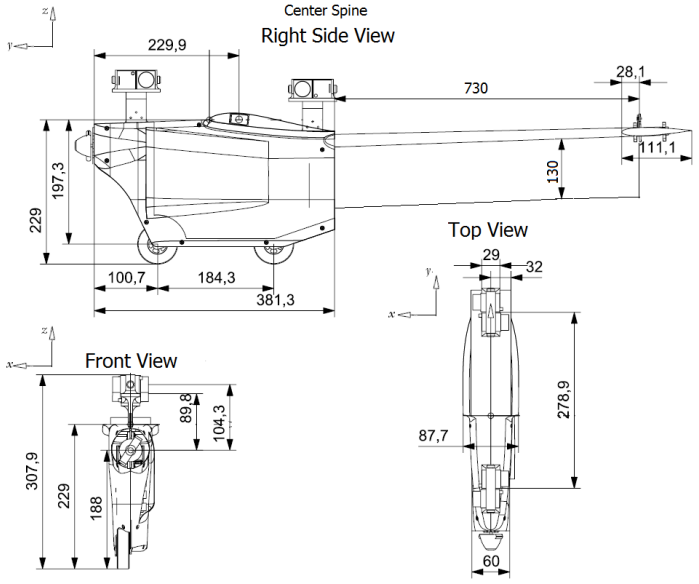

Figure B.4. Dimensioned layout of the X-HALE ATV-B center spine, units in mm

APPENDIX C. X-HALE Wing Stiffness Measurements

The vertical bending and torsional stiffness of the wings of the X-HALE unmanned aircraft were measured over the course of the aircraft development. These measurements were taken each time a new X-HALE configuration was developed and a new batch of wings were constructed. Several wings were selected from each batch and measurements of the wing's deflection at various points along the wing and under different loads were made. The individual wing stiffness was averaged from these measurements, and the average stiffness of all wings were used as the batch stiffness. This appendix details the measurements of the individual wing stiffnesses that were used to calculate the batch stiffnesses for the RRV-6A and RRV-6B presented in Table 4.1.

Table C.1. RRV-6A individual wing bending stiffness measurements

		Out-of-Plane Bending (EI)		Torsion (GJ)		
	Wing Label	Average	Std. Deviation	Average	Std. Deviation	Units
Main Wing	1	104.58	5.88	57.96	5.29	N/m^2
	2	114.61	7.22	61.29	6.42	N/m^2
	3	110.39	6.60	57.19	8.23	N/m^2
	4	103.67	5.97	59.04	5.90	N/m^2
	5	102.61	4.15	54.29	5.19	N/m^2
	6	106.71	9.13	56.70	7.13	N/m^2
	17	99.42	2.88	53.47	6.71	N/m^2
	18	103.94	6.17	55.07	7.48	N/m^2
	Batch Total	105.74	7.22	56.87	7.64	N/m^2
Dihedral Wing	7	79.40	9.21	54.08	7.15	N/m^2
	8	73.23	4.65	54.41	8.42	N/m^2
	Batch Total	76.31	7.293613	54.25	11.05	N/m^2

Table C.2. RRV-6B individual wing bending stiffness measurements

		Out-of-Plane Bending (EI)		Torsion (GJ)		
	Wing Label	Average	Std. Deviation	Average	Std. Deviation	Units
Main Wing	1	131.02	5.024	66.89	8.627	N/m^2
	2					N/m^2
	1+2	117.98	3.23	58.81	5.33	N/m^2
	Batch*	117.98	3.23	58.81	5.33	N/m^2

Stiffness measurements for the RRV-4 are detailed in Reference 63, and the tables for the RRV-6A (ATV-A) and RRV-6B (ATV-B) are taken from References 64-68.

APPENDIX D. X-HALE Aerodynamic Properties

This appendix lists the airfoil lift, viscous drag, and pitching moment coefficient polars used for the X-HALE models. The X-HALE wing has an 0.2-m chord EMX-07 reflexed airfoil. The horizontal tails have a symmetric 0.11-m chord NACA 0012. The ventral fins are modeled with a NACA 0010 airfoil, where the outboard ventral fin has a 0.48-m chord and the center fin has a 0.76-chord. The aerodynamic coefficients of the wing, tail, and ventral fin are calculated using XFOIL. The motor pod has the profile of a symmetric NACA 0018 airfoil, and the lift, drag, and moment polars were derived from wind tunnel data presented in Section 4.5.6.[78] The tail booms are modeled as rigid, cylindrical non-lifting surfaces, thus they have no associated aerodynamic coefficients.

D.1 **Lifting Surface Aerodynamic Properties**

Table D.1. XFOIL coefficients for EMX-07 (wing) airfoil at Re=1.5×10^5

Angle of Attack (deg)	c_l	c_d	c_{dp}	c_m
-6	-0.5053	0.05849	0.05468	-0.0022
-5.5	-0.4751	0.05056	0.04621	-0.0036
-5	-0.4363	0.04471	0.04028	-0.0038
-4.5	-0.3871	0.03851	0.03376	-0.006
-4	-0.3411	0.03426	0.02891	-0.0047
-3.5	-0.3054	0.03062	0.02476	-0.0013
-3	-0.265	0.02748	0.02113	0.0015
-2.5	-0.1816	0.02116	0.01254	0.0064
-2	-0.1268	0.0188	0.00976	0.0079
-1.5	-0.0737	0.01684	0.00757	0.0095
-1	-0.0228	0.01554	0.00603	0.0111
-0.5	0.0202	0.01304	0.0048	0.0135
0	0.1663	0.01252	0.00521	-0.0019
0.5	0.2178	0.0127	0.00506	-0.0013
1	0.2693	0.01291	0.00501	-0.0007
1.5	0.3208	0.01315	0.00506	-0.0001
2	0.3722	0.01345	0.00524	0.0006
2.5	0.4235	0.01381	0.00553	0.0012
3	0.4746	0.01426	0.00589	0.0019
3.5	0.5251	0.01472	0.00624	0.0028
4	0.5763	0.01518	0.00678	0.0034
4.5	0.6271	0.01575	0.00741	0.0041
5	0.6777	0.01636	0.00807	0.0049
5.5	0.7283	0.01694	0.00868	0.0057
6	0.7787	0.01763	0.00957	0.0063
6.5	0.8287	0.01839	0.01055	0.007
7	0.8786	0.01892	0.01121	0.0079
7.5	0.9281	0.01902	0.01144	0.0089
8	0.9775	0.01936	0.01203	0.0098
8.5	1.0265	0.01958	0.01248	0.0108
9	1.074	0.01958	0.0127	0.0118
9.5	1.1178	0.01998	0.01328	0.0127
10	1.1505	0.02236	0.01538	0.0137
10.5	1.1645	0.02685	0.01958	0.0156
11	1.1507	0.03305	0.02585	0.0184
11.5	1.1276	0.04114	0.03411	0.0166
12	1.1235	0.04767	0.04088	0.0157

Table D.2. Chord-normalized airfoil profile for EMX-07 (wing) airfoil at Re=1.5×10^5

Top Surface		Bottom Surface	
x	y	x	y
0.99726	0.00167	0.00274	-0.00495
0.98907	0.00212	0.01093	-0.00831
0.97553	0.00291	0.02447	-0.01113
0.95677	0.00407	0.04323	-0.01362
0.93301	0.00571	0.06699	-0.01571
0.90451	0.00793	0.09549	-0.01751
0.87157	0.01078	0.12843	-0.01916
0.83457	0.01425	0.16543	-0.02077
0.79389	0.01845	0.20611	-0.02236
0.75	0.02339	0.25	-0.02394
0.70337	0.02896	0.29663	-0.02539
0.65451	0.03504	0.34549	-0.02656
0.60396	0.04152	0.39604	-0.02744
0.55226	0.04819	0.44774	-0.02801
0.5	0.05475	0.5	-0.02825
0.44774	0.06091	0.55226	-0.02811
0.39604	0.06636	0.60396	-0.02756
0.34549	0.07074	0.65451	-0.02659
0.29663	0.0736	0.70337	-0.02502
0.25	0.07447	0.75	-0.02273
0.20611	0.07291	0.79389	-0.02013
0.16543	0.06921	0.83457	-0.01755
0.12843	0.06333	0.87157	-0.01497
0.09549	0.05555	0.90451	-0.01225
0.06699	0.04655	0.93301	-0.00947
0.04323	0.0369	0.95677	-0.00688
0.02447	0.02692	0.97553	-0.00466
0.01093	0.01679	0.98907	-0.00296
0.00274	0.00723	0.99726	-0.00189
0	0	1	-0.00152

Table D.3. XFOIL coefficients for NACA 0012 (tail) airfoil at Re=1.5×10^5

Angle of Attack (deg)	c_l	c_d	c_{dp}	c_m
-6	-0.6921	0.01672	0.00842	0.0027
-5.5	-0.655	0.0154	0.0074	0.0058
-5	-0.6168	0.01434	0.00669	0.0087
-4.5	-0.5769	0.01354	0.00619	0.0115
-4	-0.5355	0.01292	0.00588	0.0141
-3.5	-0.4927	0.01247	0.00569	0.0165
-3	-0.4486	0.01215	0.00564	0.0187
-2.5	-0.4042	0.01197	0.00572	0.0208
-2	-0.361	0.01195	0.00599	0.0233
-1.5	-0.2931	0.01218	0.00645	0.0212
-1	-0.2073	0.01249	0.00688	0.0163
-0.5	-0.1107	0.01283	0.00724	0.0096
0	0	0.01296	0.00735	0
0.5	0.1107	0.01283	0.00724	-0.0096
1	0.2073	0.01249	0.00688	-0.0163
1.5	0.293	0.01218	0.00645	-0.0212
2	0.3609	0.01195	0.00599	-0.0233
2.5	0.4041	0.01197	0.00572	-0.0208
3	0.4485	0.01215	0.00564	-0.0187
3.5	0.4926	0.01247	0.00568	-0.0164
4	0.5354	0.01292	0.00588	-0.0141
4.5	0.5768	0.01354	0.00619	-0.0115
5	0.6167	0.01434	0.00669	-0.0087
5.5	0.6549	0.01539	0.0074	-0.0058
6	0.692	0.01672	0.00842	-0.0026
6.5	0.729	0.01824	0.00974	0.0006
7	0.7669	0.01982	0.01123	0.0036
7.5	0.8057	0.0216	0.013	0.0065
8	0.846	0.02388	0.01535	0.009
8.5	0.8864	0.02681	0.01822	0.0111
9	0.9263	0.02906	0.0209	0.0137
9.5	0.9644	0.032	0.02388	0.0156
10	0.9924	0.03644	0.02895	0.0189
10.5	1.0121	0.04099	0.03416	0.0227
11	1.0318	0.04466	0.03812	0.0259
11.5	1.0402	0.05009	0.04381	0.029
12	1.0127	0.05758	0.05182	0.034

Table D.4. XFOIL coefficients for NACA 0010 (ventral fin) airfoil at Re=1.5×10^5

Angle of Attack (deg)	c_l	c_d	c_{dp}	c_m
-6	-0.6733	0.01443	0.00702	0.0001
-5.5	-0.6297	0.01326	0.00582	0.0024
-5	-0.5867	0.01203	0.0048	0.0047
-4.5	-0.5431	0.01093	0.00409	0.0067
-4	-0.4983	0.01003	0.00363	0.0084
-3.5	-0.4523	0.00933	0.00333	0.01
-3	-0.4053	0.00878	0.00315	0.0115
-2.5	-0.3569	0.00836	0.0031	0.0128
-2	-0.3036	0.00804	0.00314	0.0131
-1	-0.1461	0.00757	0.00325	0.0046
-0.5	-0.0689	0.00749	0.00328	0.0013
0	0	0.00747	0.0033	0
0.5	0.0689	0.00749	0.00328	-0.0013
1	0.1461	0.00757	0.00325	-0.0046
1.5	0.2245	0.00774	0.00318	-0.0086
2	0.3037	0.00804	0.00314	-0.0132
2.5	0.3568	0.00836	0.0031	-0.0127
3	0.4052	0.00877	0.00315	-0.0114
3.5	0.4522	0.00933	0.00333	-0.01
4	0.4982	0.01002	0.00363	-0.0084
4.5	0.5429	0.01092	0.00409	-0.0066
5	0.5866	0.01202	0.00479	-0.0047
5.5	0.6296	0.01326	0.00582	-0.0024
6	0.6732	0.01443	0.00702	-0.0001
6.5	0.7157	0.01583	0.00842	0.0023
7	0.7602	0.01714	0.00987	0.0044
7.5	0.8011	0.01946	0.01225	0.0068
8	0.846	0.02115	0.01418	0.0087
8.5	0.8893	0.02315	0.01638	0.0105
9	0.9253	0.02738	0.0209	0.0128
9.5	0.9576	0.03136	0.02546	0.0156
10	0.9855	0.03504	0.02966	0.0185
10.5	0.9973	0.04052	0.03576	0.022
11	0.9832	0.04752	0.04338	0.0263
11.5	0.9297	0.05761	0.05404	0.0273
12	0.8395	0.08211	0.07905	0.0074

D.2 **Motor Pod Aerodynamic Properties**

The lift, drag, and moment curve are derived from wind tunnel tests of the motor pod. These tests were conducted over a range of speeds from 12-20 m/s, and for angles of attack ranging from –8 to +8 degrees. Coefficient data outside of this angle of attack range was calculated using linear extrapolation. For the data presented, the motor was run at 100% power. These tests were conducted in the University of Michigan 2x2 Subsonic Wind Tunnel.

Table D.5. Aerodynamic coefficients of motor pod: fairing off

Angle of Attack (deg)	c_l	c_d	c_{dp}	c_m
-12	-0.2730	0.5373	0.5373	-0.4168
-11.5	-0.2527	0.5433	0.5433	-0.3728
-11	-0.2324	0.5492	0.5492	-0.3288
-10.5	-0.2122	0.5552	0.5552	-0.2848
-10	-0.1919	0.5611	0.5611	-0.2408
-9.5	-0.1716	0.5671	0.5671	-0.1968
-9	-0.1513	0.5731	0.5731	-0.1528
-8.5	-0.1311	0.5790	0.5790	-0.1088
-8	-0.1108	0.5850	0.5850	-0.0648
-7.5	-0.0905	0.5909	0.5909	-0.0208
-7	-0.0702	0.5969	0.5969	0.0232
-6.5	-0.0500	0.6028	0.6028	0.0672
-6	-0.0297	0.6088	0.6088	0.1112
-5.5	-0.0094	0.6147	0.6147	0.1552
-5	0.0109	0.6207	0.6207	0.1993
-4.5	0.0136	0.6201	0.6201	0.1849
-4	0.0164	0.6196	0.6196	0.1705
-3.5	0.0192	0.6191	0.6191	0.1561
-3	0.0220	0.6185	0.6185	0.1417
-2.5	0.0248	0.6180	0.6180	0.1273
-2	0.0275	0.6175	0.6175	0.1129
-1.5	0.0303	0.6169	0.6169	0.0985
-1	0.0331	0.6164	0.6164	0.0841
-0.5	0.0359	0.6159	0.6159	0.0698
0	0.0387	0.6153	0.6153	0.0554
0.5	0.0490	0.6098	0.6098	0.0584
1	0.0594	0.6043	0.6043	0.0614
1.5	0.0698	0.5988	0.5988	0.0644
2	0.0801	0.5932	0.5932	0.0675

Table D.5. Aerodynamic coefficients of motor pod: fairing off, contin.

Angle of Attack (deg)	c_l	c_d	c_{dp}	c_m
2.5	0.0905	0.5877	0.5877	0.0705
3	0.1009	0.5822	0.5822	0.0735
3.5	0.1112	0.5767	0.5767	0.0765
4	0.1216	0.5712	0.5712	0.0796
4.5	0.1320	0.5656	0.5656	0.0826
5	0.1424	0.5601	0.5601	0.0856
5.5	0.1495	0.5641	0.5641	0.0936
6	0.1567	0.5680	0.5680	0.1017
6.5	0.1638	0.5720	0.5720	0.1097
7	0.1710	0.5760	0.5760	0.1177
7.5	0.1782	0.5800	0.5800	0.1257
8	0.1853	0.5839	0.5839	0.1338
8.5	0.1925	0.5879	0.5879	0.1418
9	0.1996	0.5919	0.5919	0.1498
9.5	0.2068	0.5958	0.5958	0.1578
10	0.2140	0.5998	0.5998	0.1659
10.5	0.2211	0.6038	0.6038	0.1739
11	0.2283	0.6077	0.6077	0.1819
11.5	0.2355	0.6117	0.6117	0.1899
12	0.2426	0.6157	0.6157	0.1980

Table D.6. Aerodynamic coefficients of the motor pod: fairing on

Angle of Attack (deg)	c_l	c_d	c_{dp}	c_m
-12	-0.29369	0.41551	0.41551	-0.23481
-11.5	-0.27807	0.428796	0.428796	-0.2228
-11	-0.26245	0.442083	0.442083	-0.2108
-10.5	-0.24684	0.45537	0.45537	-0.19879
-10	-0.23122	0.468656	0.468656	-0.18678
-9.5	-0.21561	0.481943	0.481943	-0.17477
-9	-0.19999	0.49523	0.49523	-0.16277
-8.5	-0.18437	0.508516	0.508516	-0.15076
-8	-0.16876	0.521803	0.521803	-0.13875
-7.5	-0.15314	0.53509	0.53509	-0.12674
-7	-0.13753	0.548376	0.548376	-0.11474
-6.5	-0.12191	0.561663	0.561663	-0.10273
-6	-0.10629	0.574949	0.574949	-0.09072
-5.5	-0.09068	0.588236	0.588236	-0.07871

Table D.6. Aerodynamic coefficients of the motor pod: fairing on, contin.

Angle of Attack (deg)	c_l	c_d	c_{dp}	c_m
-5	-0.07506	0.601523	0.601523	-0.06671
-4.5	-0.06172	0.60135	0.60135	-0.0571
-4	-0.04838	0.601178	0.601178	-0.04748
-3.5	-0.03505	0.601005	0.601005	-0.03787
-3	-0.02171	0.600833	0.600833	-0.02826
-2.5	-0.00837	0.60066	0.60066	-0.01865
-2	0.00497	0.600487	0.600487	-0.00904
-1.5	0.018308	0.600315	0.600315	0.000569
-1	0.031646	0.600142	0.600142	0.010179
-0.5	0.044985	0.59997	0.59997	0.01979
0	0.058323	0.599797	0.599797	0.0294
0.5	0.069729	0.603335	0.603335	0.038657
1	0.081135	0.606872	0.606872	0.047914
1.5	0.092541	0.610409	0.610409	0.057171
2	0.103946	0.613947	0.613947	0.066428
2.5	0.115352	0.617484	0.617484	0.075685
3	0.126758	0.621021	0.621021	0.084942
3.5	0.138164	0.624559	0.624559	0.094199
4	0.14957	0.628096	0.628096	0.103456
4.5	0.160976	0.631633	0.631633	0.112713
5	0.172381	0.635171	0.635171	0.12197
5.5	0.18748	0.62939	0.62939	0.134197
6	0.202578	0.62361	0.62361	0.146424
6.5	0.217677	0.617829	0.617829	0.158651
7	0.232775	0.612049	0.612049	0.170878
7.5	0.247874	0.606268	0.606268	0.183106
8	0.262972	0.600487	0.600487	0.195333
8.5	0.278071	0.594707	0.594707	0.20756
9	0.293169	0.588926	0.588926	0.219787
9.5	0.308267	0.583146	0.583146	0.232014
10	0.323366	0.577365	0.577365	0.244241
10.5	0.338464	0.571585	0.571585	0.256468
11	0.353563	0.565804	0.565804	0.268695
11.5	0.368661	0.560024	0.560024	0.280922
12	0.38376	0.554243	0.554243	0.293149

D.3 **Control Surface Aerodynamic Parameters**

The horizontal elevators are modelled as fully movable surface such that the elevator deflection angle is equivalent to the angle of attack of the elevator airfoil. As such, the elevator does not have coefficient derivatives. The aileron and roll spoiler inputs are implemented as traditional control surfaces, where their aerodynamic loads are increments to the lift of the wing. Table D.7 and Table D.8 list the aerodynamic coefficient derivatives used for the aileron and roll spoiler. The aileron and roll spoiler are both treated as 100% differential control surfaces for X-HALE, meaning that the flap only deploys in one direction. The deflection angles are defined in degrees.

Table D.7. Aileron coefficients

Aileron Deployed Down	Value
Lift coefficient derivative clδ	3.5180
Moment coefficient flap derivative cdδ	-0.461
Drag coefficient derivative cmδ	0.47δ-0.063
Aileron Deployed Up	**Value**
Lift coefficient derivative clδ	3.227
Moment coefficient flap derivative cdδ	-0.5030
Drag coefficient derivative cmδ	0.2040δ-0.012

Table D.8. Roll Spoiler coefficients

Control Surface Parameter	Value
Lift coefficient derivative $c_{l\delta}$	-1.55
Drag coefficient flap derivative $c_{d\delta}$	0
Moment coefficient derivative $c_{m\delta}$	0.2

APPENDIX E. X-HALE Mass and CG Measurements

This appendix details the mass and center of gravity for the RRV-4, RRV-6A and RRV-6B. The mass was measured by placing a pair of scales underneath the front and rear wheel of each motor pod. The center of gravity coordinates calculated from this mass distribution are given with respect to the wing leading edge.

Table E.1. X-HALE assembled aircraft mass and center of gravity measurements

Configuration	RRV-4	RRV-6A	RRV-6B	Units
Front Wheel				
spine 4	--	848.0	429.0	g
spine 2	864.3	5.0	0.0	g
spine 0	669.2	568.0	453.3	g
spine 1	578.1	290.0	0.1	g
spine 3	--	526.0	575.0	g
Front Subtotal	2111.6	2237.0	1457.4	g
Rear Wheel				
spine 4	--	1657.0	1880.7	g
spine 2	1448.0	1594.0	1641.5	g
spine 0	1563.2	2084.0	2959.0	g
spine 1	1809.5	1338.0	1745.3	g
spine 3	--	1988.0	1631.0	g
Rear Subtotal	4820.7	8661.0	9857.5	g
Total				
TotalMass	6932.3	10898.0	11314.9	g
TotalMoment	88700.88	159362.4	181378.0	g-cm
Center of Gravity	23.48%	32.62%	39.65%	% chord behind leading edge
Position 4 Total Mass	--	2505.0	2309.7	g
Position 2 Total Mass	2026.1	1599.0	1641.5	g
Position 0 Total Mass	1563.2	2652.0	3412.3	g
Position 1 Total Mass	3921.1	1628.0	1745.4	g
Position 3 Total Mass	--	2514.0	2206.0	g

APPENDIX F. X-HALE Flight List

Table F.1. Flight Test Summary of the RRV-4 (2010-2011)

#	Flight Date	Configuration	DAQ System	Tests Performed
1	August 2010	4-meter, cg at 23% chord	Ground-based Cameras	TC 0 – Taxi Test TC 1 – Racetrack Loop (incomplete)
2	February 2011	4-m, 6-m, cg at 23% chord	Ground-based Cameras	Indoor Tests – Taxi Test, “Hops”, Roll
3	July 26, 2011	4-m, cg at 23% chord	Ground-based Cameras	TC 0 – Taxi Test TC 1 – Racetrack Loop
4	August 29, 2011	4-m, cg at 23% chord	Ground-based Cameras Eagletree Wireless Telemetry System	TC 0 – Taxi Test TC 1 – Racetrack Loop
5	October 6, 2011	4-m, cg at 23% chord Tail horizontal	Ground-based Cameras	TC 0 – Taxi Test TC 1 – Racetrack Loop TC 2 – Longitudinal Stability Tests with tail flipped to horizontal position
6	October 18, 2011	4-m, cg at 23% chord	Ground-based Cameras MIDG GPS/INS System Eagletree Wireless Telemetry System	TC 0 – Taxi Tests TC 1 – Racetrack Loop (incomplete) TC 2 – Longitudinal Stability Tests
7	November 7, 2011	4-m cg at 23% chord	Ground-based & Onboard Cameras MIDG GPS/INS System Eagletree Wireless Telemetry System	TC 0 – Taxi Tests TC 1 – Racetrack Loop (incomplete)
8	November 21, 2011	4-m, cg at 24% chord	Ground-based Cameras Eagletree Wireless Telemetry System	TC 0 – Taxi Tests TC 1 – Racetrack Loop (incomplete)

Table F.2. Flight Test Summary of the RRV-4 and RRV-6A (2012)

	Flight Date	Configuration	DAQ System	Tests Performed
9	May 17, 2012	4-m cg at 25% chord	Ground-based & Onboard Cameras Eagletree Wireless Telemetry System	TC 0 – Taxi Tests TC 1 – Racetrack Loop (incomplete) TC 2 – Longitudinal Stability Tests
10	June 28, 2012	4-m, c.g. at 25% chord	Ground-based & Onboard Cameras Eagletree Wireless Telemetry System	TC 0 – Taxi Tests TC 1 – Racetrack Loop TC 2 – Longitudinal Stability Tests
11	June 28, 2012	4-m, c.g. at 31.5% chord	Ground-based & Onboard Cameras	TC 0 – Taxi Tests TC 1 – Racetrack Loop TC 2 – Longitudinal Stability Tests
12	June 28, 2012	4-m, c.g. at 34% chord	Ground-based & Onboard Cameras	TC 0 – Taxi Tests TC 1 – Racetrack Loop TC 2 – Longitudinal Stability Tests
13	June 28, 2012	4-m, c.g. at 36% chord	Ground-based & Onboard Cameras	TC 0 – Taxi Tests TC 1 – Racetrack Loop TC 2 – Longitudinal Stability Tests
14	July 9, 2012	6-m, c.g. at 32% chord	Ground-based & Onboard Cameras Eagletree Wireless Telemetry System	TC 0 – Taxi Tests TC 1 – Racetrack Loop (incomplete)
15	July 10, 2012	6-m, c.g. at 32% chord	Ground-based & Onboard Cameras Eagletree Wireless Telemetry System	TC 0 – Taxi Tests TC 1 – Racetrack Loop (incomplete)
16	July 27, 2012	6-m, c.g. at 32% chord, long center tail	Ground-based & Onboard Cameras Eagletree Wireless Telemetry System	TC 0 – Taxi Tests TC 1 – Racetrack Loop (incomplete)

Table F.3. Flight Test Summary of RRV-6A (Camp Atterbury, Aug. 2012)

	Flight Date	Configuration	DAQ System	Tests Performed
17	August 28, 2012	Long Center Tail, No Outboard Ballast Mass, c.g. at 32.5%	Ground-based & Onboard Cameras Eagletree Wireless Telemetry System	TC 0 – Taxi Tests TC 1 – Racetrack Loop (incomplete)
18	August 29, 2012	Long Center Tail, Ventral Fins, c.g. at 32.62%	Ground-based & Onboard Cameras Eagletree Wireless Telemetry System	TC 0 – Taxi Tests TC 1- Racetrack Loop (incomplete)
19	August 29, 2012	Long Center Tail, Ventral Fins, c.g. at 32.62%	Ground-based & Onboard Cameras Eagletree Wireless Telemetry System	TC 0 – Taxi Tests TC 1 -- Racetrack Loop TC 2 -- Longitudinal Stability Tests with tail flipped to horizontal position
20	August 29, 2012	Long Center Tail, Ventral Fins, c.g. at 32.62%	Ground-based & Onboard Cameras Eagletree Wireless Telemetry System	TC 0 – Taxi Tests TC 1- Racetrack Loop TC 3 – Aileron Disturbance with Tail Vertical and Tail Horizontal
21	August 29, 2012	Long Center Tail, c.g. at 32.7%	Ground-based & Onboard Cameras, MIDG GPS/INS System, 5 Hole Probes, Accelerometers, Strain Gages	TC 0 – Taxi Tests
22	August 30, 2012	Long Center Tail, Ventral Fins, Fairings, c.g. at 28.26%	Ground-based & Onboard Cameras Eagletree Wireless Telemetry System	TC 0 – Taxi Tests TC 1 – Racetrack Loop

Table F.4. Flight Test Summary of RRV-6B (2014-2017)

	Flight Date	Configuration	DAQ System	Tests Performed
23	April 24, 2014	Long Center Tail, Ventral Fins, c.g. at 32.62%	Ground-based & Onboard Cameras Eagletree Wireless Telemetry System	TC 0 – Taxi Tests
24	May 14, 2014	Long Center Tail, Ventral Fins, c.g. at 32.62%	Ground-based & Onboard Cameras Eagletree Wireless Telemetry System	TC 0 – Taxi Tests TC 1- Racetrack Loop
25	May 14, 2014	Long Center Tail, Ventral Fins, c.g. at 32.62%	Ground-based & Onboard Cameras Eagletree Wireless Telemetry System	TC 0 – Taxi Tests TC 1 -- Racetrack Loop
26	May 14, 2014	Long Center Tail, Ventral Fins, c.g. at 32.62%	Ground-based & Onboard Cameras Eagletree Wireless Telemetry System	TC 0 – Taxi Tests TC 1- Racetrack Loop TC 3 – Aileron Disturbance with Tail Vertical and Tail Horizontal
27	May 16, 2014	Long Center Tail, Ventral Fins, Fairings, c.g. at 28.26%	Ground-based & Onboard Cameras Eagletree Wireless Telemetry System	TC 0 – Taxi Tests TC 1 – Racetrack Loop (incomplete)
28	May 16, 2014	Long Center Tail, Ventral Fins, Fairings, c.g. at 28.26%	Ground-based & Onboard Cameras Eagletree Wireless Telemetry System	TC 0 – Taxi Tests TC 1 – Racetrack Loop
29	May 30, 2014	Long Center Tail, Ventral Fins, c.g. at 32.62%	Ground-based & Onboard Cameras Eagletree Wireless Telemetry System	TC 0 – Taxi Tests TC 1- Racetrack Loop
30	Oct 1, 2014	Long Center Tail, Ventral Fins, Rudder c.g. at 32.62%	Ground-based & Onboard Cameras Eagletree Wireless Telemetry System	TC 0 – Taxi Tests TC 1- Racetrack Loop
31	May 14, 2017	Long Center Tail, Ventral Fins, c.g. at 32.62%	Ground-based & Onboard Cameras Pixhawk Telemetry and Ground Station	TC 0 – Taxi Tests TC 1 -- Racetrack Loop
32	June 2, 2017	Long Center Tail, Ventral Fins, c.g. at 39.7%	Ground-based & Onboard Cameras Pixhawk Telemetry and Ground Station	TC 0 – Taxi Tests TC 1- Racetrack Loop TC 3 – Roll Spoiler Injection TC4 – Elevator Injection TC 5 – Diff. Thrust Injection TC 6- Throttle Injection

BIBLIOGRAPHY

[1] Zerweckh, S. H., von Flotow, A. H., and Murray, J. E., "Flight Testing a Highly Flexible Aircraft : Case Study on the MIT Light Eagle," *Journal of Aircraft*, vol. 27, pp. 342–349.

[2] van Schoor, M. C., and von Flotow, A. H., "Aeroelastic Characteristics of a Highly Flexible Aircraft," *AIAA Journal*, vol. 27, 1990, pp. 901–908.

[3] Gupta, K., "Development of a Finite Element Aeroelastic Analysis Capability," *Journal of Aircraft*, vol. 33, 1996, pp. 995–1002.

[4] Noll, T. E., Brown, J. M., Perez-davis, M. E., Ishmael, S. D., Tiffany, G. C., and Gaier, M., *Investigation of the Helios Prototype Aircraft Mishap- Volume I Mishap Report*, 2004.

[5] Garcia, J. A., "Numerical Investigation of Nonlinear Aeroelastic Effects on Flexible High-Aspect-Ratio Wings," *Journal of Aircraft*, vol. 42, 2005, pp. 1025–1036.

[6] Seber, G., and Bendiksen, O. O., "Nonlinear Flutter Calculations Using Finite Elements in a Direct Eulerian-Lagrangian Formulation," *AIAA Journal*, vol. 46, 2008, pp. 1331–1341.

[7] Palacios, R., and Cesnik, C. E. S., "Static Nonlinear Aeroelasticity of Flexible Slender Wings in Compressible Flow," *46th AIAA/ASME/ASCE/AHS Structures, Structural Dynamics and Materials Conference*, Austin, Texas: 2005, pp. 1–10.

[8] Hallissy, B. P., and Cesnik, C. E. S., "High-fidelity Aeroelastic Analysis of Very Flexible Aircraft," *Proceedings of 52nd AIAA/ASME/ASCE/AHS/ASC Structures,Structural Dynamics and Materials Conference*, Denver, Colorado: 2011, pp. 1–22.

[9] Drela, M., "Integrated Simulation Model for Preliminary Aerodynamic , Structural , and Control-Law Design of Aircraft," *40th AIAA Structures, Structural Dynamics, and Materials Conference*, St. Louis, Missouri: 1999, pp. 1–14.

[10] Ritter, M., Cesnik, C. E. S., and Krueger, W. R., "An Enhanced Modal Approach for Large Deformation Modeling of Wing-Like Structures," *56th AIAA/ASCE/AHS/ASC*

Structures, Structural Dynamics and Materials Conference, Kissimmee, Florida: 2015, pp. 1–16.

[11] Ritter, M., Jones, J. R., and Cesnik, C. E. S., "Enhanced Modal Approach for Free-flight Nonlinear Aeroelastic Simulation of Very Flexible Aircraft," *15th Dynamics Specialists Conference*, San Diego, California: 2016, pp. 1–17.

[12] Ritter, M., Jones, J. R., and Cesnik, C. E. S., "Free-Flight Nonlinear Aeroelastic Simulations of the X-HALE UAV ny an Extended Modal Approach," *International Forum of Aeroelasticity and Structural Dynamics*, Como, Italy: 2017, pp. 1–19.

[13] Hodges, D. H., "A Mixed Variational Formulation Based on Exact Intrinsic Equations for Dynamics of Moving Beams," *International Journal of Solids and Structures*, vol. 26, 1990, pp. 1253–1273.

[14] Patil, M. J., Hodges, D. H., and Cesnik, C. E. S., "Nonlinear Aeroelastic Analysis of Aircraft with High-Aspect-Ratio Wings," *Journal of Aircraft*, 1998, pp. 1–13.

[15] Patil, M. J., Hodges, D. H., and Cesnik, C. E. S., "Nonlinear Aeroelasticity and Flight Dynamics of High-Altitude Long-Endurance Aircraft," *40th AIAA Structures, Structural Dynamics, and Materials Conferenceth AIAA/ASME/ASCE/AHS Structures, Structural Dynamics, and Materials Conference*, St. Louis, MO: 1999.

[16] Patil, M. J., Hodges, D. H., and Cesnik, C. E. S., "Nonlinear Aeroelastic Analysis of Complete Aircraft in Subsonic Flow," *Journal of Aircraft*, vol. 37, 2000, pp. 753–760.

[17] Peters, D. A., Karunamoorthy, S., and Cao, W.-M., "Finite State Induced Flow Models, Part I: Two Dimensional Thin Airfoil," *Journal of Aircraft*, vol. 32, 1995, pp. 313–322.

[18] Patil, M. J., and Hodges, D. H., "Flight Dynamics of Highly Flexible Flying Wings," *Journal of Aircraft*, vol. 43, Nov. 2006, pp. 1790–1799.

[19] Chang, C. S., Hodges, D. H., and Patil, M. J., "Flight Dynamics of Highly Flexible Aircraft," *Journal of Aircraft*, vol. 45, May 2008, pp. 538–545.

[20] Patil, M. J., and Taylor, D., "Gust Response of Highly Flexible Aircraft," *47th AIAA/ASME/ASCE/AHS/ASC Structures, Structural Dynamics, and Materials Conference*, Reston, Virigina: American Institute of Aeronautics and Astronautics, 2006, pp. 1–13.

[21] Chang, C.-S., and Hodges, D. H., "Parametric Studies on Ground Vibration Test Modeling for Highly Flexible Aircraft," *Journal of Aircraft*, vol. 44, 2007, pp. 2049–2059.

[22] Brown, E. L., "Integrated Strain Actuation in Aircraft With Highly Flexible Composite Wings," Massachusetts Institute of Technology, 2003.

[23] Shearer, C. M., and Cesnik, C. E. S., "Modified Generalized Alpha Method for Integrating Governing Equations of Very Flexible Aircraft," *47th AIAA/ASME/ASCE/AHS/ASC Structures, Structural Dynamics, and Materials Conference*, Newport, Rhode Island: 2006, pp. 1–21.

[24] Shearer, C. M., "Coupled Nonlinear Flight Dynamics, Aeroelasticity, and Control of Very Flexible Aircraft," Univeristy of Michigan, 2006.

[25] Cesnik, C. E. S., and Su, W., "Nonlinear Aeroelastic Modeling and Analysis of Fully Flexible Aircraft," *Proceedings of 46th AIAA/ASME/ASCE/AHS/ASC Structures,Structural Dynamics and Materials Conference*, Austin, Texas: 2005, pp. 1–27.

[26] Su, W., *Coupled Nonlinear Aeroelasticity and Flight Dynamics of Fully Flexible Aircraft*, 2008.

[27] Su, W., and Cesnik, C. E. S., "Strain-based geometrically nonlinear beam formulation for modeling very flexible aircraft," *International Journal of Solids and Structures*, vol. 48, 2011, pp. 2349–2360.

[28] Su, W., and Cesnik, C. E. S., "Nonlinear Aeroelasticity of a Very Flexible Blended-Wing-Body Aircraft," *Journal of Aircraft*, vol. 47, 2010, pp. 1539–1553.

[29] Su, W., Zhang, J., and Cesnik, C. E. S., "Correlations Between UM/NAST Nonlinear Aeroelastic Simulations and Experiments of a Slender Cantilevered Wing," *International Forum of Aeroelasticity and Structural Dynamics*, Seattle, Washington: 2009, pp. 1–16.

[30] Cesnik, C. E. S., Senatore, P. J., Su, W., Atkins, E. M., and Shearer, C. M., "X-HALE: A Very Flexible Unmanned Aerial Vehicle for Nonlinear Aeroelastic Tests," *AIAA Journal*, vol. 50, Dec. 2012, pp. 2820–2833.

[31] Murua, J., Hesse, H., Palacios, R., and Graham, J. M. R., "Stability and Open-Loop Dynamics of Very Flexible Aircraft Including Free-Wake Effects," *52nd AIAA Structures,*

Structural Dynamics, and Materials Conference, Denver, Colorado: 2011.

[32] Singh, A. K., and Nichols, C. W., "Derivation of an Equivalent Beam Model from a Structural Finite Element Model," *The MSC 1988 World Users Conference Proceedings, Vol.1*, 1988, p. Paper No. 14.

[33] Malcolm, D. J., and Laird, D. L., "Extraction of Equivalent Beam Properties from blade Models," *Wind Energy*, vol. 10, 2007, pp. 135–157.

[34] Smith, B., "Aeroelastically Tailored Wing Structures (ATWIST)," *NASA Technical Report*, vol. AR13-592, 2013, pp. 1–19.

[35] Love, M. H., Zink, P. S., Wieselmann, P. A., and Youngren, H., "Body Freedom Flutter of High Aspect Ratio Flying Wings," *46th AIAA/ASME/ASCE/AHS/ASC Structures, Structural Dynamics, and Materials Conference*, Austin, Texas: 2005, pp. 1–23.

[36] Jones, J. R., and Cesnik, C. E. S., "Nonlinear Aeroelastic Analysis of the X-56A Multi-Utility Aeroelastic Demonstrator," *15th Dynamics Specialists Conference*, San Diego, California: 2016, pp. 1–18.

[37] Charmbalis, G., Londono, J., and Cooper, J. E., "Vibration Testing of Aeroelastic Structures Containing Geometric Stiffness Nonlinearities," *54th AIAA/ASME/ASCE/AHS/ASC Structures, Structural Dynamics, and Materials Conference*, Boston, Massachusetts: 2013.

[38] Britt, R. T., Ortega, D., McTigue, J., and Scott, M. J., "Wind Tunnel Test of a Very Flexible Aircraft Wing," *53rd AIAA/ASME/ASCE/AHS/ASC Structures, Structural Dynamics and Materials Conference, Structures, Structural Dynamics, and Materials and Co-located Conferences*, Honolulu, Hawaii: 2012, pp. 1–24.

[39] Chang, C.-S., "Vibration and Aeroelastic Analysis of Highly Flexible HALE Aircraft," Georgia Institute of Technology, 2006.

[40] Böswald, M., Govers, Y., Vollan, A., and Basien, M., "Solar Impulse – How to Validate the Numerical Model of a Superlight Aircraft with A340 Dimensions!," *ISMA International Conference on Noise & Vibration Engineering*, Leuven, Belgium: 2010, pp. 2451–2466.

[41] Böswald, M., Vollan, A., Govers, Y., and Frei, P., "Solar Impulse – Ground Vibration Testing and Finite Element Model Validation of a Lightweight Aircraft," *International Forum of Aeroelasticity and Structural Dynamics*, Paris, France: 2011, pp. 1–20.

[42] Tang, D., and Dowell, E. H., "Experimental and Theoretical Study on Aeroelastic Response of High-Aspect-Ratio Wings," *AIAA Journal*, vol. 39, May 2001, pp. 1439–1441.

[43] Sotoudeh, Z., Hodges, D. H., and Chang, C.-S., "Validation Studies for Aeroelastic Trim and Stability of Highly Flexible Aircraft," *Journal of Aircraft*, vol. 47, Jul. 2010, pp. 1240–1247.

[44] Anon., "Accident Report of the Titan Solara 50," *National Transportation Safety Board Review*, vol. DCA15CA117, 2015.

[45] Burnett, E. L., Atkinson, C., Beranek, J., Sibbitt, B., Holm-Hansen, B., and Nicolai, L., "NDOF Simulation Model for Flight Control Development with Flight Test Correlation," *AIAA Modeleling and Simulation Technologies Conference*, Toronto, Ontario, Canada: American Institute of Aeronautics and Astronautics, 2010, pp. 1–14.

[46] Holm-hansen, B., Atkinson, C., Beranek, J., Burnett, E. L., Nicolai, L., Youssef, H., Martin, L., and Co, A., "Envelope Expansion of a Flexible Flying Wing by Active Flutter Suppression," 2010, pp. 1–10.

[47] Beranek, J., Nicolai, L., Buonanno, M., Burnett, E., Atkinson, C., Holm-hansen, B., and Flick, P., "Conceptual Design of a Multi-utility Aeroelastic Demonstrator," *10th AIAA Aviation Technology, Integration, and Operations (ATIO) Conference*, Fort Worth, Texas: American Institute of Aeronautics and Astronautics, 2010, pp. 1–15.

[48] Ryan, J. J., Bosworth, J. T., Burken, J. J., and Suh, P. M., "Current and Future Research in Active Control of Lightweight, Flexible Structures Using the X-56 Aircraft," *52nd Aerospace Sciences Meeting*, National Harbor, Maryland: 2014, pp. 1–11.

[49] Pak, C., and Truong, S., "Creating a Test-Validated Finite-Element Model of the X-56A Aircraft Structure," *Journal of Aircraft*, vol. 52, 2015, pp. 1644–1667.

[50] Bryson, D. E., and Alyanak, E. J., "Aeroelastic Modeling of the X-56A Using a Rapid

Model Generator for Conceptual Design," *52nd Aerospace Sciences Meeting*, National Harbor, Maryland: 2014, pp. 1–11.

[51] Li, W. W., and Pak, C., "Aeroelastic Optimization Study Based on X-56A Model," *AIAA Atmospheric Flight Mechanics Conference and Exhibit*, Atlanta, Georgia: 2014, pp. 1–21.

[52] Li, W. W., and Pak, C., "Mass Balancing Optimization Study to Reduce Flutter Speeds of the X-56A Aircraft," *Journal of Aircraft*, vol. 3, 2015, pp. 1–7.

[53] Reasor, D. A., Bhamidipati, K. K., and Chin, A. W., "X-56A Aeroelastic Flight Test Predictions," *54th AIAA Aerospace Sciences Meeting*, San Diego, California: 2016, pp. 1–11.

[54] Drela, M., "XFOIL: An Analysis and Design System for Low Reynolds Number Airfoils," *Low Reynolds Number Aerodynamics*, 1989, pp. 1–12.

[55] Drela, M., "ASWING 5.81 Technical Description — Steady Formulation," *ASWING Documentation* Available: http://web.mit.edu/drela/Public/web/aswing/asw_theory.pdf.

[56] Stoll, A. M., Bevirt, J., Moore, M. D., Fredericks, W. J., and Borer, N. K., "Drag Reduction Through Distributed Electric Propulsion," *Aviation Technology, Integration, and Operations Conference*, Atlanta, Georgia: 2014, pp. 1–10.

[57] Schlichting, H., *Boundary-Layer Theory*, McGraw-Hill, 1979.

[58] Cesnik, C. E. S., and Su, W., "Nonlinear Aeroelastic Simulation of X-HALE: A Very Flexible UAV," *49th AIAA Aerospace Sciences Meeting Including the New Horizons Forum and Aerospace Exposition*, Orlando, FL: 2011, pp. 1–13.

[59] Jones, J. R., and Cesnik, C. E. S., "Preliminary Flight Test Correlations of the X-HALE Aeroelastic Experiment," *Aeronautical Journal*, vol. 119, 2015, pp. 855–870.

[60] Pang, Z. Y., Cesnik, C. E. S., Davis, D., and Atkins, E. M., "In - Flight Wing Deformation Measurement System for Small Unmanned Aerial Vehicles," *55th AIAA/ASME/ASCE/AHS/ASC Structures, Structural Dynamics, and Materials Conference*, National Harbor, Maryland: 2014, pp. 1–11.

[61] Cesnik, C. E. S., and Su, W., "Nonlinear Aeroelastic Simulation of X-HALE: A Very Flexible UAV," *49th AIAA Aerospace Sciences Meeting Including the New Horizons*

Forum and Aerospace Exposition, Orlando, Florida: American Institute of Aeronautics and Astronautics, 2011, pp. 1–13.

[62] Matthews, J., "X-HALE Wing Characterization Rig Design Report," *Internal A²SRL Report*, 2010, pp. 1–25.

[63] Matthews, J., "X-HALE Wing Testing Progress Report," *Internal A²SRL Report*, University of Michigan, Ann Arbor: 2010, pp. 1–7.

[64] Moyes, A., and Han, X., "Wing Bending and Torsion Tests," *Internal A²SRL Report*, University of Michigan, Ann Arbor: 2012, pp. 1–5.

[65] Moyes, A., and DeFore, M., "Single Wing Bending/Torsion Comparisons: Post-Flight," *Internal A²SRL Report*, 2012, pp. 1–25.

[66] Lu, A., "Wing Bending/Torsion Test Data," *Internal A²SRL Report*, University of Michigan, Ann Arbor: 2016, pp. 1–40.

[67] Lu, A., and Kusulas, E., "Double Wing Bending/Torsion Test," *Internal A²SRL Report*, University of Michigan, Ann Arbor: 2016.

[68] Ganghadara, K., "Moment of Inertia of Hobby: Air Bearing Procedure," *Internal A²SRL Report*, University of Michigan, Ann Arbor: 2011.

[69] Moyes, A., and DeFore, M., "Moment of Inertia Measurements: Air Bearing," *Internal A²SRL Report*, University of Michigan, Ann Arbor: 2012, pp. 1–11.

[70] Liu, Y., and Carrier, P., "Center of Gravity and Inertia Measurements: Bifilar Pendulum," *Internal A²SRL Report*, 2014, pp. 1–7.

[71] Jardin, M. R., and Mueller, E. R., "Optimized Measurements of Unmanned-Air-Vehicle Mass Moment of Inertia with a Bifilar Pendulum," *Journal of Aircraft*, vol. 46, 2009.

[72] Lu, A., "Moment of Inertia Measurements: Bifilar Pendulum," *Internal A²SRL Report*, University of Michigan, Ann Arbor: 2016, pp. 1–8.

[73] Drela, M., and Youngren, H., "AVL: Athena Vortex Lattice Code" Available: http://web.mit.edu/drela/Public/web/avl/.

[74] Moyes, A., and Gai, A., "Aerodynamic Center Approach of X-HALE," *Internal A²SRL*

Report, 2012, pp. 1–11.

[75] Ananda, G. K., Sukumar, P. P., and Selig, M. S., "Measured Aerodynamic Characteristics of Wings at Low Reynolds Numbers," *Aerospace Science and Technology*, vol. 42, 2015, pp. 392–406.

[76] Brown, H., Han, X., McCarroll, C., and Rhodes, C., "X-HALE Pod Aerodynamic Characterization and Vertical Stabilizer Redesign," *U-M AERO 405 Project Report*, 2012, pp. 1–78.

[77] Hamilton, S., Kitson, R., and Parker, M., "X-HALE Fin Aerodynamic Characterization," *U-M Aero 405 Project Report*, 2013, pp. 1–63.

[78] Carrier, P., Liu, Y., and Logan, H., "Fairing Wind Tunnel Tests," *Internal A²SRL Report*, University of Michigan, Ann Arbor: 2014, pp. 1–16.

[79] Feraboli, P., and Miller, M., "Damage resistance and tolerance of carbon/epoxy composite coupons subjected to simulated lightning strike," *50th ASME/ASCE/AHS/ASC Structures, Structural Dynamics, and Materials Conference*, Palm Springs, Texas: 2009, pp. 1–13.